UNIVERSITÀ DEGLI STUDI DI PADOVA

Dipartimento di Ingegneria Industriale DII

Corso di Laurea Magistrale in Ingegneria Aerospaziale

Numerical Modelling of Hybrid Rocket Boundary Layer Combustion

Relatore: Dr. Francesco Barato

Laureando: Andrea Burel

Matricola: 2063072

Anno Accademico 2024/2025

Abstract

The objective of this work is to numerically model the combustion within the boundary layer of hybrid engines in order to determine, in addition to the classic parameters of internal ballistics, also the efficiency of propellant use. To this end, a quasi – one-dimensional quasi – stationary model of a cylindrical port solid grain was developed, which provides information on the internal ballistics of the hybrid engine. This model is then coupled with the semi-empirical modelling of the boundary layer and the flame within it, developed from Marxman's classical hybrid combustion theory, with the aim of estimating the amount of propellant that actually participates in the combustion process. The latter is a parameter that is not very considered in theoretical publications on hybrid combustion, but it represents a key element in the determination of combustion efficiency. The modelling was done in the MATLAB environment in order to obtain a useful tool during preliminary sizing that allows, without the need for computationally expensive numerical fluid dynamics simulations, to obtain an estimate of the combustion behaviour of the hybrid engine and to investigate in a simplified way the influence of some physical parameters on it.

In Chapter 1 the main characteristics of a hybrid rocket engine will be described, emphasizing the advantages and disadvantages of this type of engine compared to liquid and solid engines.

In Chapters 2 and 3, Marxman's theory is discussed. This theory allows to characterize the physics of hybrid combustion for the classic combinations of oxidizer and fuel in hybrid engines.

In chapter 4 a methodology for the preliminary sizing of a hybrid engine starting from the mission requirements is proposed.

In Chapter 5 a quasi-one-dimensional quasi-stationary model is described for the study of the internal ballistics of a hybrid engine and the influence of some physical parameters on the behaviour of the fluid inside the combustion chamber is evaluated.

In Chapter 6 a numerical model for the boundary layer with a hybrid combustion is proposed. This model implements some corrections to Marxman's theory to better adapt it to the description of the boundary layer inside a closed duct. Starting from the model of the boundary layer above a flat plate in an open environment, a model for the boundary layer inside a closed duct is proposed. The effects of the grain size, the oxidizer mass flux and the type of oxidizer used are evaluated by means of a parametric study.

In Chapter 7 the 1D model and the boundary layer model are coupled, obtaining the 1D with boundary layer model, which allows to describe the internal ballistics of a hybrid engine and evaluate the combustion efficiency. The numerical results related to combustion efficiency will be compared between those obtained experimentally [18] and those obtained from numerical simulations under the same operating conditions, in order to evaluate the validity of the proposed model.

Sommario

L'obiettivo di questo elaborato è quello di modellare numericamente la combustione all’interno dello strato limite dei motori ibridi con il fine di determinare, oltre ai parametri classici della balistica interna, anche l’efficienza di impiego del propellente. A tal fine è stato sviluppato un modello quasi – monodimensionale quasi – stazionario di un grano solido a porta cilindrica, che fornisce le informazioni sulla balistica interna del motore ibrido. A questo modello è stata poi accoppiata la modellazione semi-empirica dello strato limite e della fiamma al suo interno, sviluppata a partire dalla teoria della combustione ibrida classica di Marxman, con l’obiettivo di stimare la quantità di propellente che partecipa effettivamente al processo combustivo. Quest’ultimo è un parametro che viene poco considerato nelle pubblicazioni teoriche riguardanti la combustione ibrida, ma rappresenta un elemento chiave nella determinazione dell'efficienza di combustione. La modellazione è stata fatta in ambiente MATLAB in maniera tale da ottenere uno strumento utile in sede di dimensionamento preliminare che permetta, senza la necessità di onerose simulazioni numeriche fluidodinamiche, di ottenere una stima del comportamento combustivo del motore ibrido e di investigare in maniera semplificata l'influenza di alcuni parametri fisici su di esso.

Nel Capitolo 1 verranno descritte le principali caratteristiche di un motore a razzo ibrido, sottolineando i vantaggi e gli svantaggi di questa tipologia di motore rispetto ai motori liquidi e solidi.

Nei capitoli 2 e 3 verrà descritta approfonditamente la teoria di Marxman che permette di caratterizzare la fisica della combustione ibrida per le classiche combinazioni di ossidante e combustibile nei motori ibridi.

Nel capitolo 4 è proposta una metodologia per il dimensionamento preliminare di un propulsore ibrido a partire dai requisiti di missione.

Nel Capitolo 5 viene riportato un modello quasi – monodimensionale quasi – stazionario per lo studio della balistica di un motore ibrido e viene valutata l'influenza di alcuni parametri fisici sul comportamento del fluido all'interno della camera di combustione.

Nel Capitolo 6 viene proposto un modello numerico per lo strato limite con combustione ibrida che implementa alcune correzioni alla teoria di Marxman per meglio adattarla alla descrizione dello strato limite all'interno di un condotto chiuso. A partire dal modello di strato limite sopra una lastra piana in ambiente aperto, viene proposto un modello per lo strato limite in un condotto prima rettangolare e poi cilindrico. Gli effetti della dimensione del condotto, del flusso di massa di ossidante e della tipologia di ossidante impiegato sono valutati mediante uno studio parametrico.

Nel Capitolo 7 il modello monodimensionale e il modello per lo strato limite vengono accoppiati, ottenendo un modello denominato 1D con modellazione dello strato limite, che permette di descrivere la balistica interna di un motore ibrido e valutarne l'efficienza di combustione. In particolare, verranno confrontati i risultati numerici relativi all'efficienza di combustione tra quelli ottenuti sperimentalmente [18] e quelli ottenuti da simulazioni numeriche nelle stesse condizioni operative, con l'obiettivo di valutare la validità del modello.

Table of Contents

List of Figures

Nomenclature

a, b	Coefficient of thermodynamic quantities profiles
a_1	Constant coefficient
a_x, a	Regression rate coefficient
A	Area
A_b	Burning area
A_{lat}	Lateral area
A_p	Port area
B	Blowing parameter
c^*	Characteristic velocity
C_f	Skin friction coefficient
c_F	Thrust coefficient
C_H	Stanton number
c_p	Specific heat at constant pressure
c_v	Specific heat at constant volume
$\mathcal{D}$	Mass diffusivity
D	Port diameter or generic diameter
D_0	Initial port diameter
Da	Damkhöler number
D_H	Port hydraulic diameter
dt	Instant of time
dx	Volume control element size
F	Fuel entering flame or fuel mass flow (1D model)
f_o	O/F function for the oxidizer flux case
f_t	O/F function for the total flux case

g_0	Standard acceleration of gravity
G	Mass flux
GOX	Gaseous oxygen
h	Enthalpy
HTPB	Hydroxyl-terminated polybutadiene
h, w	Dimensions of the rectangular section duct
h_v	Effective heat of gasification
h_r^0, h_p^0	Enthalpies of formation per unit mass of the reactants and products
I_{sp}	Specific impulse
k	Heat capacity ratio
K_{in}	Inert species mass fraction
K_f	Fuel mass fraction
K_{f_w}	Fuel mass fraction at the grain surface
K_{ox}	Oxidizer mass fraction
K_{ox_e}	Oxidizer mass fraction at the edge of the boundary layer (core flow)
K_{pr}	Combustion products mass fraction
L	Grain length
Le	Lewis number
m	Length exponent or mass
m_{res}	Propellant residual mass
M	Mach number
M_m	Molecular mass
$\dot{m}$	Mass flow rate
$\dot{m}_f''$	Fuel mass flux
$\dot{m}_{f,x}$	Fuel mass flow rate (per unit grain depth) from the grain wall
$\dot{m}_{f,flame}$	Fuel mass flow rate that reaches the flame
$\dot{m}_{ox,bl}$	Oxidizer mass flow rate from the freestream
$\dot{m}_{ox,flame}$	Oxidizer mass flow rate that reaches the flame
$\dot{m}_\delta$	Total mass flow rate inside the boundary layer
$\dot{m}_{\delta,ox}$	Oxidizer mass flow rate inside the boundary layer
$\dot{m}_{\delta,f}$	Fuel mass flow rate inside the boundary layer
$\dot{m}_{\delta,pr}$	Combustion products mass flow rate inside the boundary layer

MEOP	Maximum expected operating pressure
n	Flux exponent or ϕ exponent
O	Oxidizer entering flame or oxidizer mass flow (1D model)
O/F	Oxidizer to fuel mass ratio
$[O/F]_{bl}$	Oxidizer to fuel mass ratio in the boundary layer
$[O/F]_{flame}$	Oxidizer to fuel mass ratio at the flame
$[O/F]_{glob}$	Average (target) oxidizer to fuel mass ratio
$[O/F]_{react}$	Oxidizer to fuel mass ratio of reaction
$[O/F]_{st,mass}$	Oxidizer to fuel mass stoichiometric ratio
$[O/F]_{st,molar}$	Oxidizer to fuel molar stoichiometric ratio
P	Port perimeter
p	Pressure
PMMA	Poly methyl methacrylate
Pr	Prandtl number
q_{comb}	Heat transfer per unit mass of products
Q_{comb}	Heat of reaction
$\dot{Q}$	Rate of heat transfer
R	Specific gas constant or diameter ratio or port radius
$\mathcal{R}$	Universal gas constant
r, θ, x	Cylindrical coordinate system
$\dot{r}$	Regression rate
$\bar{\dot{r}}$	Average regression rate
$\dot{r}_0$	Regression rate based on G_{ox}
$\dot{r}_L$	Regression rate at the exit plane
$\dot{r}_{min}$	Minimum regression rate
$\bar{\dot{r}}_{ox}$	Regression rate averaged over the grain length based on the oxidizer mass flux G_{ox}
$\bar{\dot{r}}_t$	Regression rate averaged over the grain length based on the total mass flux G_t
Re	Reynolds number
$res_{\%}$	Percentage of propellant residual mass
Sc	Schmidt number

t	Time
T	Thrust
t_b	Burn time
u, v	Axial and normal velocity
V	Volume
VL	Volume loading
w	Web thickness
x, y	Cartesian coordinate system
$x_{fd,h}$	Hydrodynamic entry length
x_m	Boundary layer merging length
$x_{m,f}$	Position where the flame reaches the duct axis
x_{min}	Distance at minimum regression rate
y_b	Distance of the flame from the wall
z	Shvab-Zeldovich scalar variable
α	Thermal diffusivity or O/F parameter for the oxidizer flux case
β	O/F parameter for the total flux case
δ	Boundary layer thickness
δ^*	Displacement thickness
Δh	Enthalpy difference between the flame and the wall
$\Delta h/h_v$	Thermochemical parameter
ε	Emissivity
ϵ	Turbulent eddy diffusivity or area ratio
η	Dimensionless normal distance in boundary layer
η_{c^*}	Combustion efficiency
η_{comb}	Propellant combustion efficiency
η_{c_F}	Nozzle efficiency
θ	Momentum thickness
κ	Thermal conductivity
μ	Dynamic viscosity
ν	Kinematic viscosity
ξ_{ox}	Percentage of oxygen in the diluted oxidizer
ρ	Density

ρ_f	Fuel density
σ	Stefan-Boltzmann constant
τ	Viscous shear stress
τ_c	Fluid dynamic time scale
τ_k	Chemical reaction time scale
ϕ	Dimensionless velocity profile

Subscripts

0	Without blowing or total thermodynamic quantity or initial
1	Referred to the entrance of the control volume
2	Referred to the exit of the control volume
a	Ambient
b	Flame zone (burned gas) value
bl	Boundary layer
c	Convective
cc	Combustion chamber
e	Boundary layer edge (core flow) value or nozzle exit section
f	Fuel or final
g	Gas value
i	Internal (to the grain)
I	Interface solid/gas
L	Exit plane
nr	Non-reacting case
ox	Oxidizer
pr	Combustion products
$prop$	Propellant (sum of oxidizer and fuel)
rad	Radiative
ref	Reference
rem	Remaining
s	Surface or solid

t	Total
th	Nozzle throat
w	Wall (surface) value

Symbols

$\propto$	Proportional

Chapter 1

Introduction

In chemical rocket engines the energy released by a high-pressure combustion reaction of chemical propellants heat the reaction product gasses to high temperatures. The gases are then expanded inside a supersonic nozzle and expelled at high speed, obtaining the required propulsive thrust by principle of action and reaction. According to the physical state of the stored propellant, chemical rockets are divided into three main categories: solids, liquids and hybrids (Fig.1.1). In a solid rocket, fuel and oxidizer are mixed in a solid grain stored inside the combustion chamber. In a liquid rocket, the liquid fuel and oxidizer are stored in separate tanks and injected into the combustion chamber. In a (classic) hybrid engine, the fuel is solid and stored in the combustion chamber, while the oxidizer is stored in a tank and injected in the liquid or gaseous phase.

Nowadays, solid and liquid engines are the most widely used in the military and commercial fields, limiting the use of hybrid engines in research programs and in the academic and amateur fields. The reason is related to the characteristics of those propulsion systems. Solid engines are conceptually simple, reliable, require limited maintenance and could reach the highest value of impulse density, making them ideal for military applications, sounding rockets and booster where the size and integrability of the propulsion system play a fundamental role. Liquid rockets can obtain the highest specific impulse, they are throttable, and they can be stopped and started multiple times in flight, making them the type of propulsion system that is generally used for launchers and spacecraft. Hybrid engines have long been considered as intermediate case between those two types, without any clear advantages over either in a performance-oriented environment.

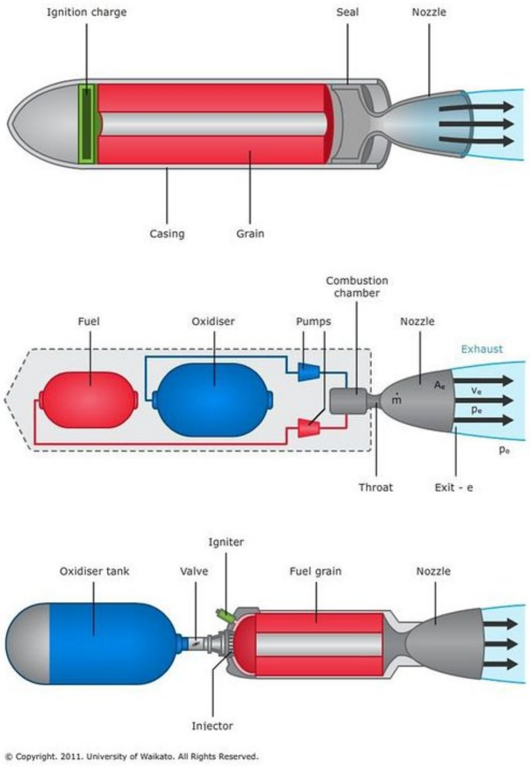

© Copyright. 2011. University of Waikato. All Rights Reserved.

Figure 1.1: Solid (top), liquid (middle) and hybrid (bottom) rocket simplified schematics.

The changes in space business have led to more attention toward safety, reliability, cost, and environmental friendliness of the propulsion system, thus making hybrid engines an interesting choice for many applications. The reasons for the characteristics of a hybrid propulsion system are to be found in the different physics of combustion that occurs in this type of system rather than in solid or liquid engines. In a solid rocket the fuel and the oxidizer are mixed in a single solid phase at a precise (and uniform) O/F ratio and burn with a thin flame next to the surface. The amount of realised propellant depends on the regression rate of the grain surface which in turn is strongly influenced by the chamber pressure. In a liquid engine both the oxidizer and the fuel are injected and mixed near the injector plate, obtaining a uniform mixture whose O/F ratio depends on the corresponding mass flow rates injected into the combustion chamber. For both propulsion system, the O/F ratio and the delivered mass flow rate are therefore independent parameters. On the contrary, in hybrid engines the oxidizer injected at the head of the combustion chamber mixes with the pyrolyzed fuels in a macroscopic turbulent diffusion flame. Moreover, only the oxidizer flow can be directly controlled, while the fuel mass flow rate is dependent on the complex coupling of fluid dynamics and combustion physics. As a result, in a hybrid engine the O/F ratio varies along the grain length and over time, thus making the O/F ratio and mass flow rate two dependent variables.

Due to its peculiar characteristics, hybrid propulsion presents several advantages compared to solids and liquids:

- Safety and reliability. In hybrid engines, the fuel is inert. The system is not explosive as an intimate mixture of oxidizer and fuel is not possible: in fact, unless hypergolic combinations are used, the contact between fuel in the solid phase and oxidizer in the liquid or gaseous phase without an ignition mechanism does not produce any combustion. Furthermore, the way in which hybrid combustion takes place, i.e. through a macroscopic turbulent diffusion flame in which the heat flux towards the wall is regulated (mainly) by convection, accounts for the lower sensitivity to defects of various kinds (e.g. fuel grain cracks) and pressure, making easier the manufacture of the fuel grain (therefore reducing costs) and guarantying the system reliability even with respect to non-nominal conditions. In case of an abort, a hybrid engine, like a liquid-propellant one, can be shut down simply by interrupting the flow of liquid oxidizer.

- Throttling and shutdown. The thrust provided by the engine can be modulated by acting only on the oxidizer mass flow rate injected into the combustion chamber (throttling). This operation is easier than in liquid engines where the fuel and oxidizer mass flow rates must be modulated simultaneously to ensure the correct oxidizer to fuel ratio at any time. The hybrid engine can be started and stopped multiple times if it is equipped with a proper ignition system.

- Propellant versatility and performance. The selection of propellant to be used in hybrid engines is much greater than both solid and liquid engines. Since liquid oxidizer are more energetic than solid oxidizer used in solid propulsion, hybrid engines can obtain values of the theoretical specific impulse comparable to those of liquid engines that use storable propellant (Fig.1.2) and impulse density values between those of solid and liquid systems, particularly for metal loaded fuels.

- Temperature sensitivity. Because the temperature effect on burn rate is small (as in liquids), ambient launch temperature variations have little effect on operating chamber pressure. Thus, the concern in solid rockets in designing for a maximum expected operating pressure (MEOP) is greatly reduced.

- Low cost. Given the lower number of components that contribute to the inert mass of the propulsion system, the cost of a hybrid engine is generally intermediate between the complex and expensive liquid engine and the simple and cheaper solid. The total operating costs of a hybrid engine greatly benefit from its safety features and the use of an inert propellant, which make the production of solid grain easier, safer and cheaper. Furthermore, the system can tolerate larger design margins, resulting in a lower fabrication cost.

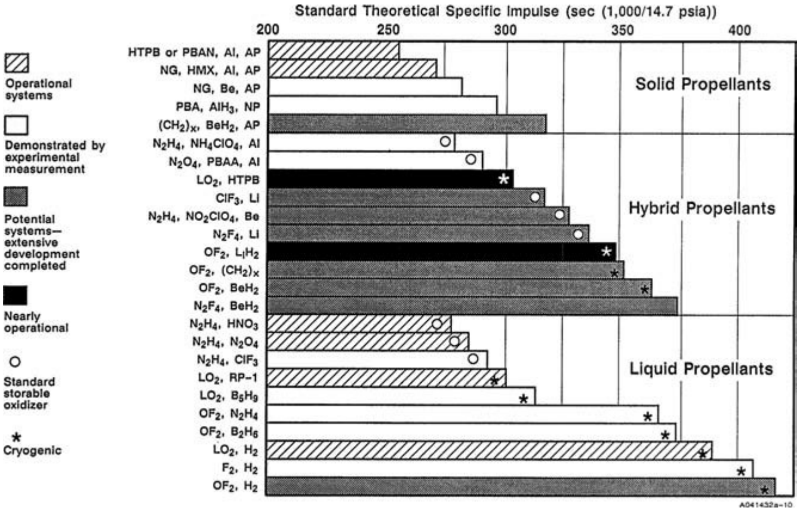

Figure 1.2: Theoretical I_{sp} for various solid, liquid, and hybrid rocket propellants [5].

- Environmental friendliness. Common propellant combinations for hybrid propulsion usually have environmentally clean exhaust without hydrogen chloride or aluminum oxide, which can be ecologically damaging.

Classical hybrid rockets also display several disadvantages with respect to other chemical propulsion systems, including the following:

- Low regression rate. Hybrid engines are generally characterized by low regression rates, mainly due to the limited heat flux exchange by convection between the flame and the solid grain surface, which cannot be solved by using more energetic propellant due to the typical blocking effect related to the blowing of the pyrolyzed

fuel. The problem could be solved with particular configurations (such as multiport grain, diaphragms and vortex injection) and through the use of liquefying propellant, but still without reaching the regression rate values typical of solid rockets.
Moreover, the low regression rate requires small web thickness, which results in poor volume loading (solid propellant volume/total combustion chamber volume). The problem is increased with scale-up, so the main solution used in the past has been the use of multiport grain configurations. However multiport design implies several other problems such as structural issues and the problem of deviation of regression rate for different ports, leading to an increase in complexity and production costs. Hybrid rockets have a limited field of applicability due to the impossibility of combining high thrust, burning time and volume loading.

- Low volumetric loading. In addition to low regression rates leading to poor volumetric loading, the use of aft combustion chambers downstream of the fuel grain to complete the mixing and combustion of fuel and oxidizer further aggravates the mass fraction disadvantage compared to liquid and solid systems. Conventional hybrid propulsion systems, therefore, typically require a larger envelope.

- Packaging issues. In a hybrid rocket the liquid oxidizer tanks can be easily packaged as in a liquid rocket. The geometry of the combustion chamber is dictated by the geometry of the solid grain. Due to the complex dependence of hybrid regression rate on internal fluid dynamics, the possible geometries of the solid grain are much more limited than those that can be used in solid propulsion. Unlike solid engine, in a hybrid engine the fuel mass flow tends to change over time, resulting in a significant variation of the O/F ratio even for a constant mass flow of oxidizer.

- Low combustion efficiency. The nature of the diffusive flame combustion process results in a lower level of mixing due to the stratification of the main flow and therefore a lower specific impulse than its theoretical value. This loss is typically $1-2\%$ greater than in solid and liquid engines. The problem of low combustion efficiency can be greatly reduced by employing configuration that promote the mixing of the flow, such as aft combustion chambers, diaphragms and vortex injection.

- O/F shift. Unlike solid and liquid systems, hybrid rockets usually show a variation over time and with throttling of the O/F ratio of the combustion products, thus leading to a variation in the performance of the system.

- Slower transients. Ignition transients are typically slower for hybrid engines than for liquid engines and so is the response to throttling. This is related to the larger size of the combustion chamber compared to those of a liquid engine and the variability of the operating conditions (primarily the mass flow rate and grain temperature), which makes liquid engines the most appropriate choice when accurate, repeatable and fast responses from the propulsion system are required.

The fact that the theoretical performances of hybrid engines (specific impulse and impulse density) are intermediate between solid and liquid engines make them less attractive when the propulsion system needs to be optimized with respect to only a few performance parameters. On the other hand, the hybrid system provides an interesting alternative to solid and liquid engines if the required characteristics are low cost, safety and operational flexibility. The following list shows some examples of applications for hybrid rocket motors:

- Sounding rockets. Thanks to their low cost, simplicity and operational safety, the most common application of hybrid propulsion systems is for sounding rockets for amateur and academic purposes.

- Auxiliary power units. Hybrid systems can be used as hot gas generators to be used for ignition systems and powering turbines.

- Tactical rockets. If a compact envelope is not too restrictive, a hybrid system has a significant advantage over solid engines because its throttling (energy management) capability.

- Space engines. The hybrid features of throttling and the possibility of multiple ignitions make this type of engines an attractive choice for space manoeuvres.

- Launch boosters. Hybrid systems are also used in small launchers (generally with thrusts below $110\ kN$) for low altitude orbits and limited payload masses.

- Planet landing. The greater simplicity of construction of a hybrid system compared to a liquid and the ability to throttle make very interesting the use of hybrid rockets for possible landing on planets. Furthermore, given the high tolerance on the type of fuel that can be used, they are ideal for exploiting the in-situ production of propellant.

- Space tourism. Due to their high operational safety, hybrid systems would be ideal for use in space tourism application.

Chapter 2

Hybrid Rocket Combustion Theory

The regression rate of a hybrid engine can be limited either by the kinetics of the gas and solid phase reactions or by the convective and radiative heat transfer from the diffusion-limited flame within the boundary layer [9]. The nature of hybrid combustion, in which the vaporizing fuel from the grain must mix and react with an oxidizer flowing above the grain (Fig.2.1) suggests that the second mechanism is usually the limiting process, i.e. the rate of regression is controlled by the fluid dynamics of the turbulent boundary layer that forms above the solid grain and regulates the heat exchange. Experimentally it has also been observed that at low chamber pressure the reaction kinetics can become slow enough to become the limiting mechanism to the regression rate, although the reaction kinetics are of secondary importance in almost all operating pressure ranges and thus can be ignored for practical purposes [9].

The key parameter that influences the fuel grain design and consequently the overall hybrid propulsion system design is the regression rate, defined as the rate at which the solid-phase fuel vaporizes into the gaseous phase and thus as the linear regression rate of the solid surface. The combustion process in a hybrid engine is substantially different from that in a solid or liquid engine. In particular, the prediction of the regression rate in a hybrid engine is very difficult as it varies in time, space and as a function of the scale of the engine: this is due to the fact that the regression rate depends on the chemical and physical characteristics of the chosen propellants as well as on the geometric and fluid dynamic characteristics of the engine itself (i.e. grain geometry and type of injection). Although many physical components of the feeding and thermal protection systems are common to those of other chemical engines, the grain design, internal ballistics, and performance evaluation are different for a hybrid engine.

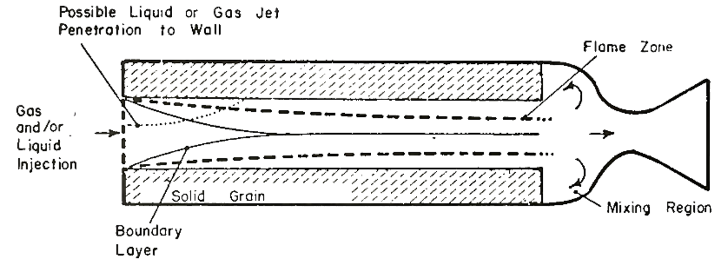

(a) Overall Schematic

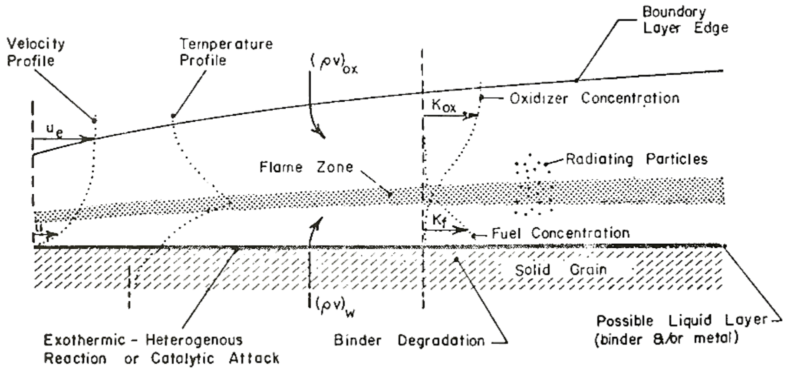

(b) Boundary Layer Schematic

Figure 2.1: Hybrid rocket overall (a) and boundary layer (b) schematic [30].

Hybrid combustion involves the coupling of several fluid dynamic, chemical and thermal processes [5]: pyrolysis of the solid grain, homogenous combustion in gaseous phase, convective and radiative heat transfer in gaseous phase, conduction heat transfer in the solid grain and mass transport of the chemical species.

The injected oxidizer flow above the solid grain results in the formation of a turbulent boundary layer due to the typically high injection Reynolds numbers and the blowing from the solid grain wall that helps the transition. It should be noted that in almost all real hybrids the oxidizer injection is not uniform, and its effects dominate at the head of the grain. These effects tend to greatly increase the local regression rate [7].

The heat from an ignition source reaches the surface of the grain and vaporizes a thin layer of fuel which is then injected in a direction perpendicular to the wall into the flow of the boundary layer. This phenomenon is called blowing and it influences the fluid dynamics and combustion inside a hybrid engine. The mechanisms of transport of the oxidizer and fuel to the flame are diffusive in nature, either turbulent or (to a lesser extent) molecular. The combustion zone in the form of a macroscopic diffusive flame is established where an approximate stoichiometric mixture ratio has been achieved. This position is usually about $10-20\%$ of the boundary layer thickness from the wall, while the thickness of the flame zone is about 10% of the boundary layer thickness [11]. Interestingly, in hybrid engines combustion has been observed fuel-rich [8][11], thus leading to considerably lower flame temperature than the stoichiometric one. A fraction of the vaporized fuel (about $10\ \%$) flows axially below the flame zone without participating to the combustion process; this fuel typically has to be mixed with the remaining oxidizer in an aft combustion chamber to recover the full performance potential of the hybrid system [11].

Once the engine has been started, the combustion process is self-sufficient and self-regulating. The convective and radiative heat transfer from the flame allows grain vaporization (generally the radiative heat contribution is about $5-10\%$ of the convective heat [9], except for special configurations). Increasing the oxidizer mass flow rate leads to a greater convective heat transfer to the wall, thus enhancing the fuel vaporization rate. However, the increased fuel blowing has a blocking effect on a further transfer of convective heat due to the raise of the flame from the surface, reducing the vaporization rate until an equilibrium is reached. This trend towards a self-regulating interaction between heat flux and blowing produces a limit to the rate of regression that can be obtained. Considering that the heat transfer by convection from the flame is lower than what can be exchanged by conduction (which occurs in solid engines), the result is a much lower regression rate of the grain than solid rockets, from a few tenths of mm/s to a few mm/s.

This basic model is based on empirical observation of Schlieren photography (Fig.2.2).

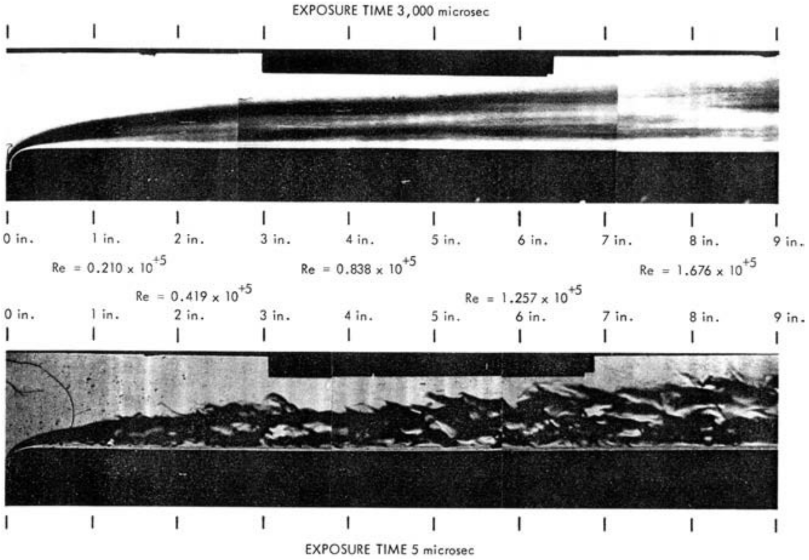

Figure 2.2: Hybrid combustion boundary layer Schlieren photographs [5].

2.1 Marxman’s Theory of Hybrid Combustion

The fundamental theory of hybrid combustion and fuel regression was developed by Marxman and coworkers at the beginning of the '60s [8][9][11]. As already described, within the boundary layer there is a mixture of the oxidizer that diffuses from the external flow and the fuel that evaporates from the wall. The concentration profiles of the chemical species will have a trend that results from the balance of diffusion and convection, while the flame develops where the correct mixture ratio occurs. In a typical hybrid rocket motor, the rate at which chemical reactions occur is much faster than the time required by the reactants to reach the flame. Introducing the Damkhöler number $Da = \frac{\tau_c}{\tau_k}$, defined as the ratio between the fluid dynamic time scale τ_c and the chemical reaction time scale τ_k, it can be said that for hybrid engines $Da \gg 1$, i.e. the combustion is controlled by diffusion rather than chemical kinetics. Therefore, it can be assumed that the combustion at the flame occurs at an infinite fast rate.

It can be demonstrated that in a laminar boundary layer where there is an infinite fast reaction rate the thickness of the flame goes to zero and combustion occurs where the ratio of the concentrations of the reactants is equal to the stoichiometric value. From a mathematical point of view, the flame can therefore be approximated as a line where the concentration of the reactants is zero. This approximation is called flame – sheet approximation. In the case of turbulent boundary layers (such as in hybrid engines) the physics is much more complex as local time and space fluctuations must be taken into account. As observed experimentally by Marxman, these fluctuations lead to a thickening of the flame to values of the order of 10% of the boundary layer thickness. This aspect is usually neglected in order to be able to handle the problem.

Marxman's model therefore assumes the flame-sheet approximation as valid, allowing the division of the boundary layer into two zones: the zone between the solid wall of the grain and the flame in which there is the vaporized fuel and part of reaction product gases; the zone between the flame and the upper edge of the boundary layer where there is the oxidizer and the remaining combustion products.

Marxman's theory considers the simple case of an oxidizer flow over a flat plate (i.e. the solid grain surface) in an open environment. Referring to Fig.2.3, the steady-state energy balance for a control volume of finite thickness on the grain surface is [10]:

$$\dot{Q}_{convection} + \dot{Q}_{radiation\ in} = \dot{Q}_{conduction\ out} + \dot{Q}_{phase\ change} + \dot{Q}_{radiation\ out} \tag{2.1}$$

which can be written per unit area as:

$$\kappa_g \left(\frac{\partial T}{\partial y}\right)_{y=0^+} + \alpha \varepsilon_g \sigma T_b^4 = \kappa_f \left(\frac{\partial T}{\partial y}\right)_{y=0^-} + \rho_f \dot{r} h_v + \varepsilon_w \sigma T_w^4 \tag{2.2}$$

where h_v is the effective heat (enthalpy) of gasification, defined as the energy per unit mass required to vaporize the fuel from the initial temperature of the solid.

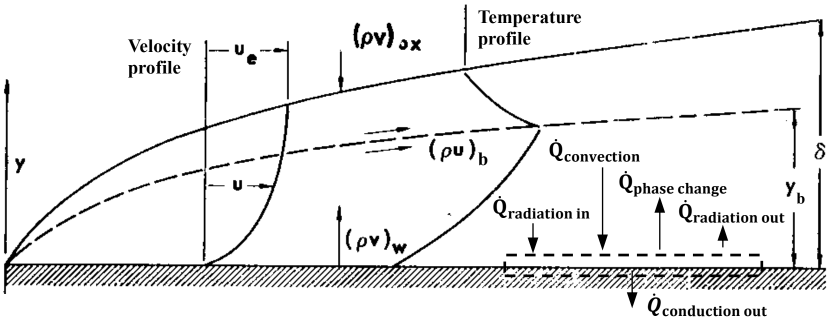

Figure 2.3: Boundary layer combustion model. Adapted from [11].

For many non-metal loaded fuels, the radiative heat flux is negligible. Moreover, since the thermal conductivity of the fuel is usually very low and the hybrid regression rate is sufficiently high, the heat does not have the time to spread inwards the grain leading to an exponential decay of the surface temperature [5]. The conductive contribution of heat is therefore also negligible. In his first theory Marxman neglects the radiative and conduction heat contributions stating that convection heat is the most relevant heat source responsible for the vaporization of the grain. With the above simplifications, under steady-state conditions the convective heat exchanged by the flame with the surface is exactly balanced by the enthalpy flux resulting from the sublimation of the solid grain:

$$\dot{Q}_w = \dot{r} \rho_f h_v \tag{2.3}$$

The heat flux through the boundary layer is proportional to the temperature gradient according to the relation [4]:

$$\dot{Q}_w = -\kappa_g \frac{\partial T}{\partial y} = -\frac{\kappa_g}{c_p}\frac{\partial h}{\partial y} \tag{2.4}$$

Marxman’s theory requires the introduction of some dimensionless numbers [3][10]:

- Reynolds number, Re_x, that measures the ratio between inertia and viscous forces:

$$Re_x = \frac{\rho u x}{\mu} \tag{2.5}$$

- Prandtl number, Pr, that measures the ratio of momentum diffusivity to thermal diffusivity:

$$Pr = \frac{\nu}{\alpha} = \frac{c_p \mu}{\kappa_g} \tag{2.6}$$

- Stanton number, C_H, that measures the ratio of heat transferred into a fluid to the thermal capacity of fluid:

$$C_H = \frac{\dot{Q}}{\rho u \Delta h} \tag{2.7}$$

- Skin-friction coefficient, C_f, a dimensionless quantity defined from the wall shear stress:

$$C_f = \frac{\tau_w}{\frac{1}{2}\rho_e u_e^2} \tag{2.8}$$

- Schmidt number, Sc, defined as the ratio of momentum diffusivity and mass diffusivity:

$$Sc = \frac{\mu}{\rho \mathcal{D}} \tag{2.9}$$

- Lewis number, Le, defined as the ratio of thermal diffusivity to mass diffusivity:

$$Le = \frac{\alpha}{\mathcal{D}} = \frac{\kappa_g}{\rho_e c_p \mathcal{D}} \tag{2.10}$$

  The Lewis number can also be expressed in terms of the Prandtl number and Schmidt number as $Le = Sc/Pr$.

The definition of Stanton number (2.7) can be rewritten as:

$$\dot{Q}_w = C_H \rho_b u_b \Delta h \tag{2.11}$$

Marxman assumes the Prandtl and Lewis numbers (and therefore also the Schmidt number) equal to one between the wall and the flame zone, which is equivalent to stating that all boundary layers (moment, thermal and concentration) have the same thickness. Consequently, it is assumed that the thermal and molecular diffusion mechanisms associated with energy and momentum transfers within the boundary layer are driven by similar turbulent mixing processes.

To evaluate the Stanton number, Marxman employs the Reynolds analogy. The Reynolds analogy states that, under conditions of zero pressure gradient in the direction of flow (as in the case of a flat plate in an open environment) and assuming that $Pr = Sc = 1$, the momentum, energy and concentration equations of the boundary layer have the same form, leading to the relation: $\frac{C_f}{2} = C_H$ [1]. As a result, the enthalpy profile $(\partial h/\partial y)$ in the boundary layer is similar to the velocity profile $(\partial u/\partial y)$ (and to the chemical species concentration profile) and they are linear to each other. The important implication of the Reynolds analogy is that the Stanton number C_H can be evaluated from the knowledge of the velocity profile within the boundary layer as a function of the skin-friction coefficient C_f, whose values for turbulent flow over a flat plate can be obtained experimentally.

Moreover, Marxman considered the fluid as incompressible, a strong (and incorrect) hypothesis but necessary to obtain an analytical solution.

The Reynolds analogy is written as the equivalence of the ratio between heat and the enthalpy gradient and the ratio between viscous stress and the radial gradient of axial velocity:

$$\frac{\dot{Q}}{\partial h/\partial y} = \frac{\tau}{\partial u/\partial y} \tag{2.12}$$

In steady-state conditions the heat flux is constant through the boundary layer, thus equation (2.12) can be integrated between the wall and the generic position as:

$$\frac{\dot{Q}}{\dot{Q}_w} = \frac{\tau}{\tau_w} \tag{2.13}$$

Similarly, equation (2.12) may be integrated from the wall to the flame zone since the object of invoking the Reynolds analogy is to link values at these two points:

$$\frac{\dot{Q}_w}{h_b - h_w} = \frac{\tau_w}{u_b - u_w} \tag{2.14}$$

Since $u_w = 0$ and $\Delta h = h_b - h_w$, equation (2.14) gives:

$$\frac{\dot{Q}_w}{\Delta h} = \frac{\tau_w}{u_b} \tag{2.15}$$

or:

$$\dot{Q}_w = \tau_w \frac{\Delta h}{u_b} \tag{2.16}$$

Recalling the definitions of Stanton number (2.7) and skin-friction coefficient (2.8), from equation (2.16) an alternative expression of the Stanton number in terms of the wall shear stress τ_w or the skin-friction coefficient C_f is derived

$$C_H = \frac{\tau_w}{\rho_b u_b^2} = \frac{1}{2} C_f \frac{\rho_e u_e^2}{\rho_b u_b^2} \tag{2.17}$$

Substituting equation (2.17) into equation (2.11) gives:

$$\dot{Q}_w = \frac{1}{2} \rho_e u_e C_f \frac{u_e}{u_b} \Delta h \tag{2.18}$$

Finally, substituting equation (2.18) into equation (2.3) gives:

$$\dot{r} \rho_f = \frac{1}{2} C_f \rho_e u_e \left(\frac{u_e}{u_b}\right) \left(\frac{\Delta h}{h_v}\right) \tag{2.19}$$

Note that this expression can be derived even without the introduction of Stanton number or an explicit form of the heat flux, simply by combining the expressions (2.3) and (2.15). This reminds that the solution is fundamentally based on writing the regression rate in terms of the energy absorption rate of the fuel and then approximating this rate by assuming that the transfer of energy and momentum are analogous in the region between the flame and the wall [7].

The moment transfer (represented by the skin-friction coefficient) in a turbulent boundary layer with mass injection from the wall need to be described. If no combustion occurs, heat is transfer between the surface and the undisturbed flow and therefore the density and velocity at the flame are equal to those of the undisturbed flow (i.e. $\rho_b = \rho_e$ and $u_b = u_e$). In this case, the Reynolds analogy can be written as:

$$C_{H_0} = \frac{C_{f_0}}{2} \tag{2.20}$$

where the subscript 0 indicates the absence of blowing.

In hybrid combustion, the vaporized fuel flow is perpendicular to the surface of the grain. This is physically analogous to blowing gas through holes on the plate, hence the name. The presence of blowing alters the velocity profile and shear stress compared to the case without blowing. In fact, the mass flow rate evaporating from the grain leads to a thickening of the boundary layer with a consequent reduction of the velocity gradient and therefore of the shear stress and heat flux at the wall.

To be able to link the friction coefficient with blowing to that known from the empirical laws on a flat plate without blowing, it is necessary to make a further assumption. In the current model, the boundary layer extends because of the vaporized fuel being blown from the surface. Since by the Reynolds analogy blowing is expected to have a similar effect on heat and momentum exchange, it can be written:

$$\frac{C_H}{C_{H_0}} = \frac{C_f}{C_{f_0}} \tag{2.21}$$

The skin-friction coefficient without blowing can be evaluated by the well-known empirical law for turbulent boundary layer ($Re_x > 10^5$) with $Pr = 1$ above a flat plate [4]:

$$\frac{C_{f_0}}{2} = 0.03 Re_x^{-0.2} \tag{2.22}$$

where the local Reynolds number Re_x is defined in terms of the properties of the undisturbed current outside the boundary layer. By employing this relationship, two assumptions are implicitly made. First, that the presence of blowing does not change the nature of the phenomenon and does not invalidate the possibility of expressing the friction coefficient with blowing as the corresponding value without blowing and a corrective factor. Second, that the empirical law valid for a flat plate also adequately describes the flow through a typically cylindrical grain. In particular, the latter hypothesis is generally accepted for hybrid engines with axial injection, because the scale of the boundary layer is at least an order of magnitude lower than the radius of curvature of the grain.

Eq. (2.19) can therefore be rewritten as:

$$\dot{r}\rho_f = \frac{1}{2}\left(\frac{C_f}{C_{f_0}}\right) C_{f_0} \rho_e u_e \left(\frac{u_e}{u_b}\right)\left(\frac{\Delta h}{h_v}\right) \tag{2.23}$$

Considering the expression of C_{f_0} in the case of turbulent flow (2.22), finally the basic expression of the regression rate in a hybrid engine can be obtained:

$$\dot{r}\rho_f = 0.03\left(\frac{C_f}{C_{f_0}}\right)\left(\frac{\Delta h}{h_v}\right)\rho_e u_e\left(\frac{u_e}{u_b}\right)Re_x^{-0.2} \tag{2.24}$$

otherwise written as:

$$\dot{r}\rho_f = 0.03\left(\frac{\mu}{x}\right)^{0.2} G^{0.8}\left(\frac{C_f}{C_{f_0}}\right)\left(\frac{u_e}{u_b}\right)\left(\frac{\Delta h}{h_v}\right) \tag{2.25}$$

This equation reflects the fact that the heat transfer to the solid grain is governed by the fluid dynamics of the turbulent boundary layer [9]. The intimate coupling between the regression rate and the flow within the boundary layer is quite complex. For example, the term $C_f/C_{f_0} = C_H/C_{H_0}$ accounts for the partial blocking of the heat flux towards the grain due to the injection of mass from the surface. Consequently, this ratio is a function of the regression rate: it is $0 < C_f/C_{f_0} \leq 1$ and it is equal to unity when there is no combustion.

Using experimental data, Marxman [9] evaluated the influence of blowing by showing its effect on the friction coefficient C_f, the latter expressed as a function of the blowing parameter B (mass – transfer number), defined as the ratio between the fuel mass flux $\dot{m}_f'' = \rho_f \dot{r}$ and the shear stress at the wall:

$$B = \frac{\dot{m}_f''}{\rho_e u_e \frac{C_f}{2}} \tag{2.26}$$

The blowing parameter represents the adimensional form of the vertical flow and is therefore a parameter that allows similarity: different configurations that have the same blowing parameter also have similar velocity profiles. In the case of a flat plate with holes through which the vertical flow is introduced, the blowing parameter B can achieve any value as the external flow and the vertical flow are independent of each other. On the other hand, in a hybrid rocket motor the oxidizer flow can be arbitrarily chosen while the regression rate (and therefore the magnitude of the vertical flow) depends on the physics of hybrid combustion, thus making the blowing parameter B univocally determined.

Comparing equations (2.19) and (2.26), the blowing parameter can also be written as:

$$B = \left(\frac{u_e}{u_b}\right)\left(\frac{\Delta h}{h_v}\right) \tag{2.27}$$

and equation (2.24) can be rewritten as:

$$\dot{r}\rho_f = 0.03\left(\frac{C_f}{C_{f_0}}\right)\rho_e u_e Re_x^{-0.2} B \tag{2.28}$$

In hybrid combustion, the blowing parameter B is a thermochemical parameter determined by the choice of the type of propellant. In fact, the velocity ratio (u_e/u_b) is a function of the position of the flame within the boundary layer that depends upon the combustion properties of the propellant. The enthalpy difference between the flame and the wall (Δh) is strictly based on thermochemistry, while the effective heat of vaporization (h_v) depends on the solid propellant. For equi-diffusive case (i.e. $Le = Pr = 1$), the blowing parameter is a similarity parameter of the boundary layer, i.e. if $B = const$ than the velocity, species concentration and enthalpy profiles are similar and vice versa [7][9]. Because the diffusivities cannot always be assumed equal, some researchers [7] distinguish between the thermochemical blowing parameter B as defined by equation (2.27) and the aerodynamic blowing parameter B' as defined by equation (2.26).

The ratio C_f/C_{f_0} that appears in the regression rate equation represents the reduction of the wall shear stress and therefore the effect of partial blocking due to the blowing on the wall heat transfer (represented by the ratio C_H/C_{H_0}). Its value is expected to be equal to 1 when $B = 0$ and continously decreasing as $B \to \infty$. According to Marxman's analysis [8][9]:

$$\frac{C_f}{C_{f_0}} = \left[\frac{\ln(1+B)}{B}\right]^{4/5}\left[\frac{1+\frac{13}{10}B+\frac{4}{11}B^2}{(1+B)\left(1+\frac{B}{2}\right)^2}\right]^{1/5} \tag{2.29}$$

As can be seen in Fig.2.4, in the range $5 \leq B \leq 100$ the theoretical formula (2.29) is accurately approximated by the simple empirical relationship:

$$\frac{C_f}{C_{f_0}} = 1.2\, B^{-0.77} \tag{2.30}$$

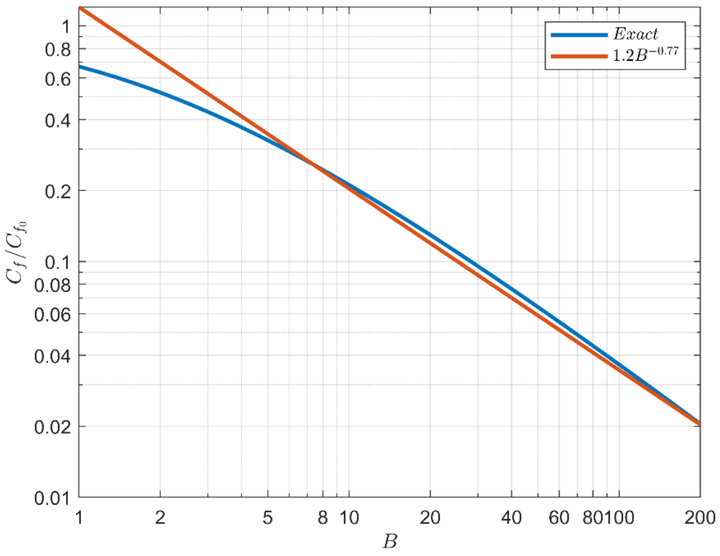

Figure 2.4: Influence of wall mass injection upon skin friction coefficient. Adapted from [9].

However, in the range $5 \leq B \leq 20$, which is of interest in most hybrid system, the formula:

$$\frac{C_f}{C_{f_0}} = B^{-0.68} \tag{2.31}$$

fits Marxman's expression much better (Fig.2.5).

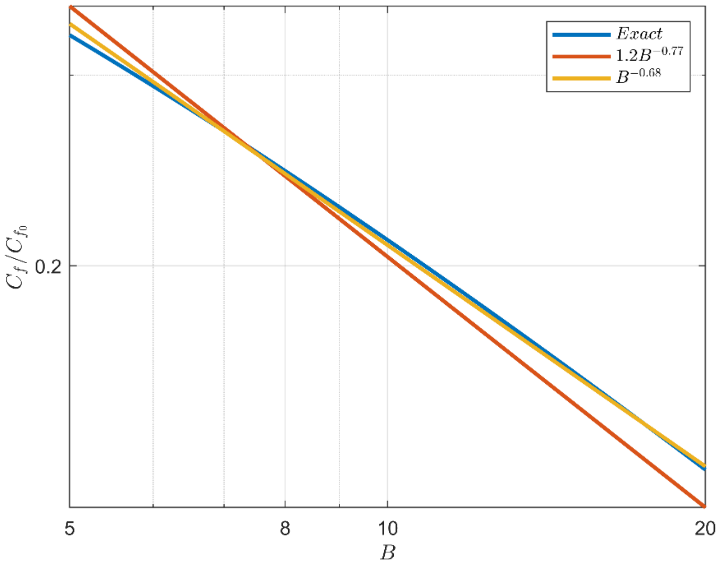

Figure 2.5: Comparison of the expressions for C_f/C_{f_0} in the range $5 \leq B \leq 20$.

Substituting the simplified correction of the Marxman blowing parameter (2.30) in equation (2.28) gives:

$$\dot{r}\rho_f = 0.036 \cdot \rho_e u_e Re_x^{-0.2} B^{0.23} \tag{2.32}$$

or in terms of specific mass flow:

$$\dot{r}\rho_f = 0.036 \cdot G \left(\frac{Gx}{\mu_e}\right)^{-0.2} B^{0.23} \tag{2.33}$$

where the term $G^{0.8} = G \cdot G^{-0.2}$ is typical of convective heat transfer. The equation (2.33) is the classic form of the regression rate formula derived by Marxman (neglecting radiative heat transfer), although it is generally preferred to collect the constant terms and express the regression rate as:

$$\dot{r} = a_1 G^{0.8} x^{-0.2} \tag{2.34}$$

which is very different with respect to the simple empirical expression of the regression rate for a solid motor ($\dot{r} = ap_{cc}^n$) [4].
Combining the blowing parameter with the other constants is justifiable if it is assumed that, as long as $\Delta h/h_v$ does not vary with Re_x, the local regression rate is such that B is constant over the entire length of the grain [9]. While this is not completely true, it is expected B to change very little. The small exponent of B ensures that even a significant change in Δh or h_v will produce negligible effect on the regression rate. The physical explanation for this phenomenon is related to the fluid dynamic coupling that affects hybrid combustion. As Δh increases (or h_v decreases), the regression rate tends to increase. However, the increase of mass injection from the grain surface strengthens the blocking effect, leading to a reduction of convective heat transfer from the flame towards the grain surface and thus reducing the regression rate. As a result, most of the propellants combinations used in hybrid propulsion have regression rates that belong to a small range of values, regardless of the type of fuel used. This effect is different in the case of a system in which radiative heat transfer is significant, because this heat transfer mechanism is coupled differently with the regression

rate: in this type of systems, a significant variation of the regression rate can be achieved by varying Δh or h_v [9].

Fig.2.6 shows the regression rate (2.32) as a function of the position x for several values of the blowing parameter B. $B = 0$ represents the case without combustion. As B increase, there are two concurrent effects: a higher vaporized fuel flux from the surface and a reduction of heat transfer due to the reduction of C_f/C_{f_0} (i.e. to the boundary layer thickening). However, the reduction of C_f/C_{f_0} with B is lower than the increase of B, thus an increase of the blowing parameter B leads to an increase of the regression rate. For high values of B the further increase in the blowing coefficient tends to progressively reduce the further increase of the regression rate: the physical reason for this phenomenon is related to the blocking effect typical of hybrid combustion.

It is necessary to underline that the trend for $x \to 0$ of the regression rate is not correct. In fact, equation (2.32) is singular (i.e. the regression rate goes to ∞) for $x \to 0$ because equation (2.22) is not valid close to the leading edge of the boundary layer. At this point, the regression rate assumes a finite value that depends on the complex (and configuration dependent) fluid dynamics at the leading edge of the grain.

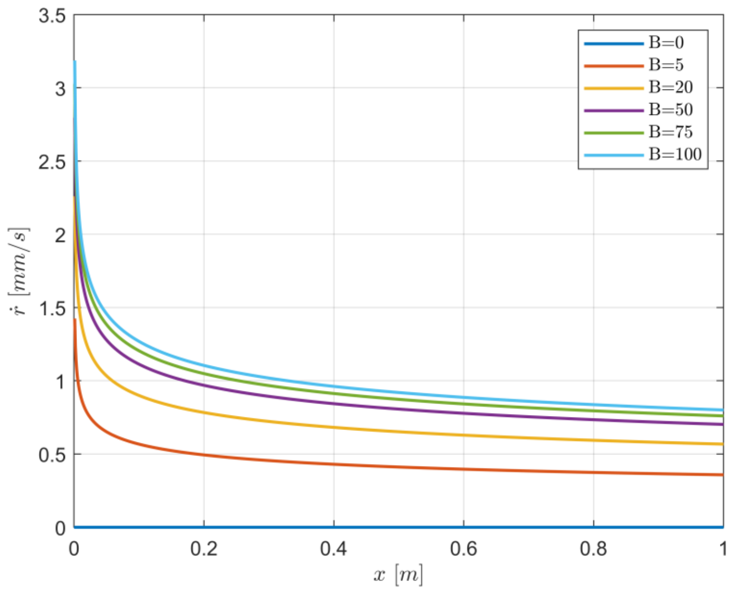

Figure 2.6: Regression rate value as a function of the position x for several values of the blowing parameter B.

Since equation (2.34) is obtained for a turbulent boundary layer with combustion above a flat plate, the experimental measurement of the local regression rate for a hybrid engine is better described by the relation:

$$\dot{r} = a_x G^n x^m \tag{2.35}$$

where a_x, n and m are experimentally evaluated coefficients. The difference in the coefficients values compared to what Marxman predicted should not be surprising given the numerous approximations that have been made to develop the analytical expression of the regression rate. Despite the imperfect coherence with physical reality, Marxman's theory represented a fundamental breakthrough for hybrid propulsion as it has allowed for the first time to understand what are the fundamental parameters that characterize hybrid combustion, while providing a mathematical description of the physical phenomenon.

Equation (2.35) allows to evaluate the physics of the regression rate behaviour in a hybrid engine. If the radiative heat flux is negligible, the local regression rate is independent on the chamber pressure and determined mainly by the local mass flux, which takes into account the injected oxidizer flow rate and all the fuel sublimated upstream of the section x. Therefore, the local flow G, and thus the local regression rate $\dot{r}$, depend on the value of $\dot{r}$ at all points upstream of x.

Moreover, the local mass flux G is inversely proportional to the instantaneous port area along the grain. Therefore, since the port area tends to increase over time, it is expected that both G and $\dot{r}$ are going to increase with axial position and decrease with time. However, it must be considered that the regression rate also shows a weak negative dependence on the axial position, which reflects the effects of the boundary layer growth and the corresponding reduction of the skin-friction coefficient and heat transfer. As the boundary layer thickness increase in the downstream direction, the boundary layer temperature and velocity radial gradients become less intense and the convective heat transfer decreases, thus slowing the combustion. As predicted by Marxman and Gilbert [9], the concurrent effects of increasing mass flow and increasing boundary layer thickness in the downstream direction suggest that there is a position where the regression rate has a minimum. In fact, the regression rate is relatively high near the leading edge of the fuel grain (given the proximity of the flame to the wall) but decreases with the axial position until it reaches a minimum beyond which the regression rate increase. This point of minimum regression rate corresponds to the equilibrium of the two competing effects of boundary layer growth and increase in the local mass flux. The typical trend of the regression rate with the distance from the leading edge is as depicted in Fig.2.7.

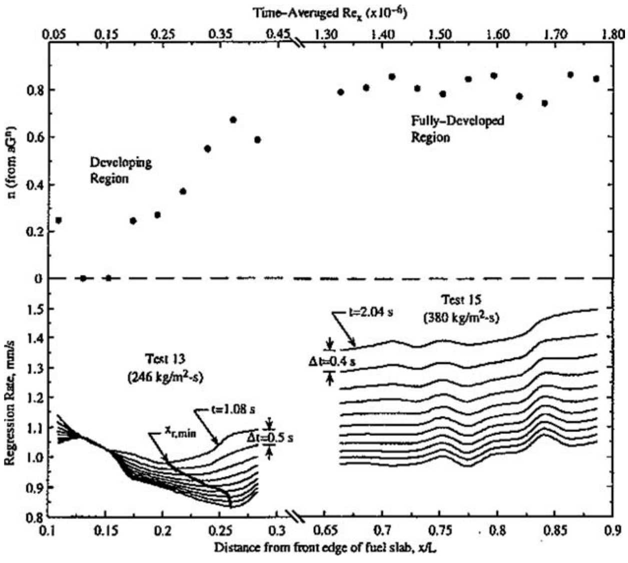

Figure 2.7: Internal ballistic behaviour in a laboratory-scale, slab-geometry hybrid motor [5].

The regression rate expressed by equation (2.35) is defined at a specific axial position x where the port cross-sectional area is $A_p(x)$. The total mass flux is:

$$G(x) = G_{ox} + G_f(x) = \frac{\dot{m}_{ox}}{A_p(x)} + \frac{\dot{m}_f(x)}{A_p(x)} \tag{2.36}$$

where G_{ox} and $G_f(x)$ are the oxidizer and fuel specific mass flux respectively. The form of the regression rate equation that explicitly shows the dependence on x is therefore:

$$\dot{r}(x) = a_x\left[G_{ox} + G_f(x)\right]^n x^m \tag{2.37}$$

where $G_f(x)$ is obtained by integration of the fuel mass flow rates that accumulate along the grain:

$$G_f(x) = 4\rho_f \int_0^x \frac{\dot{r}(x)}{D_H(x)}\, dx \tag{2.38}$$

where $D_H(x) = 4A_p(x)/P(x)$ is the port hydraulic diameter [4]. Due to the implicit nature of equations (2.37) and (2.38), those must be solved numerically, leading to plots such as Fig.2.8 and Fig.2.9 for port diameter and regression rate respectively.

Ignoring the trend for $x \to 0$ (for the same reason explained for equation (2.32)), a hybrid engine allows for a roughly constant regression rate along the entire length of the grain. This relative uniformity of combustion is the result of the increase in the boundary layer thickness represented by the term x^m which causes a reduction in the heat flux exchanged by the flame that progressively moves away from the wall, roughly balanced by the increase in total mass flux due to fuel vaporization.

Moreover, there is an additional compensatory effect over time. As previously mentioned, the concurrent effects of the boundary layer growth and the increase of the local mass flux determine a condition of minimum regression rate beyond which there is an increase of the vaporization rate. It follows that the grain linear regression will be more significant in some sections than in others. The non-uniform distribution of the port cross-sectional areas causes a non-uniform distribution of the specific mass flow rates that leads to higher regression rate where the port area is smaller and vice versa. In conclusion, hybrid combustion down the fuel port provides fairly constant burn rates [4].

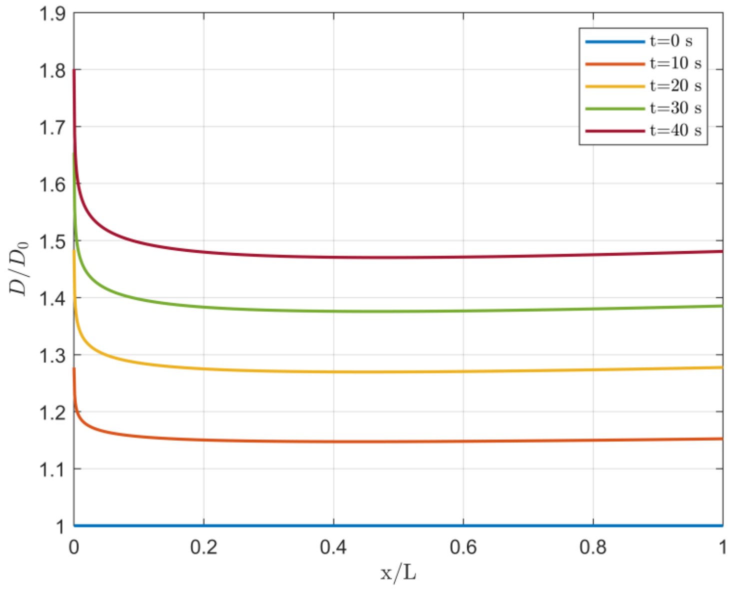

Figure 2.8: Dimensionless port contour D/D_0 (D_0 is the initial port diameter) as a function of dimensionless position x/L along the fuel grain and time.

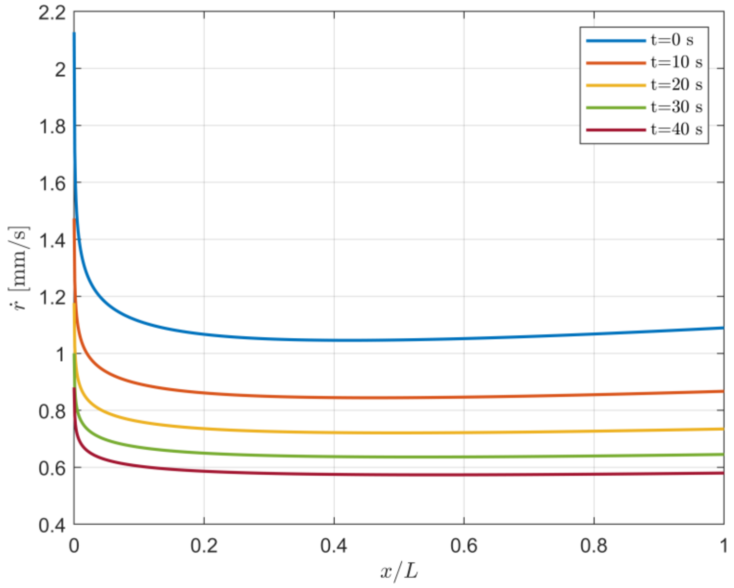

Figure 2.9: Regression rate $\dot{r}$ distribution as a function of dimensionless position x/L along the fuel grain and time.

2.2 Non-Ideal Effect

Marxman's first theory discussed in the previous paragraph is based on several assumptions to achieve a closed form solution that allows to understand which are the most significant parameters in hybrid combustion. The difference of the results obtained by Marxman's theory compared to those experimentally evaluated are caused by some non-ideal effects described briefly in the following.

2.2.1 Radiation

One effect that Marxman neglected at the beginning in deriving his theory is the radiative heat transfer contribution to the total wall heat transfer. Radiative heat transfer in systems where this contribution is negligible is of the order of $5-10\%$ of the convective heat transfer [9]. The radiative heat flux component may originate from various sources, such as the product of combustion, the soot made by incomplete burning of hydrocarbon and metal or other particles liberated from pyrolysis of the solid fuel. Assuming that the burn rates is controlled by heat transfer from the flame to the grain, that the Reynolds analogy is valid and that $Le = Pr = 1$ outside the flame zone, Marxman [7][9] obtained the following equation for the regression rate that considers both the convective and radiative heat contributions:

$$\rho_f \dot{r} = 0.036 \cdot G^{0.8} \left(\frac{x}{\mu}\right)^{-0.2} B^{0.23} + \frac{\sigma \varepsilon_w \left(\varepsilon_g T_b^4 - T_w^4\right)}{h_v} \tag{2.39}$$

where σ is the Stefan – Boltzmann constant, ε_w and ε_g are the wall and the gas emissivity inside the combustion chamber respectively, T_b is the flame temperature (about $3000 - 3500\ K$), T_w is the temperature at the grain surface (about $500 - 1000\ K$). This correction, although simple, does not consider the strong coupling between the heat transfer and the blowing effect. The addition of radiative heat flux increases the fuel vaporization rate which tends to reduce the convective heat transfer to the wall by moving the flame away from the grain surface and therefore reducing the thermal gradient. This behaviour is treated quantitatively by Marxman [9] considering a corrective factor in the form:

$$\frac{B_{rad}}{B} = 1 + \frac{\dot{Q}_{rad}}{\dot{Q}_c} \left(\frac{B_{rad}}{B}\right)^{0.77} \tag{2.40}$$

with

$$\dot{Q}_c = 0.036 \cdot G^{0.8} h_v \left(\frac{x}{\mu}\right)^{-0.2} B^{0.23} \tag{2.41}$$

$$\dot{Q}_{rad} = \sigma \varepsilon_w \left(\varepsilon_g T_b^4 - T_w^4\right) \tag{2.42}$$

Equation (2.40) cannot be solved explicitly, but for most of the values of $0 < \dot{Q}_{rad}/\dot{Q}_c < 3$, the solution can be approximated as:

$$\frac{B_{rad}}{B} = e^{1.3\frac{\dot{Q}_{rad}}{\dot{Q}_c}} \tag{2.43}$$

Combining the previous relationships, the regression rate can be written as:

$$\rho_f \dot{r} = \frac{\left| \dot{Q}_c e^{-\frac{\dot{Q}_{rad}}{\dot{Q}_c}} + \dot{Q}_{rad} \right|}{h_v} \tag{2.44}$$

Equation (2.44) shows that for small values of $\dot{Q}_{rad}/\dot{Q}_c$ the decrease in the convective heat flux is balanced by the radiative heat contribution and therefore the regression rate remains almost unchanged. The correction of $\dot{r}$ is in fact less than 6% for $\dot{Q}_{rad}/\dot{Q}_c < 0.2$. As $\dot{Q}_{rad}/\dot{Q}_c$ increase, the total heat flux $\dot{Q}_w$ towards the grain surface slowly increases and for $\dot{Q}_{rad} \to \infty$ it becomes directly proportional to the radiative heat flux. The coupling between the two forms of heat transfer is clearly visible in Fig.2.10. For $\dot{Q}_{rad} = \dot{Q}_c$ the total heat flux does not double but just increase by 37%, due to the increase of mass injection that moves away the flame, thus reducing the convective heat contribution.

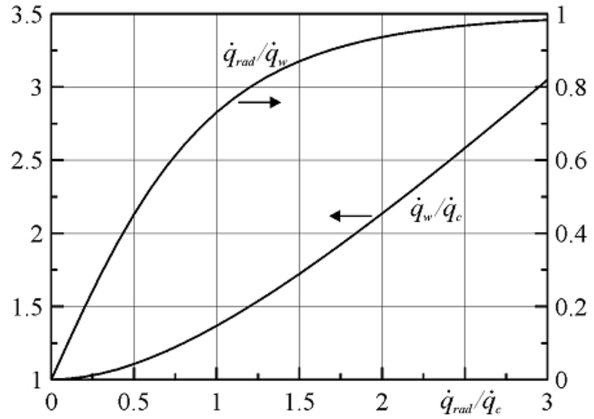

Figure 2.10: Coupling between radiative and convective heat fluxes [8].

An aspect not to be overlooked regarding radiative heat transfer is its dependence on the pressure in the combustion chamber through the density of radiating particles [7]. Fig.2.11 shows the change in the regression rate with the oxidizer mass flow rate for several chamber pressures. At low pressures, for which the radiative term is negligible, the regression rate is the one obtained with the classical convective model, even for low oxidant fluxes. For moderate and high pressures, however, the regression rate trend tends to deviate mainly due to the contribution of radiative heat transfer.

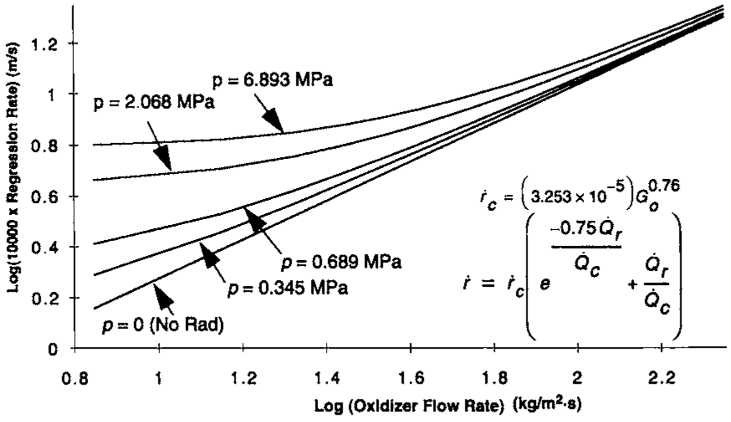

Figure 2.11: Radiation effect on fuel regression rate. Increases in pressure tend to increase regression rate at the lower oxidizer flux [4].

2.2.2 Chemical Kinetics

The diffusion-controlled model developed by Marxman assumes that reactions take place much faster than the diffusion rate and therefore that the flame zone is thin compared to the boundary layer. However, equation (2.34) is no longer valid for high mass fluxes. In fact, under this condition the latency time of the reactants is reduced, and it is no longer possible to states that the ratio between the fluid dynamic time scale and the chemical reaction time scale (i.e. Damkhöler number) is large. Consequently, chemical kinetics can represent the limiting factor to the regression rate, because the rate at which the reactants are transported by diffusion at the flame zone is greater than the rate at which they are consumed. However, the reduction of the regression rate is limited by high chamber pressure conditions which tends to favour chemical processes.

The effects of radiative heat transfer and chemical kinetics on the regression rate can be graphically reported in a double logarithmic diagram of the regression rate as a function of the oxidizer mass flux (Fig.2.12). In fact, in a logarithmic plot Marxman basic relation appears as a straight line with a slope equal to the exponent n. For typical values of oxidizer mass flux, the regression rate is mainly determined by the convective heat transfer and its variation could be due to effects of scale, geometry and additives in the propellant. For high mass flux the slope of the curve decreases because of the limit of chemical kinetic, the effect of which is reduced by an increase in the chamber pressure and chemical reactivity of the propellants. For low mass flux the slopes tend to flatten because of the contribution of the radiative term, with the chamber pressure and the metal particles concentration that tend to amplify the effect.

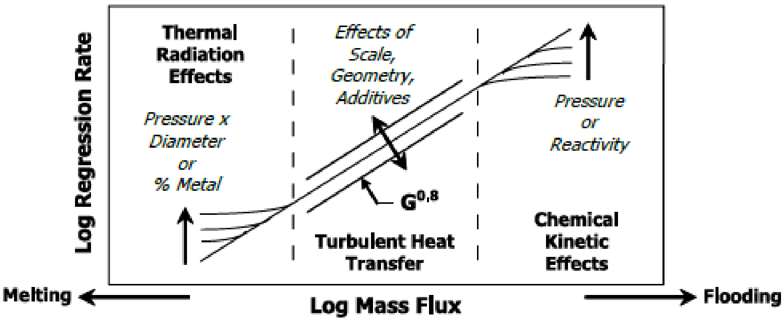

Figure 2.12: Regimes of regression rate dependency [5].

2.2.3 Prandtl Number

The hypothesis $Pr = 1$ could be relaxed to $Pr = const$ [7]. In this case, the thermochemical blowing parameter B differs from the aerodynamic similarity parameter B' according to:

$$B = B' Pr^{0.67} \tag{2.45}$$

As a result, equation (2.33) can be written as:

$$\rho_f \dot{r} = 0.036G \left(\frac{Gx}{\mu}\right)^{-0.2} B^{0.23} Pr^{-0.15} \tag{2.46}$$

Since $Pr \sim 1$ for most gases even at high temperatures, the effect of $Pr^{-0.15}$ remains small enough that correction can be neglected in most cases.

2.2.4 Fluid Properties

Among the simplifications made by Marxman in the development of his theory, the strongest are the incompressibility and the uniformity of the properties of the flow in the boundary layer. The deviation from the ideal condition can have significant consequences on the wall heat transfer and the regression rate due to the variation of the internal gas dynamic and due to the molecular mass of the fuel decomposition products [5][25]. To account for the variability of properties in the boundary layer, some modifications to classical Marxman's theory have been proposed.

The problem was first addressed by Marxman [8] by resorting to a semi-empirical method based on the Howarth-Dorodnitsyn coordinate transformation to relate the actual variable-propriety turbulent boundary layer to an equivalent incompressible boundary layer. By means of the above-mentioned coordinate transformation (valid only in the in the case of constant pressure flows) equation (2.33) is therefore modified into the following one:

$$\rho_f \dot{r} = 0.036G\left(\frac{\rho_{ref}}{\rho_e}\right)^{0.6}\left(\frac{Gx}{\mu}\right)^{-0.2} B^{0.23} \tag{2.47}$$

The reference state ratio ρ_{ref}/ρ_e is determined from a semi-empirical relation described in terms of previously defined parameters and the boundary layer thickness δ that must be measured experimentally. Assuming a linear profile of the density on both sides of the flame, Marxman derived the following relationships [8][28]:

$$\eta_b = \frac{(\rho_b/\rho_e + 1)\eta_{b_{ref}}}{(\rho_w/\rho_e + \rho_b/\rho_e) - (\rho_w/\rho_e - 1)\eta_{b_{ref}}} \tag{2.48}$$

$$\frac{\rho_{ref}}{\rho_e} = \frac{(\delta/x)Re_x^{0.2}\{(\rho_b/\rho_e) + 1 + [(\rho_w/\rho_e) - 1]\eta_b\}}{2\left[\frac{0.0281}{I(B)}(1+B)\frac{\ln(1+B)}{B}\right]^{0.8}} \tag{2.49}$$

where the quantities with the subscript ref are those relative to the reference incompressible boundary layer. The term $I(B)$ is defined in Chapter 3.

Another solution is provided by Paul et al. [46] with a new regression rate law obtained incorporating these features:

$$\rho_f \dot{r} = 0.056 G^{0.8} \left(\frac{x}{\mu}\right)^{-0.2} \left(\frac{\rho_b}{\rho_e}\right)^{0.71} \left(\frac{\rho_w}{\rho_e}\right)^{0.14} B(1+B)^{-0.73+0.002\frac{\rho_w}{\rho_e}} \qquad (2.50)$$

where ρ_w, ρ_b and ρ_e are the densities at the wall, at the flame and outside the boundary layer respectively. However, the strange exponent of the term $(1 + B)$ caused many researchers to raise doubt about the validity and correctness of the above equation.

Due to the added complexity and low reliability, the variable-density corrections are rarely used.

2.2.5 Injection

Marxman theory is based on a diffusion flame formed in a turbulent boundary layer over a flat plate. However, the way the oxidizer is injected can lead to a significant departure from this ideal model by heavily influencing the internal fluid dynamics. As shown by numerous authors, the types of oxidizer injectors influence the regression rate, as well the combustion efficiency and the combustion stability [5][66][67][68]. Several injection geometries have been tested, from simple axial injection to swirl injection which tends to enhance the regression rate [5][69].

2.2.6 Entrainment

The theory for the combustion of liquefying high regression rate fuels, such as paraffins, shown schematically in Fig.2.13, is based on the work done by Karabeyoglu et al. [62][63][64][65]. The solid fuel grain melts and forms a supercritical liquid layer on the surface. The shear force from the incoming oxidizer flow creates roll waves and rips droplets from the melt layer that, because of the turbulence, overcome the flame and burns outside the fuel rich zone. The mechanical rip of droplets is an additional mechanism to the thermal one in the regression of the grain, and it is not subject to the blocking effect unlike the convective heat exchange from the diffusive flame. The result is a dramatically increase of the regression rate by a factor of $3-4$ with respect to classical polymeric fuels.

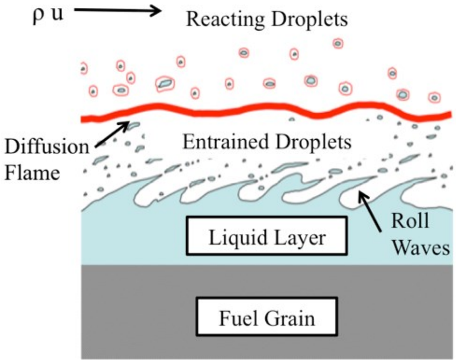

Figure 2.13: Conceptual sketch of the entrainment mechanism predicted for high regression rate hybrid fuels. Oxidizer flow is from left to right [65].

2.3 Averaged Expressions of the Regression Rate

The relative smooth behaviour of hybrid combustion as described before, allow the use of special averaged expression of equation (2.35) for preliminary calculations. In fact, due to the dependence of internal ballistics on mass flow, parameters such as pressure, thrust and O/F ratio vary during engine operation even at constant oxidizer mass flux. In general, it is useful and more convenient to use simple analytical expressions that can predict the behaviour of the various ballistic parameters with reasonable accuracy, based on parameters that are known.

One of the most used averaged expressions of the regression rate is the one based on the oxidizer mass flux G_{ox} injected in the combustion chamber. The average value of the regression rate (2.35) over the grain length is:

$$\bar{\dot{r}} = \frac{1}{L}\int_0^L \dot{r}\, dx = \frac{1}{L}\int_0^L a_x G^n x^m \, dx \tag{2.51}$$

If it is assumed that the O/F ratio is high enough, as generally happens in hybrid propulsion, then $G(x) \sim G_{ox}$, and naming $\dot{r}_0$ the previous average regression rate, then:

$$\dot{r}_0 = \frac{1}{L} a_x G_{ox}^n \int_0^L x^m \, dx = \frac{1}{L} a_x G_{ox}^n \frac{L^{m+1}}{m+1} = \underbrace{\left(\frac{a_x}{1+m}\right) L^m}_{a} G_{ox}^n \tag{2.52}$$

The averaged expression of the regression rate is therefore:

$$\dot{r}_0 = a G_{ox}^n \tag{2.53}$$

where a is the regression coefficient that incorporates the term relative to the length of the grain (L^m). As in the case of the local regression rate expression, there is no dependence on the chamber pressure, but only on the oxidizer mass flux. To obtain the best accuracy from this simplified relationship, it is necessary to experimentally evaluate the constants a and n. Typical values of n are 0.5 ÷ 0.8.

Karabeyoglu, Cantwell and Zilliac [6] derive further expressions for the regression rate averaged over the grain length as a function of two known mass fluxes. In their paper, the authors assumed that the regression rate is constant along the entire length of the grain, reducing the two-dimensional spatial averaging problem to a more manageable one-dimensional problem. Consequently, the port area diameter at a given time is also considered uniform along the grain. Omitting calculations for brevity (available in [6]), the authors derived the exact formula of the average regression rate over the grain length as a function of the oxidizer mass flux G_{ox} and engine characteristics $O/F, n$ and m:

$$\frac{\dot{\bar{r}}_{ox}}{a_x G_{ox}^n L^m} = \frac{1}{1+m} \frac{1-n}{\left[\left(1+\frac{1}{O/F}\right)^{1-n} - 1\right] O/F} = \frac{1}{1+m} f_o(O/F) \tag{2.54}$$

where the corrective factor is:

$$f_o(O/F) = \frac{1-n}{\left[\left(1+\frac{1}{O/F}\right)^{1-n} - 1\right] O/F} = \frac{1-n}{\alpha(O/F)} \tag{2.55}$$

and the parameter α is:

$$\alpha = \left(1 + \frac{1}{O/F}\right)^{1-n} - 1 \tag{2.56}$$

In a similar way, the exact formula of the average regression rate over the length of the grain as a function of the total mass flux $G_t = G_{ox} + G_f$ and engine characteristics $O/F, n$ and m is also derived:

$$\frac{\bar{\dot{r}}_t}{a_x G_t^n L^m} = \frac{1}{1+m} \frac{1-n}{\left[1 - \left(\frac{O/F}{1+O/F}\right)^{1-n}\right](1+O/F)} = \frac{1}{1+m} f_t(O/F) \tag{2.57}$$

where the corrective factor is:

$$f_t(O/F) = \frac{1-n}{\left[1 - \left(\frac{O/F}{1+O/F}\right)^{1-n}\right](1+O/F)} = \frac{1-n}{\beta(1+O/F)} \tag{2.58}$$

and the parameter β is:

$$\beta = 1 - \left(\frac{O/F}{1+O/F}\right)^{1-n} \tag{2.59}$$

Parameters α and β (Fig.2.14) and corrective factors $f_o(O/F)$ and $f_t(O/F)$ (Fig.2.15) are plotted as a function of O/F for various n exponents. For $O/F \rightarrow \infty$, as in the case of very short motors or with low regression rate (i.e. small variation of the mass flux along the grain), the parameters α and β go to zero, while the corrective factors become unity: this is absolutely predictable since for $O/F \rightarrow \infty$ the mass flux in a section (including the final one) tends to the oxidizer flow only.

It is also observed that both corrective factors are more significant for low O/F ratios, because of the much greater increase of the mass flux along the grain, and for high coefficients n, which further amplify the variation of the specific flow by increasing the regression rate. For $n = 0$ (not of practical interest for hybrid engines, but didactically interesting), the corrective factors become unity, due to the loss of dependence of the regression rate on the mass flux.

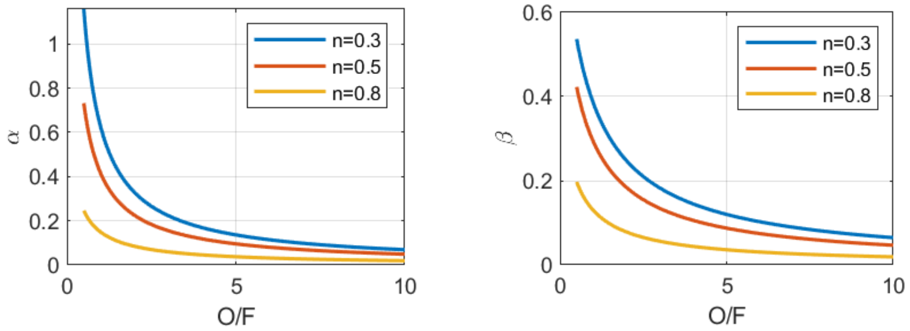

Figure 2.14: Coefficients α and β as a function of O/F for various n exponents.

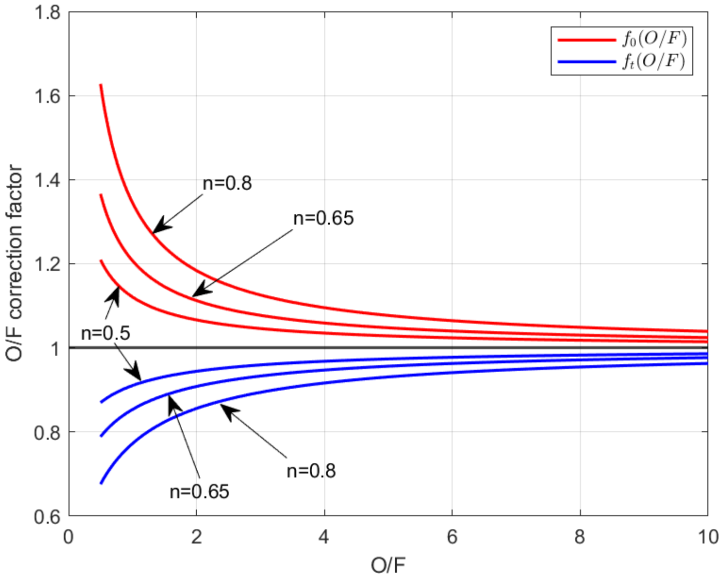

Figure 2.15: Effect of the motor O/F on the regression rate formula based on the oxidizer mass flux and total mass flux [6].

The equations (2.54) and (2.57) obtained by the authors allow the definition of different expressions for the regression rate averaged over the length of the grain, depending on the type of mass flux used (G_{ox} or G_t). In those expressions, the effect of grain length on regression rate is considered in the term $1/(1+m)$ which results from the integration of the position along the grain (i.e. x^m). The primary physical cause of this term is the boundary layer thickening. The flux effect is represented by a complex function of O/F, $f_o(O/F)$ and $f_t(O/F)$.

It is possible to make a comparison between the various expressions of the averaged regression rate. In particular, the value of the average regression rate calculated from the local regression rate formula (2.35):

$$\dot{\bar{r}} = \overline{a_x G^n x^m} \tag{2.60}$$

will be compared with the values obtained with equations (2.53), (2.54) and (2.57) with and without the correction factors, and with the formula based on the average mass flux $(G_{ox} + G_t)/2$ without any correction factor:

$$\dot{\bar{r}}_m = \frac{a_x}{1+m}\left(\frac{G_{ox} + G_t}{2}\right)^n L^m \tag{2.61}$$

Since O/F ratio usually varies (O/F shift), also α, β and the corrective factors are also functions of time. The following figures show the regression rate distribution (2.35) as a function of the axial position. Fig.2.16 shows the comparison between the expressions, considering the corresponding corrective factors for $\dot{\bar{r}}_{ox}$ and $\dot{\bar{r}}_t$: values from all expressions are practically coincident with equation (2.60).

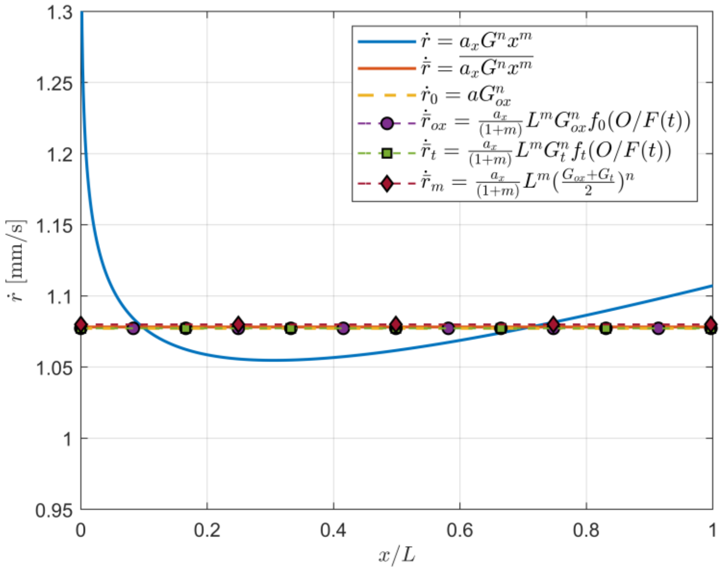

Figure 2.16: Comparison between different expressions for average regression rate, considering the correction factors and referring to the instantaneous global value of O/F, α and β.

Fig.2.17 shows the comparison between the expressions without considering the corresponding corrective factors. In this case, the only expressions that coincides with the average value of the local regression rate (2.60) is the one considering the average specific mass flow (2.61) and equation (2.53), while the expression of $\dot{\bar{r}}_{ox}$ underestimates its value (because $f_o(O/F) > 1$) and the expression of $\dot{\bar{r}}_t$ overestimates its value (because $f_t(O/F) < 1$).

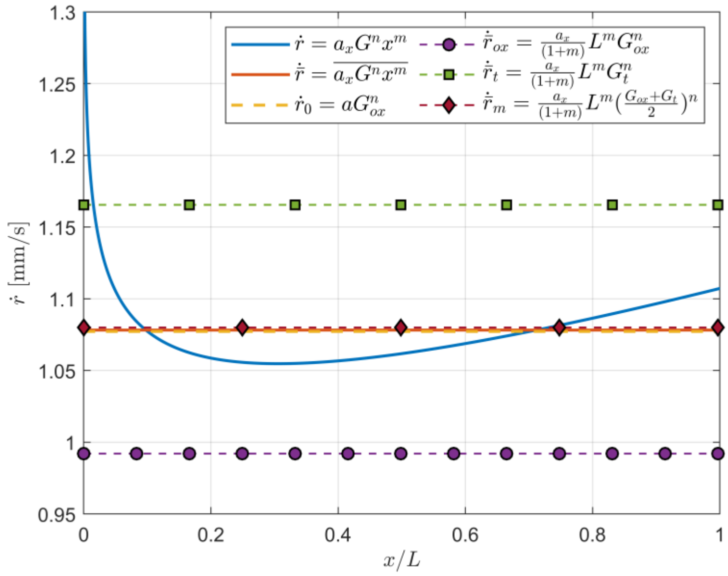

Figure 2.17: Comparison between different expressions for average regression rate, without considering the correction factors and referring to the instantaneous global value of O/F, α and β.

If the corrective factors are calculated with the average global O/F ratio, an error is made in the average regression rate estimation due to the incorrect evaluation of instantaneous parameters α and β. Fig.2.18 shows the comparison between the expressions with the corresponding corrective factors.

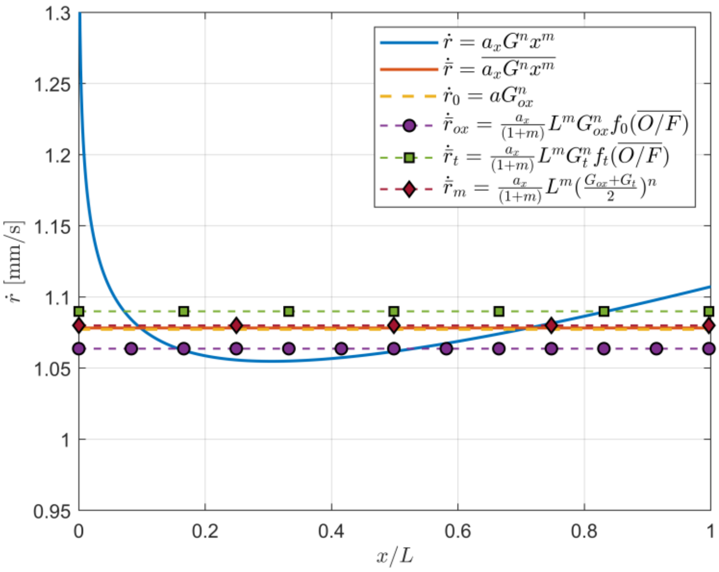

Figure 2.18: Comparison between different expressions for average regression rate, considering the correction factors and referring to the global average value of O/F, α and β.

2.4 Flooding and Cooking Limits

Most empirical and theoretical investigations have shown that the regression rate of the solid grain is highly dependent on the local mass flow. However, the range of regression rate values of practical interest is defined by two mass flow extreme values: the upper limit, often called the flooding limit, and the lower limit referred to as the cooking limit [7][9].

Flooding corresponds to a situation where the oxidizer flow is high enough to prevent combustion or has increased to the point where the flame is blown out of the combustion chamber, presumably due to finite reaction rates that cannot keep up with fluid dynamic mixing rates at high mass flux levels or at the development of very oxidizer rich conditions. The flooding limit also seems to depend on the specific propellant combination and chamber pressure, thus becoming less problematic when highly reactive propellants are used. Typical values of the maximum oxidizer mass flux to avoid flooding are around $800 - 1000\ kg/(m^2 s)$, although higher flows rate can be used by increasing the pressure in the combustion chamber.

On the other hand, at very low mass flows, the limited amount of oxidizer could also extinguish combustion. In addition, the convective heat flux to the fuel surface and therefore the regression rate are low, and the heat can spread deep into the grain of the solid fuel. This situation is called cooking. Depending on the specific type of fuel, this situation can lead to cooking reactions that can cause the fuel substrate to undergo depolymerization reactions well below the surface, thus altering its mechanical properties. According to Marxman [9] this situation can lead to unwanted changes in fuel properties and poor combustion efficiency. For Plexiglas/oxygen systems, Marxman showed that the minimum regression rate before this phenomenon becomes important is about $0.1\ mm/s$, which is probably lower than any practical application. Typical values for the minimum oxidizer flux are around $5 - 10\ kg/(m^2 s)$.

2.5 O/F shift

A peculiar feature of hybrid combustion is that a real steady-state condition is never achieved, due to the variation of propellant mass flow with time and throttling (i.e. variation of the thrust by varying the oxidizer flow injected into the combustion chamber). This phenomenon is generally referred to as O/F shift and leads to a variation of the propulsion system performances. Considering the regression rate described with equation (2.53) the fuel mass flux is given by:

$$G_f = \frac{\dot{r}_0 \rho_f P L}{A_p} = \frac{a G_{ox}^n \rho_f P L}{A_p} \tag{2.62}$$

where P, L, A_p are evaluated at position x. The expression of the O/F ratio for circular port (similar considerations can also be made for non-circular port [4]) is:

$$O/F = \frac{\dot{m}_{ox}^{1-n} D^{2n-1}}{4^n \rho_f \pi^{1-n} a L} \tag{2.63}$$

where it is clear the dependence of the O/F ratio on port diameter D and oxidizer flow rate $\dot{m}_{ox}$. Fig.2.19 shows the O/F shift as a function of the diameter ratio $R = D/D_0$ for several regression rate coefficient n with constant oxidizer flow rate $\dot{m}_{ox}$. Since the exponent of D

is $2n - 1$, if $n = 0.5$, no O/F shift occurs. In this case, all global parameters (fuel mass flow, chamber pressure and motor thrust) remain constant even after the increase in the port area. If $n > 0.5$ then the O/F ratio increase due to a higher reduction of regression rate in respect to the increase in burning area, leading to a reduction of fuel mass flow, chamber pressure and motor thrust. If $n < 0.5$, the lower sensitivity of the regression rate to the port diameter leads to a lower reduction in the regression rate on which prevails the increase in the burning area. The result is a reduction of the O/F ratio and an increase of propellant mass flow, chamber pressure and engine thrust.

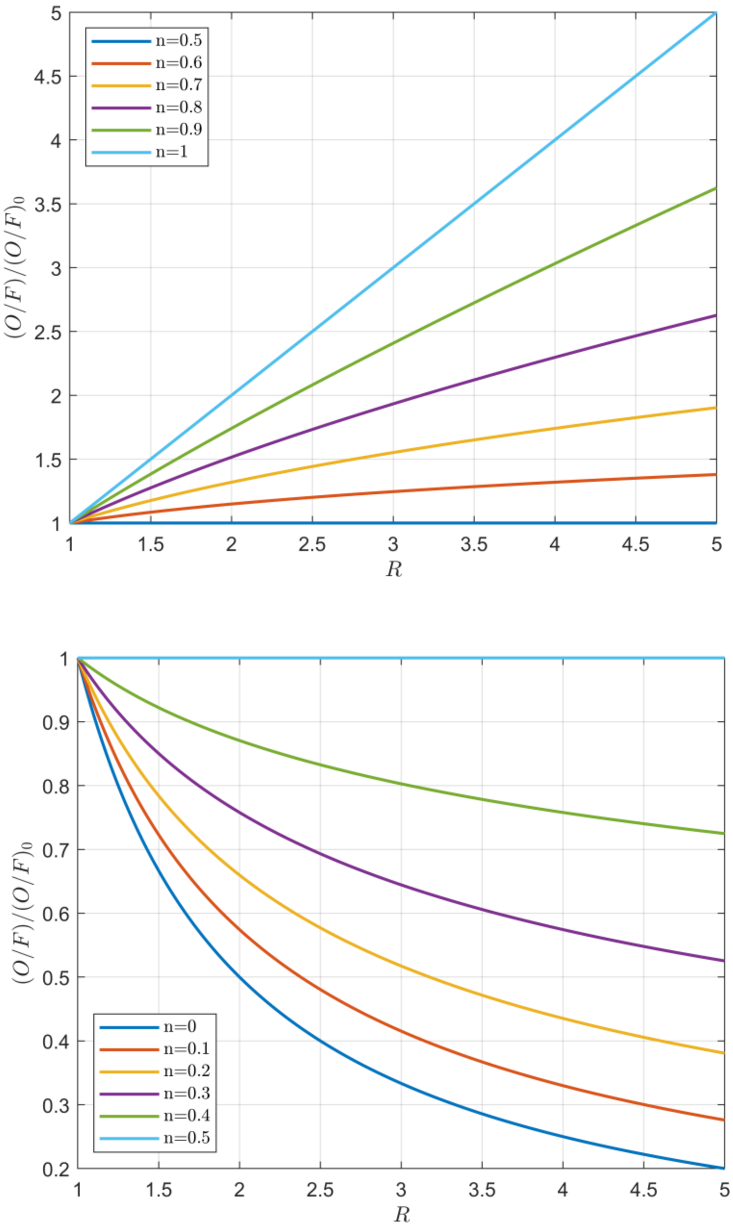

Figure 2.19: O/F shift with diameter ratio R for several regression rate exponents n.

Equation (2.63) shows that the O/F ratio is also influenced by throttling obtained by varying the oxidizer mass flow rate injected into the combustion chamber. In fact, the variation in the oxidizer mass flow rate produces a variation of G_{ox} and therefore of regression rate. This effect is usually overlapped to the one caused by the variation of the port area and leads to a variation of $\dot{m}_f$, G_f and, ultimately, of the O/F ratio.

Fig.2.20 shows the O/F shift with throttling for several regression rate exponents n with constant port area:

$$\frac{(O/F)}{(O/F)_0} = \left(\frac{\dot{m}_{ox}}{\dot{m}_{ox_0}}\right)^{1-n} \tag{2.64}$$

For $n = 1$ there is no O/F shift due to throttling (however, there is O/F shift due to the variation of the port area because $n \neq 0.5$), while if $n \neq 1$ there is O/F shift. The O/F ratio increase if $\dot{m}_{ox}$ increase and vice versa, with a sub-linear trend that tends to linearity as $n \to 0$.

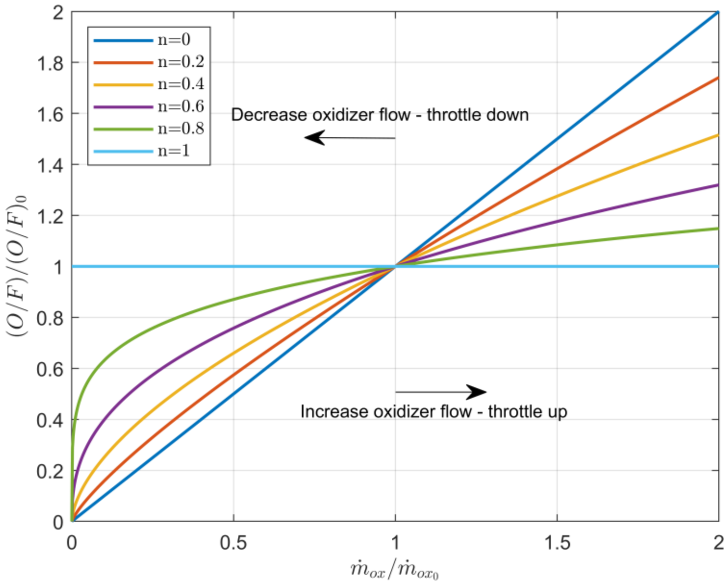

Figure 2.20: O/F shift with throttling for several regression rate exponents n.

Chapter 3

Boundary Layer in Hybrid Combustion

The boundary layer is defined as the thin layer of fluid in the immediate vicinity of a surface. It is possible to define several types of boundary layers. A consequence of the viscous fluid-surface interaction is the development of a region in the fluid through which the velocity varies from zero at the surface to fulfil the no slip condition to the velocity of the undisturbed current. This region of the fluid is known as velocity boundary layer. Moreover, if the surface and the flow temperatures differ, there will be a region of the fluid through which the temperature changes from the value of the incoming flow to the wall temperature. This region is called the thermal boundary layer region. Finally, the concentration boundary layer is defined as the region in which concentration gradients exists, thus where the chemical concentration changes from the value of the undisturbed flow to the value at the wall.

The dimensionless number introduced in Chapter 2 describe the ratios between the thickness of the various type of boundary layer [1]. The Prandtl number Pr provides a measure of the relative effectiveness of momentum and energy transport by diffusion in the velocity and thermal boundary layer. It therefore determines the ratio between the velocity and the temperature boundary layer thickness. The Schimdt number Sc provides a measure of the relative effectiveness of momentum and mass transport by diffusion in the velocity and concentration boundary layer, thus it determines the ratio between the velocity and the concentration boundary layer thickness. The Lewis number $Le = Sc/Pr$ therefore measure the ratio between the thermal and the concentration boundary layer thickness.

In the laminar boundary layer the fluid flow is highly ordered, while the turbulent boundary layer is highly irregular and it is characterized by random three-dimensional motion of relatively large parcels of fluid. Moreover, the turbulent boundary layer is characterized by strong surface gradients of velocity, temperature and species concentration, and mass, momentum, and energy transport are dominated by turbulence.

The turbulent boundary layer that forms above the grain in a hybrid engine originates from the interaction between the fluid dynamic boundary layer due to the viscosity of the injected oxidizer and the blowing produced by the fuel pyrolysis. Inside the boundary layer, in a restricted area where the concentrations of oxidizer and fuel allow combustion, a macroscopic diffusive flame is formed.

3.1 Boundary Layer in Marxman’s Hybrid Combustion Theory

As already mentioned, the hypotheses assumed by Marxman in describing the physics of what happens inside the boundary layer are the validity of the Reynolds analogy and that $Pr = Le = 1$: consequently, the moment, thermal and concentration boundary layer thicknesses are equal and the velocity, temperature and concentration profiles are similar and linear to each other. Moreover, considering that chemical kinetic is generally dominant when compared to diffusion (i.e. $Da \gg 1$), Marxman stated that the flame zone can be modelled as an infinitely thin discontinuity (flame-sheet approximation) for temperature and concentration profiles. Therefore, the boundary layer consists of two zones: the region between the surface of the grain and the flame in which there is the vaporized fuel and part of reaction product gases; the region between the flame and the upper edge of the boundary layer where there is the oxidizer and the remaining combustion products.

3.2 Velocity Profile

To be able to describe the influence of mass injection represented by the blowing coefficient B on the regression rate in hybrid combustion, the velocity profile within the boundary layer must be evaluated. In Marxman's theory, the expression of the velocity profile is obtained based on the combustion model represented in Fig.3.1, in which it is assumed that the reactions are confined to a flame sheet of negligible thickness at a height y_b from the grain surface. Moreover, it is assumed that the combustion does not change the velocity profile compared to that with blowing and no combustion. It is also assumed that the density within the boundary layer is constant and equal to that of the undisturbed flow.

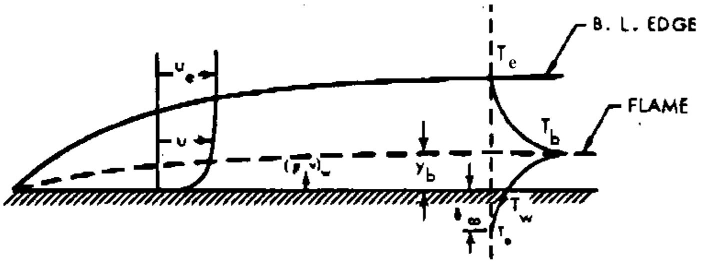

Figure 3.1: Boundary layer combustion model. Adapted from [9].

Neglecting body forces, continuity and x-momentum equations for a steady incompressible flow are:

$$\rho \frac{\partial u}{\partial x} + \rho \frac{\partial v}{\partial y} = 0 \tag{3.1}$$

$$\rho u \frac{\partial u}{\partial x} + \rho v \frac{\partial u}{\partial y} = -\frac{\partial p}{\partial x} + \frac{\partial \tau}{\partial y} \tag{3.2}$$

where u and v are the x (axial) – and the y (normal) – component of the velocity respectively. Close to the wall, $u \approx 0$ and $\partial u/\partial x \approx 0$ so that continuity equation becomes $\rho v = (\rho v)_w$. In the absence of an axial pressure gradient, the momentum equation can be written as:

$$(\rho v)_w \frac{\partial u}{\partial y} = \frac{\partial \tau}{\partial y} \tag{3.3}$$

Appling Prandtl's mixing length theory [36], the integration of equation (3.3) between the wall and the generic coordinate y provides the shear stress expression:

$$\tau = (\mu + \rho\epsilon)\left(\frac{du}{dy}\right) = \tau_w\left[1 + B\left(\frac{u}{u_e}\right)\right] \tag{3.4}$$

where μ is the dynamic viscosity and ϵ is the turbulent eddy diffusivity [11]. By using the dimensionless variables of velocity $\phi = u/u_e$ and position $\eta = y/\delta$, the previous equation can be written as:

$$\frac{d\phi}{d\eta} = \left[\frac{\frac{\tau_w\delta}{u_e}}{\mu + \rho\epsilon}\right](1 + B\phi) = f(y, B)(1 + B\phi) \tag{3.5}$$

For $B = 0$, i.e. without blowing from the grain surface, $f(y, 0) = (d\phi/d\eta)_{B=0}$. When there is no mass injection from the grain wall, the turbulent velocity profile can be adequately described by the empirical power-law:

$$\phi = \eta^n \tag{3.6}$$

with $n = 1/7$ in the case of flow over a flat plate. Therefore,

$$\left(\frac{d\phi}{d\eta}\right)_{B=0} = n\eta^{n-1} \tag{3.7}$$

To account for the blowing effect, it will be assumed that in equation (3.5) $f(y, B) = An\eta^{n-1}$, where $A = A(B)$ and $A(0) = 1$. Furthermore, as a first approximation, the corrective term due to blowing can be written as $B\phi = B\eta^n$. Those considerations lead to describe the velocity profile within a turbulent boundary layer with blowing through the following differential equation:

$$\frac{d\phi}{d\eta} = An\eta^{n-1}(1 + B\eta^n) \tag{3.8}$$

where A and the integration constant are evaluated by imposing the boundary conditions, i.e. $\phi(0) = 0$ (no-slip condition) and $\phi(1) = 1$ (freestream condition at boundary layer edge). The expression of the dimensionless velocity profile within the boundary layer is:

$$\phi = \frac{u}{u_e} = \frac{\eta^n(1 + 0.5B\eta^n)}{1 + 0.5B} \tag{3.9}$$

which simplifies to $\phi = \eta^n$ when there is no blowing (i.e. $B = 0$). Fig.3.2 shows the dimensionless velocity profile of the boundary layer in hybrid combustion according to Marxman theory for several values of the blowing parameter B. As B increase, the velocity profile becomes “thinner” while reducing the gradient at the wall. This is consistent with Marxman's theory according to which the increase of blowing reduces the viscous stress at the wall and therefore the skin-friction coefficient. Furthermore, the variation of the velocity profile with respect to the case without blowing is significant even for low values of B; for B between 5 and 20 (typical range for hybrid engines) the difference is reduced but still important; for B greater than 20, even a significant increase in the blowing coefficient does not produce an appreciable change in the dimensionless velocity profile with respect to lower values of B.

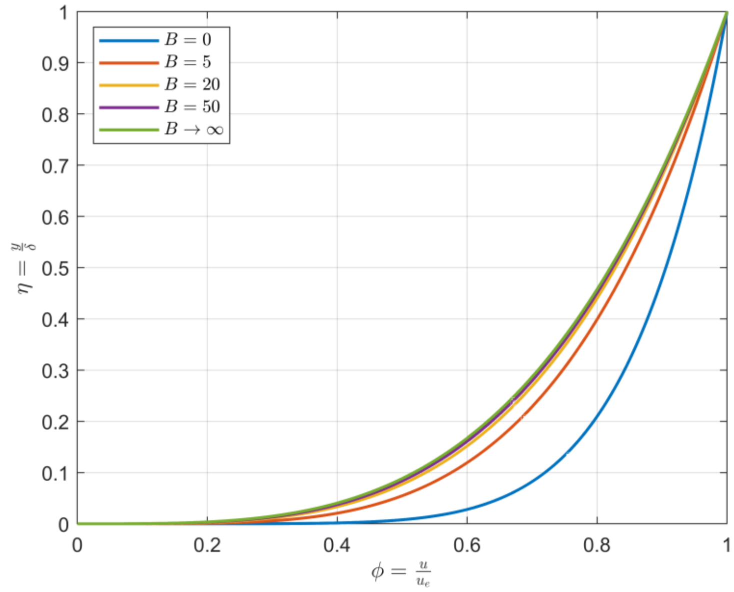

Figure 3.2: Dimensionless velocity profile of the boundary layer in hybrid combustion according to Marxman theory for several values of the blowing parameter B.

A closer examination of equations (3.6) and (3.9) shows that the power-law profile cannot be valid near the wall, since the velocity gradient $(d\phi/d\eta)|_{\eta=0} = (du/dy)|_{y=0}$ is infinite there. In addition, those equations cannot be precisely valid even at the boundary layer edge because they do not give $(d\phi/d\eta)|_{\eta=1} = (du/dy)|_{y=\delta} = 0$. However, they do provide a reasonable approximation to the measured velocity profile.

3.3 Flame Position and Velocity

The evaluation of the blowing coefficient B with equation (2.27) requires the knowledge of the flame dimensionless velocity $\phi_b = u_b/u_e$. Marxman's theory [9][11] allows to find the flame position in the boundary layer as a function of the reaction O/F ratio, the freestream oxidizer concentration K_{ox_e} and the thermochemical parameter $\Delta h/h_v$. Moreover, Marxman's theory assumes that the hybrid combustion is diffusion limited. This suggests that the flame will be well above the laminar sublayer, so that at the flame the molecular diffusivity $\mathcal{D} \ll \epsilon$ and can be neglected [11].
Let's consider the two volumes separated by the flame zone [9], as shown in Fig.3.3.

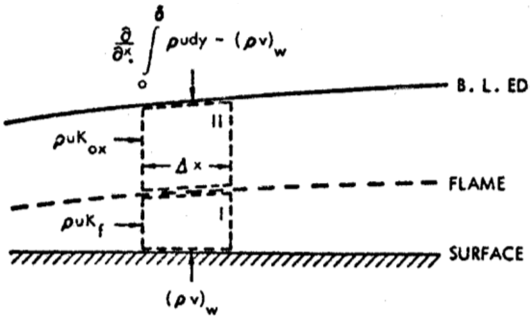

Figure 3.3: Control volumes for determination of flame height. Adapted from [9].

From control volume I, the fuel mass flow rate that sublimates from the grain and reaches the flame is:

$$F = \left[(\rho v)_w - \frac{\partial}{\partial x}\int_0^{y_b} K_f \rho u \, dy\right]\Delta x \tag{3.10}$$

where K_f is the local fuel mass fraction and y_b is the flame height above surface. The first term is related to the overall mass flow rate sublimated from the grain while the second term represents the axial fuel flow rate below the flame.

Similarly, for control volume II, the oxidizer mass flow rate reaching the flame is:

$$O = \left\{ \left[\frac{\partial}{\partial x} \int_0^\delta \rho u \, dy - (\rho v)_w \right] K_{ox_e} - \frac{\partial}{\partial x} \int_{y_b}^\delta \rho u K_{ox} \, dy \right\} \Delta x \tag{3.11}$$

where K_{ox} is the local oxidizer mass fraction. The first term is related to the oxidizer mass flow rate that enters in the boundary layer from the freestream while the second term represents the axial oxidizer flow rate above the flame.

The ratio between the two above flows is the local O/F ratio at the flame:

$$[O/F] = \frac{\left\{ \left[\frac{\partial}{\partial x} \int_0^\delta \rho u \, dy - (\rho v)_w \right] K_{ox_e} - \frac{\partial}{\partial x} \int_{y_b}^\delta \rho u K_{ox} \, dy \right\} \Delta x}{\left[(\rho v)_w - \frac{\partial}{\partial x} \int_0^{y_b} K_f \rho u \, dy \right] \Delta x} \tag{3.12}$$

Retaining only the first order terms, assuming that the oxidizer concentration at the upper edge of the flame is negligible and considering the definition of the momentum thickness θ (defined such that $\rho_e u_e^2 \theta$ is the momentum loss in the actual flow because of the presence of the boundary layer [21]),

$$\theta = \int_0^\delta \frac{u}{u_e} \left(1 - \frac{u}{u_e} \right) dy = \delta \int_0^1 \phi (1 - \phi) \, d\eta \tag{3.13}$$

it is obtained:

$$\frac{(\rho v)_w}{\rho_e u_e} \left([O/F] + K_{ox_e} \right) = \frac{K_{ox_e}}{1 - \phi_b} \frac{d\theta}{dx} \tag{3.14}$$

The Von Karman boundary layer momentum integral equation for an incompressible flow above a flat plate with mass injection:

$$\frac{d\theta}{dx} = \frac{C_f}{2}(1 + B) \tag{3.15}$$

can be substituted into equation (3.14) to obtain an equation for the velocity ratio at the flame as a function of the O/F ratio of reaction, the freestream oxidizer concentration K_{ox_e} and the thermochemical parameter $\Delta h/h_v$:

$$\phi_b = \frac{u_b}{u_e} = \frac{[O/F]\left(\frac{\Delta h}{h_v}\right)}{K_{ox_e} + \left([O/F] + K_{ox_e}\right)\left(\frac{\Delta h}{h_v}\right)} \tag{3.16}$$

The flame position η_b is related to ϕ_b and B through equation (3.9) as:

$$\eta_b = \frac{y_b}{\delta} = \left[\frac{-1 + \sqrt{1 + 2B\phi_b(1 + 0.5B)}}{B}\right]^{1/n} \tag{3.17}$$

3.4 Combustion Mixture Ratio

Marxman's theory assumes some hypotheses as valid. The first hypothesis is that the oxidizer and the fuel reach the flame zone mainly by diffusion and that diffusivity is equal for each of the species considered. It has also been assumed that reactions are infinitely fast, so that species react immediately and completely in the flame zone without having the possibility of trespassing it. If those hypotheses actually reflected the reality of the hybrid combustion physics, the flame would be positioned where the local O/F ratio is equal to the stoichiometric one. Experimentally, combustion has been observed to be fuel-rich [8][11], therefore with the flame closer to the wall and with combustion temperature lower than the stoichiometric one. Despite this, the O/F ratio of reaction is close enough to the stoichiometric ratio to still be able to consider the reaction kinetics predominant on the diffusive processes and therefore to be able to assume the flame zone as a thin line of discontinuity characterized by a single O/F value.

The cause of this phenomenon is to be found in the magnitude of the mechanisms by which the reactants move within the boundary layer. The oxidizer convective flux is expected to be almost tangential to the flame sheet and it is proportional to the oxidizer mass fraction which is small near the flame where it is consumed by the combustion reaction. The convective flow is superimposed to the diffusion flow which is proportional to the concentration gradient in the direction normal to the flame, and therefore maximum in here. Ultimately, the oxidizer flow towards the flame is controlled by diffusion which represents its limiting factor, while the convective contribution is negligible. On the other hand, the fuel vaporizes from the grain and reaches the flame through equally important diffusive and convective mechanisms.

If we add to this consideration the dependence of diffusivity on temperature (which is variable within the boundary layer) and the non-negligible presence of oxidizer below the flame zone experimentally observed, it can be concluded that combustion will not take place in the position where the O/F ratio is stoichiometric but closer to the wall and therefore in fuel-rich conditions.

If the Reynolds analogy is assumed to be valid, the relationship describing the oxidizer flux towards the flame in the direction normal to the wall is [11]:

$$|(\rho v)_{ox}|_b = \left| \rho_b (\epsilon + \mathcal{D})_b \left(\frac{\partial K_{ox}}{\partial y} \right)_b \right| = [O/F](\rho v)_w \tag{3.18}$$

where $\mathcal{D}$ is the molecular diffusivity. This expression states that the flame happens at a point within the boundary layer where the oxidizer $|(\rho v)_{ox}|_b$ and fuel $(\rho v)_w$ fluxes meet in the proportions required for combustion to take place at the experimentally observed fuel-rich O/F ratio. Because of the unknown a priori real value of the O/F ratio of reaction, in this work it is assumed that it is equal to the stoichiometric ratio, and this will be referred to as $[O/F]_{react}$.

3.5 Thermochemical Parameter $\Delta h/h_v$ Calculation

To complete the evaluation of the blowing parameter B, the thermochemical parameter $\Delta h/h_v$ must be known.

h_v is the effective heat (enthalpy) of gasification, defined as the energy per unit mass required to vaporize the fuel from the initial temperature of the solid. In the case of a polymer-type fuel such as Plexiglass [11], effective heat of gasification includes the heat necessary to raise the surface temperature of the fuel from the initial value (of equilibrium with the external environment) to the sublimation temperature, the energy of depolymerization and the latent heat of sublimation of the monomer (in the simplistic hypothesis that the polymer splits into its monomer). In particular, it is possible to break down the gasification process by means of the following reactions that take place at the grain surface:

$$\begin{aligned} &\text{polymer (s)} \rightarrow \text{monomer (l)} + \Delta H_1 \qquad &&\text{(heat of decomposition)} \\ &\text{monomer (l)} \rightarrow \text{monomer (g)} + \Delta H_2 \qquad &&\text{(heat of vaporization)} \end{aligned} \tag{3.19}$$

If c_{p_f} is the heat capacity of solid fuel and T_s and T_i are the surface temperature and the steady-state internal temperature of fuel respectively, for this process h_v is:

$$h_v = \Delta H_1 + \Delta H_2 + c_{p_f}(T_s - T_i) \tag{3.20}$$

Δh is the enthalpy variation between the flame and the wall. If the average specific heat $\bar{c}_{p_b}$ is assumed to be independent of temperature [9], flame enthalpy can be defined with respect to a convenient reference temperature T_{ref} as:

$$h_b = \bar{c}_{p_b}\left(T_b - T_{ref}\right) \tag{3.21}$$

Heat of reaction is defined as:

$$Q_b = \sum K_r h_r^0 - \sum K_p h_p^0 \tag{3.22}$$

where h_r^0, h_p^0 are the enthalpies of formation per unit mass of the reactants and products at the reference temperature T_{ref} respectively, and K_r, K_p are the mass fractions of reactant and product species respectively. If the process is considered adiabatic, then there is no net change in the total enthalpy, i.e. $Q_b = h_b$.

The enthalpy in the gas phase at the wall is given by:

$$h_w = \bar{c}_{p_w}(T_w - T_0) \tag{3.23}$$

where $\bar{c}_{p_w}$ is the specific heat at the wall. Experimental measurements have shown that the vaporization temperature of the monomer is approximately $600\ K$ [9].

Thus:

$$\Delta h = h_b - h_w \tag{3.24}$$

For systems where the oxidizer is diluted, it can be assumed that the inert diluent merely adds additional mass to the system, so that the heat released per unit mass is decreased.

3.6 Profiles of Thermodynamic, Chemical and Mechanical Quantities within the Boundary Layer

The basic assumptions that allowed the development of Marxman's theory of hybrid combustion are the validity of the Reynolds analogy and that the Prandtl and Lewis numbers are unitary. The first of these hypotheses allows to state that, at least below the flame, the moment and thermal profiles are proportional to each other. Moreover, stating that $Pr = 1$ is equivalent to say that the thickness of the moment boundary layer is equal to the thermal one, while $Le = 1$ it is equivalent to state that the thermal and chemical species concentration profiles are similar. With those assumptions, it is therefore correct to assume that the temperature and concentration profiles can be described as linear function of the velocity profile. Mathematically this means that those profiles can be written in the form $a\phi + b$, where a and b are constants that depend on the boundary conditions for the specific quantity.

Velocity profile. As previously demonstrated, the dimensionless velocity profile within the boundary layer (Fig.3.4) is described by the relation (3.9).

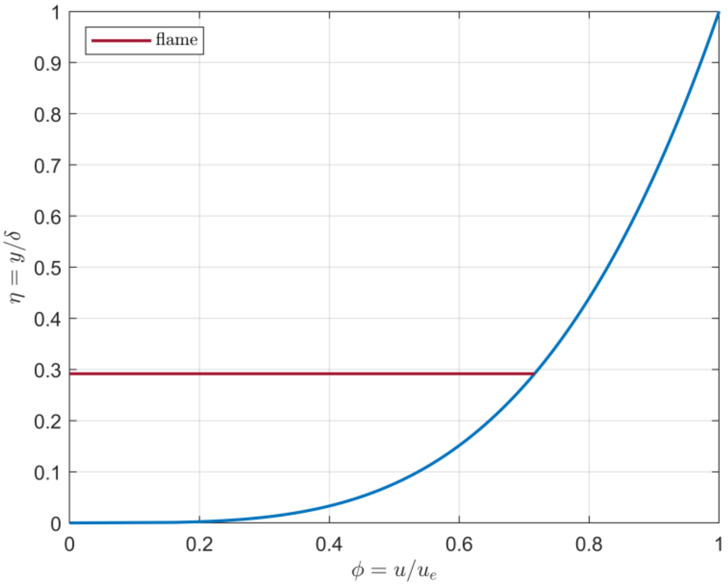

Figure 3.4: Dimensionless velocity profile ϕ as a function of dimensionless position η in the boundary layer.

Concentration profiles. To describe the concentration profiles (Fig.3.5), it is necessary to distinguish the boundary layer in the two regions below and above the flame. The flame is assumed infinitely thin (flame-sheet approximation). As a result, above the flame ($\eta_b < \eta \leq 1$) the oxidizer, any diluent and part of the combustion products will be present, at the flame ($\eta = \eta_b$) the mixture consists only of the reaction gases, below the flame ($0 \leq \eta < \eta_b$) there are only the fuel and the remaining combustion products.

The products concentration below the flame goes from zero at the wall ($\eta = 0$) to unity at the flame ($\eta = \eta_b$), thus the following system of conditions must be solved:

$$\begin{cases} K_{pr}(\eta) = a\phi(\eta) + b \\ K_{pr}(\eta = 0) = 0 \\ K_{pr}(\eta = \eta_b) = 1 \end{cases} \tag{3.25}$$

Calculations give:

$$K_{pr}(\eta = 0) = a\phi(0) + b = 0 \rightarrow b = 0 \tag{3.26}$$

$$K_{pr}(\eta = \eta_b) = a\phi(\eta_b) + b = 1 \rightarrow a = \frac{1}{\phi_b} \tag{3.27}$$

therefore:

$$K_{pr} = \frac{\phi}{\phi_b} = \frac{\eta^n(1 + 0.5B\eta^n)}{\eta_b^n(1 + 0.5B\eta_b^n)} \qquad (0 \leq \eta \leq \eta_b) \tag{3.28}$$

The products concentration profile is opposite to that of the fuel, which goes from unity at the wall to zero at the flame. Therefore:

$$K_f = 1 - K_{pr} = 1 - \frac{\phi}{\phi_b} = 1 - \frac{\eta^n(1 + 0.5B\eta^n)}{\eta_b^n(1 + 0.5B\eta_b^n)} \qquad (0 \leq \eta \leq \eta_b) \tag{3.29}$$

Above the flame, the oxidizer concentration goes from the value of the freestream mass fraction K_{ox_e} to zero at the flame, thus the following system of conditions must be solved:

$$\begin{cases} K_{ox}(\eta) = a\phi(\eta) + b \\ K_{ox}(\eta = \eta_b) = 0 \\ K_{ox}(\eta = 1) = K_{ox_e} \end{cases} \tag{3.30}$$

Solving with the same procedure seen above:

$$\begin{aligned} K_{ox} &= K_{oxe}\frac{\eta^n(1 + 0.5B\eta^n) - \eta_b^n(1 + 0.5B\eta_b^n)}{1 + 0.5B - \eta_b^n(1 + 0.5B\eta_b^n)} \\ &= K_{ox_e}\frac{\phi - \phi_b}{1 - \phi_b} \qquad (\eta_b \leq \eta \leq 1) \end{aligned} \tag{3.31}$$

Any diluent species will have a concentration equal to $K_{in_e} = 1 - K_{ox_e}$ at the boundary layer edge and equal to zero at the flame, therefore:

$$\begin{aligned} K_{in} &= (1 - K_{oxe})\frac{\eta^n(1 + 0.5B\eta^n) - \eta_b^n(1 + 0.5B\eta_b^n)}{1 + 0.5B - \eta_b^n(1 + 0.5B\eta_b^n)} \\ &= (1 - K_{oxe})\frac{\phi - \phi_b}{1 - \phi_b} \qquad (\eta_b \leq \eta \leq 1) \end{aligned} \tag{3.32}$$

Since above the flame must be $K_{ox} + K_{in} + K_{pr} = 1$, then:

$$K_{pr} = 1 - K_{ox} - K_{in} \tag{3.33}$$

from which, considering the expressions (3.31), (3.32), it is obtained:

$$K_{pr} = 1 - \frac{K_{ox}}{K_{oxe}} = \frac{1 - \phi}{1 - \phi_b} \qquad (\eta_b \leq \eta \leq 1) \tag{3.34}$$

Similarly:

$$K_{in} = 1 - K_{ox} - K_{pr} \tag{3.35}$$

therefore, given the relationship (3.34), it is obtained:

$$K_{in} = \frac{K_{ox}}{K_{oxe}} - K_{ox} \qquad (\eta_b \leq \eta \leq 1) \tag{3.36}$$

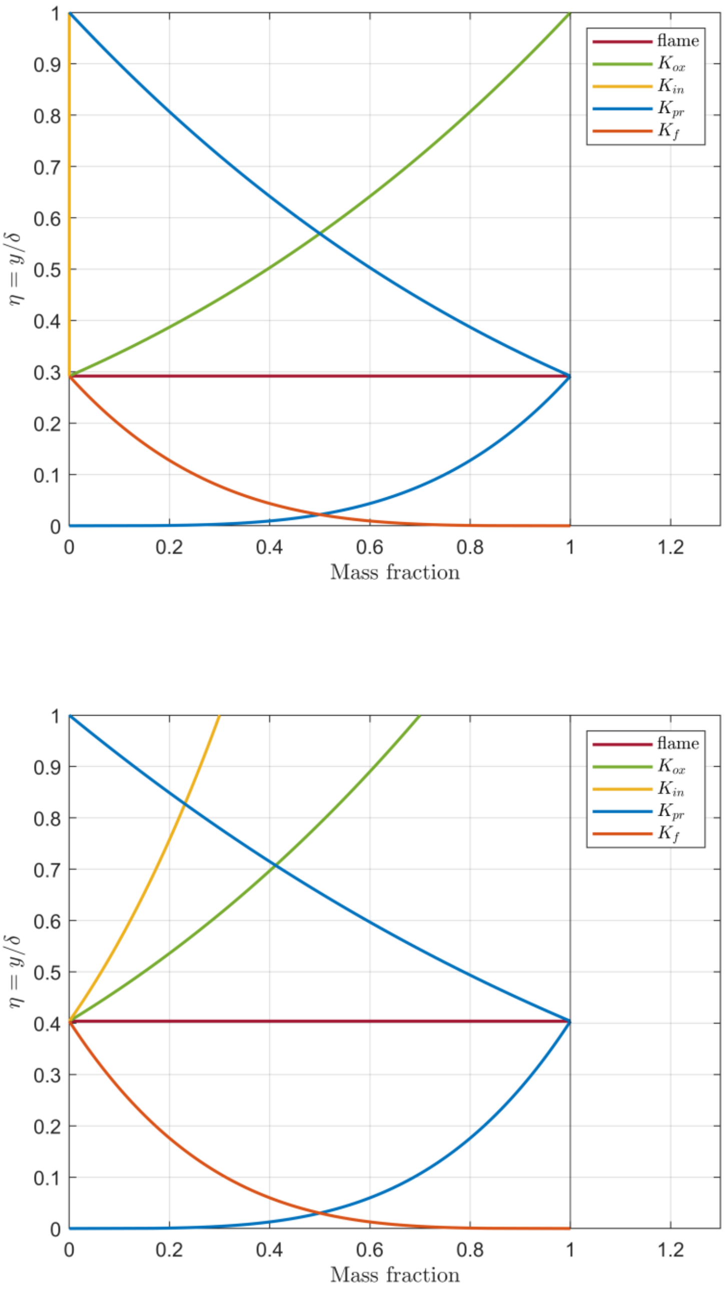

Figure 3.5: Concentration profiles as a function of dimensionless position η in the boundary layer with $K_{ox_e} = 1$ (top) and $K_{ox_e} < 1$ (bottom).

In hybrid propulsion systems, it is not uncommon to use oxidizers diluted with another element (i.e. $K_{ox_e} < 1$), as in the case of hydrogen peroxide (H_2O_2) or nitrous oxide (N_2O). In those cases, in the numerical simulations it is still possible to assume $K_{ox_e} = 1$ as the boundary condition for the oxidizer concentration at the boundary layer edge, provided that an adequate O/F ratio of reaction is employed.

For example, let's consider the reaction $H_2O_2 - C_2H_4$ (hydrogen peroxide – polyethylene). From the stoichiometric combustion reaction:

$$C_2H_4 + 6H_2O_2 \rightarrow 2CO_2 + 8H_2O \tag{3.37}$$

it is $[O/F]_{st\,(H_2O_2),mass} = 7.29$.

Otherwise, if pure oxygen is used as oxidizer, from the stoichiometric reaction:

$$C_2H_4 + 3O_2 \rightarrow 2CO_2 + 2H_2O \tag{3.38}$$

it is $[O/F]_{st\,(O_2),mass} = 3.43$.

It can be demonstrated that, if a diluted oxidizer is used, it is equivalent to consider K_{ox_e} equal to the percentage of oxygen ξ_{ox} and $[O/F]_{st\,(O_2)}$ or assume that all the oxidizer is oxygen (i.e. $K_{ox_e} = 1$) and use the stoichiometric O/F ratio with the diluted oxidant, which in general is:

$$[O/F]_{st\,(diluted\ ox)} = \frac{[O/F]_{st\,(O_2)}}{\xi_{ox}} \tag{3.39}$$

For example, H_2O_2 (100%) has 47% of O_2, thus it can be assumed $K_{ox_e} = 0.47$ and $[O/F]_{st(O_2)} = 3.43$ or $K_{ox_e} = 1$ and $[O/F]_{st(H_2O_2)} = 7.29$.

In the following, it will always be $K_{ox_e} = 1$ with the stoichiometric O/F ratio with the diluted oxidant.

Temperature profile. To describe the temperature profile in the boundary layer, it is necessary to distinguish between the regions below and above the flame. Below the flame the temperature goes from the wall temperature of the gaseous fuel (around $600\ K$) to the flame temperature T_b, while above the flame the temperature drops until it reaches the freestream temperature T_e at the edge of the boundary layer (Fig.3.6). It can be obtained:

$$T = T_w + (T_b - T_w)\frac{\phi}{\phi_b} = T_w + (T_b - T_w)K_{pr} \qquad (0 \le \eta \le \eta_b) \qquad (3.40)$$

$$T = T_e + (T_b - T_e)\frac{1-\phi}{1-\phi_b} = T_e + (T_b - T_e)K_{pr} \qquad (\eta_b \le \eta \le 1) \qquad (3.41)$$

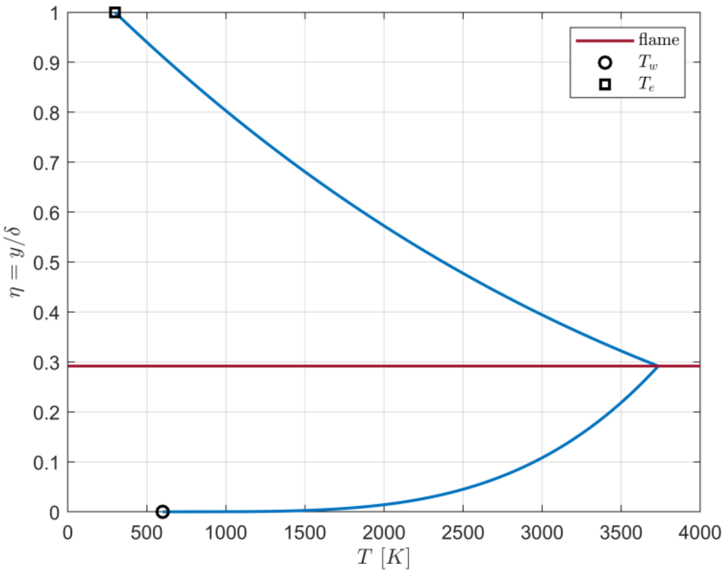

Figure 3.6: Temperature profile as a function of dimensionless position η in the boundary layer.

Pressure profile. For a turbulent boundary layer above a flat plate without mass injection, the pressure in the normal direction is uniform and equal to that of the freestream current [21]. Blowing produces a radial velocity component and therefore pressure is not uniform on the section. To a first approximation, this effect is neglected.

Molecular mass and gas constant profiles. Again, a distinction must be made between the above and below flame positions. The mixture molecular mass distribution (Fig.3.7) can be evaluated with the following expressions:

$$M_m = \frac{1}{\frac{1}{M_{m_f}} K_f + \frac{1}{M_{m_{pr}}} K_{pr}} \qquad (0 \le \eta \le \eta_b) \tag{3.42}$$

$$M_m = \frac{1}{\frac{1}{M_{m_{ox}}} K_{ox} + \frac{1}{M_{m_{in}}} K_{in} + \frac{1}{M_{m_{pr}}} K_{pr}} \qquad (\eta_b \le \eta \le 1) \tag{3.43}$$

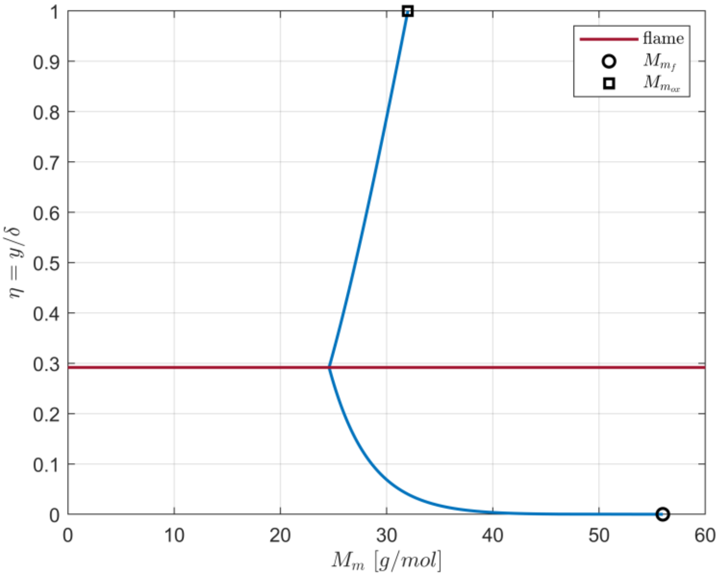

Figure 3.7: Molecular mass profile as a function of dimensionless position η in the boundary layer.

The products molecular mass can be evaluated with any thermochemical code (in this work CProPep [12] is used), while that of the gaseous fuel (monomer) can be evaluated by literature (e.g. from Fig.3.8).

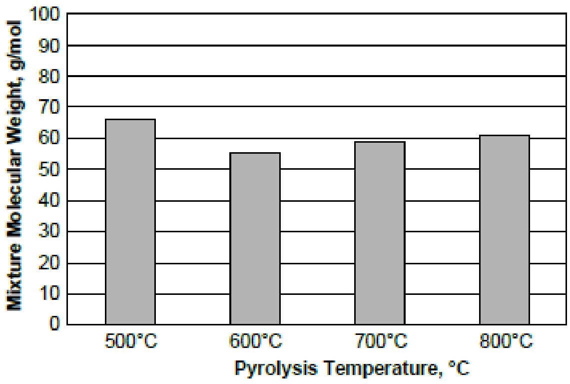

Major pyrolysis product species M_i, chemical formula	Heat of formation ΔH_f^o, J/g	Mass fractions of pyrolysis products at various temperatures, K			
		773	873	973	1073
Ethene, C_2H_4	1865.69	—	5.59	3.05	6.58
Propene, C_3H_6	485.49	—	—	4.90	10.99
1,3–Butadiene, C_4H_6	2037.27	77.4	89.06	66.1	41.07
3–Pentene–1–Yne, C_5H_6	2119.82	—	—	9.20	10.28
Benzene, C_6H_6	1062.29	—	—	10.3	22.02
Toluene, C_7H_8	542.97	—	—	6.41	9.06
4-Vinyl–cyclohexene, C_8H_{12}	280.78	22.6	5.35	—	—

Figure 3.8: Decomposition products and mean molecular mass of HTPB [25].

Once the molecular mass profile is known, the specific gas mixture constant profile (Fig.3.9) can be evaluated with its definition:

$$R = \frac{\mathcal{R}}{M_m} \tag{3.44}$$

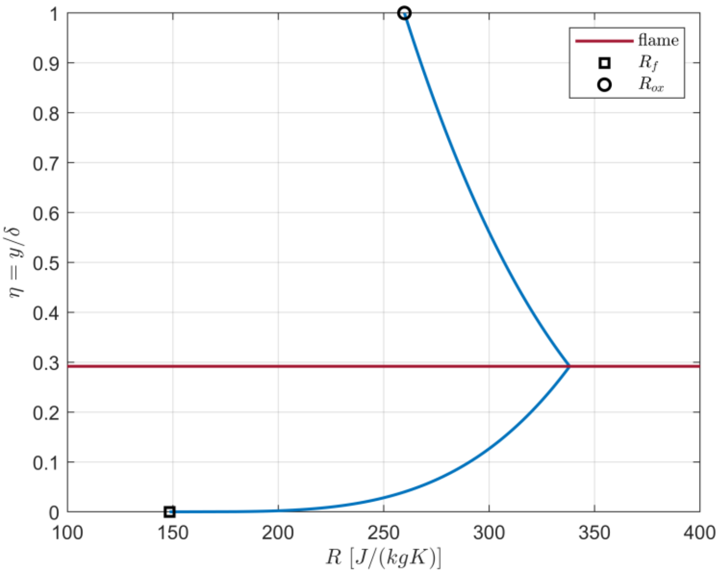

Figure 3.9: Gas constant profile as a function of dimensionless position η in the boundary layer.

Density profile. Marxman's theory assume a constant density in the boundary layer, whose value is equal to the freestream one. In reality, density varies greatly in the boundary layer (Fig.3.10) and can be calculated using the ideal gas law:

$$\rho = \frac{p}{RT} \tag{3.45}$$

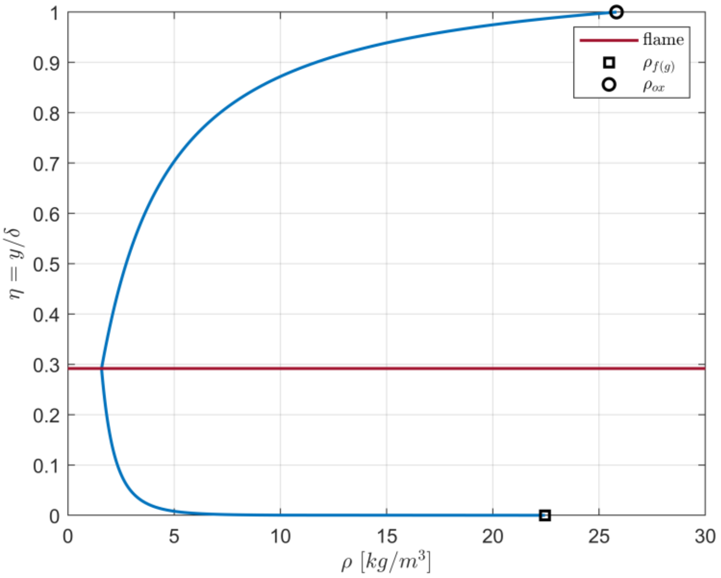

Figure 3.10: Density profile as a function of dimensionless position η in the boundary layer.

3.7 Derivation of Marxman's Blowing Correction C_f/C_{f_0} and Boundary Layer Thickness δ Equation

The factor C_f/C_{f_0} accounts for the reduction in skin friction (or heat transfer) caused by the surface mass addiction. According to Marxman [8] the expression for C_f/C_{f_0} determined from a simple "film-theory" approach by Lees:

$$\frac{C_f}{C_{f_0}} = \frac{\ln(1+B)}{B} \tag{3.46}$$

is not sufficiently correct, because it neglects the effect of mass injection on the well-known boundary layer thickening. By fully nondimensionalizing equation (3.4) using $Re_\delta = \rho_e u_e \delta/\mu$, $\eta = y/\delta$, $\phi = u/u_e$ and τ_w, Marxman [7] obtained:

$$\frac{1}{2}C_f(1 + B\phi) = Re_\delta^{-1}\left(1 + \frac{\rho\epsilon}{\mu}\right)\frac{\partial\phi}{\partial\eta} \tag{3.47}$$

According to Prandtl's mixing length concept, $\epsilon \propto \eta^2 \partial\phi/\partial\eta$. For the purpose of estimating ϵ a power law profile such as $\phi = \eta^n$ may be used, thus $\partial\phi/\partial\eta = n\eta^{n-1}$. Furthermore, since $n = 1/7$ is small, the eddy diffusivity becomes:

$$\epsilon \approx c\eta^{1+n} \approx c\eta \tag{3.48}$$

where c represents a constant that is proportional to the mixing length. Replacing the expression of ϵ (3.48) into equation (3.47) yields to:

$$\frac{1}{2}C_f(1 + B\phi) = Re_\delta^{-1}\left(1 + \frac{\rho}{\mu}c\eta\right)\frac{\partial\phi}{\partial\eta} \tag{3.49}$$

Integrating from the wall to the edge of the boundary layer, i.e. from 0 to 1 for both η and ϕ, the following expression for the skin-friction coefficient as a function of Re_δ and B can be obtained:

$$\frac{1}{2}C_f = G(Re_\delta)\frac{\ln(1 + B)}{B} \tag{3.50}$$

Marxman [8] argues that the Reynolds number and the blowing dependencies can be neatly separated in the expression for C_f, thus the functional form of $G(Re_\delta)$ can be obtained by comparing equation (3.50) to the known empirical expression without blowing [20], namely:

$$\frac{1}{2}C_{f_0} = G(Re_\delta) = 0.0225Re_\delta^{-0.25} \tag{3.51}$$

Therefore:

$$\frac{1}{2}C_f = 0.0225 Re_\delta^{-0.25} \frac{\ln(1+B)}{B} \tag{3.52}$$

Combining the equations (3.51) and (3.52) yields to:

$$\frac{C_f}{C_{f_0}} = \left(\frac{\delta_0}{\delta}\right)^{0.25} \frac{\ln(1+B)}{B} \tag{3.53}$$

where (δ_0/δ) accounts for the boundary layer thickening effect of mass addition.

δ must be described as a function of B. This relationship can be obtained through the momentum integral formulation of a control volume within the boundary layer (Fig.3.11).

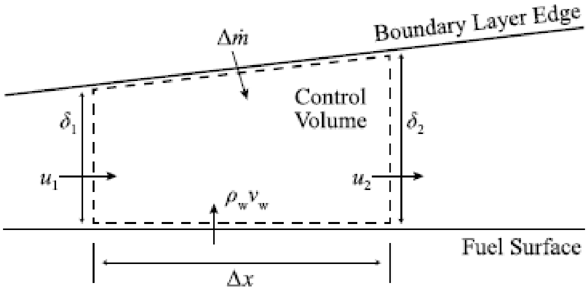

Figure 3.11: Sketch of the control volume for the momentum integral analysis [7].

For this control volume continuity and axial momentum equations can be written as:

continuity:
$$\Delta\dot{m} + \int_0^{\delta_1} \rho u_1 \, dy + \rho_w v_w \Delta x - \int_0^{\delta_2} \rho u_2 \, dy = 0 \tag{3.54}$$

momentum:
$$u_e \Delta\dot{m} + \int_0^{\delta_1} \rho u_1^2 \, dy - \tau_w \Delta x - \int_0^{\delta_2} \rho u_2^2 \, dy = 0 \tag{3.55}$$

Developing and nondimensionalizing previous equations:

continuity:
$$\Delta\dot{m} + \frac{1}{2} C_f \rho u_e B \Delta x = \rho u_e \delta_2 \int_0^1 \phi \, d\eta - \rho u_e \delta_1 \int_0^1 \phi \, d\eta \tag{3.56}$$

$$\frac{\Delta\dot{m}}{\rho u_e \Delta x} + \frac{1}{2} C_f B = \frac{\delta_2 - \delta_1}{\Delta x} \int_0^1 \phi \, d\eta \tag{3.57}$$

momentum: $$u_e \Delta\dot{m} - \frac{1}{2} C_f \rho u_e^2 \Delta x = \rho u_e^2 \delta_2 \int_0^1 \phi^2 \, d\eta - \rho u_e^2 \delta_1 \int_0^1 \phi^2 \, d\eta \tag{3.58}$$

$$\frac{\Delta\dot{m}}{\rho u_e \Delta x} - \frac{1}{2} C_f = \frac{\delta_2 - \delta_1}{\Delta x} \int_0^1 \phi^2 \, d\eta \tag{3.59}$$

Combining continuity equation (3.57) and momentum equation (3.59) yields to:

$$\frac{\delta_2 - \delta_1}{\Delta x} = \frac{1}{2} C_f \frac{1 + B}{\int_0^1 \phi(1 - \phi) \, d\eta} = \frac{1}{2} C_f \frac{1 + B}{I(B)} \tag{3.60}$$

where $I(B) = \int_0^1 \phi(1 - \phi) \, d\eta$ is related to the momentum thickness θ by the relationship:

$$\theta(x) = \int_0^{\delta(x)} \frac{u}{u_e}\left(1 - \frac{u}{u_e}\right) dy = \delta(x) \int_0^1 \phi(1 - \phi) \, d\eta = \delta(x) I(B) \tag{3.61}$$

The expression for ϕ (3.9) allows the evaluation of $I(B)$ from its definition:

$$I(B) = \int_0^1 \phi(1 - \phi) \, d\eta = \frac{7\left(1 + \frac{13B}{10} + \frac{4B^2}{11}\right)}{72\left(1 + \frac{B}{2}\right)^2} \tag{3.62}$$

In the limit as $\Delta x \to 0$, the equation (3.60) is reduced to:

$$\frac{d\delta}{dx} = \frac{1}{2} C_f \frac{1 + B}{I(B)} \tag{3.63}$$

Substituting the equation of the skin-friction coefficient (3.52) leads to:

$$\begin{aligned} \frac{d\delta}{dx} &= 0.0225 Re_{\delta}^{-0.25} \frac{\ln(1+B)}{B} \frac{1+B}{I(B)} \\ &= 0.0225 \frac{\ln(1+B)}{B} \frac{1+B}{I(B)} \left(\frac{\rho u_e}{\mu}\right)^{-0.25} \delta^{-0.25} \end{aligned} \tag{3.64}$$

By considering B constant (i.e. similar velocity profiles) and integrating on the boundary layer, the expression of the boundary layer thickness as a function of the position along the grain (Fig.3.12) is obtained:

$$\frac{\delta}{x} = \left[0.02813 \frac{\ln(1+B)}{B} \frac{1+B}{I(B)}\right]^{0.8} Re_x^{-0.2} \tag{3.65}$$

which is different from the expression of the boundary layer thickness without blowing [22]:

$$\frac{\delta}{x} = 0.370\, Re_x^{-0.2} \tag{3.66}$$

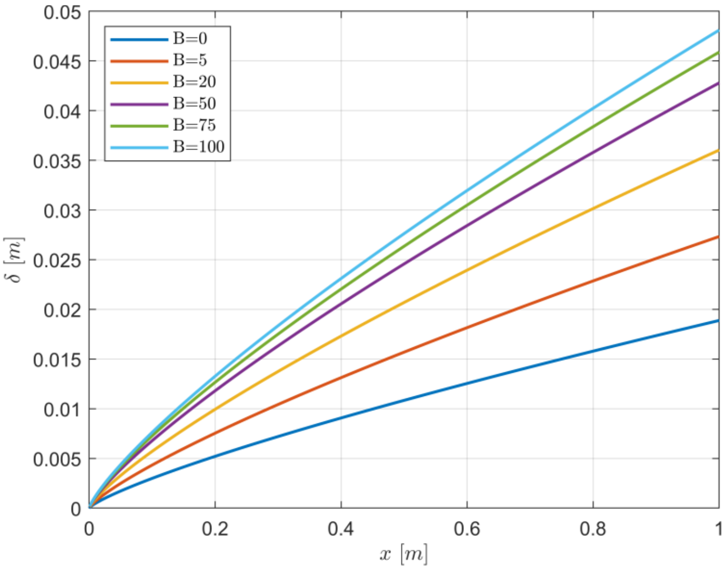

Figure 3.12: Boundary layer thickness in hybrid combustion as a function of the position for several values of the blowing parameter B. $B = 0$ represents the case without combustion.

In the equation (3.65), the term

$$f(B) = \left[0.02813 \frac{\ln(1+B)}{B} \frac{1+B}{I(B)}\right]^{0.8} \tag{3.67}$$

accounts for the boundary layer thickening due to the blowing with respect to the case without blowing. Fig.3.13 shows $f(B)$ divided by its value in the case without blowing $f(B=0) = f(0)$. Typical values of $5-20$ for the blowing parameter B leads to a boundary layer thickening of about $45-90\%$.

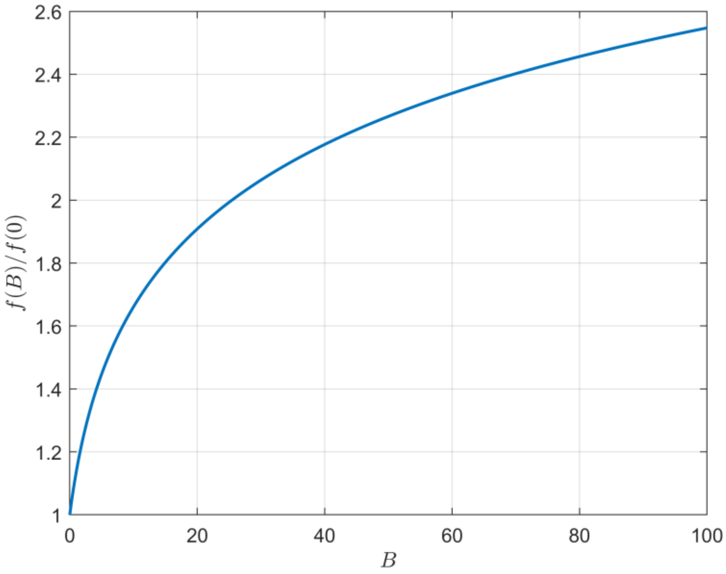

Figure 3.13: $f(B)/f(0)$ ratio as a function of the blowing parameter B.

From previous equations it can be obtained:

$$\frac{\delta_0}{\delta} = \left[\frac{I(B)}{I(0)} \frac{B}{(1+B)\ln(1+B)}\right]^{0.8} \tag{3.68}$$

Combining equations (3.53) and (3.68) yields to:

$$\frac{C_f}{C_{f_0}} = \left[\frac{I(B)}{I(0)} \frac{1}{1+B}\right]^{0.2} \left[\frac{\ln(1+B)}{B}\right]^{0.8} \tag{3.69}$$

If there is no blowing (i.e. $B = 0$), $I(B)$ is equal to $I(0) = 7/72$, thus:

$$\frac{I(B)}{I(0)} = \frac{\left(1 + \frac{13B}{10} + \frac{4B^2}{11}\right)}{\left(1 + \frac{B}{2}\right)^2} \tag{3.70}$$

The blowing corrective factor C_f/C_{f_0} as a function of the blowing parameter B (Fig.3.14) is therefore:

$$\frac{C_f}{C_{f_0}} = \left[\frac{\ln(1+B)}{B}\right]^{0.8} \left[\frac{1 + \frac{13B}{10} + \frac{4B^2}{11}}{(1+B)\left(1 + \frac{B}{2}\right)^2}\right]^{0.2} \tag{3.71}$$

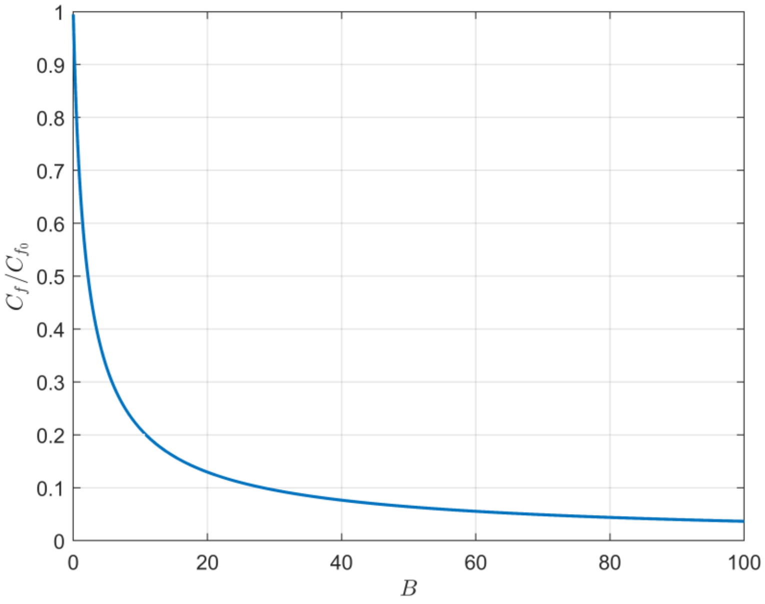

Figure 3.14: C_f/C_{f_0} ratio as a function of the blowing parameter B.

3.8 Influence of Thermochemical Parameters on Hybrid Flame Characteristics

In Marxman's theory, thermochemical parameters B, $[O/F]_{react}$, $\Delta h/h_v$ and K_{ox_e}, influence the characteristics of the hybrid flame. Let's refer to the Marxman's theory equations $(2.27), (3.16), (3.17)$ and (3.71). The influence of each parameter is evaluated while keeping the other constant.

Influence of B. The increase of the blowing parameter B represent a greater grain regression rate and thus boundary layer thickening. Therefore, the flame moves away from the grain surface (Fig.3.15) and its speed is increased (Fig.3.16).
The value of $\Delta h/h_v$ as a function of B (Fig.3.17) can be evaluated by substituting equation (2.27) into equation (3.16). Solving for $\Delta h/h_v$ yields to:

$$\frac{\Delta h}{h_v} = \frac{B[O/F]_{react} - K_{ox_e}}{[O/F]_{react} + K_{ox_e}} \tag{3.72}$$

It should be noted that the condition $\Delta h/h_v = 0$ does not corresponds to $B = 0$, because of the approximations to derive equation (3.16). As a result, Marxman's model as presented is not perfectly consistent when $B \to 0$, although this condition is far from the typical operating conditions. If B increase, then the skin-friction coefficient C_f/C_{f_0} decreases (Fig.3.18).

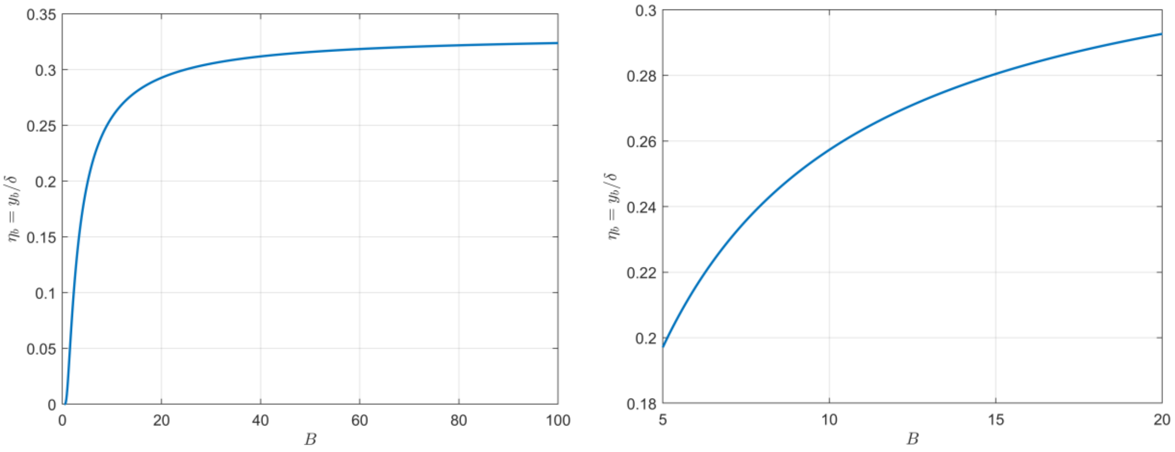

Figure 3.15: Dimensionless position of the flame η_b as a function of the blowing parameter B for a broad range of values (left) and for typical values in hybrid rockets (right).

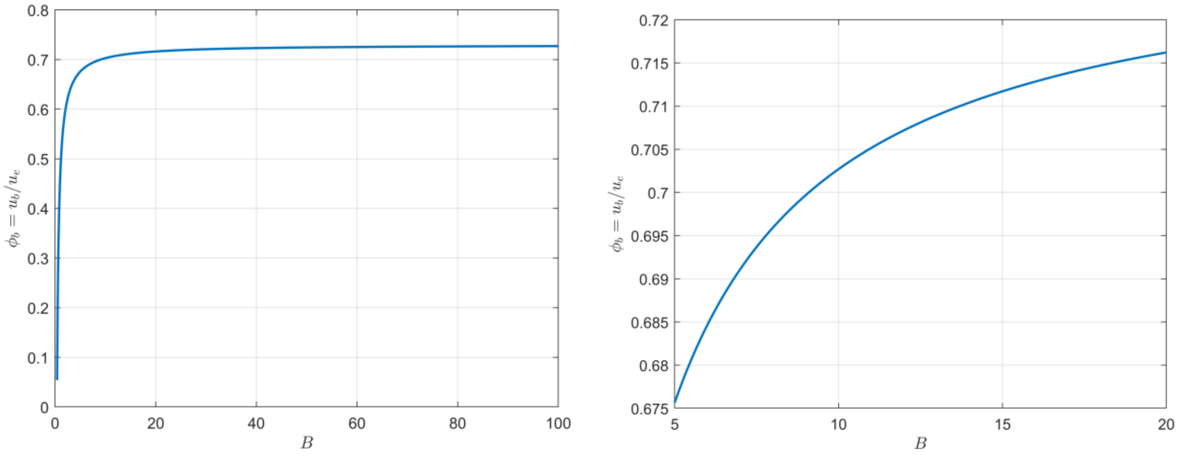

Figure 3.16: Dimensionless velocity of the flame ϕ_b as a function of the blowing parameter B for a broad range of values (left) and for typical values in hybrid rockets (right).

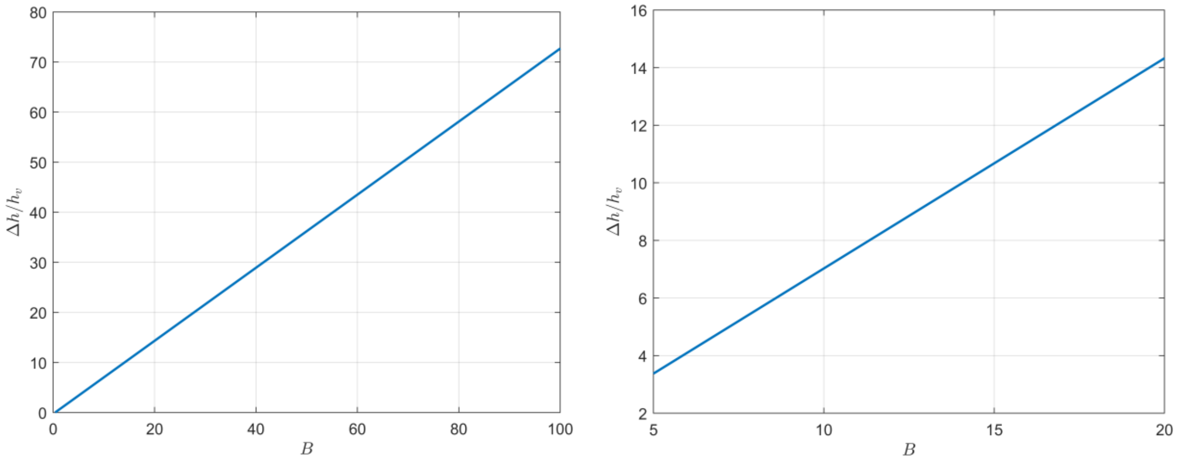

Figure 3.17: Thermochemical parameter $\Delta h/h_v$ as a function of the blowing parameter B for a broad range of values (left) and for typical values in hybrid rockets (right).

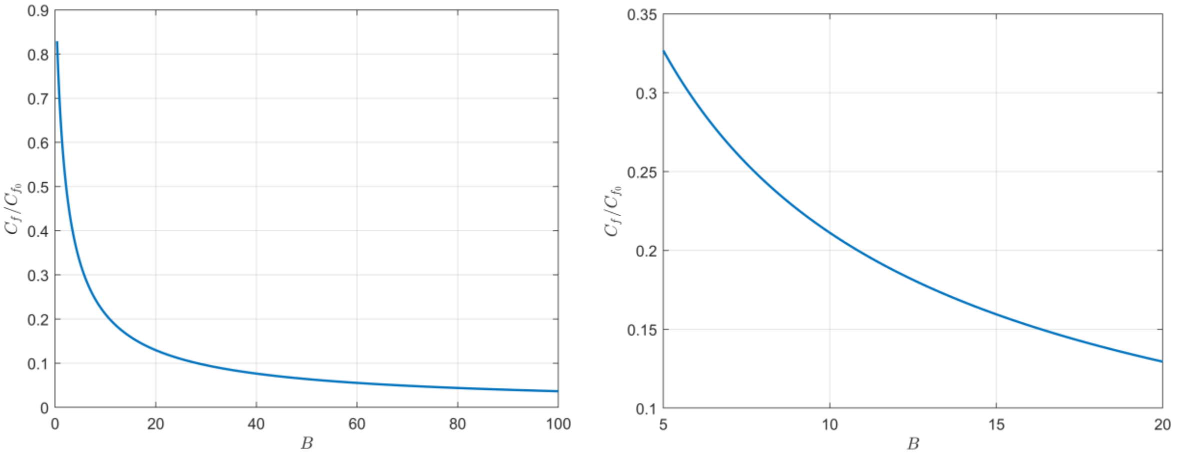

Figure 3.18: C_f/C_{f_0} ratio as a function of the blowing parameter B for a broad range of values (left) and for typical values in hybrid rockets (right).

Influence of $\Delta h/h_v$. The increase of the thermochemical parameter $\Delta h/h_v$ is equivalent to an increase of the heat transfer between the flame and the grain and/or of the reduction of the effective heat of gasification. The blowing parameter B increases (Fig.3.19), although flame position (Fig.3.20) and velocity (Fig.3.21) increase. However, with regard to the latter two parameters, in the common configurations of hybrid engines the variation is still limited, because of the characteristic blocking effect. The increase of B cause a reduction of C_f/C_{f_0} (Fig.3.22).

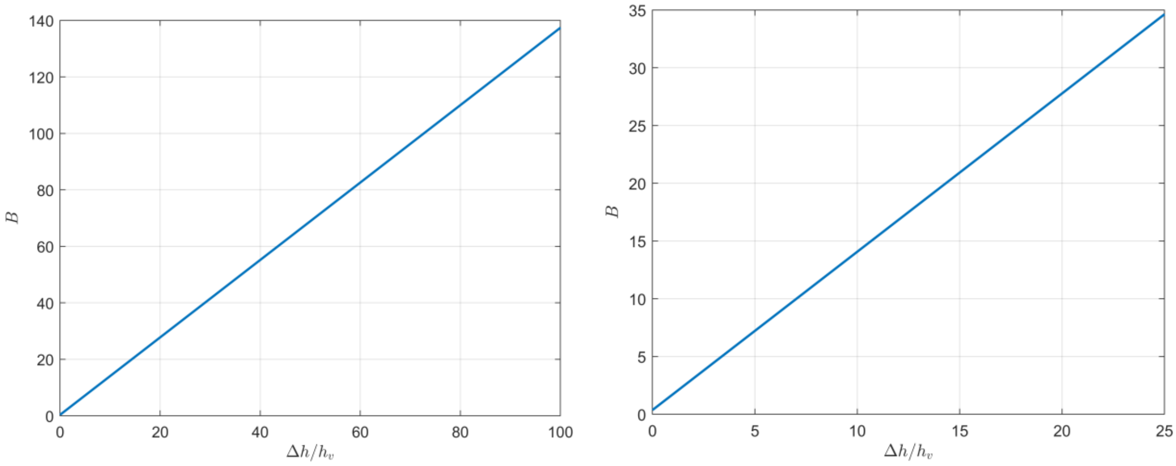

Figure 3.19: Blowing parameter B as a function of the thermochemical parameter $\Delta h/h_v$ for a broad range of values (left) and for typical values in hybrid rockets (right).

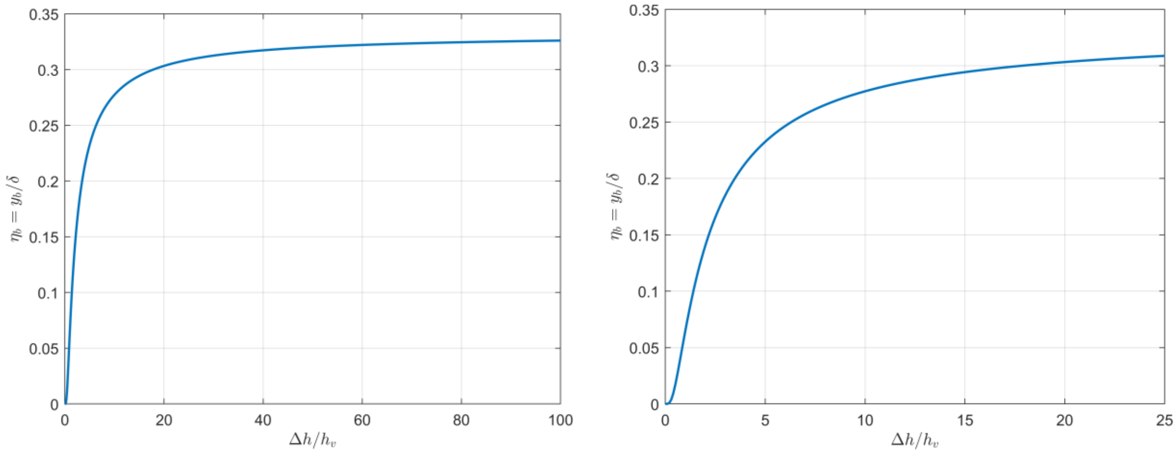

Figure 3.20: Dimensionless flame position η_b as a function of the thermochemical parameter $\Delta h/h_v$ for a broad range of values (left) and for typical values in hybrid rockets (right).

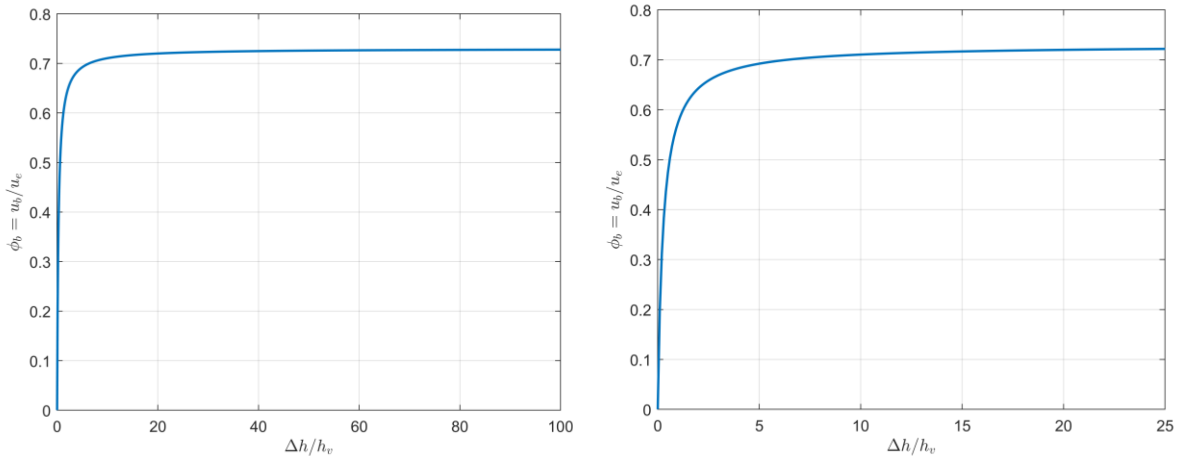

Figure 3.21: Dimensionless flame velocity ϕ_b as a function of the thermochemical parameter $\Delta h/h_v$ for a broad range of values (left) and for typical values in hybrid rockets (right).

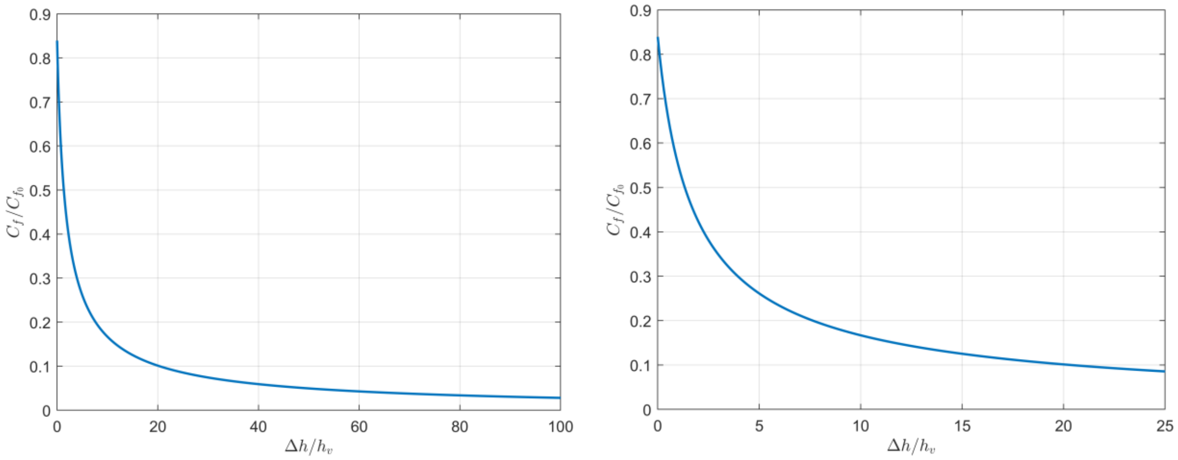

Figure 3.22: C_f/C_{f_0} ratio as a function of the thermochemical parameter $\Delta h/h_v$ for a broad range of values (left) and for typical values in hybrid rockets (right).

Influence of $[O/F]_{react}$. The value of the combustion O/F ratio ($[O/F]_{react}$) has an important influence on the flame position and velocity. If $[O/F]_{react}$ ratio increases, the flame moves away from the grain towards regions richer in oxidant, i.e. towards the boundary layer edge (Fig.3.23). The greater height of the flame produces a reduction of the thermal gradient towards the wall, with a consequent reduction of the heat exchanged and of the blowing parameter B. Reducing the blowing effect results in an increased C_f/C_{f_0} ratio (Fig.3.24).

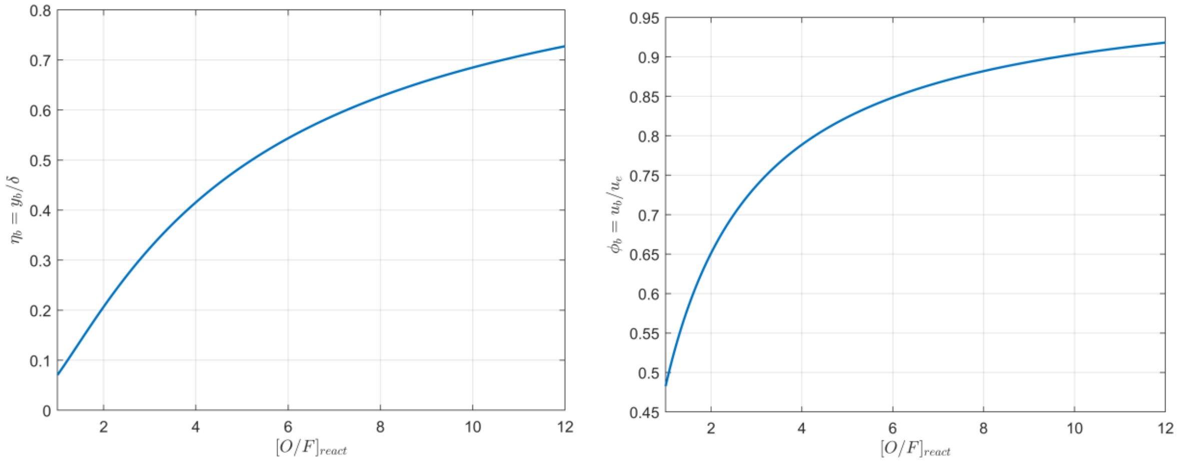

Figure 3.23: Dimensionless flame position η_b (left) and velocity ϕ_b (right) as a function of the $[O/F]_{react}$ ratio.

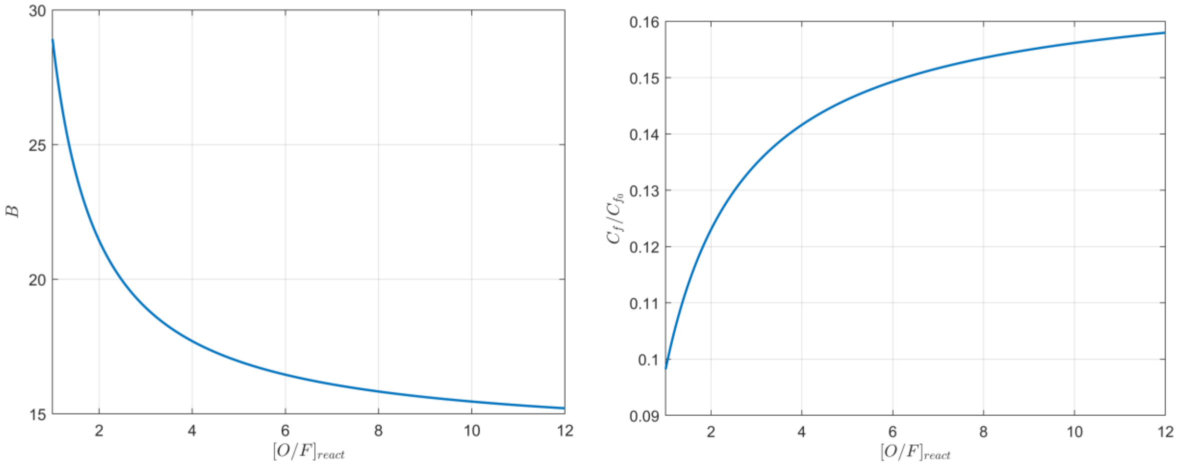

Figure 3.24: Blowing parameter B (left) and C_f/C_{f_0} ratio (right) as a function of the $[O/F]_{react}$ ratio.

Influence of K_{ox_e}. In order to obtain the $[O/F]_{react}$ ratio, the increase of the oxygen mass fraction in the freestream must necessarily verify a lowering of the flame, i.e. the flame moves towards regions with a higher concentration of fuel (Fig.3.25). The lowering of the flame produces a greater heat transfer to the wall, so the blowing coefficient increases and C_f/C_{f_0} decreases with it (Fig.3.26).

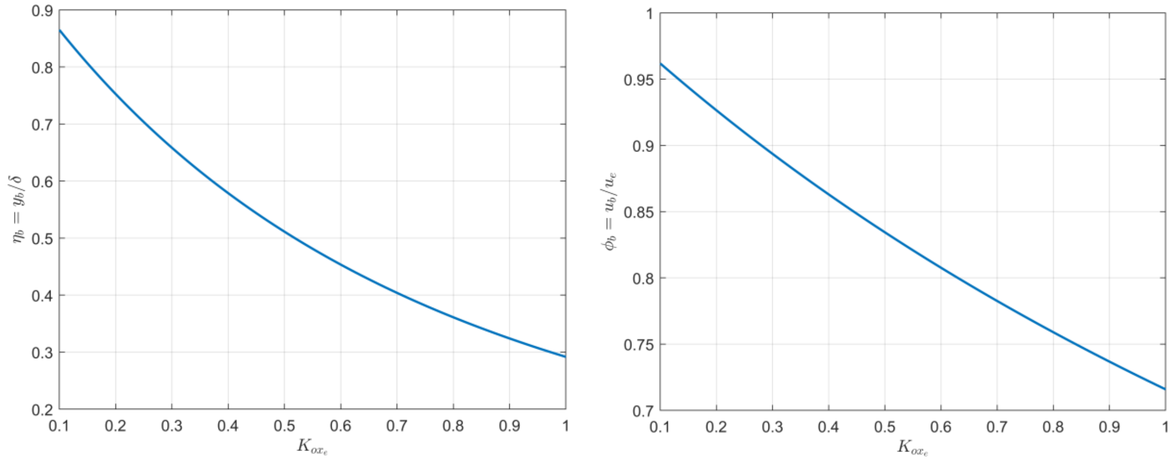

Figure 3.25: Dimensionless flame position η_b (left) and velocity ϕ_b (right) as a function of K_{ox_e}.

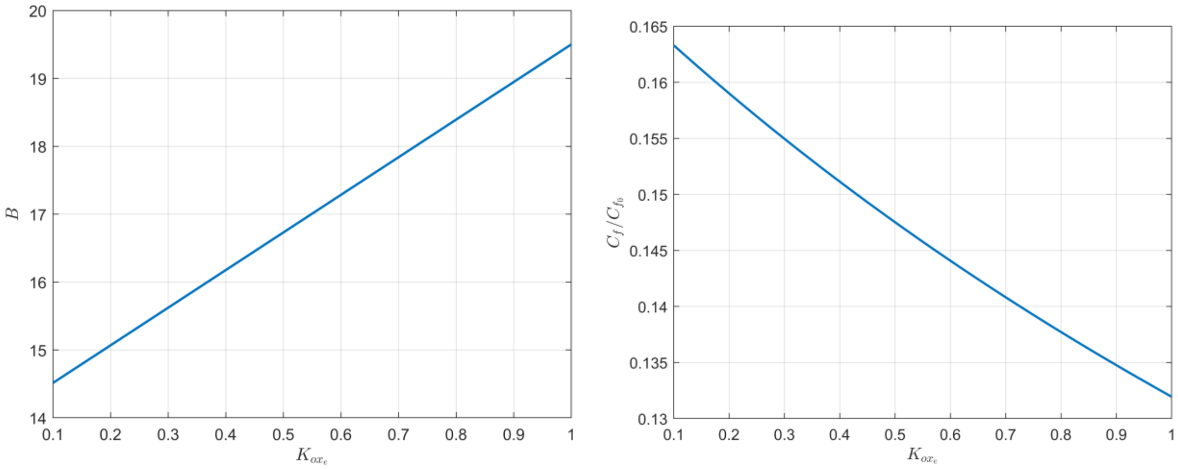

Figure 3.26: Blowing parameter B (left) and C_f/C_{f_0} ratio (right) as a function of K_{ox_e}.

3.9 Mass Fluxes in the Boundary Layer

Let's consider the control volume to be the region within the boundary layer between the leading edge of the grain and the generic location x (Fig.3.27). The net mass flow (per unit grain depth) in the control volume through the entire control surface has three contributions: the inflow oxidizer mass flow rate $\dot{m}_{ox,bl}$ by diffusion from the freestream, the inflow vaporized fuel vertical mass flow $\dot{m}_{f,x}$ from the surface and the outflow mass flow rate $\dot{m}_{\delta}$ at the boundary layer cross sectional area at x coordinate. Part of $\dot{m}_{ox,bl}$ and $\dot{m}_{f,x}$ flows reach the flame, namely $\dot{m}_{ox,flame}$ and $\dot{m}_{f,flame}$ respectively. The remaining fractions, namely $\dot{m}_{\delta,ox}$ and $\dot{m}_{\delta,f}$, exits from the control volume flowing above and below the flame respectively. Together with the combustion product mass flow $\dot{m}_{\delta,pr}$ inside the boundary layer, those last two flows contribute to the outflow mass flow rate $\dot{m}_{\delta}$:

$$\dot{m}_{\delta}(x) = \dot{m}_{\delta,ox}(x) + \dot{m}_{\delta,f}(x) + \dot{m}_{\delta,pr}(x) \qquad (3.73)$$

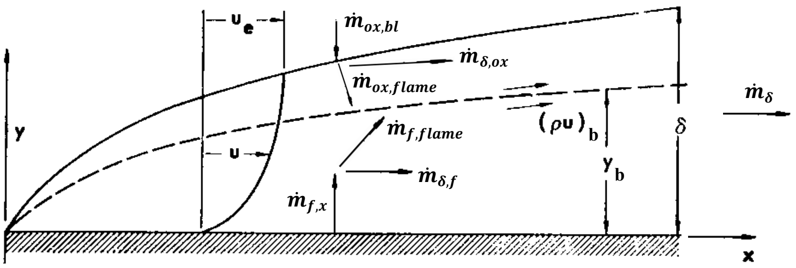

Figure 3.27: Boundary layer schematic. Adapted from [11].

Mass conservation principle yields to the following expressions:

$$\dot{m}_{\delta}(x) = \dot{m}_{ox,bl}(x) + \dot{m}_{f,x}(x) \qquad (3.74)$$

$$\dot{m}_{ox,bl}(x) = \dot{m}_{ox,flame}(x) + \dot{m}_{\delta,ox}(x) \qquad (3.75)$$

$$\dot{m}_{f,x}(x) = \dot{m}_{f,flame}(x) + \dot{m}_{\delta,f}(x) \qquad (3.76)$$

In Marxman's theory, the density within the boundary layer is assumed to be constant and equal to that of the freestream [9]. Therefore, the total flow rate can be calculated as:

$$\dot{m}_{\delta}(x) = \rho_e u_e \int_0^{\delta(x)} \phi(\eta)\, dy \tag{3.77}$$

and its components are determined by referring to the corresponding mass fractions:

$$\dot{m}_{\delta,ox}(x) = \rho_e u_e \int_0^{\delta(x)} K_{ox}(\eta)\phi(\eta)\, dy \tag{3.78}$$

$$\dot{m}_{\delta,f}(x) = \rho_e u_e \int_0^{\delta(x)} K_{f}(\eta)\phi(\eta)\, dy \tag{3.79}$$

$$\dot{m}_{\delta,pr}(x) = \rho_e u_e \int_0^{\delta(x)} K_{pr}(\eta)\phi(\eta)\, dy \tag{3.80}$$

It can be noticed that the fuel mass flow rate above the flame $\dot{m}_{\delta,f}$ is usually very small. This is because the fuel mass fraction is maximum at the surface where the velocity is zero, while moving away from the wall the velocity increases but at the same time the concentration decreases until it becomes zero at the flame.

The mass flow rate leaving the control volume within the boundary layer can be evaluated using the concept of displacement thickness. The displacement thickness δ^* is the distance by which the wall would have to be displaced outward in a hypothetical frictionless flow to maintain the same mass flux as that in the actual viscous flow. The quantity $\rho_e u_e \delta^*$ therefore represents the flow deficit in the boundary layer due to the slowing down of the flow due to viscous friction at the wall [21]. This means that the displacement thickness can be interpreted as the distance by which streamlines outside the boundary layer are displaced due to the presence of the boundary layer. The definition of displacement thickness leads to:

$$\delta^*(x) = \int_0^{\delta(x)} 1 - \frac{u}{u_e}\, dy = \delta(x) \int_0^{1} (1 - \phi)\, d\eta \tag{3.81}$$

The displacement thickness δ^* allows to evaluate $\dot{m}_\delta$ as:

$$\dot{m}_\delta(x) = \rho_e u_e \big(\delta(x) - \delta^*(x)\big) \tag{3.82}$$

In hybrid combustion, the phenomenology of the boundary layer is more complex due to the fuel blowing from the wall. If the dimensionless velocity profile is described by the equation (3.9), then the displacement thickness can be expressed as a function of the blowing parameter by solving the integral (3.81) [28]:

$$\delta^* = \frac{9 + 8B}{36(2 + B)}\delta \tag{3.83}$$

For typical values of $B = 5 - 20$ the displacement thickness is about 20% of the boundary layer thickness.

The dimensionless velocity profile ϕ (3.9) in the integrals of equations (3.77), (3.78), (3.79) and (3.80) is defined as a function of the dimensionless position $\eta = y/\delta$. By applying a change of variable (and therefore of the interval of integration) the flow rates can be rewritten as:

$$\dot{m}_\delta(x) = \rho_e u_e \delta(x) \int_0^1 \phi(\eta)\, d\eta \tag{3.84}$$

$$\dot{m}_{\delta,ox}(x) = \rho_e u_e \delta(x) \int_0^1 K_{ox}(\eta)\phi(\eta)\, d\eta \tag{3.85}$$

$$\dot{m}_{\delta,f}(x) = \rho_e u_e \delta(x) \int_0^1 K_f(\eta)\phi(\eta)\, d\eta \tag{3.86}$$

$$\dot{m}_{\delta,pr}(x) = \rho_e u_e \delta(x) \int_0^1 K_{pr}(\eta)\phi(\eta)\, d\eta \tag{3.87}$$

Since the velocity (and therefore the concentration) profiles are similar along the grain, the ratios between the flow rates and the thickness of the boundary layer are quantities independent on the axial coordinate.

The vaporized fuel mass flow rate at x coordinate can be written as:

$$\dot{m}_{f,x}(x) = \int_0^x \rho_f \dot{r}(x)\, dx \tag{3.88}$$

where the regression rate is expressed with equation (2.28).
Because of mass continuity, the oxidizer mass flow rate that enters in the boundary layer by diffusion from the freestream is:

$$\dot{m}_{ox,bl}(x) = \dot{m}_{\delta}(x) - \dot{m}_{f,x}(x) \tag{3.89}$$

while the oxidizer and fuel flow rates that reach the flame are:

$$\dot{m}_{ox,flame}(x) = \dot{m}_{ox,bl}(x) - \dot{m}_{\delta,ox}(x) \tag{3.90}$$

$$\dot{m}_{f,flame}(x) = \dot{m}_{f,x}(x) - \dot{m}_{\delta,f}(x) \tag{3.91}$$

It is therefore possible to calculate the flame mixture ratio $[O/F]_{flame}$ in the generic section x as:

$$[O/F]_{flame}(x) = \frac{\dot{m}_{ox,flame}(x)}{\dot{m}_{f,flame}(x)} \tag{3.92}$$

By numerically solving the flat plate in an open environment model with ϕ_b calculated with the equation (3.16) a value of $[O/F]_{flame}$ different than $[O/F]_{react}$ (which is used to evaluate the flame velocity and therefore position) is obtained. The reason for this error (about 5%) is due to the simplifications made in the formulation of ϕ_b (3.16) as well for the use of empirical expressions for the definition of δ (3.65) and C_f/C_{f_0} (3.71).

In addition, it is expected that the value of $[O/F]_{flame}$ is independent on the axial position. In fact, the vaporized fuel mass flow rate has a lower than linear trend with x due to the term $Re_x^{-0.2}$ in equation (2.28):

$$\dot{m}_{f,x}(x) = \int_0^x \rho_f \dot{r}(x)\ dx \propto \int_0^x Re_x^{-0.2}\ dx \propto \int_0^x x^{-0.2}\ dx \propto x^{0.8} \tag{3.93}$$

Similarly, the boundary layer thickness δ described by equation (3.65) has the same trend:

$$\delta(x) \propto x Re_x^{-0.2} \propto x^{0.8} \tag{3.94}$$

As a result, the flow rates leaving the control volume are all proportional to $x^{0.8}$:

$$\dot{m}_{\delta}(x) \propto \delta(x) \propto x^{0.8} \tag{3.95}$$

$$\dot{m}_{\delta,ox}(x) \propto \delta(x) \propto x^{0.8} \tag{3.96}$$

$$\dot{m}_{\delta,f}(x) \propto \delta(x) \propto x^{0.8} \tag{3.97}$$

and therefore, the oxidizer flow rate that enters in the boundary layer and the oxidizer and fuel flow rates that reach the flame too, verifying that $[O/F]_{flame}$ does not changes along the length of the grain.

3.10 $[O/F]_{bl}$ Ratio

In this work, $[O/F]_{bl}$ ratio is defined as the ratio between the inflow oxidizer mass flow rate $\dot{m}_{ox,bl}$ from the freestream and the inflow vaporized fuel mass flow rate $\dot{m}_{f,x}$ from the grain into the boundary layer:

$$[O/F]_{bl} = \frac{\dot{m}_{ox,bl}}{\dot{m}_{f,x}} \tag{3.98}$$

From numerical simulations it can be easily observed that $[O/F]_{bl} \gg [O/F]_{react}$. This means that, to obtain the correct oxidizer/fuel ratio at the flame, $\dot{m}_{ox,bl}$ must be much greater than $\dot{m}_{ox,flame}$, because of the significant $\dot{m}_{\delta,ox}$ carried away above the flame.

Influence of $\Delta h/h_v$. If the thermochemical parameter $\Delta h/h_v$ increases, also the flame height, the blowing parameter B, the inflow vaporized fuel mass flow rate, the boundary layer thickness and the outflow mass flow rate $\dot{m}_\delta$ increase. Calculations show that the increase of $\dot{m}_{f,x}$ is greater than that of $\dot{m}_{ox,bl}$ (Fig.3.28), leading to a decrease of $[O/F]_{bl}$ (Fig.3.29). For $\Delta h/h_v \to 0$ it is $\dot{m}_{f,x} \to 0$ and $[O/F]_{bl} \to \infty$. The asymptotic trend for $\Delta h/h_v \to \infty$ is due to the typical blocking effect of hybrid combustion.

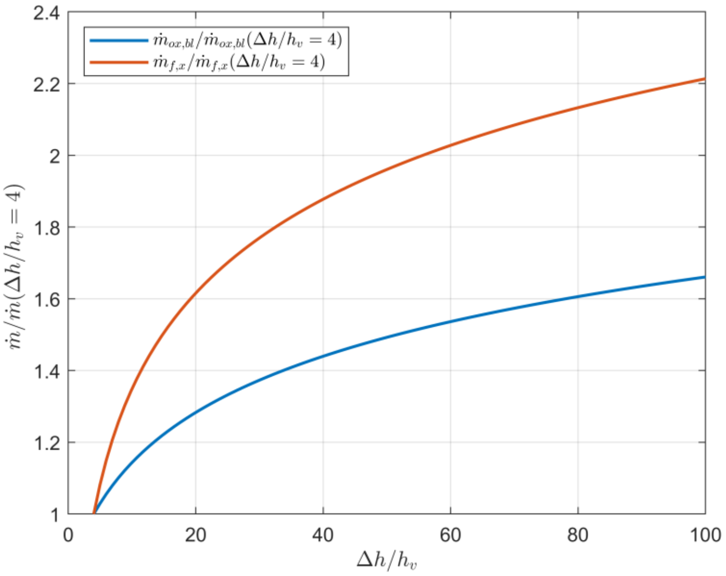

Figure 3.28: Dimensionless oxidizer and fuel flows entering in the boundary layer and fuel mass flow rate with respect to the correspondingly values for $\Delta h/h_v = 4$ as a function of the thermochemical parameter $\Delta h/h_v$.

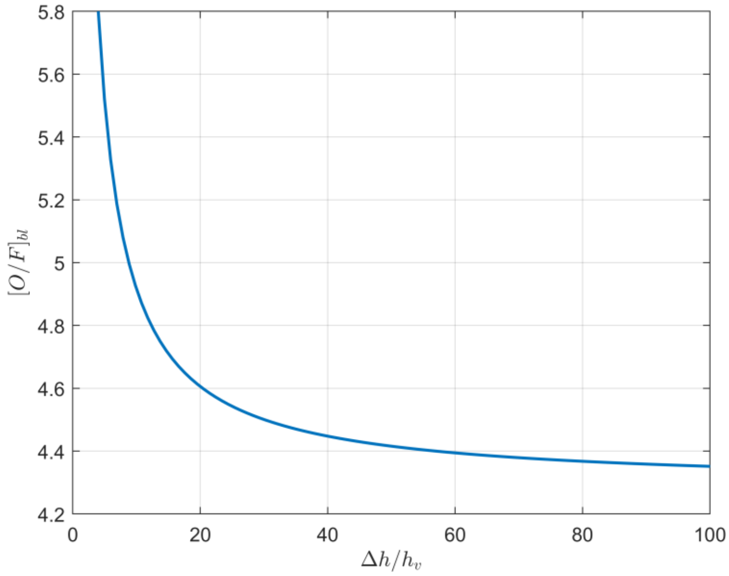

Figure 3.29: $[O/F]_{bl}$ as a function of the thermochemical parameter $\Delta h/h_v$.

If $[O/F]_{react}$ increase, while keeping the same value for $\Delta h/h_v$, then the flame moves away from the grain surface leading to a reduction of the blowing parameter B and of the boundary layer thickness. Moreover, the regression rate and thus the inflow vaporized fuel mass flow rate decrease. However, calculations show that the inflow oxidizer mass flow rate $\dot{m}_{ox,bl}$ increases, leading to a slightly growth of $[O/F]_{bl}$ ratio (Fig.3.30).

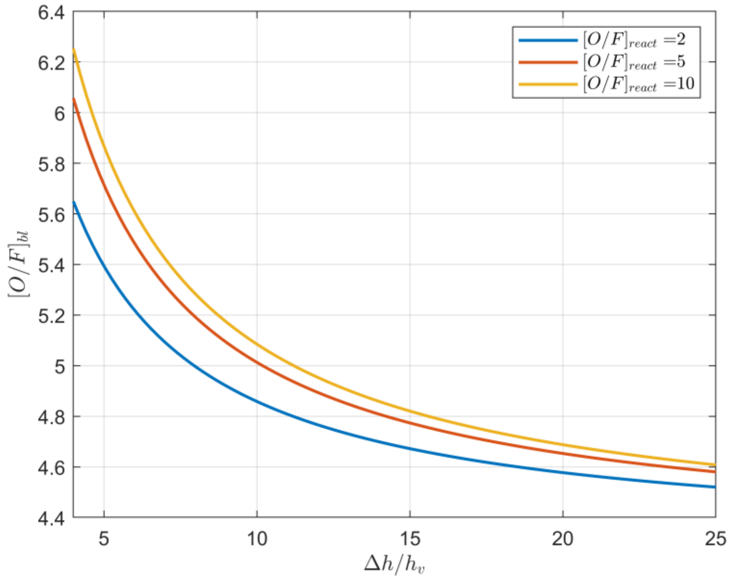

Figure 3.30: $[O/F]_{bl}$ as a function of the thermochemical parameter $\Delta h/h_v$ for several values of $[O/F]_{react}$.

Influence of $[O/F]_{react}$. Considering the same value for the thermochemical parameter $\Delta h/h_v$, the increase of the $[O/F]_{react}$ ratio value leads the flame to move away from the grain surface and to a reduction of the blowing parameter B and of the boundary layer thickness. Calculations show the reduction of $\dot{m}_{\delta}, \dot{m}_{f,x}$ and $\dot{m}_{ox,bl}$. However, the reduction of $\dot{m}_{f,x}$ is greater than the reduction of $\dot{m}_{ox,bl}$ (Fig.3.31), thus leading to a small increase of $[O/F]_{bl}$ as $[O/F]_{react}$ ratio grows (Fig.3.32).

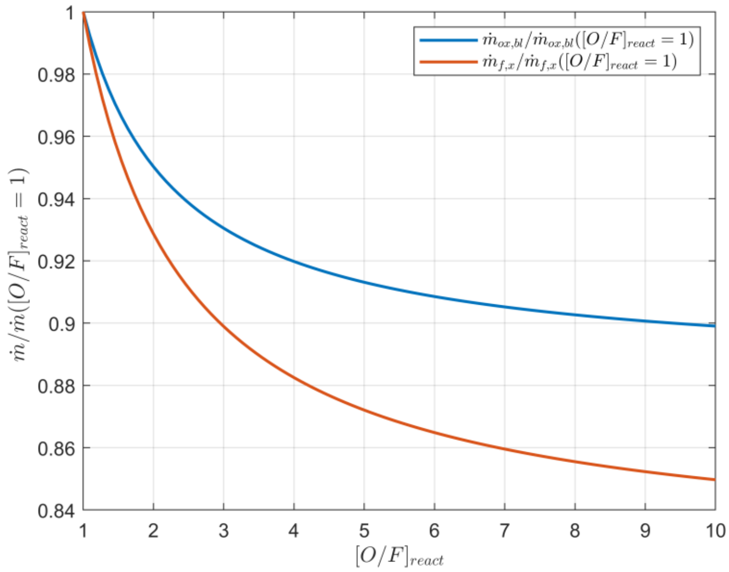

Figure 3.31: Dimensionless oxidizer and fuel mass flow rate with respect to the correspondingly values for $[O/F]_{react} = 1$ as a function of the $[O/F]_{react}$ ratio.

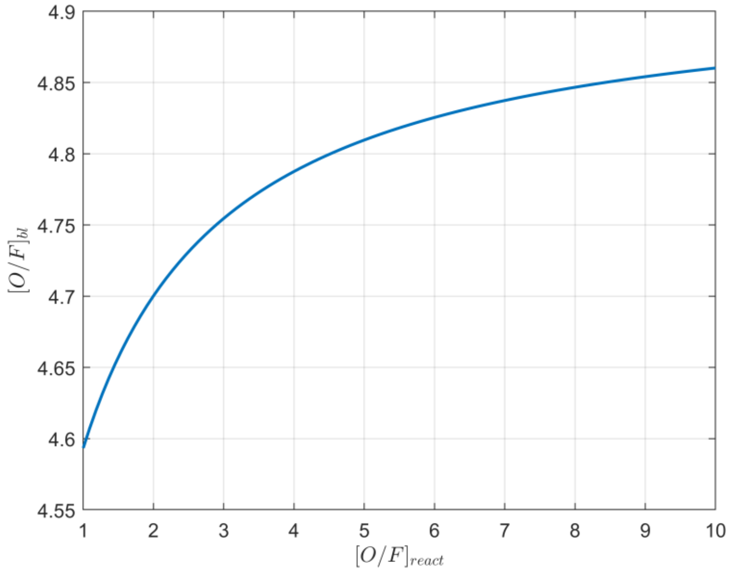

Figure 3.32: $[O/F]_{bl}$ as a function of the $[O/F]_{react}$ ratio.

If $[O/F]_{bl}$ is divided by $[O/F]_{react}$, it can be seen that this ratio decreases as $[O/F]_{react}$ increases, meaning that as $[O/F]_{react}$ ratio increase the inflow oxidizer mass flow rate must decrease (thus $[O/F]_{bl}$ too) in order to verify the correct oxidizer/fuel ratio at the flame (Fig.3.33). An increase of the thermochemical parameter $\Delta h/h_v$ value causes a greater increase of $\dot{m}_{f,x}$ than of $\dot{m}_{ox,bl}$ leading to a small reduction of $[O/F]_{bl}/[O/F]_{react}$ (Fig.3.34).

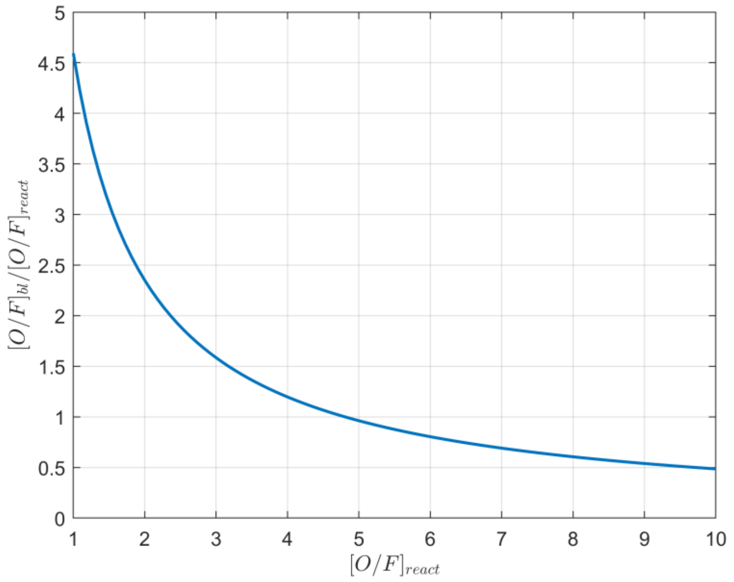

Figure 3.33: $[O/F]_{bl}/[O/F]_{react}$ as a function of the $[O/F]_{react}$ ratio.

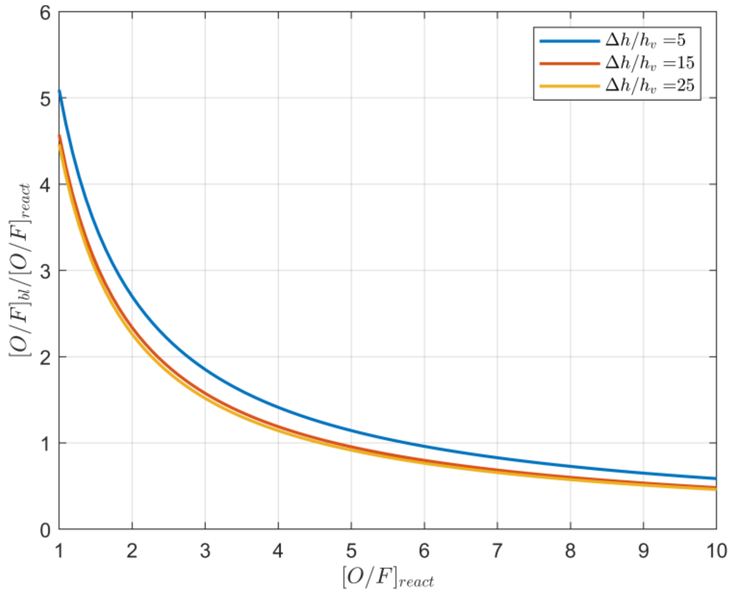

Figure 3.34: $[O/F]_{bl}/[O/F]_{react}$ as a function of the $[O/F]_{react}$ ratio for several values of the thermochemical parameter $\Delta h/h_v$.

3.11 Combustion Efficiency

The combustion efficiency η_{c^*} for chemical rockets is the ratio of the actual energy released to the ideal heat of reaction per unit of propellant mass and represents a measure of the source efficiency [3]. In hybrid rockets combustion efficiency is significantly dependent on the level of mixing of the oxidizer and fuel within the engine. Therefore, in this work the propellant combustion efficiency, defined as the ratio between the mass flow (fuel or oxidizer) that participate to the combustion process to the corresponding total mass flow that enters the boundary layer will be named η_{comb}. With this definition in mind, the fuel combustion efficiency is:

$$\eta_{comb,f} = \frac{\dot{m}_{f,flame}}{\dot{m}_{f,x}} \tag{3.99}$$

and the oxidizer combustion efficiency is:

$$\eta_{comb,ox} = \frac{\dot{m}_{ox,flame}}{\dot{m}_{ox,bl}} \tag{3.100}$$

Influence of $\Delta h/h_v$. An increase of the thermochemical parameter $\Delta h/h_v$ causes the flame to move away from the surface grain thus leading $\dot{m}_{\delta,f}$ to be a greater percentage of $\dot{m}_{f,x}$. As a result, the fuel combustion efficiency decreases due to the higher fuel mass flow rate carried away below the flame, while oxidizer combustion efficiency increases because of $\dot{m}_{\delta,ox}$ reduction (Fig.3.35). In fact, for $\Delta h/h_v \rightarrow 0$, the flame goes to the grain surface, thus all vaporized fuel mass flow reaches the flame, therefore the fuel combustion efficiency becomes unity while the oxidizer combustion efficiency becomes zero. Those effects are amplified by the further rising of the flame because of the $[O/F]_{react}$ ratio (Fig.3.36). The asymptotic behaviour for $\Delta h/h_v \rightarrow \infty$ is due to the typical blocking effect of hybrid combustion.

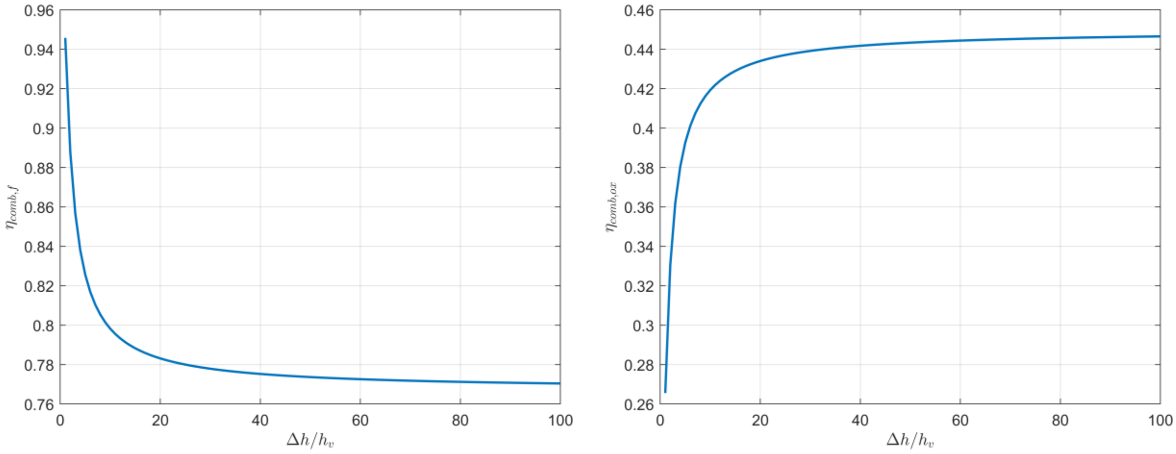

Figure 3.35: Combustion efficiency for the fuel $\eta_{comb,f}$ (left) and for the oxidizer $\eta_{comb,ox}$ (right) as a function of the thermochemical parameter $\Delta h/h_v$.

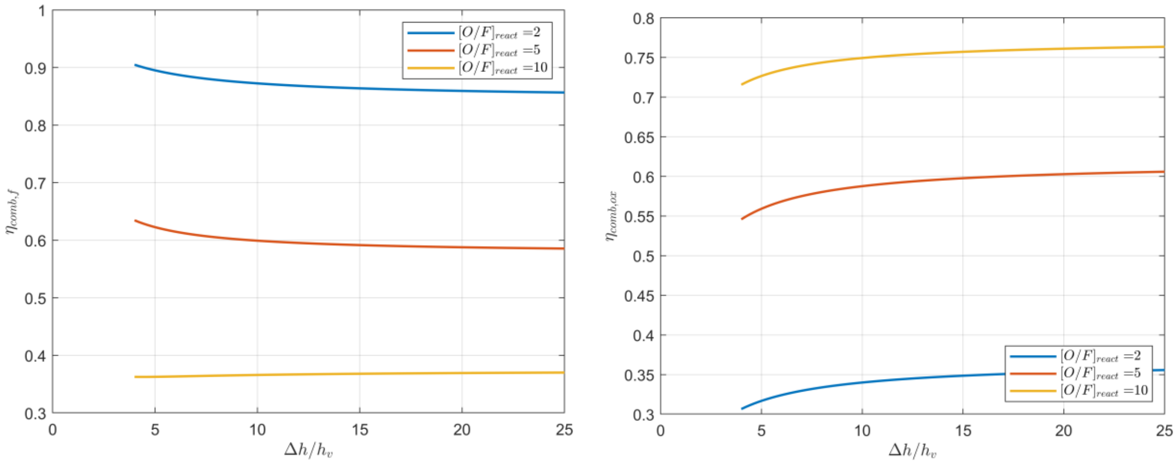

Figure 3.36: Combustion efficiency for the fuel $\eta_{comb,f}$ (left) and for the oxidizer $\eta_{comb,ox}$ (right) as a function of the thermochemical parameter $\Delta h/h_v$ for several values of the $[O/F]_{react}$ ratio.

Influence of $[O/F]_{react}$. The effects of changing $[O/F]_{react}$ ratio value is the same of $\Delta h/h_v$, because the increase in both parameter leads to a rise of the flame position. Therefore, the higher the flame position the greater is $\dot{m}_{\delta,f}$ and the lower is $\dot{m}_{\delta,ox}$, leading to an increase of $\eta_{comb,ox}$ and a reduction of $\eta_{comb,f}$ (Fig.3.37).

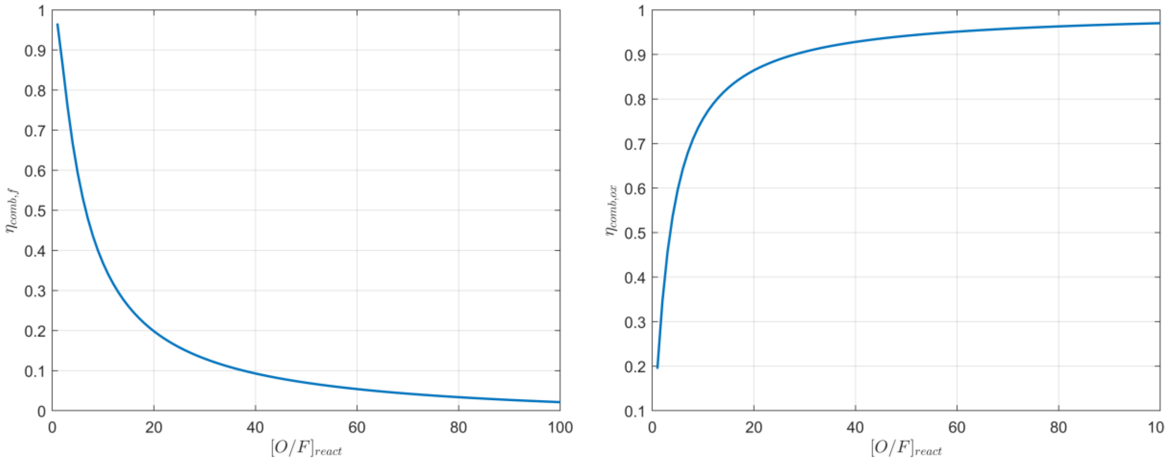

Figure 3.37: Combustion efficiency for the fuel $\eta_{comb,f}$ (left) and for the oxidizer $\eta_{comb,ox}$ (right) as a function of the $[O/F]_{react}$ ratio.

By increasing the value of the thermochemical parameter $\Delta h/h_v$ (i.e. moving further away the flame) a slightly decrease and increase of fuel and oxidizer combustion efficiency respectively is observed (Fig.3.38).

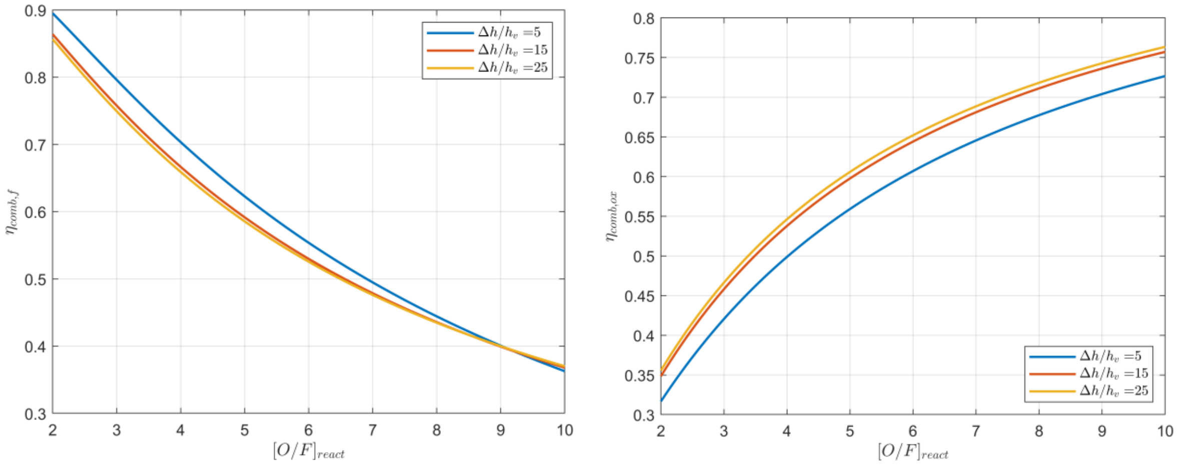

Figure 3.38: Combustion efficiency for the fuel $\eta_{comb,f}$ (left) and for the oxidizer $\eta_{comb,ox}$ (right) as a function of the $[O/F]_{react}$ ratio for several values of the thermochemical parameter $\Delta h/h_v$.

Evaluating the propellant combustion efficiency as a function of $[O/F]_{flame}/[O/F]_{bl}$ ratio, it is expected that the fuel and oxidizer combustion efficiencies are equal when the percentage of oxidizer and fuel that reach the flame are equal, therefore when $[O/F]_{flame} = [O/F]_{bl}$. In fact, considering:

$$\eta_{comb,f} = \frac{\dot{m}_{f,flame}}{\dot{m}_{f,x}} = \eta_{comb,ox} = \frac{\dot{m}_{ox,flame}}{\dot{m}_{ox,bl}} \tag{3.101}$$

yields to:

$$\frac{\dot{m}_{ox,flame}}{\dot{m}_{f,flame}} = \frac{\dot{m}_{ox,bl}}{\dot{m}_{f,x}} \tag{3.102}$$

The left term of the previous equation is $[O/F]_{flame}$, while the right term is $[O/F]_{bl}$. Once again, the numerical simulation shows that the previous statement is true only if the $[O/F]_{flame}$ ratio value is considered rather than $[O/F]_{react}$, because of the simplification to evaluate ϕ_b (Fig.3.39).

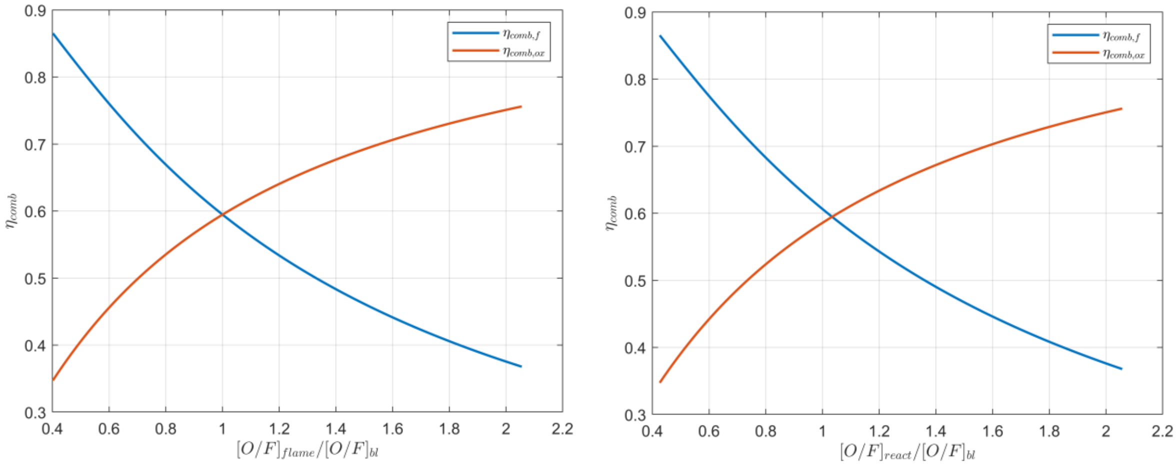

Figure 3.39: Combustion efficiency for the fuel $\eta_{comb,f}$ and for the oxidizer $\eta_{comb,ox}$ as a function of the $[O/F]_{flame}/[O/F]_{bl}$ ratio (left) and of the $[O/F]_{react}/[O/F]_{bl}$ ratio (right).

3.12 Hybrid Combustion Variable-Density Boundary Layer

The aerodynamic structure of boundary layers with gas injection through a porous surface in the absence of chemical transformations has been studied extensively, while there is a lack of experimental information on the structure of reacting boundary layers with heat and mass transfer processes. The reason is the complexity of the experimental equipment, the effect of radiation and chemical transformations, of heat and mass transfer and of the turbulent characteristic of the flow. As a result, the limited availability of experimental information significantly complicates the analysis and generalization of results.

Most available experimental studies involve the study of the reactive boundary layer with a propane or ethanol - air diffusion flame [48][50][52]. In those studies, it can be seen that the concentration and temperature profiles have a qualitatively similar trend to that assumed by Marxman and described in this chapter. The temperature distribution (Fig.3.40) has a peak at the flame zone, which tends to thicken because of the turbulent characteristic of the flow and when the flame is not able to burn all reagents sufficiently fast. The flame zone coincides with the maximum concentration of combustion products and with the minimum concentration of the reactants (Fig.3.41). In both laminar and turbulent flow, secondary reaction products can be found between the flame and the wall. Fig.3.41 also shows the density profile, which is strongly influenced by combustion because of the heat releasing that significantly reduces the density of the mixture over the entire boundary layer thickness. At the same time, the molecular weight of the mixture, except for the region immediately adjacent to the wall, remains almost constant and close to the molecular weight of air.

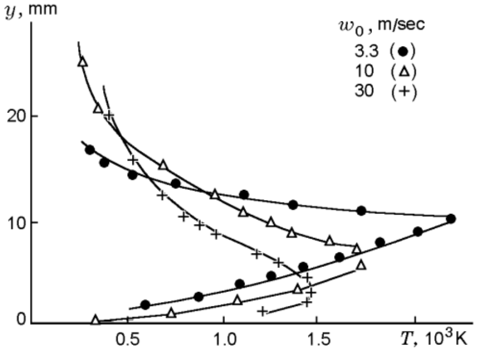

Figure 3.40: Temperature profiles in the boundary layer with ethanol combustion. The flow is laminar for the velocity $w_0 = 3.3\ m/s$ and turbulent for higher velocity [52].

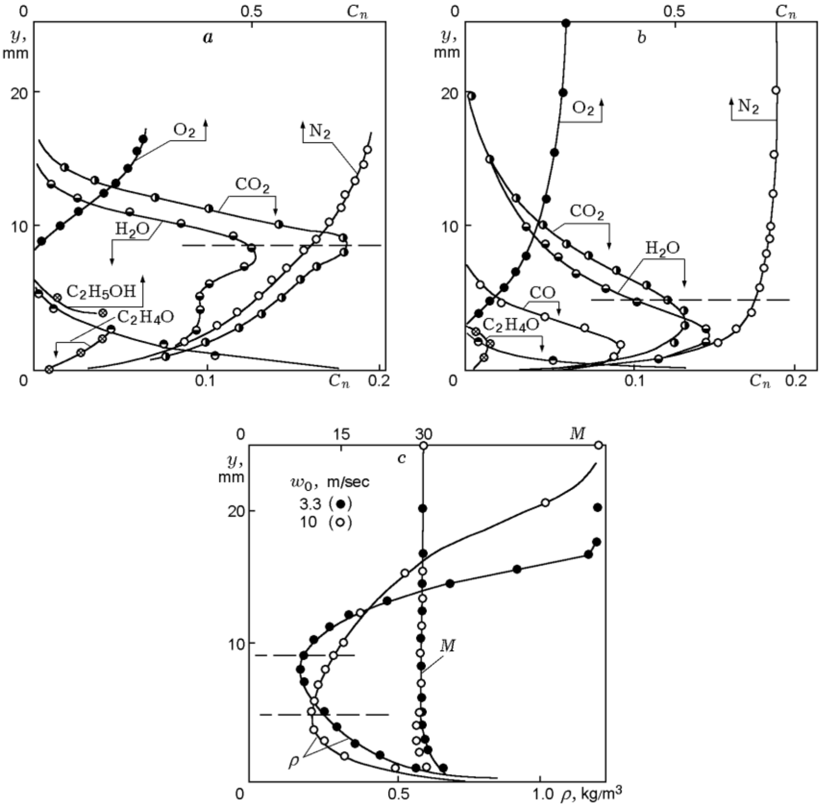

Figure 3.41: Distribution of component concentration (a, for laminar flow regime; b, for turbulent flow regime), and density and molar weight (c) of the substances in the reacting boundary layer with ethanol combustion. The dashed lines indicate the flame front position [52].

In experimental studies of the aerodynamic structure with a diffusion flame, a velocity peak was observed at the flame zone (usually slightly below the temperature peak) due to a decrease in density and associated strong expansion of the mixture (Fig.3.42). In fact, the flame acts as an obstacle and creates a pressure increase just upstream of the flame attachment point. This leads to a significant favourable pressure gradient downstream and the subsequent acceleration of the flow [42]. In addition, because of the reduction in density due to the rise in temperature, the gas is more sensitive to local acceleration caused by the inertia of the incoming horizontal oxidizer flow which does not allow the gas to expand normally and to local pressure gradient. The local maximum can significantly exceed the velocity in the flow core (typically $u_b/u_e = 1.1 \div 1.3$ [42]), and its magnitude and position depend on the fuel-injection velocity and longitudinal pressure gradient.

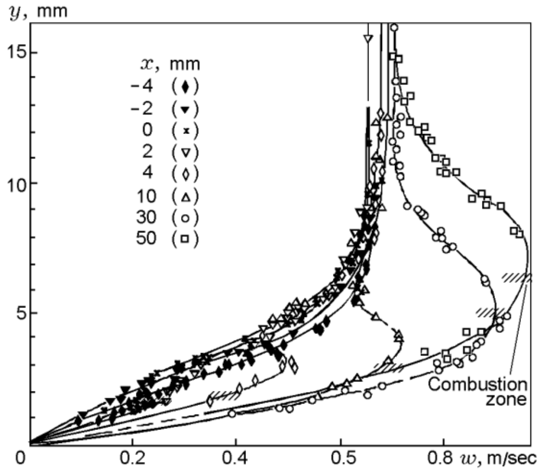

Figure 3.42. Velocity profiles in the boundary layer with propane – air diffusion flame [52].

Numerous numerical investigation [40][41][47][54] confirm this feature in a boundary layer with diffusive flame. However, the few analytical formulations (e.g. [47]) proposed to describe the velocity profile do not allow the generalization of the results.

Chapter 4

Single-Port Hybrid Rocket Combustion Chamber Preliminary Sizing

The goal of this chapter is to outline one of the many approaches that can be used for preliminary sizing a hybrid propulsion system. In particular, the focus here is on the top-level geometric design and mass estimate of the combustion chamber and single-port fuel grain, not on detailed design of those and other components (e.g. pressurization system, nozzle, etc.) for which reference is made to literature [3][4][29]. Performance estimation will be done using a 0D model, from whose output information it is possible to confirm the successfully design of the engine system. If not, an iterative procedure is applied until the mission requirements are verified. To realistically estimate the performances, the engine's operation over time has to be numerically simulated with an internal ballistic model.

4.1 Hybrid Rocket Combustion Chamber Preliminary Sizing

Let's assume, for example, that the overall mission requirement for a propulsion system design is that it is able to deliver a specified constant thrust T for a burning time t_b in a certain environment. The mission environments, particularly the thermal and dynamic environments (shock and vibration), can drive the design by limiting the selection of propellants [29].

The propellants (fuel and oxidizer), the average combustion chamber pressure p_{cc}, the average O/F ratio ($[O/F]_{glob}$), the nozzle shape and the pressurization mechanism are then selected. Several factors contribute to the propellant selection, including performance, density and costs (which depends not only on the type of propellant, but also to its safe management). By using the average chamber pressure and the O/F ratio into a thermochemical code (e.g. CEA, CProPep) it is possible to determine the theoretical characteristic velocity c^* (Fig.4.1), the combustion product characteristics (k, M_m, c_p, chemical composition, etc.) and the flame temperature for the chosen propellants.

The selection of chamber pressure and O/F ratio impact the mass and volume of the system and the throat erosion during operations. For example, an increase in combustion chamber pressure will generally increase the ideal specific impulse of the motor and leads to a reduction in the size and mass of the nozzle because of the reduction of both throat and exit areas for the same area ratio. However, increasing the chamber pressure may result in a greater chamber structural mass (if the chamber wall thickness is above material thickness). In hybrid engines, a variation of the delivered O/F ratio can generally be observed (O/F shift), therefore the value of the chosen average O/F ratio (which is used in the sizing of the propulsion system) is usually the one that allows working around optimal conditions. Typically, the O/F ratio is large for hybrid rocket motor propellant combinations, as the performance tends to optimize at higher O/F ratio.

As already discussed in Chapter 2, the regression rate varies along the grain port accordingly to equation (2.35). This leads to coupling of the fuel regression rate with the unknown a priori mass flux, therefore substantially complicating the modelling. As a result, in the combustion chamber preliminary sizing the regression rate is calculated as a function only of the specific oxidizer flow rate by using equation (2.53), where the parameters a and n can be derived from the literature [4][29]. Measured values of the exponent n are a function of the selected propellants and are typically in the range of 0.3– 0.8. The value of n is the key to understanding the overall motor ballistics since it influences the O/F shift of the motor.

The lasts required inputs are the nozzle area ratio $\epsilon = A_e/A_{th}$ and the initial oxidizer mass flux G_{ox_0}, the value of which must be below the flooding limit for the chosen pair of propellants, taking into account that during combustion it is necessary to limit the minimum flow rate to values sufficiently distant from the cooking limit.

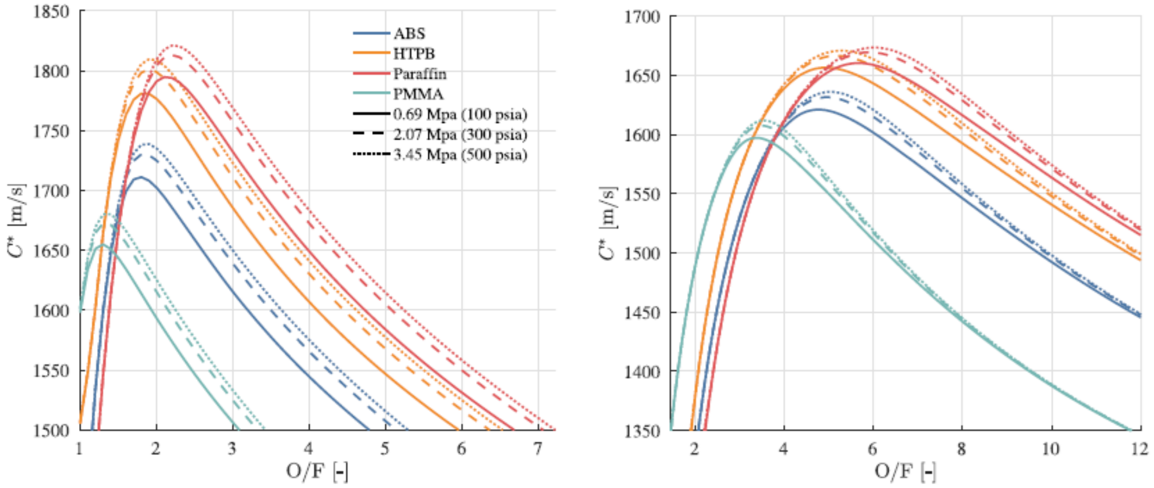

(a) $GOx - O_2$ (g) (b) H_2O_2 (L)

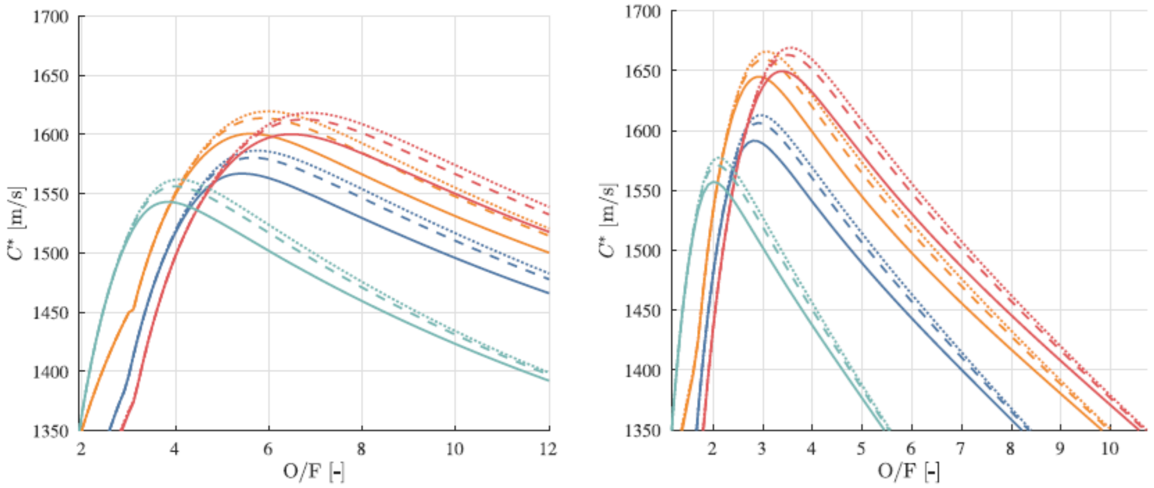

(c) N_2O (L) (d) N_2O_4 (L)

Figure 4.1: Ideal c^* as a function of O/F ratio and chamber pressure for selected hybrid propellant combinations determined using CEA thermochemical code assuming equilibrium combustion conditions. The legend in (a) applies to all figures [29].

Let's consider a single-port cylindrical fuel grain (which is the simplest and most efficient grain geometry) with an initial diameter D_0 and length L inside the combustion chamber (Fig.4.2), where the injected oxidizer mass flow rate is kept constant. Similar considerations to the following one can also be made for the preliminary sizing of multi-port (even non-circular ones) grain configurations [4].

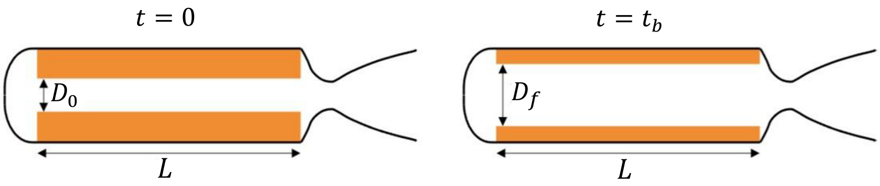

Figure 4.2: Schematic of a single-port hybrid rocket before and after combustion. Adapted from [29].

Knowing the average chamber and environment pressures and the nozzle area ratio, it is possible to evaluate the thrust coefficient with equation:

$$c_F = \sqrt{k}\left(\frac{2}{k+1}\right)^{\frac{k+1}{2(k-1)}}\sqrt{\frac{2k}{k-1}\left[1-\left(\frac{p_e}{p_{cc}}\right)^{\frac{k-1}{k}}\right]} + \frac{A_e}{A_{th}}\left(\frac{p_e}{p_{cc}} - \frac{p_a}{p_{cc}}\right) \tag{4.1}$$

Therefore, the theoretical specific impulse, $I_{sp,ideal}$, is:

$$I_{sp,ideal} = \frac{c_F c^*}{g_0} \tag{4.2}$$

The real specific impulse calculation requires the knowledge of the nozzle efficiency η_{c_F}, and the combustion efficiency η_{c^*}. The nozzle efficiency value depends on several factors including divergence losses, two-phase flow losses, boundary layer/wall friction losses, chemical kinetic losses (due to chemical reactions within the nozzle), nozzle throat erosion, nozzle submergence and other losses [3][4]. With a correct nozzle design, the nozzle efficiency could be as high as $0.96 - 0.99$. The combustion efficiency represents a combined effectiveness of the combustion chamber and the injector design. Its value is influenced by incomplete mixing or combustion (this is particularly critical for hybrid engines) and by real gas properties. The combustion efficiency for single port grain without any mixing enhancing configuration is usually in the range of $0.75 - 0.90$ [29]. The real value of η_{c_F} and η_{c^*} it is not known at the beginning of the preliminary sizing, therefore their value must be assumed and verified during the performance evaluation at the end of the design procedure. The real specific impulse, $I_{sp,real}$, can be calculated as:

$$I_{sp,real} = I_{sp,ideal}\eta_{c_F}\eta_{c^*} \tag{4.3}$$

The average propellant mass flow, $\dot{m}_{prop}$, can be determined as:

$$\dot{m}_{prop} = \frac{T}{I_{sp,real} g_0} \tag{4.4}$$

The oxidizer and fuel mass flow rate are related to the average propellant mass flow through the O/F ratio:

$$\dot{m}_{prop} = \dot{m}_{ox} + \dot{m}_f = \dot{m}_{ox}\left(1 + \frac{1}{O/F}\right) \tag{4.5}$$

therefore:

$$\dot{m}_{ox} = \frac{\dot{m}_{prop}}{1 + \frac{1}{O/F}} \tag{4.6}$$

$$\dot{m}_f = \frac{\dot{m}_{prop}}{1 + O/F} \tag{4.7}$$

The corresponding propellant masses can be calculated easily based on the propellant mass flow rate and the burn time:

$$m_{prop} = \dot{m}_{prop} t_b \tag{4.8}$$

$$m_{ox} = \dot{m}_{ox} t_b \tag{4.9}$$

$$m_f = \dot{m}_f t_b \tag{4.10}$$

The propellants volumes can be calculated as:

$$V_{ox} = \frac{m_{ox}}{\rho_{ox}} \tag{4.11}$$

$$V_f = \frac{m_f}{\rho_f} \tag{4.12}$$

The throat area and diameter are calculated by using the expression for the chocked mass flow rate through a nozzle [4]:

$$A_{th} = \frac{\dot{m}_{prop} c^* \eta_{c^*}}{p_{cc}} = \frac{T}{c_F \eta_{c_F} p_{cc}} \tag{4.13}$$

$$D_{th} = \sqrt{\frac{4A_{th}}{\pi}} \tag{4.14}$$

By using the definition of area ratio, the nozzle exit area and diameter are evaluated:

$$A_e = \epsilon A_{th} \tag{4.15}$$

$$D_e = \sqrt{\frac{4A_e}{\pi}} \tag{4.16}$$

Using the value of the initial oxidizer mass flux G_{ox_0}, the initial port area and diameter can be determined:

$$A_{p_0} = \frac{\dot{m}_{ox}}{G_{ox_0}} \tag{4.17}$$

$$D_0 = \sqrt{\frac{4A_{p_0}}{\pi}} \tag{4.18}$$

A hybrid rocket motor requires a specific fuel grain geometry (Fig.4.3) to achieve the desired performance similarly to a solid rocket motor.

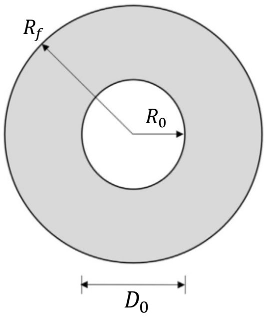

Figure 4.3: Fuel grain geometry. Adapted from [29].

The port diameter, D, will set the oxidizer mass flux, which changes with time based on the regression rate equation (2.53) as:

$$\frac{dD}{dt} = 2\dot{r} = 2aG_{ox}^{n} \tag{4.19}$$

Developing the previous equation gives:

$$\dot{r} = \frac{1}{2}\frac{dD}{dt} = aG_{ox}^{n} = a\left(\frac{4\dot{m}_{ox}}{\pi D^2}\right)^{n} = a\left(\frac{4\dot{m}_{ox}}{\pi}\right)^{n} D^{-2n} \tag{4.20}$$

Separating the variables and integrating between $t = 0$ and the generic time t yields to:

$$\int_{D_0}^{D} D^{2n}\, dD = 2a\left(\frac{4\dot{m}_{ox}}{\pi}\right)^{n} \int_{0}^{t} dt \tag{4.21}$$

The integration allows to derive the port diameter as a function of time with the equation:

$$D = \left[2a(2n+1)\left(\frac{4\dot{m}_{ox}}{\pi}\right)^{n} t + D_0^{2n+1}\right]^{\frac{1}{2n+1}} \tag{4.22}$$

Considering the burn time t_b, the final port diameter is:

$$D_f = \left[2a(2n+1)\left(\frac{4\dot{m}_{ox}}{\pi}\right)^{n} t_b + D_0^{2n+1}\right]^{\frac{1}{2n+1}} \tag{4.23}$$

Equation (4.23) can be written also as a function of the diameter ratio $R = D_f/D_0$ [13]:

$$R^{2n+1} = (4n+2)\frac{aG_{ox_0}^{n} t_b}{D_0} + 1 \tag{4.24}$$

The web thickness is therefore:

$$w = \frac{D_f - D_0}{2} \tag{4.25}$$

The design of the solid grain is such that the achievement of the average operating conditions (O/F ratio and chamber pressure) is obtained at about half the burning time. From the knowledge of the fuel volume and the initial and final port diameters, the grain length is:

$$L = \frac{V_f}{\frac{\pi}{4}\left(D_f^2 - D_0^2\right)} \tag{4.26}$$

The combustion chamber volume is instead:

$$V_{cc} = \frac{\pi}{4} D_f^2 L \tag{4.27}$$

Figure of merit of the hybrid propulsion system is the port volume loading, defined as the ratio between the fuel volume and the combustion chamber volume:

$$VL = \frac{V_f}{V_{cc}} = 1 - \frac{1}{R^2} \tag{4.28}$$

As can be seen from the previous equation, the VL (or equivalently the diameter ratio R) is a parameter that allows to evaluate the filling efficiency of the combustion chamber. A high value of VL (i.e. of R) is indicatory of a "full" engine, i.e. in which most of the volume of the combustion chamber is occupied by fuel. The port volume loading increases asymptotically up to 1 with R (Fig.4.4). Typically, it is recommended to have a diameter ratio R at least between 2 and 3 in order to achieve a reasonable VL, while for greater values of R the further increase of VL is not too much meaningful. In addition, low volume loading values should be avoided as they lead to an “empty” engine, i.e. the combustion chamber is not efficiently filled.

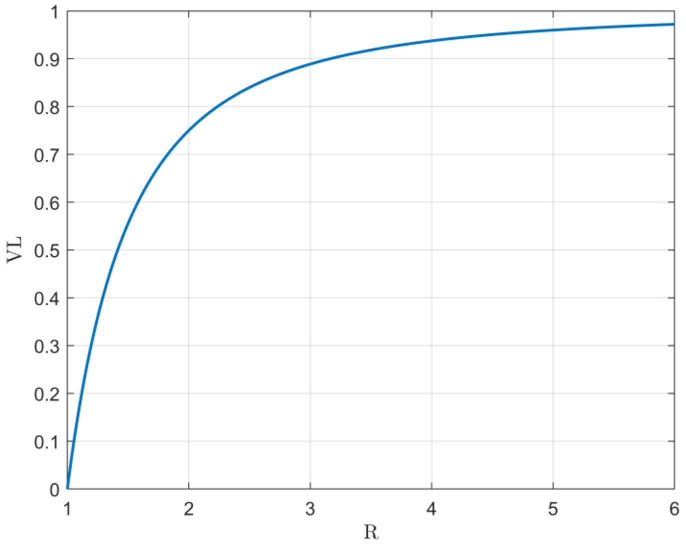

Figure 4.4: Port volume loading VL as a function of diameter ratio R.

4.2 Performance predictions. 0D model

Once the preliminary sizing of the hybrid rocket motor is completed, there are enough information to simulate the system performance over time, including the regression rate $\dot{r}(t)$, the fuel mass flow rate $\dot{m}_f(t)$, the oxidizer to fuel ratio $O/F(t)$, the chamber pressure $p_{cc}(t)$ and the thrust $T(t)$. A 0D (zero dimensional) model of the hybrid rocket combustion chamber and nozzle can be implemented. This model provides the system performance variation over time due to the area port increase because of fuel grain regression. For this preliminary design, it is assumed that there is no throat erosion. This assumption is optimistic, as the throat erosion tends to decrease the nozzle expansion ratio and thus the overall specific impulse.

Assuming for simplicity a constant oxidizer flow rate $\dot{m}_{ox}$, the specific oxidizer flow rate $G_{ox}(t)$ as a function of time is written in terms of the instantaneous port diameter $D(t)$:

$$G_{ox}(t) = \frac{4\dot{m}_{ox}}{\pi D(t)^2} \tag{4.29}$$

Since the regression rate constants a and n are known, the instantaneous regression rate $\dot{r}(t)$ can be solved with equation (2.53). The fuel mass flow rate is calculated using the regression rate and the port diameter:

$$\dot{m}_f(t) = \rho_f \pi D(t) L \dot{r}(t) \tag{4.30}$$

Therefore, the propellant mass flow is:

$$\dot{m}_{prop}(t) = \dot{m}_{ox} + \dot{m}_f(t) \tag{4.31}$$

and the O/F ratio is:

$$O/F(t) = \frac{\dot{m}_{ox}}{\dot{m}_f(t)} \tag{4.32}$$

Unless $n = 0.5$, O/F shift is expected.
The chamber pressure can be modelled as a function of time as:

$$p_{cc}(t) = \frac{\dot{m}_{prop}(t) c^*(t) \eta_{c^*}(t)}{A_{th}} \tag{4.33}$$

c^* and η_{c^*} are functions of $O/F(t)$ and of the chamber pressure and, as such, are also functions of time. For simplicity, c^* can often be treated as a constant in early design if n is close to 0.5 or for short burns [29]. Otherwise, for more accurate precision of system performance, an iterative procedure must be performed: for example, assuming a p_{cc} value, any thermochemical code provides the characteristic velocity c^* of the mixture, which is used in equation (4.33) for evaluating the chamber pressure at the nozzle entrance; its value is compared with the assumed p_{cc} value, iterating to convergence. As a first approximation, also η_{c^*} can be assumed constant.
The knowledge of environment pressure (which requires coupling of the presented model with a dynamic rocket model if the system operates in atmosphere at different altitudes) allows to evaluate the thrust coefficient $c_F(t)$ with equation (4.1). For simplicity, η_{c_F} can

be assumed constant. Therefore, it is possible to solve for the specific impulse with the following equation:

$$I_{sp}(t) = \frac{c_F(t)\eta_{c_F}(t)c^*(t)\eta_{c^*}(t)}{g_0} \tag{4.34}$$

Finally, the rocket thrust is calculated as:

$$T(t) = \dot{m}_{prop}(t)I_{sp}(t)g_0 \tag{4.35}$$

4.3 Influence of Motor Design Parameters

The results provided by the system performance simulation are compared with the mission requirements defined at the beginning of the preliminary sizing procedure. Therefore, it is possible to evaluate if those requirements have been achieved or not. If not, we can iteratively optimize the design by varying the decision parameters, based on the results from the simulation.

First, it must be noted that a characteristic feature of hybrid rockets is the impossibility of optimizing thrust, burn time and volumetric loading at the same time. Barato, Paccagnella, and Pavarin [13] provide a good explanation for this feature. Equation (4.24) can be rewritten as:

$$\frac{aG_{ox_0}^n t_b}{D_0} = \frac{R^{2n+1} - 1}{2(2n+1)} \tag{4.36}$$

The term on the left is called adimensional reference web thickness. This quantity is dimensionless because the numerator is divided by the initial port diameter, while it is called reference because it represents the web thickness that would be required if the regression rate is kept constant and equal to its initial value. Therefore, the adimensional reference web thickness is greater than the real one, because of the regression rate decay due to the increase of the port area with time.

To achieve the same VL (and R), equation (4.36) shows a direct proportionality between motor size (i.e. the initial port diameter D_0) and burn time, while the increase of the regression rate capability makes this dependence less significant (Fig.4.5).

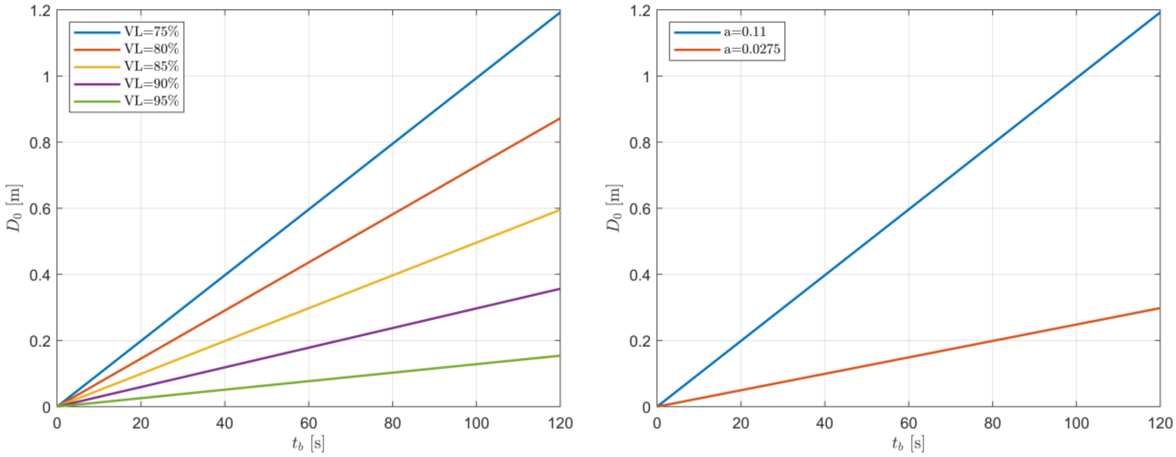

Figure 4.5: Initial diameter port D_0 as a function of the burn time t_b for several values of port volume loading VL and of regression rate coefficient a: $a = 0.11$ (representative of paraffins) and $a = 0.0275$ (representative of non-liquefying propellants) [13].

A larger thrust and a lower burn time yield to a drop of the port volume loading, because of the increase of port diameter and reduction of web thickness. In fact, the increase of the required thrust translates into greater propellant and oxidizer mass flows. As a result, for a fixed G_{ox_0}, it is:

$$A_{p_0} = \frac{\dot{m}_{ox}}{G_{ox_0}} = \frac{\pi}{4} D_0^2 \propto T \tag{4.37}$$

Therefore:

$$D_0 \propto \sqrt{T} \tag{4.38}$$

Moreover, an increase of D_0 leads to a greater final port diameter D_f for the same burn time, thus reducing the volume loading VL (Fig.4.6).

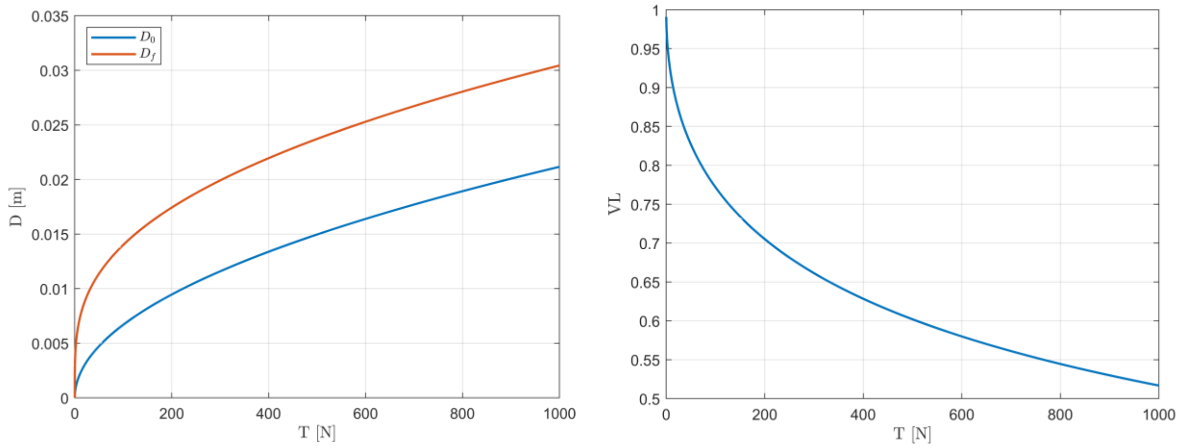

Figure 4.6: Initial and final port diameter (left) and volume loading (right) as a function of thrust.

Equation (4.36) shows that an increase in initial oxidizer mass flux has a positive effect on volume loading. However, the final G_{ox}, related to the initial one by the equation:

$$\frac{G_{ox_0}}{G_{ox_f}} = R^2 \tag{4.39}$$

must be kept above the minimum value of cooking limit. The need to limit the initial mass flux to avoid flooding and limit pressure losses due to high Mach number, and to achieve a minimum final mass flux to ensure adequate proximity of the flame to the solid grain wall (avoiding excessive heat propagation inside the grain), necessarily leads to a limitation on the burn time, related to the thrust according to the following proportionality:

$$m_{prop} \propto T t_b \propto T^{3/2} \qquad (R = const) \tag{4.40}$$

$$t_b \propto \sqrt{T} \tag{4.41}$$

Fig.4.7 shows the mission envelope for a single port hybrid rocket motors by using equation (4.36) with typical R value between 2 (i.e. $VL = 75\%$) and 6 (i.e. $VL = 97.22\%$). Hybrid rockets are suitable for missions where size and burning time are inside the region defined by the two straight lines. This region shifts to lower size and high burn time for low regression rate propellant and towards high size and low burning time for high regression rate propellant. The regression rate can be enhanced for the particular application selecting the appropriate propellant.

It can therefore be concluded that hybrid engines are not suitable (i.e. they do not represent the most efficient propulsion configuration) for missions where high thrust is required for a low burn time or low thrust for an excessively high burn time, while ensuring a good volume loading value.

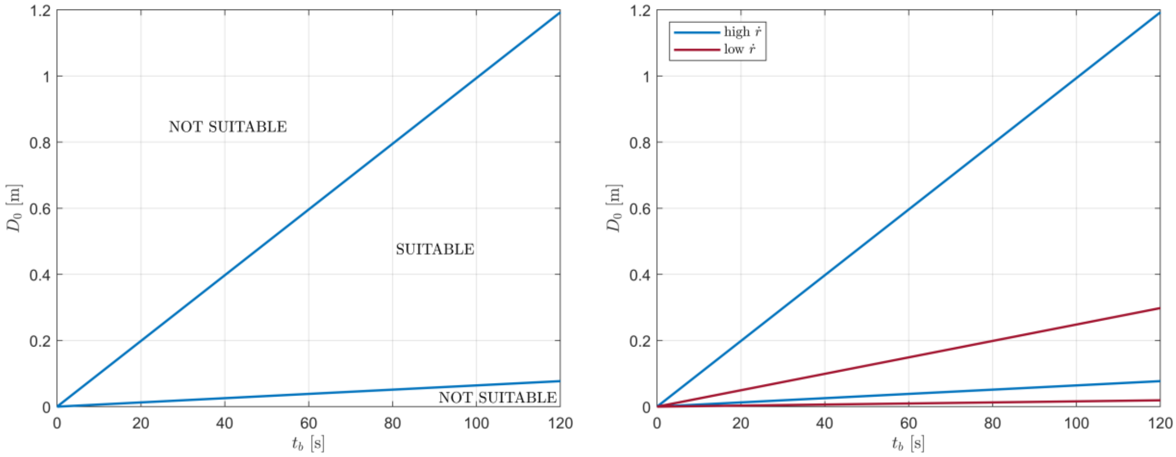

Figure 4.7: Mission envelope for a single port hybrid rocket motor [13].

The design of hybrid rocket motor can be optimized varying the decision parameters, including the regression rate coefficients a and n, the O/F ratio, the initial oxidizer mass flux G_{ox_0}, the average pressure p_{cc}, the burn time t_b and the required thrust T. To better understand the result of changing one of those parameters, it is useful to keep the others constant at the same time.

An increase of the regression rate coefficients a and n leads to a greater regression rate. If the burn time is kept constant, the consequent increase in the final port diameter leads to higher values of the loading volume VL. The increase in the regression rate makes possible to reduce (with the same fuel mass flow rate) the length of the solid grain and the motor slenderness L/D_f. In particular, the value of the coefficient n impacts the overall motor ballistics since it influences the O/F shift of the motor. Fig.4.8 and Fig.4.9 show the O/F ratio shift as a function of time and throttling for several values on the regression rate coefficient n. As described by equation (2.63), the O/F shift happens because of time (i.e. variation of port diameter) if $n \neq 0.5$ and/or because of throttling if $n \neq 1$. It's interesting to observe that if $n = 0.5$ there is O/F shift because of throttling (represented in the discontinuity in the O/F value) but, unlike what happen when $n \neq 0.5$ and 1, when the oxidizer mass flow rate returns back to its initial value, also the motor O/F ratio returns to its initial value.

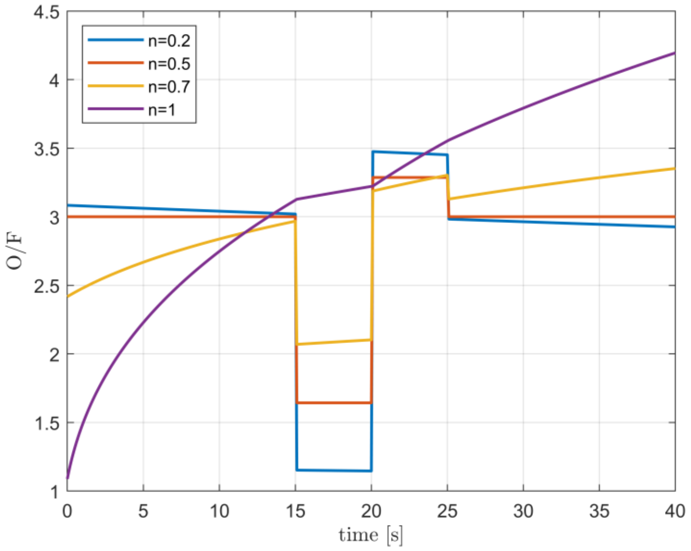

Figure 4.8: O/F ratio as a function of time for several values of the regression rate coefficient n, with throttling at $t = 15{,}20$ and $25\ s$.

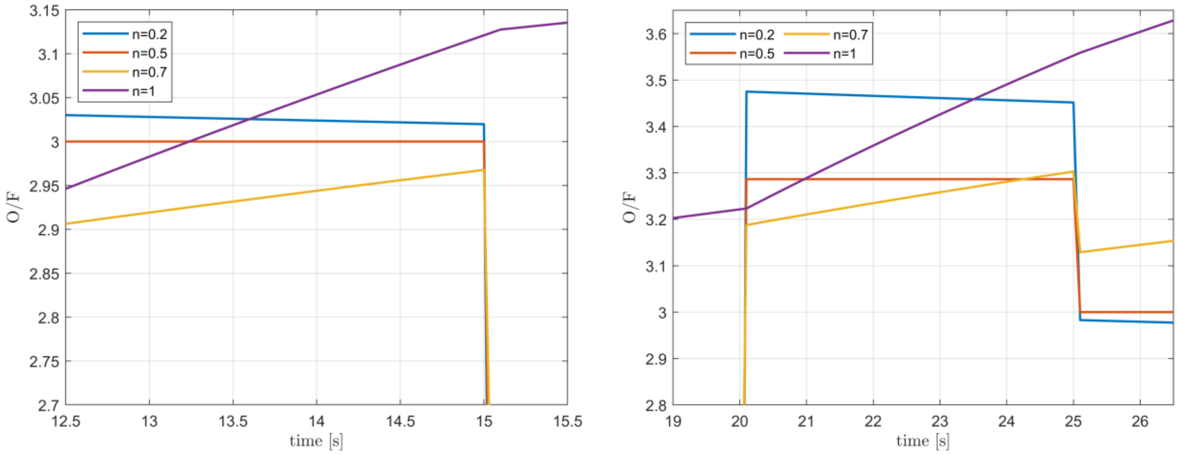

Figure 4.9: Details of figure 4.8.

The O/F ratio has a significant influence on solid grain size. As the O/F ratio increase, the lower demand for fuel mass flow (with the same amount of propellant mass flow which is a function of the required thrust), makes it possible to reduce the mass, volume and length of the solid grain and the system slenderness. However, the corresponding increase in the oxidizer flow rate (with the same G_{ox_0}) yields to an increase of the initial port diameter as $D_0 \propto \sqrt{O/F}$ and of the final port diameter such that the loading volume VL decreases.

The increase of the design chamber pressure p_{cc} allows to slightly increase performance and at the same time to reduce the Mach number along the port area (typically $M < 0.3$, therefore the fluid in the 0D combustion chamber model can be considered incompressible, thus an increase of p_{cc} leads to a greater fluid density for the same specific flow $G = \rho u$), thus reducing the pressure drop. In addition, a rise in chamber pressure allows to employ greater values for G_{ox_0} before facing the flooding limit and to reduce the throat area, thus reducing the exit area for the same area ratio or allowing a greater area ratio for the same exit area. However, increasing the chamber pressure may result in an increase chamber structural mass.

The initial oxidizer specific mass flow G_{ox_0} influences the regression rate value. If $\dot{m}_{ox}$ is kept constant, a greater G_{ox_0} leads to a decrease of the initial port diameter as $D_0 \propto G_{ox_0}^{-0.5}$. The following reduction of the final port diameter is partially limited by the increase of the regression rate, such that the volume loading increase. However, it should be considered that an increase of G_{ox_0} also implies higher Mach numbers along the grain port, and therefore higher pressure drop.

The variation of the grain length with G_{ox_0} is a function of the regression rate coefficient n. In fact, it is

$$A_{p_0} = \frac{\pi}{4} D_0^2 = \frac{\dot{m}_{ox}}{G_{ox_0}} \rightarrow D_0 \propto \frac{1}{G_{ox_0}^{0.5}} \tag{4.42}$$

$$\dot{m}_f = \rho_f A_b \dot{r} \rightarrow A_b \propto \frac{1}{\dot{r}} \propto \frac{1}{G_{ox_0}^{n}} \tag{4.43}$$

therefore:

$$L = \frac{A_b}{\pi D_0} \propto \frac{1}{G_{ox_0}^{n}} G_{ox_0}^{0.5} = G_{ox_0}^{0.5-n} \tag{4.44}$$

As a result, if $n < 0.5$ then an increase of G_{ox_0} leads to a longer grain and vice versa for $n > 0.5$, while for $n = 0.5$ the grain length is independent of G_{ox_0} (Fig.4.10). The same considerations can be done also for the grain slenderness L/D_f.

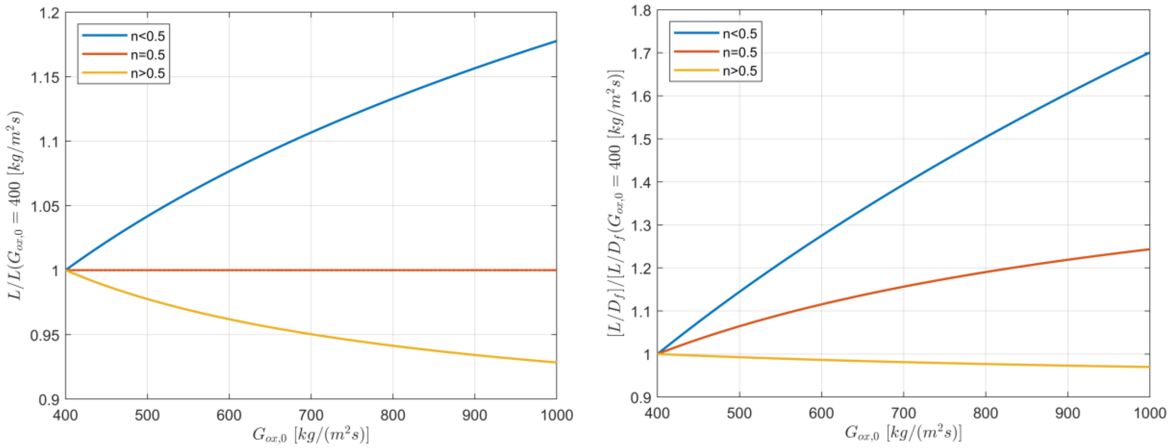

Figure 4.10: Dimensionless grain length (left) and dimensionless grain slenderness (right) with respect to the corresponding value for $G_{ox_0} = 400\ kg/(m^2 s)$ as a function of the initial oxidizer mass flux, parametric with the regression rate coefficient n.

The increase in the required thrust, as already mentioned, leads to an increase of the mass flow rates and of the propellants mass and volume. In particular, the greater fuel mass flow rate results in an increase of the burning area and grain length, which leads to an increase in slenderness. A greater initial port diameter due to higher required thrust leads to a reduction in loading volume.

A greater burn time yields to an increase of the propellants mass and volume, although the increase in the final port diameter allows to improve the volume loading of the system. A crude zero order approximation of the influence of t_b on grain length can be made:

$$L = \frac{V_f}{\frac{\pi}{4}\left(D_f^2 - D_0^2\right)} \propto \frac{m_f}{D_f^2} \propto \frac{t_b}{\left(t_b^{1/(2n+1)}\right)^2} \propto t_b^{\frac{2n-1}{2n+1}} \tag{4.45}$$

As a result, the grain length slightly decreases with t_b if $n < 0.5$ and vice versa if $n > 0.5$, while it remains constant for $n = 0.5$ (Fig.4.11). This has an influence on the grain slenderness L/D_f as a function of the burn time, such that an increase of t_b yields always to a reduction of L/D_f which is more significant for lower value of n.

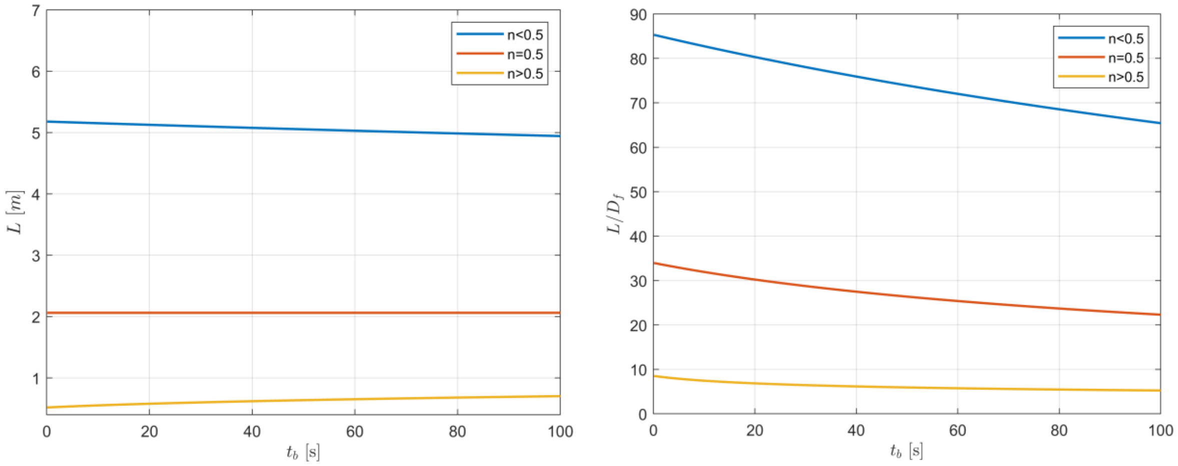

Figure 4.11: Grain length (left) and grain slenderness (right) as a function of burn time t_b, parametric with the regression rate coefficient n.

As previously stated, during preliminary sizing throat erosion is not considered, although it can lead to a significant reduction of the rocket's performances. The effect of throat erosion on engine operation is strongly influenced by the propellants used as well as the O/F ratio. Both those design choices have consequences on the chamber temperature and on the chemical composition of the combustion products. In particular, the higher the reaction products temperature, the greater is the throat regression rate due to an increase in reaction kinetics. In addition, oxidizer rich mixture induces greater throat erosion because of the more reactive environments. However, the fluid stratification typical of hybrid combustion allows the fuel flow near the wall to protects the throat material with the same physical principle of film cooling.

Small engines (i.e. with small throat area) are more sensitive to throat erosion because of the higher percentage change in throat diameter when compared to bigger engines. In addition, it is necessary to consider the variation of the chemical composition of the reaction products due to O/F shift.

Chapter 5

1D Combustion Chamber Model

To correctly characterize the performances of a hybrid engine, it is necessary to evaluate as accurately as possible the internal ballistics, i.e. the thermo-fluid dynamic behaviour of the fluid inside the combustion chamber. In this chapter, after briefly introducing the equations and hypotheses used to solve the problem, the internal ballistics of a hybrid engine is analysed with a quasi-stationary 1D model. In this simplified model, the propellant combustion efficiency (i.e. the amount of propellant that reaches the flame and thus participates in the combustion process) it is assumed to be known.

5.1 Mathematical Model

The solution of the internal ballistics of a hybrid engine requires to consider the fundamental equations of fluid dynamics (continuity, momentum and energy equations) [2]. Those equations, coupled with an appropriate equation of state for the gases, allow the knowledge of all the thermodynamic and mechanical quantities of interest. Several hypothesis are applied to reduce the complexity of the physics of the problem:

- Quasi one-dimensional flow. It is assumed that all flow proprieties are uniform across any given cross section of the flow, and hence are functions of the axial coordinate x only.

- Quasi-stationary flow. It is assumed that the flow of the fluid is steady, thus its properties are independent of time at every point in the flow field. The only variation in time considered is that of the port diameter and it is assumed that the flow pass through physical states of thermodynamic equilibrium (that are stationary if the boundary conditions remain fixed, which does not happen due to the variation of the port diameter).

- Continous flow. The fluid proprieties vary continuously without presenting discontinuity phenomena (e.g. shock waves).

- Ideal and thermally perfect gas. The fluid is considered an ideal gas, whose specific heats depends only on temperature and chemical composition.

Let’s consider the calculation domain of a classic hybrid rocket motor depicted in Fig.5.1. Algebraic equation for steady quasi-one-dimensional flow can be obtained by applying the integral form of the conservation equations to the control volume for an element size of dx sketched in Fig.5.2. The subscripts 1 and 2 refers to the terms at the entrance and at the exit cross sections of the control volume respectively.

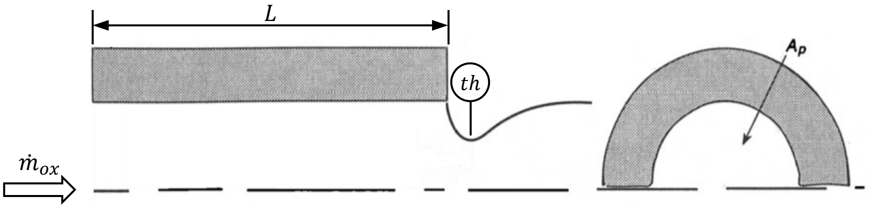

Figure 5.1: Calculation domain. Adapted from [4].

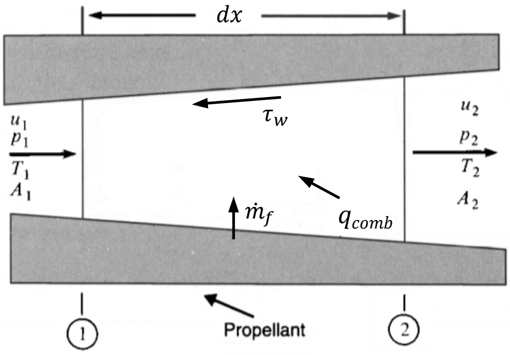

Figure 5.2: Finite control volume for quasi-one-dimensional flow. Adapted from [4].

For steady flow, the overall mass flux balance when integrated over the control volume can be expressed as:

$$\dot{m}_1 + \dot{m}_f = \dot{m}_2 \tag{5.1}$$

or

$$\rho_1 u_1 A_1 + \dot{m}_f = \rho_2 u_2 A_2 \tag{5.2}$$

The fuel mass flow rate is evaluated in terms of the regression rate:

$$\dot{m}_f = \dot{r}\rho_f A_{lat} = \dot{r}\rho_f \pi D dx \tag{5.3}$$

where $A_{lat} = Pdx = \pi D dx$ is the lateral area of the control volume and P is the section perimeter. The regression rate it is calculated with equation (2.35), therefore it is necessary to impose a limit to its value at $x = 0$.

An exothermic oxidation reaction takes place inside the combustion chamber. From the theory of hybrid combustion, it has been seen that this reaction takes place in fuel-rich conditions and that a fraction of the sublimated fuel does not participate but flows axially below the flame. As a result, a term representing the fuel combustion efficiency, $\eta_{comb,f}$, is introduced and assumed to be known. F and O respectively indicate the fuel and oxidizer flow rates that participate in the combustion process:

$$F = \eta_{comb,f}\dot{m}_f \tag{5.4}$$

$$O = [O/F]_{react} F \tag{5.5}$$

At the exit cross section of the control volume, the oxidizer, fuel and combustion products flow rates can be expressed respectively as:

$$O_{rem_2} = O_{rem_1} - [O/F]_{react}\, F \tag{5.6}$$

$$F_{rem_2} = F_{rem_1} + \dot{m}_f - F \tag{5.7}$$

$$\dot{m}_{pr_2} = \dot{m}_{pr_1} + O + F \tag{5.8}$$

where the subscripts rem indicates the species flow rate that remains in the main flow mixture at the exit of the control volume.

The integral form of the momentum equation applied to the control volume in Fig.5.2, assuming steady flow and no body forces, becomes

$$p_1 A_1 + \rho_1 u_1^2 A_1 + \int_{A_1}^{A_2} p\, dA - \tau_w A_{lat} = p_2 A_2 + \rho_2 u_2^2 A_2 \tag{5.9}$$

Note that it is not a strictly algebraic equation because of the integral term which represents the pressure force on the sides of the control surface between location 1 and 2. As a crude approximation, it can be assumed $\int_{A_1}^{A_2} p\, dA \cong (A_2 - A_1)\left(\frac{p_1+p_2}{2}\right)$. The shear stress at the wall, τ_w, can be evaluated with equation (2.8) where it must be taken into consideration the reduction of the skin-friction due to the blowing from the grain. The term C_f can be evaluated with equation (2.29), with C_{f_0} calculated with equation (2.22). Moreover, the small exponent of Re_x in equation (2.22) allows to approximate the dynamic viscosity μ and specific flow G with average values over the cross section.

The integral form of the energy equation applied to the control volume in Fig.5.2, and assuming steady flow with no body forces, yields to:

$$\dot{m}_1\left(h_1 + \frac{u_1^2}{2}\right) + q_{comb} = \dot{m}_2\left(h_2 + \frac{u_2^2}{2}\right) \tag{5.10}$$

In describing the first law of thermodynamics, any radiation and conduction (through the solid grain) fluxes are neglected. The combustion can be modelled as an external heat exchange to the main stream. The heat of reaction and the heat transfer per unit mass of products to the flow are respectively:

$$Q_{comb} = c_{p_{pr}}(T_b - T_{ref}) \tag{5.11}$$

$$q_{comb} = (1 + [O/F]_{react})FQ_{comb} \tag{5.12}$$

The heat of reaction can be evaluated with any thermochemical code. T_{ref} is the reference state temperature and it is set equal to $298.15\ K$.

The flow inside the combustion chamber can be assumed as an ideal mixture of ideal gases, therefore the ideal gas law is valid:

$$p = \rho RT = \rho \frac{\mathcal{R}}{M_m} T \tag{5.13}$$

where $\mathcal{R} = 8.314\ J/(mol\ K)$ is the universal gas constant and M_m is the average molar mass of the mixture calculated from the mass fractions of the components:

$$\frac{1}{M_m} = \frac{1}{M_{m_{ox}}}\frac{O_{rem}}{\dot{m}} + \frac{1}{M_{m_f}}\frac{F_{rem}}{\dot{m}} + \frac{1}{M_{m_{pr}}}\frac{\dot{m}_{pr}}{\dot{m}} \tag{5.14}$$

In the presented model, the following boundary conditions are set:

$$\dot{m}_{pr}(x = 0) = 0 \tag{5.15}$$

$$F_{rem}(x = 0) = 0 \tag{5.16}$$

$$O_{rem}(x = 0) = \dot{m}_{ox} \tag{5.17}$$

Enthalpy is expressed by its definition:

$$h = c_p(T - T_{ref}) \tag{5.18}$$

where the specific heat is calculated from the mass fractions of the components:

$$c_p = \frac{c_{p_{ox}}O_{rem} + c_{p_f}F_{rem} + c_{p_{pr}}\dot{m}_{pr}}{\dot{m}} \tag{5.19}$$

$$c_v = c_p - \frac{\mathcal{R}}{M_m} \tag{5.20}$$

In the nozzle, the flow is assumed to be isentropic, with uniform proprieties across any section. In addition, because of the low Mach number of the flow coming from the combustion chamber, the gas can be therefore considered as stagnant and then expanded to high supersonic velocities in the divergent portion of the nozzle. The (chocked) mass flow through a rocket nozzle is calculated with the expression:

$$\dot{m} = \frac{p_{cc} A_{th}}{c^*} \tag{5.21}$$

The presented model solves the 1D internal ballistic of a hybrid engine through the iterative resolution of a system of 4 equations (continuity (5.2), momentum (5.9), energy (5.10), ideal gas law (5.13)) involving 4 variables (pressure, density, temperature, velocity). In this work, the following algorithm is used. The numerical domain is subjected to a discretization in the time (dt) and in the space (dx) domains. For each time step, the pressure at the head of the grain is assumed; for each control volume for an element size of dx, the above system of equations is solved. Once that the pressure distribution in the combustion chamber is known, the pressure at the aft-end of the propellant grain is compared to the one obtained from the expression of the chocked mass flow through the nozzle (5.21). The value of the pressure at the head of the grain is then corrected and the algorithm is iterated until convergence is achieved, thus moving to the next timestep.

An aspect not to be underestimated is the correct evaluation of the regression rate coefficients. In particular, since in the preliminary sizing an average regression speed was used for the grain design, the coefficient a_x in the equation (2.35) is obtained by correcting the coefficient a (from literature) referring to the expression (2.54), hence $a = \frac{a_x}{1+m} L^m f_o\left([O/F]_{glob}\right)$.

5.2 Parametric Study of the 1D Internal Ballistics

Because the internal ballistics of a hybrid engine can be modelled as a combination of a flow with heat exchange (i.e. combustion) and mass addition, with friction (although it has a small influence due to blowing) and with cross-section area variation, it is expected the flow to accelerate, to heat up, to expand and to suffer a total pressure loss over the length of the grain. In this section, the effect of some design parameters on the internal ballistics will be analysed with the aim of confirming and extending the theoretical discussion.

The regression rate (2.35) would see its maximum value equal to infinity at the leading edge. As already mentioned, this value is physically meaningless, therefore a limit on the regression rate value at $x = 0$ is imposed. Because of the fuel pyrolysis, the propellant flow rate increases progressively along the grain port. Part of the oxidizer and of the fuel flow rates reaches the flame, where the reactants are transformed in combustion products. Therefore, the oxidizer flow rate decreases, while a small fraction of the fuel flow rate accumulates in the main flow. In the case that the $[O/F]_{glob}$ value is close enough to $[O/F]_{react}$, a condition may occur whereby all the oxidizer is burned before the end of the grain, resulting in a greater accumulation of fuel that dilutes the main stream.

Given its proportionality with the mass flux G, the regression rate at a given position is maximum at $t = 0$, when the specific mass flux through the port area is maximum. The distribution of the regression rate at a given time along the grain port (Fig.5.3) confirms what Marxman's theory predicts about the contraposition of two concurrent effects: the increase in mass flux and the thickening of the boundary layer in the downstream direction. Near the leading edge of the fuel surface, the effect of boundary layer growth dominates the regression rate of the solid fuel, but further downstream, the mass flux effect prevails. As a result, a position where the regression rate has minimum value exists.

Over time, the port area increases, the specific mass flow decreases and with it the Mach number, leading to a reduction in the difference between the static and the corresponding total properties. Moreover, the variation of the port area over time generally produces the change of the motor O/F ratio (O/F shift). The progressive "levelling" of the port diameter along the grain length over time is due to the influence of the port area on the regression rate, as already described.

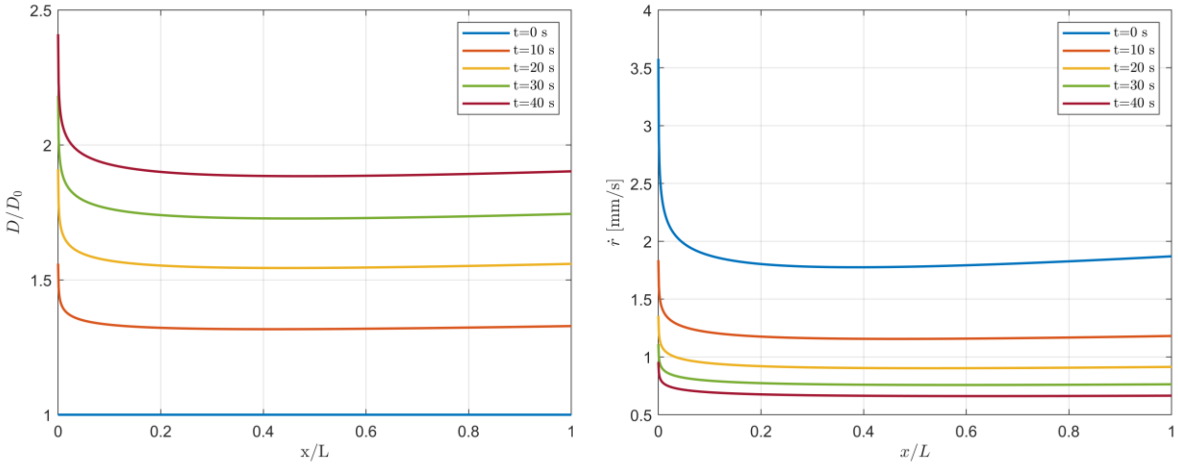

Figure 5.3: Dimensionless port diameter (left) and regression rate (right) as function of the dimensionless position x/L and of time.

The validation of the presented 1D model has been carried out by comparing its results with the analytical formulation for $n = 0.5$ proposed by Karabeyoglu, Cantwell and Zilliac [6]. From the regression rate definition, $2\dot{r} = \partial D/\partial t$, the variation of the port diameter over time can be written as:

$$\frac{\partial D}{\partial t} = C_D \frac{\dot{m}^n x^m}{D^{2n}} \tag{5.22}$$

with

$$C_D = a_x \frac{2^{2n+1}}{\pi^n} \tag{5.23}$$

In quasi-stationary flow hypothesis, the mass balance through the cross section can be written as:

$$\frac{\partial \dot{m}}{\partial x} = C_m \frac{\dot{m}^n x^m}{D^{2n-1}} \tag{5.24}$$

with

$$C_m = a_x \rho_f 2^{2n} \pi^{1-n} \tag{5.25}$$

Equations (5.22) and (5.24) are a system of two nonlinear first order partial differential equations which can be solved to determine the space-time variation of the flow rate $\dot{m}(x,t)$ and of the port diameter $D(x,t)$. The initial and boundary conditions needed to solve the problem are the oxidizer flow rate time history, $\dot{m}(x=0,t) = \dot{m}_{ox}(t)$, and the initial port diameter distribution, $D(x,t=0) = D_0(x)$, respectively.

An exact solution can be obtained only for a flux exponent of $n = 0.5$. In this particular situation, the mass flow rate equation loses its explicit dependency on the port diameter, therefore its integration in the x variable yields to:

$$\dot{m}(x,t) = \left[\sqrt{\dot{m}_{ox}(t)} + \frac{0.5C_m}{m+1}x^{m+1}\right]^2 \tag{5.26}$$

For the special case of constant oxidizer mass flow rate, substituting equation (5.26) in equation (5.22) and integrating in the time variable, gives the exact solution for the port diameter as a function of time and distance:

$$D(x,t) = \left[D_0^2(x) + C_D x^m t\left(2\sqrt{\dot{m}_{ox}} + \frac{C_m}{m+1}x^{2m+1}\right)\right]^{1/2} \tag{5.27}$$

An excellent agreement can be seen with the analytical solution proposed by the authors (Fig.5.4). It is expected that the numerical solutions would be highly accurate at other values of the flux exponent n for which no exact solutions exist.

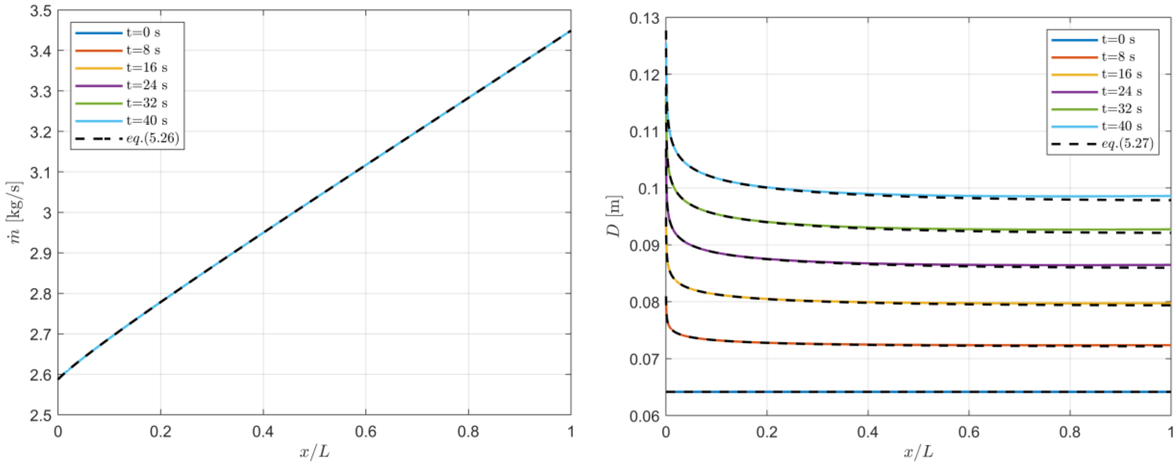

Figure 5.4: Comparison between the numerical results for the proposed 1D model and equations (5.26) and (5.27).

In the following, the numerical simulations results will be presented to understand how some design choices affect the internal ballistics of a hybrid engine.

Influence of the design $[O/F]_{glob}$ *with respect to* $[O/F]_{react}$. Typically, the solid grain is designed in a way that the $[O/F]_{glob}$ ratio occurs roughly in the middle of the burn. Therefore, the initial O/F ratio is different from $[O/F]_{glob}$ and it is lower or greater than it if n is greater or lower than 0.5 respectively, because of the O/F shift. In the simulations it is considered $n > 0.5$, which is a condition verified in most hybrid engine. In addition, it is assumed $\eta_{comb,f} = 1$.

The selected value for $[O/F]_{glob}$, and thus of the initial O/F ratio, with respect to the $[O/F]_{react}$ at the flame, could influence significantly the internal ballistic of the motor by changing the location where the combustion ends. If $[O/F]_{glob}$ is large enough compared to $[O/F]_{react}$, then the motor O/F ratio is always greater than the latter. Therefore, the quantity of oxidizer introduced into the combustion chamber is high enough to allow the combustion along the entire length of the grain, without any accumulation of fuel if $\eta_{comb,f} = 1$ (Fig.5.5 to 5.7). The flow entering the nozzle will then consist of the combustion products and the remaining oxidizer. If the motor O/F ratio is equal to $[O/F]_{react}$, then at the exit from the grain there will only be the combustion products.

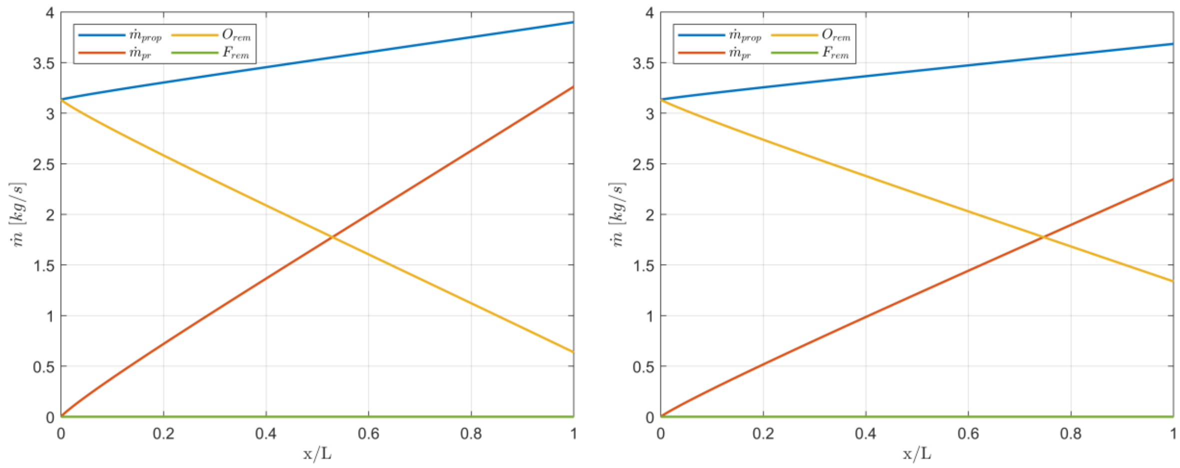

Figure 5.5: Mass flow rates as a function of the dimensionless position along the grain port at $t = 0\ s$ (left) and at the end of the burn (right).

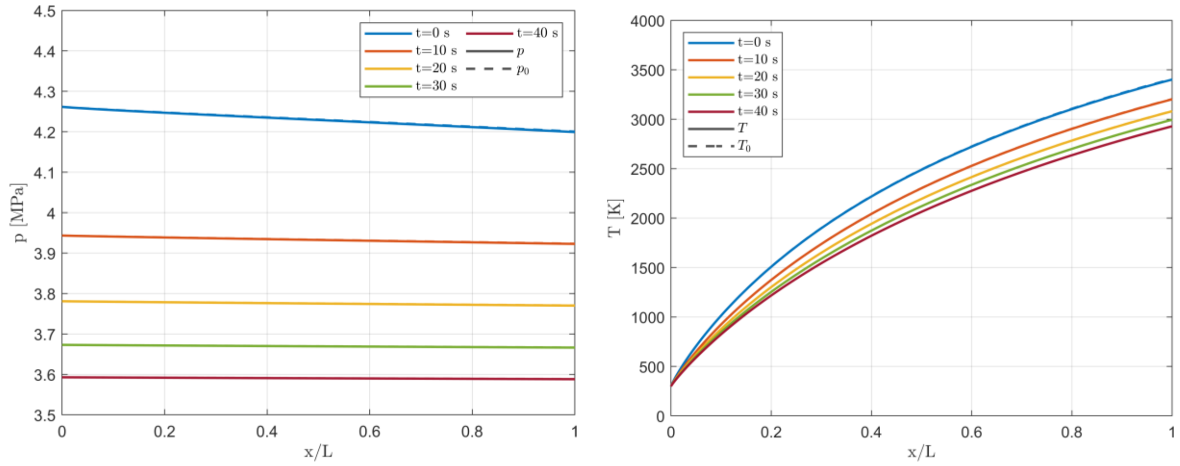

Figure 5.6: Pressure (left) and temperature (right) distribution as a function of the dimensionless position along the grain and time.

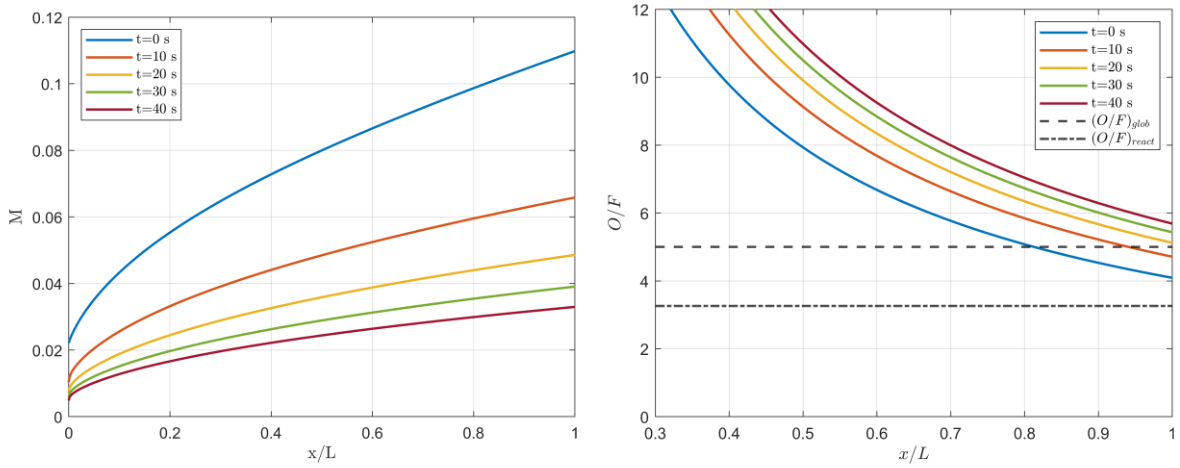

Figure 5.7: Mach number (left) and O/F ratio (right) distribution as a function of the dimensionless position along the grain and time.

If $[OF]_{glob}$ (and thus the initial O/F ratio) is close enough to $[O/F]_{react}$ or lower, then the combustion process can stop before the end of the grain. In this condition, the oxidizer mass flow rate is completed consumed while that of combustion products remains constant and there is a progressive accumulation of fuel that sublimates due to the heat exchange with the hot flow, which is consequently cooled (Fig.5.8). In Fig.5.9 and Fig.5.10, this condition is represented by the evident change in the slope of the curves. This condition can occur only for part of the burning time and is no longer present when the motor O/F ratio is greater then $[O/F]_{react}$.

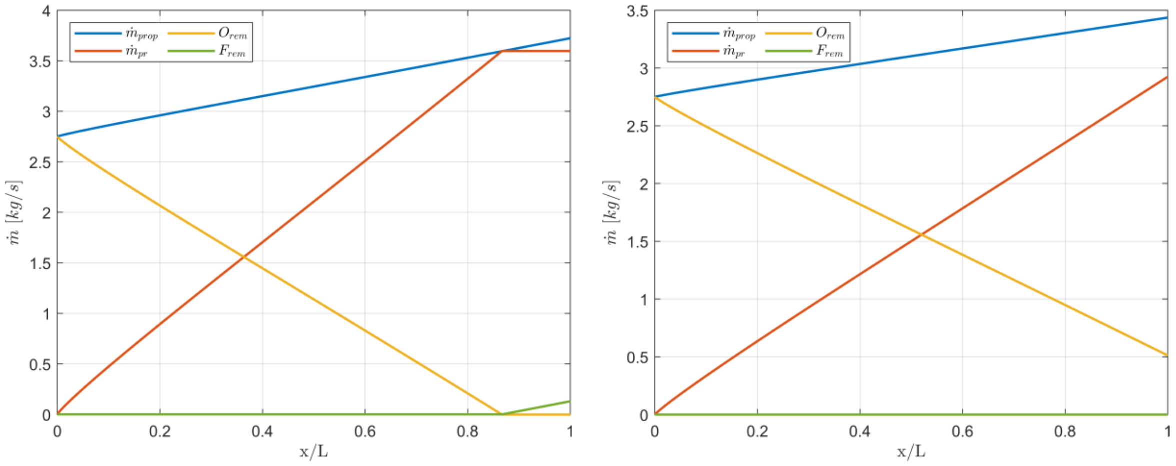

Figure 5.8: Mass flow rates as a function of the dimensionless position along the grain port at $t = 0\ s$ (left) and at the end of the burn (right).

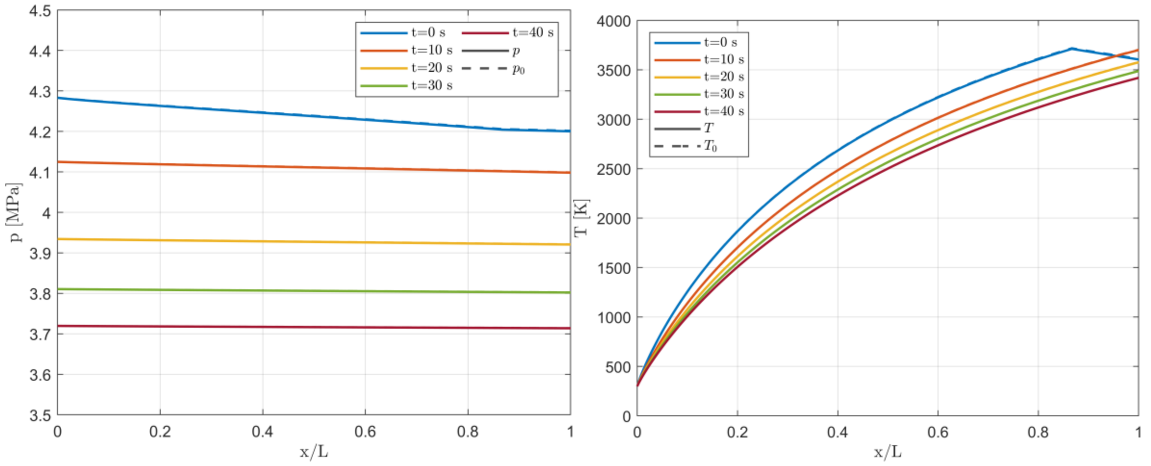

Figure 5.9: Pressure (left) and temperature (right) distribution as a function of the dimensionless position along the grain and time.

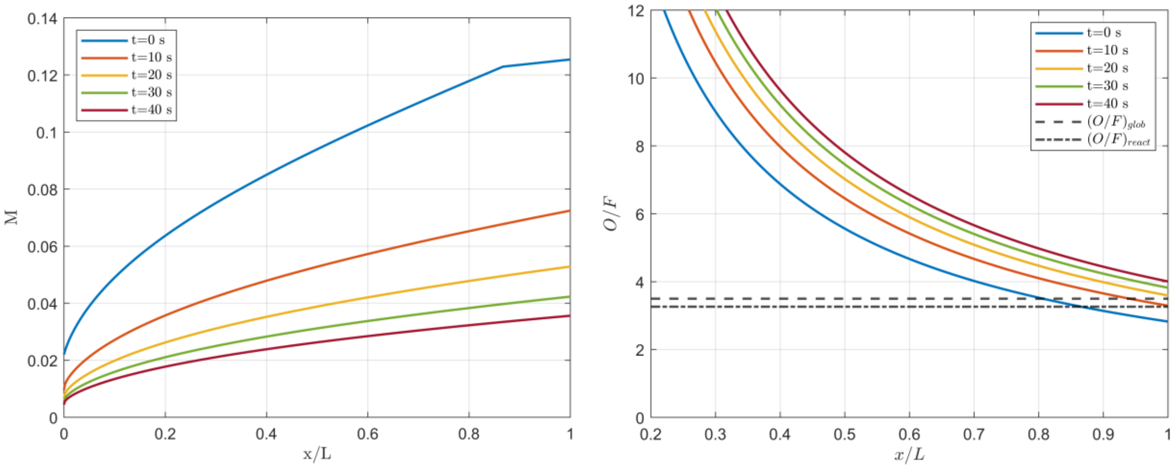

Figure 5.10: Mach number (left) and O/F ratio (right) distribution as a function of the dimensionless position along the grain and time.

If $[O/F]_{glob}$ is so much smaller than $[O/F]_{react}$ that the motor O/F ratio is always lower than $[O/F]_{react}$, then the combustion ends before the nozzle during all the burn time (Fig.5.11 to 5.13).

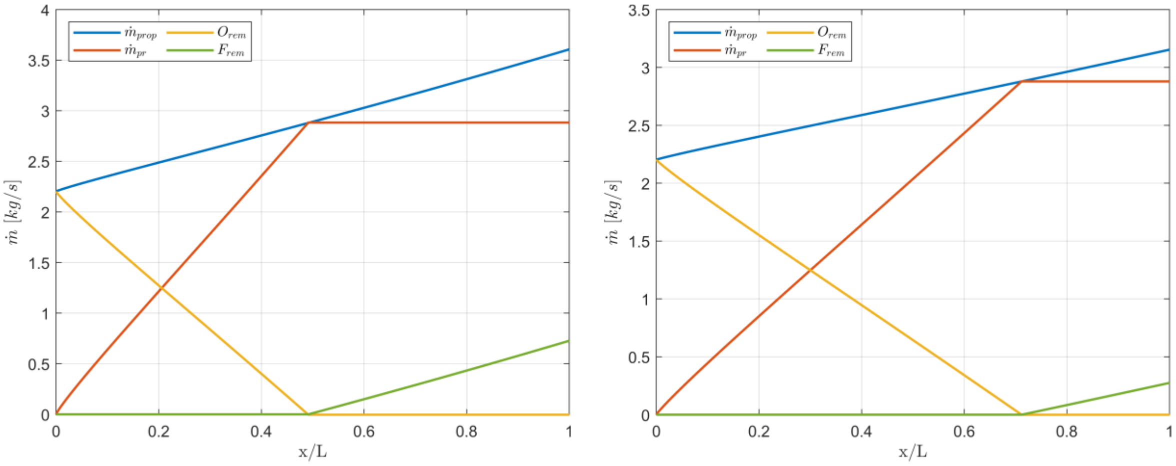

Figure 5.11: Mass flow rates as a function of the dimensionless position along the grain port at $t = 0\ s$ (left) and at the end of the burn (right).

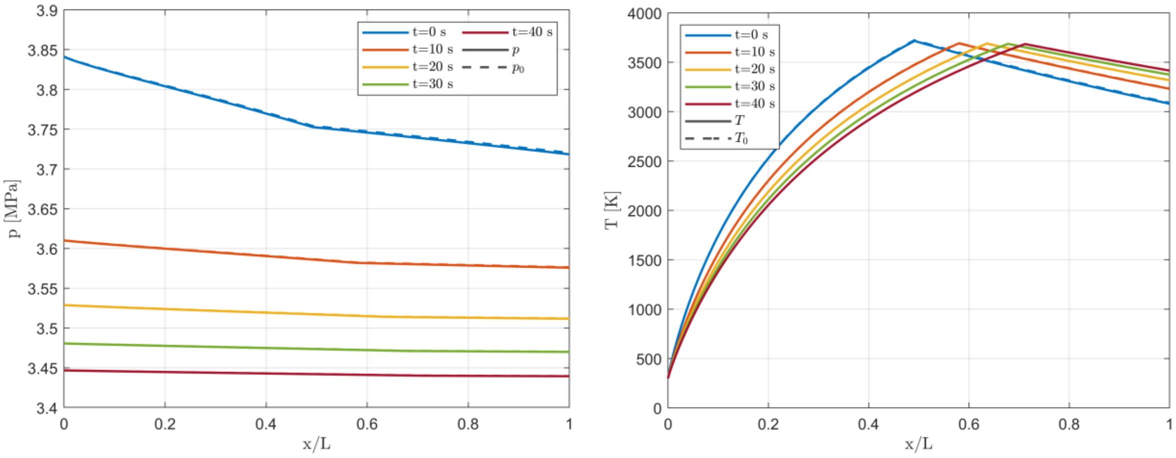

Figure 5.12: Pressure (left) and temperature (right) distribution as a function of the dimensionless position along the grain and time.

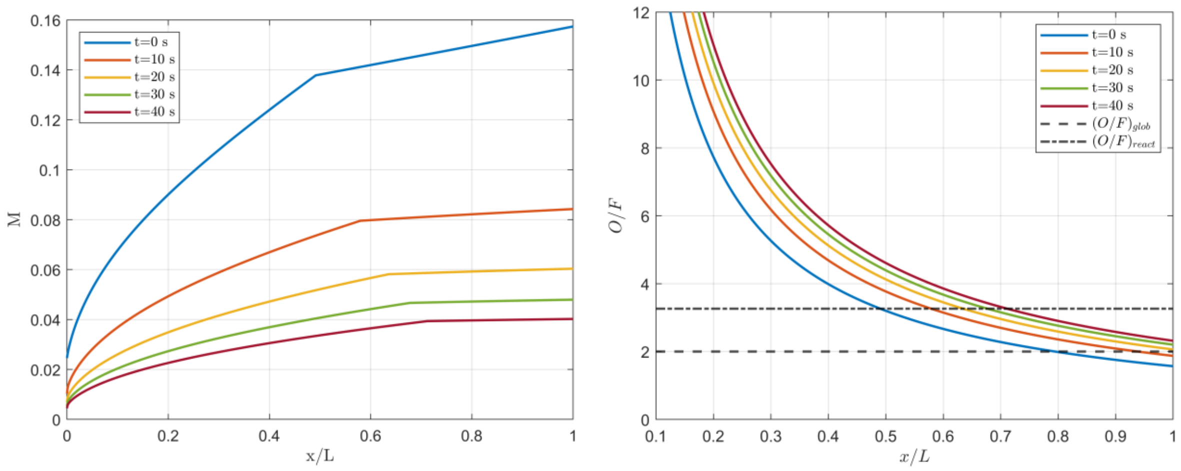

Figure 5.13: Mach number (left) and O/F ratio (right) distribution as a function of the dimensionless position along the grain and time.

Influence of $\eta_{comb,f}$. As already mentioned, the fuel combustion efficiency $\eta_{comb,f}$ takes into consideration the amount of sublimated fuel that actually reaches the flame zone and reacts in a combustion reaction with the oxidizer with respect to the total vaporized flow. This condition occurs due to the convection transport of the fuel below the flame by the boundary layer flow. The effect on internal ballistics of fuel accumulation is the dilution of the main stream.

Influence of n. The value of the regression rate coefficient n influences both the regression rate and the O/F shift, therefore it has a meaningful effect on the internal ballistic. If $n > 0.5$ (as it is generally in hybrid engines) the increase of the port diameter with time leads to an increase of the motor O/F ratio due to the lower sublimated fuel flow. As a result of the reduction of the propellant mass flow, the chamber pressure decreases over time (Fig.5.14) and tends to level along the grain due to a reduction of the Mach numbers (Fig.5.15).

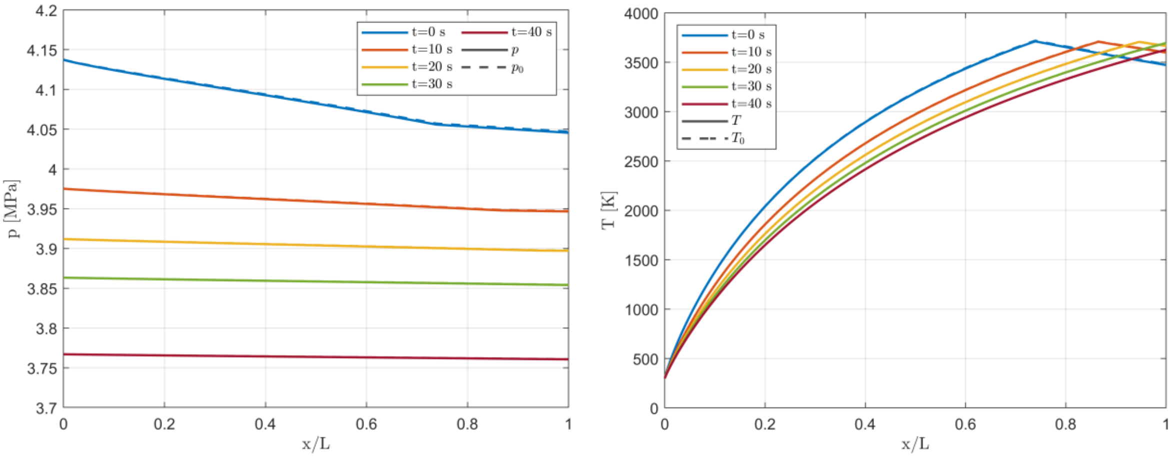

Figure 5.14: Pressure (left) and temperature (right) distribution as a function of the dimensionless position along the grain and time ($n > 0.5$).

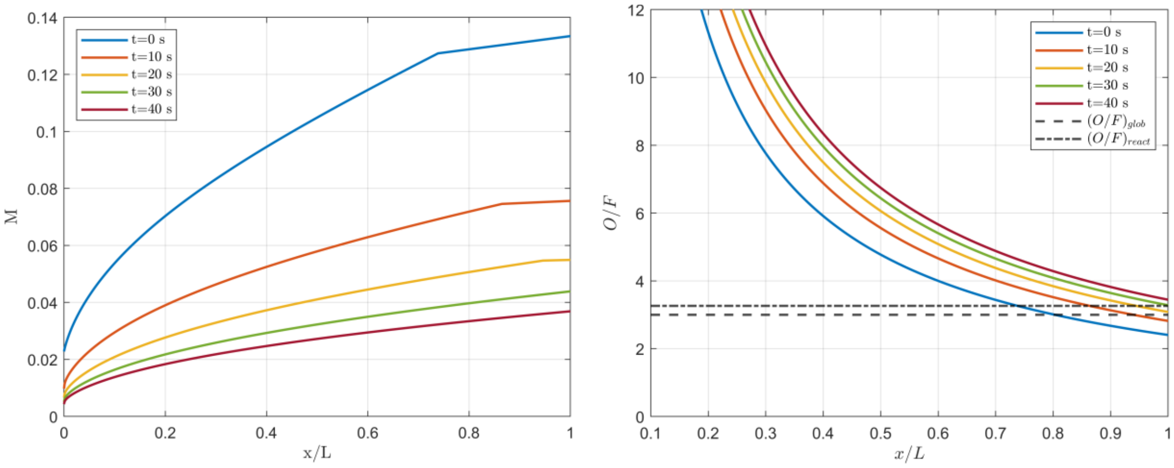

Figure 5.15: Mach number (left) and O/F ratio (right) distribution as a function of the dimensionless position along the grain and time ($n > 0.5$).

If $n = 0.5$ then no O/F shift occurs due to the port area variation over time. The constant propellant mass flow yields to a constant pressure at the nozzle inlet (Fig.5.16). The Mach number is higher at the beginning of the combustion due to the lower port area (Fig.5.17), therefore leading to much greater change in chamber pressure along the grain port.

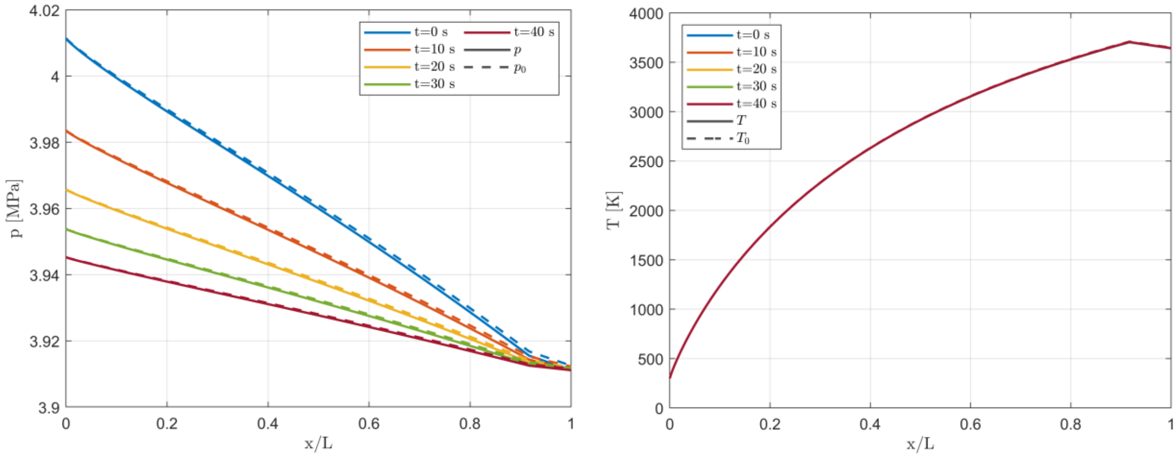

Figure 5.16: Pressure (left) and temperature (right) distribution as a function of the dimensionless position along the grain and time ($n = 0.5$).

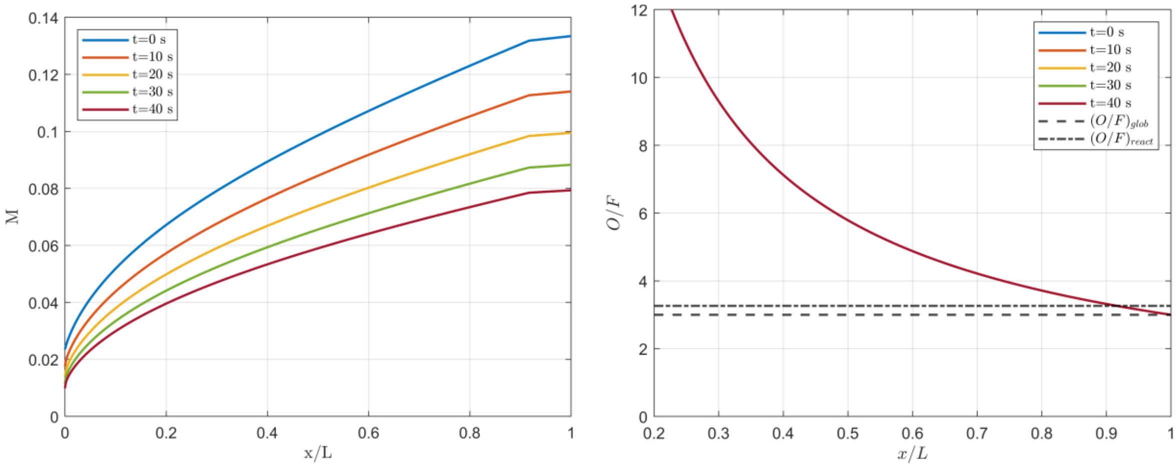

Figure 5.17: Mach number (left) and O/F ratio (right) distribution as a function of the dimensionless position along the grain and time ($n = 0.5$).

If $n < 0.5$, the O/F shifting towards lower value is due to the increase of the vaporized fuel mass flow rate due to the port area variation over time. As a result, the propellant mass flow rate and thus the chamber pressure at the nozzle inlet increase over time (Fig.5.18,5.19).

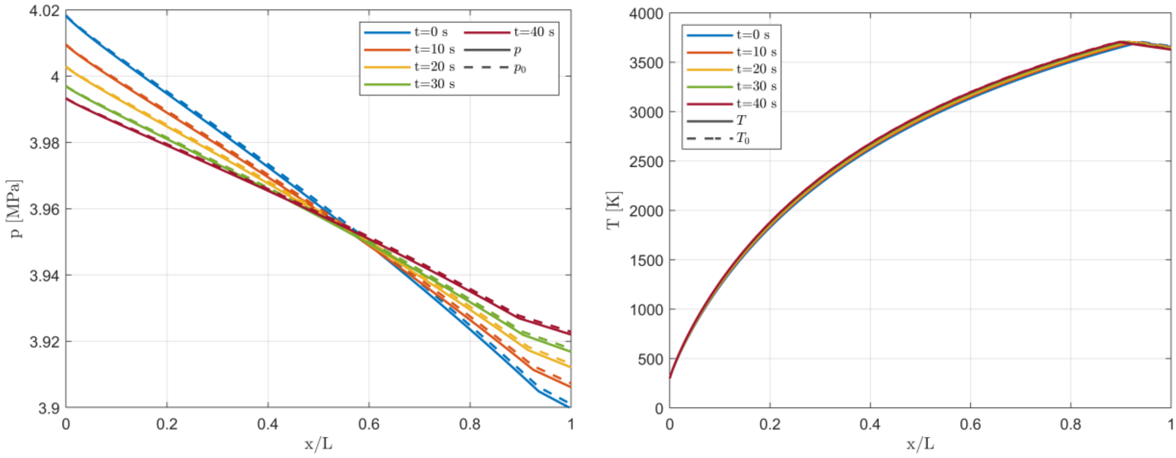

Figure 5.18: Pressure (left) and temperature (right) distribution as a function of the dimensionless position along the grain and time ($n < 0.5$).

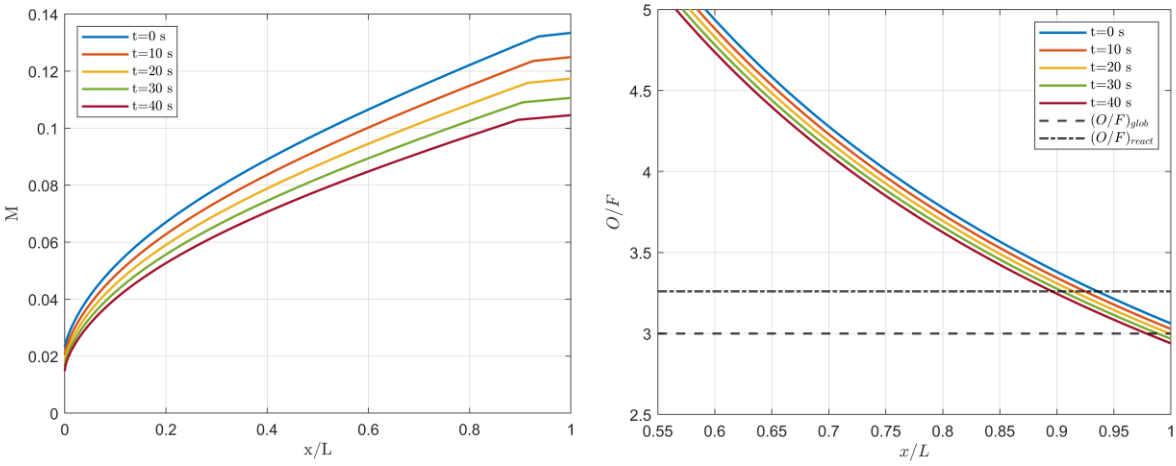

Figure 5.19: Mach number (left) and O/F ratio (right) distribution as a function of the dimensionless position along the grain and time ($n < 0.5$).

5.3 Influence of Friction on the Internal Ballistics

In the momentum equation (5.9), the shear stress at the wall τ_w can be evaluated with equation (2.8) where it must be taken into consideration the reduction of the skin-friction due to the blowing from the grain represented by the blowing parameter B (2.26). The term C_f can be evaluated with equation (2.29), with C_{f_0} calculated with equation (2.22). In order to evaluate the influence of friction on the combustion chamber internal ballistics, 3 solutions for different blowing coefficient values are compared: $B = 10$, value in the typical range for hybrid engines $(5 \leq B \leq 20)$; $B = 0$ (i.e. no blowing), thus $C_f/C_{f_0} = 1$; $B \rightarrow \infty$, thus $C_f/C_{f_0} \rightarrow 0$. As expected, the pressure at the head of the grain is higher when B is small, due to the reduction of the blowing effect on the shear stress at the wall. For each value of B considered, the differences of the pressure (Fig.5.20), temperature (Fig.5.21) and Mach number (Fig.5.22) distributions are negligible. Therefore, it can be deduced that it is not essential to know the exact value of the blowing parameter in order to be able to study, at least in the early stage of design, the internal ballistics of a hybrid engine.

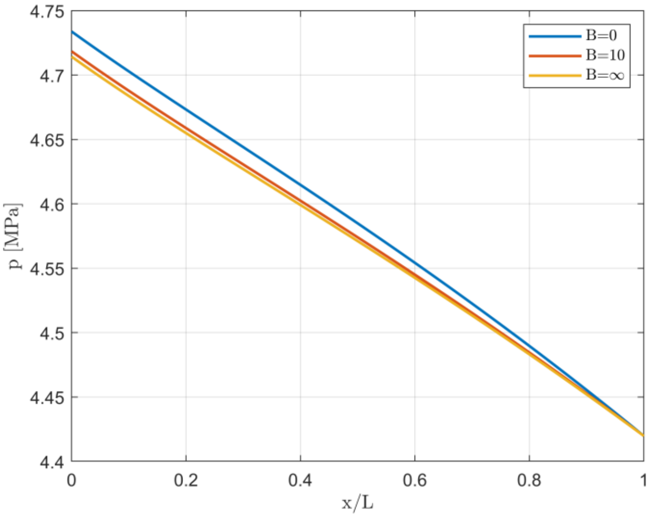

Figure 5.20: Pressure distribution as a function of the dimensionless position for several values of the blowing parameter B.

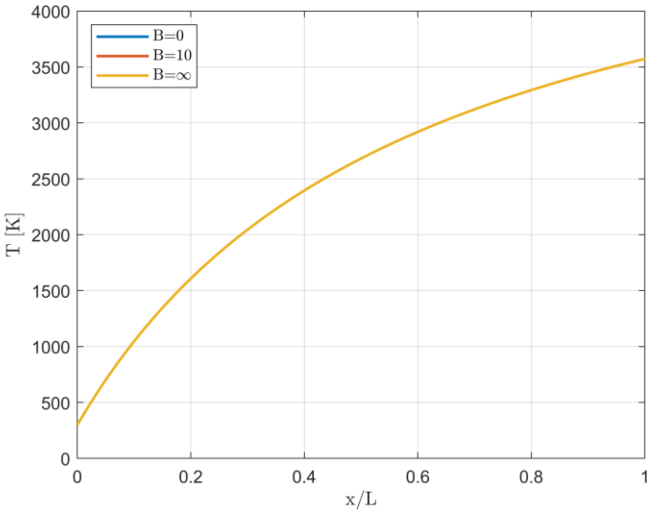

Figure 5.21: Temperature distribution as a function of the dimensionless position for several values of the blowing parameter B.

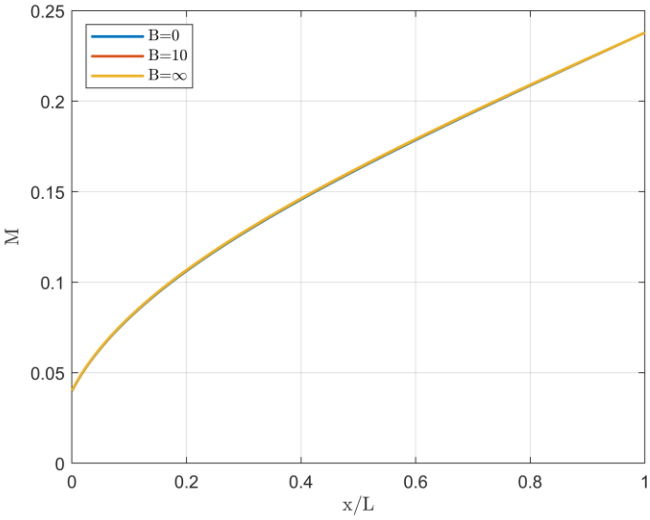

Figure 5.22: Mach number distribution as a function of the dimensionless position for several values of the blowing parameter B.

5.4 The Point of Minimum Regression Rate

The concurrent effects of increasing mass flow and boundary layer thickening in the downstream direction suggest that there is a position where the regression rate has a minimum. Karabeyoglu, Cantwell and Zilliac [6] propose two analytical equations for the evaluation of the position in which the condition of minimum regression rate occurs and the corresponding regression rate value. Here the correct version of those equations is written:

$$\frac{x_{min}}{L} = \left[\frac{-m(1-n)}{\alpha(m+n)}\right]^{\frac{1}{m+1}} \tag{5.28}$$

$$\frac{\dot{r}_{min}}{\dot{r}_L} = \left[\frac{n(m+1)}{(1+\alpha)(m+n)}\right]^{\frac{n}{1-n}} \left[\frac{m(n-1)}{\alpha(m+n)}\right]^{\frac{m}{m+1}} \tag{5.29}$$

with L the grain length, $\dot{r}_L$ the regression rate at $x = L$ and α calculated with equation (2.56). Fig.5.23 shows the comparison between the values of x_{min} and $\dot{r}_{min}$ evaluated with the previous equations and the corresponding values from the numerical simulation. The results are the same only at the beginning of the simulation, due to the constant port area hypothesis assumed by the authors, which is verified by the numerical 1D model only at $t = 0$. For $t > 0$, the larger port diameter in the first part of the grain (when compared to the average one) leads to a lower mass flux, therefore reducing the flux effect on the regression rate that cause a greater downstream displacement of the point of minimum regression rate.

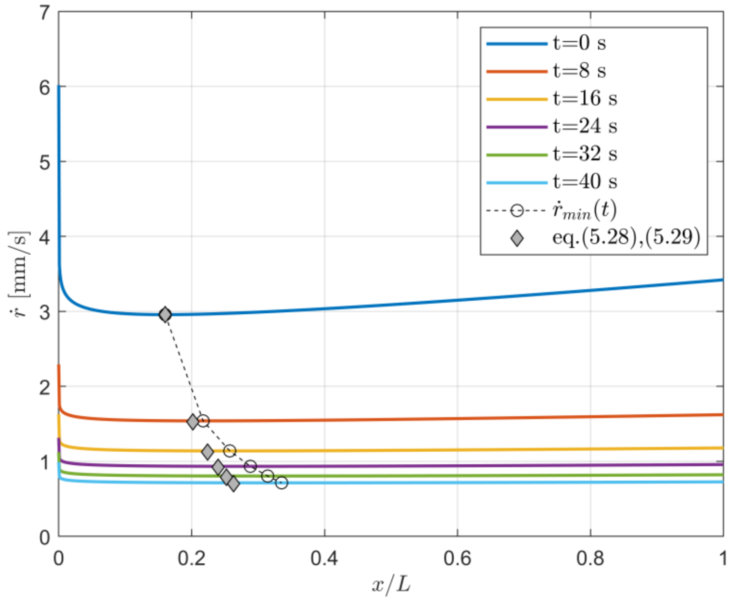

Figure 5.23: Comparison between the values of x_{min} and $\dot{r}_{min}$ evaluated with equations (5.28) and (5.29) and the corresponding values from the numerical simulation.

In the following, the influence of some parameters on the minimum regression rate condition will be discussed.

Influence of n. The coefficient n value affects the flux term of the regression rate. As a result, a higher value of n leads to a greater flux effect, thus bringing the position of minimum regression rate more upstream along the grain port. In addition, n influences the O/F shift. Therefore: if $n < 0.5$, the increase in fuel mass flow rate leads x_{min} to move upstream over time; if $n = 0.5$, no O/F shift occurs and x_{min} is constant; if $n > 0$, the reduction in fuel flux leads x_{min} to move downstream over time (Fig.5.24).

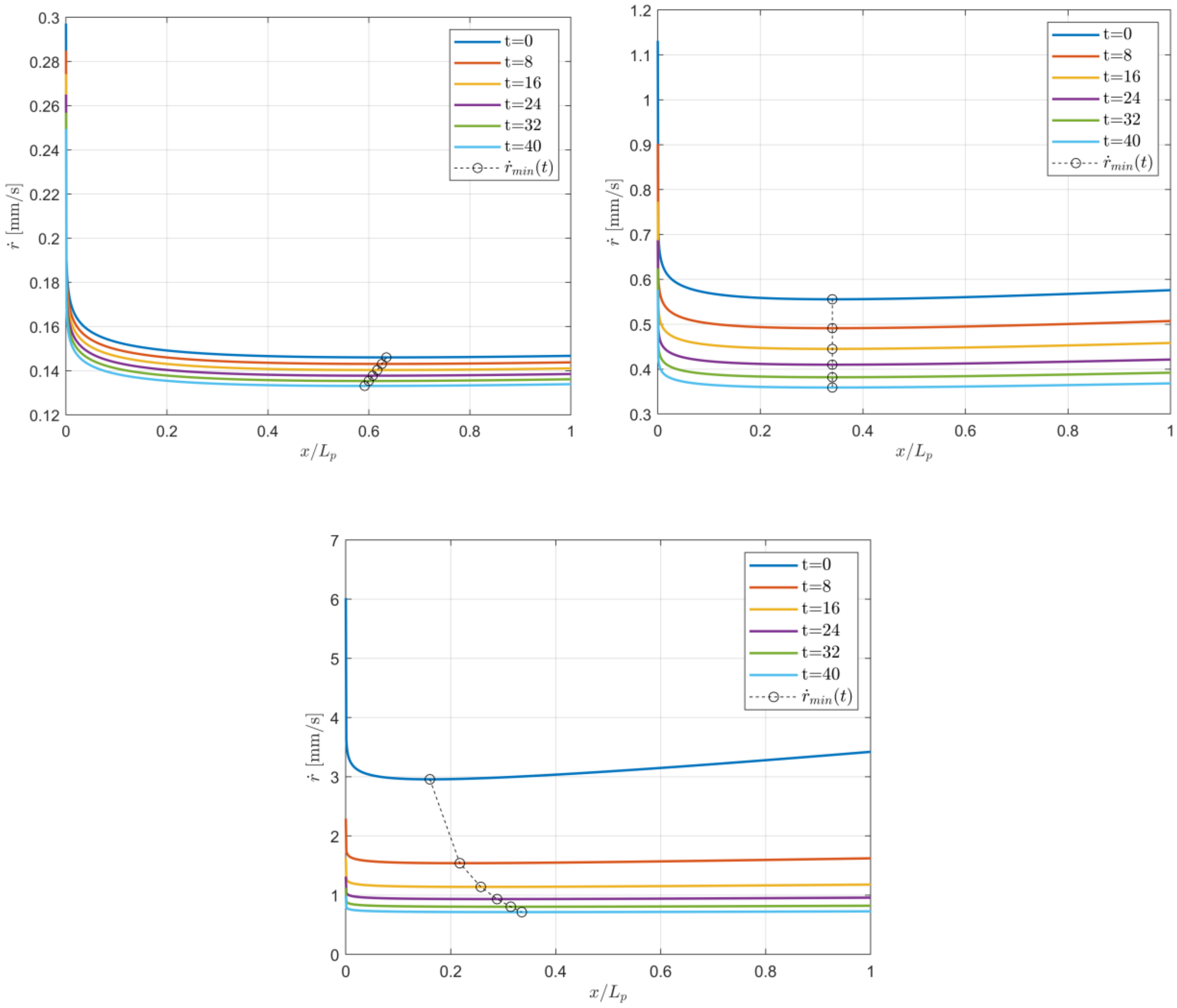

Figure 5.24: Regression rate minimum location and value as a function of time for $n < 0.5$ (top left), $n = 0.5$ (top right) and $n > 0.5$ (bottom).

Influence of m. The regression rate coefficient $m < 0$ is representative of the thickening of the boundary layer. Therefore, an increase in the modulus of m leads to a downstream displacement of the point of minimum regression rate (Fig.5.25). For $m = 0$ (as in the case of paraffin), the position of minimum regression rate is at the head of the grain and its axial coordinate does not change over time. If the modulus of m is high enough, x_{min} can be outside the combustion chamber.

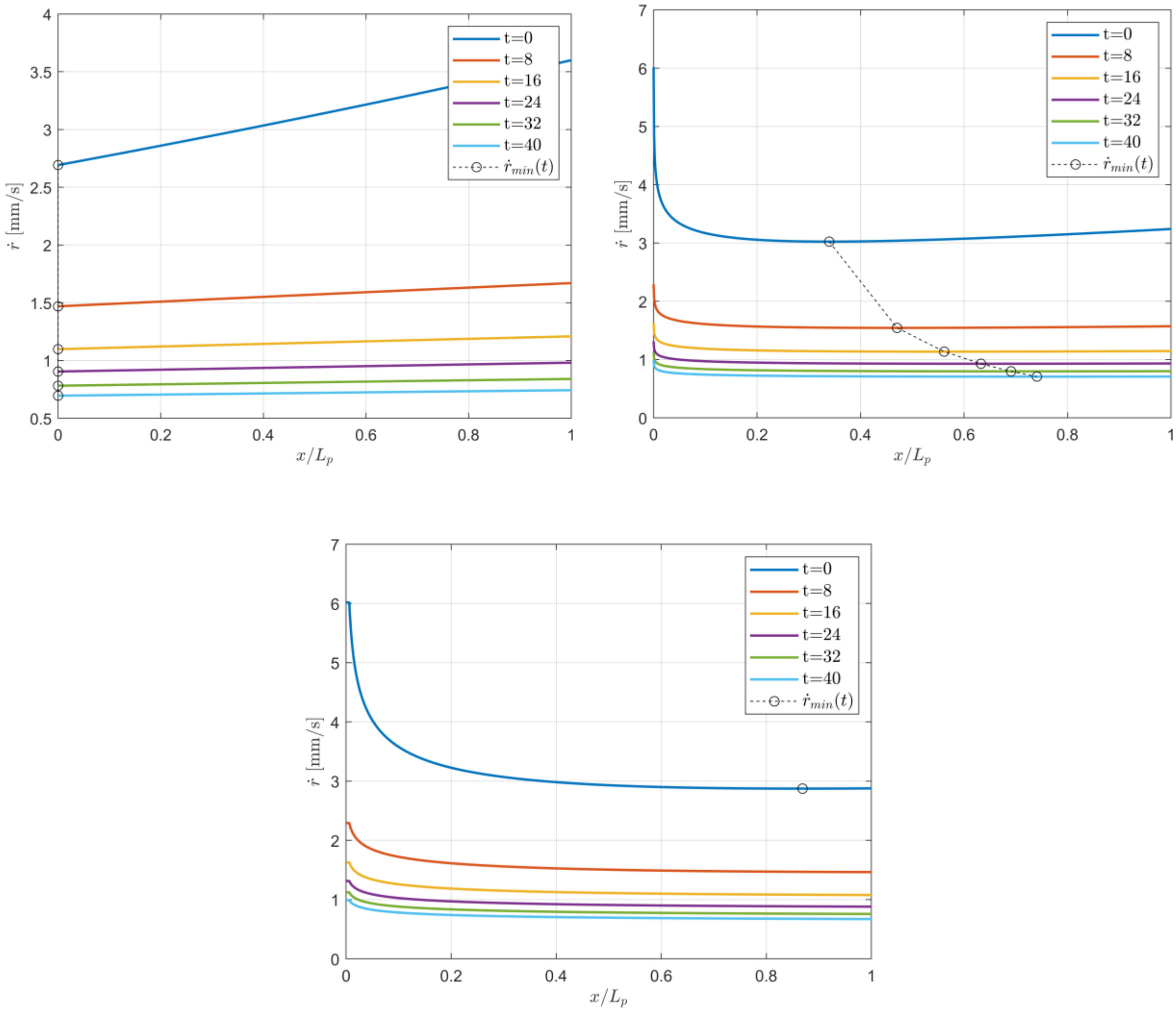

Figure 5.25: Regression rate minimum location and value as a function of time for $m = 0$ (top left), $m = -0.1$ (top right) and $m = -0.2$ (bottom).

Influence of $[O/F]_{glob}$. As seen in Chapter 4, an increase in the average O/F ratio (i.e. $[O/F]_{glob}$), with the same required thrust and burn time, leads to an increase in the oxidizer flow rate and a reduction of the fuel one. The greater oxidant flow rate is also associated, with the same G_{ox_0}, to an increase in the port area. Because the fuel mass flux G_f is inversely proportional to the port area, then an increase of $[O/F]_{glob}$ leads to a lower flux effect on the regression rate, thus moving the position of minimum regression rate more downstream along the grain port (Fig.5.26).

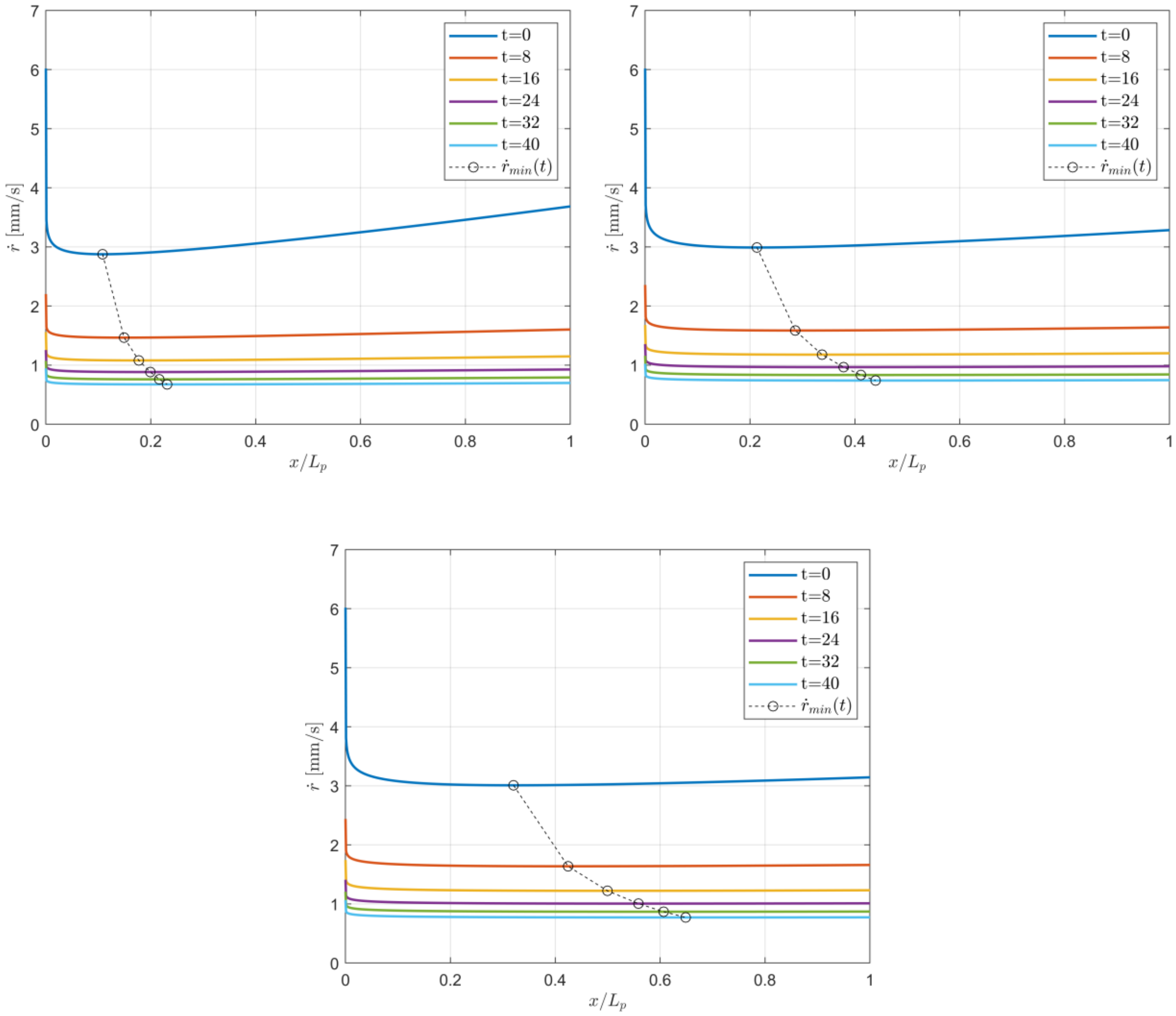

Figure 5.26: Regression rate minimum location and value as a function of time for $[O/F]_{glob} = 2$ (top left), $[O/F]_{glob} = 4$ (top right) and $[O/F]_{glob} = 6$ (bottom).

Influence of G_{ox_0}. The increase in G_{ox_0}, with the same required thrust, leads to a reduction of port area, thus strengthening the flux effect on the regression rate. As a result, a larger G_{ox_0} moves the position of minimum regression rate more upstream along the grain port (Fig.5.27). In addition, the greater variation of port area over time, yields to a greater downstream displacement of x_{min} for higher value of G_{ox_0}.

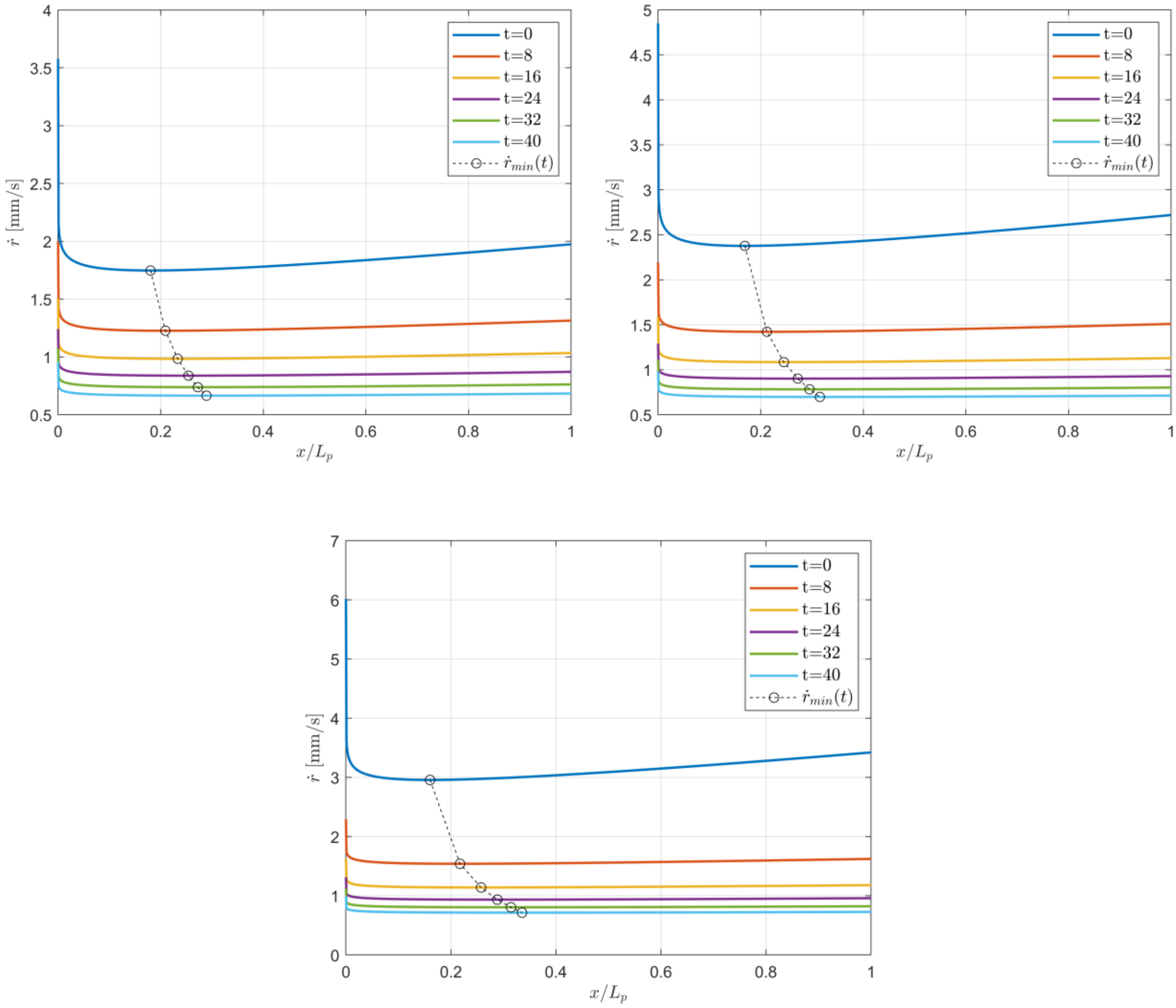

Figure 5.27: Regression rate minimum location and value as a function of time for $G_{ox_0} = 400\ kg/(m^2 s)$ (top left), $G_{ox_0} = 600\ kg/(m^2 s)$ (top right) and $G_{ox_0} = 800\ kg/(m^2 s)$ (bottom).

5.5 Propellant Residuals

Because of the non-uniform distribution of the regression rate over the grain length, at the end of the combustion there will be residuals of propellant grain in the combustion chamber, which represents a loss in the engine's performance. In order to be able to analytically assess the extent of the residuals, it is useful to assume $m = 0$ (as in the case of paraffin). Therefore, the regression rate (2.35) loses its dependence on the axial coordinate, thus monotonically increasing with x.

If the oxidizer flow is stopped when all the grain at $x = L$ is consumed, the residuals mass and its percentage with respect to the grain initial one can be calculated with:

$$m_{res} = \rho_f \frac{\pi}{4} \int_0^L D_f^2 - D^2(x)\, dx \tag{5.30}$$

$$res_{\%} = \frac{m_{res}}{m_f} = \frac{\int_0^L D_f^2 - D^2(x)\ dx}{\left(D_f^2 - D_0^2\right)L} \tag{5.31}$$

where D_0 and D_f are the initial and final (at $x = L$) port diameters, and $D(x)$ is the port diameter at the generic axial position at the end of the burn. The value of the final port diameter at $x = 0$ and $x = L$, as well as the average final port diameter, can be estimated using the regression rate definition. At $x = 0$ the only flow is that of the oxidizer, thus:

$$\dot{r} = \frac{1}{2}\frac{dD}{dt} = a_x G_{ox}^n = a_x \left(\frac{\dot{m}_{ox}}{A_p}\right)^n = a_x \left(\frac{4\dot{m}_{ox}}{\pi D^2}\right)^n = a_x \left(\frac{4\dot{m}_{ox}}{\pi}\right)^n D^{-2n} \tag{5.32}$$

Integrating the previous equation between $t = 0$ and the burn time yields to:

$$\int_{D_0}^{D_{f_0}} D^{2n}\, dD = 2a_x \left(\frac{4\dot{m}_{ox}}{\pi}\right)^n \int_0^{t_b} dt \tag{5.33}$$

$$\frac{1}{2n+1} D^{2n+1}\Big|_{D_0}^{D_{f_0}} = 2a_x \left(\frac{4\dot{m}_{ox}}{\pi}\right)^n t_b \tag{5.34}$$

Therefore, the final port diameter at $x = 0$ is:

$$D_{f_0} = \left[a_x(4n+2)\left(\frac{4}{\pi}\dot{m}_{ox}\right)^n t_b + D_0^{2n+1}\right]^{\frac{1}{2n+1}} \tag{5.35}$$

The average final port diameter D_{f_m} is calculated with equation (4.23), where it is assumed an average value for the regression rate (equation (2.53)). The final port diameter at $x = L$ can be evaluated by using the average O/F ratio used for the preliminary sizing of the engine:

$$\dot{r} = \frac{1}{2}\frac{dD}{dt} = a_x G^n = a_x\left(\frac{\dot{m}_{ox}+\dot{m}_f}{A_p}\right)^n = a_x\left[\frac{4\dot{m}_{ox}}{\pi D^2}\left(\frac{O/F+1}{O/F}\right)\right]^n D^{-2n} \tag{5.36}$$

Integrating the previous equation between $t = 0$ and the burn time yields to:

$$\int_{D_0}^{D_{f_0}} D^{2n}\,dD = a_x\left[\frac{4\dot{m}_{ox}}{\pi D^2}\left(\frac{O/F+1}{O/F}\right)\right]^n \int_0^{t_b} dt \tag{5.37}$$

$$\frac{1}{2n+1} D^{2n+1}\Big|_{D_0}^{D_{f_0}} = a_x\left[\frac{4\dot{m}_{ox}}{\pi D^2}\left(\frac{O/F+1}{O/F}\right)\right]^n t_b \tag{5.38}$$

$$D_{f_L} = \left\{a_x(4n+2)\left[\frac{4}{\pi}\dot{m}_{ox}\left(\frac{O/F+1}{O/F}\right)\right]^n t_b + D_0^{2n+1}\right\}^{\frac{1}{2n+1}} \tag{5.39}$$

The previous equations can be used to estimate the percentage of residuals. If it is assumed that $D_{f_L} = D_f$ (i.e. at the end of the grain all propellant has been burnt), then from simple geometry, the residuals percentage can be calculated with:

$$res_{\%} = \frac{\left[1 - \frac{1}{3} - \frac{1}{3}\left(\frac{D_{f_0}}{D_{f_L}}\right)^2 - \frac{1}{3}\left(\frac{D_{f_0}}{D_{f_L}}\right)\right]}{1 - \left(\frac{D_0}{D_{f_L}}\right)^2} \cdot 100 \tag{5.40}$$

Developing the port diameter equations in [6], in particular conditions the residuals percentage can be evaluated as:

$$res_{\%} = \left[1 - \frac{1-n}{\alpha (O/F)^{1-n}\left(1+(O/F)\right)^{n}}\right] \cdot 100 \ ; \ \text{for } t_b \to 0 \qquad (5.41)$$

$$res_{\%} = \frac{\alpha}{2(\alpha+1)} \cdot 100 \qquad ; \ \text{for } n = 0.5 \qquad (5.42)$$

The percentage residuals mass is greater for high value of the flux coefficient n because of the higher regression rate variation along the grain (Fig.5.28). On the contrary, using a large value for $[O/F]_{glob}$, the percentage residuals mass is reduced due to the lower increase in mass flux along the grain port that limits the variation of the port distribution.

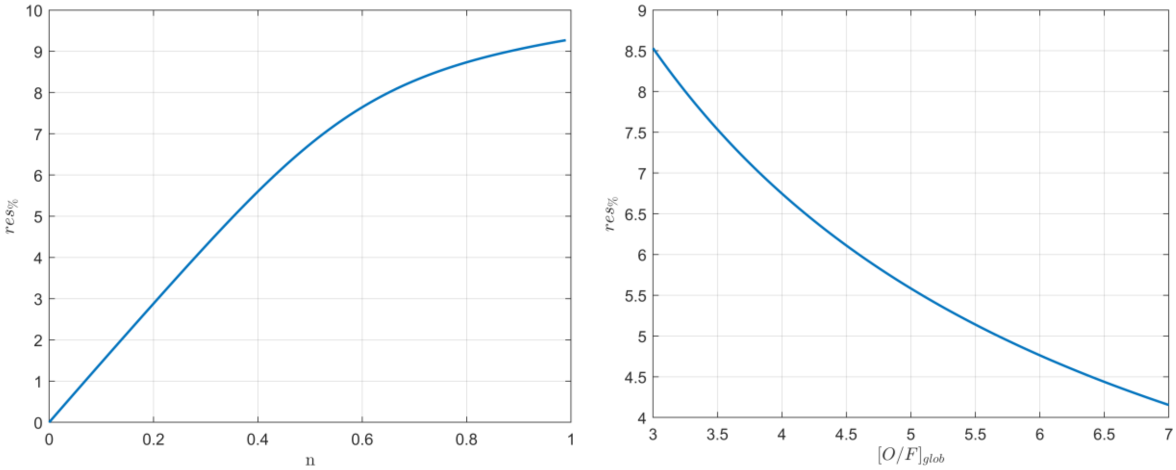

Figure 5.28: Example of percentage residuals mass as a function of the flux coefficient n (left) and of the $[O/F]_{glob}$ (right).

5.6 Scale Effect

An important characteristic of hybrid engines is that the regression rate depends on the engine scale. From Marxman's theory [8][9], the regression rate coefficient a should decrease as the scale at -0.2, while experimental measurements generally suggest slightly lower values for plastic fuels, and it is almost negligible for paraffin wax [5][13]. However, since large engines require high regression rates to have acceptable volume loading, this effect is the opposite of what is desired.

In the following figures (Fig.5.29 to 5.31) a qualitatively comparison of the internal ballistics between a low thrust and a high thrust engine it is made. It is important to notice that, due to the higher port area and thus to the lower mass flux, an engine designed to provide a higher thrust will be characterized by a lower regression rate at the same dimensionless position along the grain port. In addition, the location of the minimum regression rate will be more downstream because of the lower flux effect. This behaviour, in addition to the decrease of the coefficient a, explains why high thrust hybrid engines are characterized by lower regression rate than low thrust engine (while the other design parameters are kept constant).

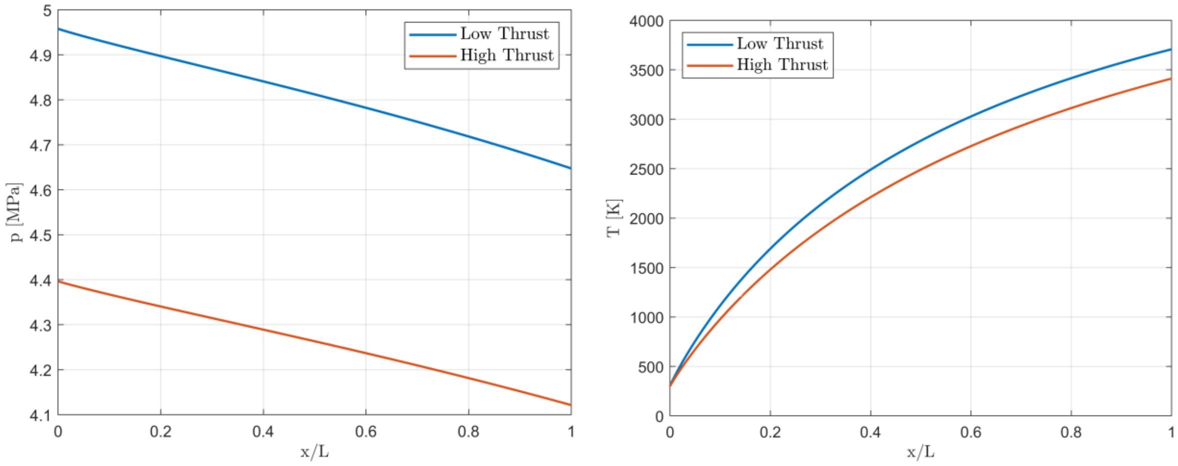

Figure 5.29: Comparison of pressure (left) and temperature (right) distribution as a function of the dimensionless position along the grain for low and high thrust engines.

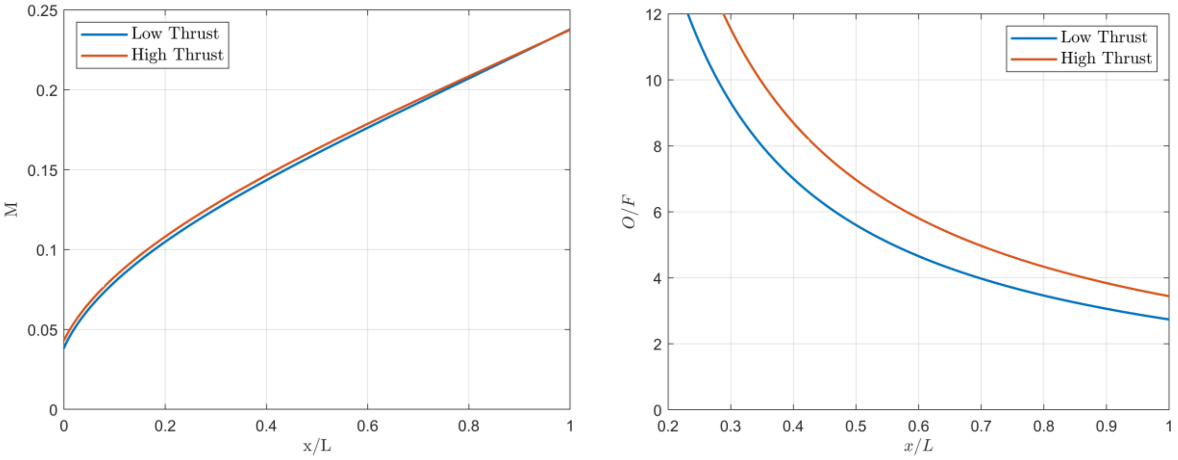

Figure 5.30: Comparison of Mach number (left) and O/F ratio (right) distribution as a function of the dimensionless position along the grain for low and high thrust engines.

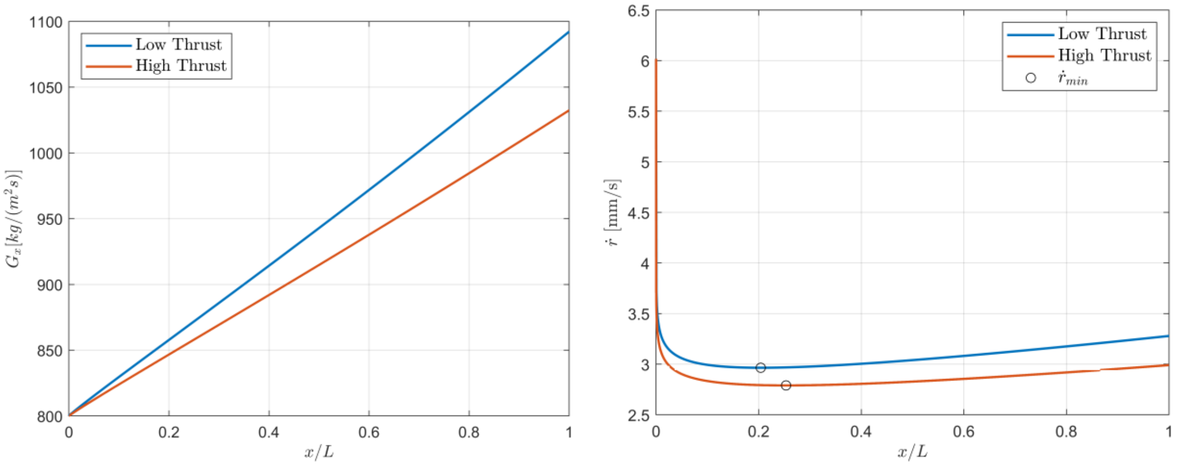

Figure 5.31: Comparison of mass flux (left) and regression rate (right) distribution as a function of the dimensionless position along the grain for low and high thrust engines.

In addition, it is interesting to observe that a hight thrust engine with the same $[O/F]_{glob}$ of a low thrust engine is characterized by a higher slenderness L/D_f. In fact, if L/D_f is imposed to be the same for the two engines, the average motor O/F ratio achieved by the high thrust engine will be greater than the one of the low thrust engine, because of the reduction in regression rate with the scale (Fig.5.32).

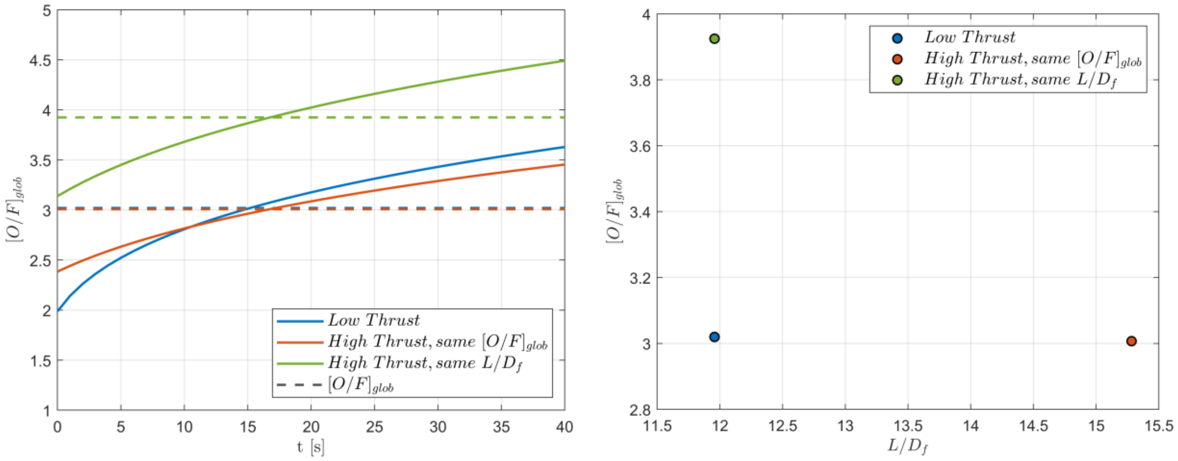

Figure 5.32: Comparison of the motor O/F ratio over time for different engine configurations (left) and of the achieved $[O/F]_{glob}$ as a function of the motor slenderness (right).

Chapter 6

Numerical Modelling of Hybrid Combustion Boundary Layer

Marxman's theory is a valid starting point for evaluating the internal ballistics of a hybrid engine. However, as already mentioned, it makes use of some simplifications and has inconsistencies that are problematic when it is used to describe hybrid combustion in a closed duct. In the following, some corrections are presented that will be employed to describe more accurately the boundary layer. The aim is to provide a sufficiently accurate description of the turbulent boundary layer with hybrid combustion which can be implemented in the 1D with boundary layer model presented in Chapter 7.

6.1 Determination of Fuel Mass Fraction at the Surface in the Reactive Turbulent Boundary Layer

In Marxman's theory, the fuel mass fraction at the wall, K_{f_w}, is assumed to be unitary. However, mass transfer concepts applied to the mathematical description of the evaporation phenomenon show that its value is always less than one [33].

Karabeyoglu and coworkers [31] proposed to evaluate the fuel mass fraction at the grain surface applying the Reynolds analogy between the flame zone and the surface:

$$\frac{h_b - h_w}{h_v} = \frac{\Delta h}{h_v} = \frac{K_{f_b} - K_{f_w}}{K_{f_w} - 1} \tag{6.1}$$

Based on the flame sheet approximation, the fuel mass fraction at the flame can be assumed to be zero, thus $K_{f_b} = 0$. Under this condition, equation (6.1) can be used to solve for the fuel mass fraction at the surface, leading to an expression for K_{f_w} as a function of the thermochemical parameter $\Delta h/h_v$ only:

$$K_{f_w} = \frac{\Delta h/h_v}{\Delta h/h_v + 1} \tag{6.2}$$

Since the thermochemical parameter $\Delta h/h_v$ can be assumed constant along the grain port as long as there is no dilution (i.e. there is no more combustion since all the oxidizer has been consumed), also the fuel mass fraction at the surface can be assumed constant. When there is no dilution, variation of the $\Delta h/h_v$ value can be caused by small changes of the grain surface temperature, which are not considered in the current model.

Fig.6.1 shows the fuel mass fraction at the grain wall as a function of the thermochemical parameter $\Delta h/h_v$ described by equation (6.2). The increase of $\Delta h/h_v$ is equivalent to an increase of the vaporized fuel mass flow rate which leads to a greater value of K_{f_w}.

For typical conditions encountered in hybrid rockets, the surface mass fraction is expected to be in the range of 0.75-0.90 [31].

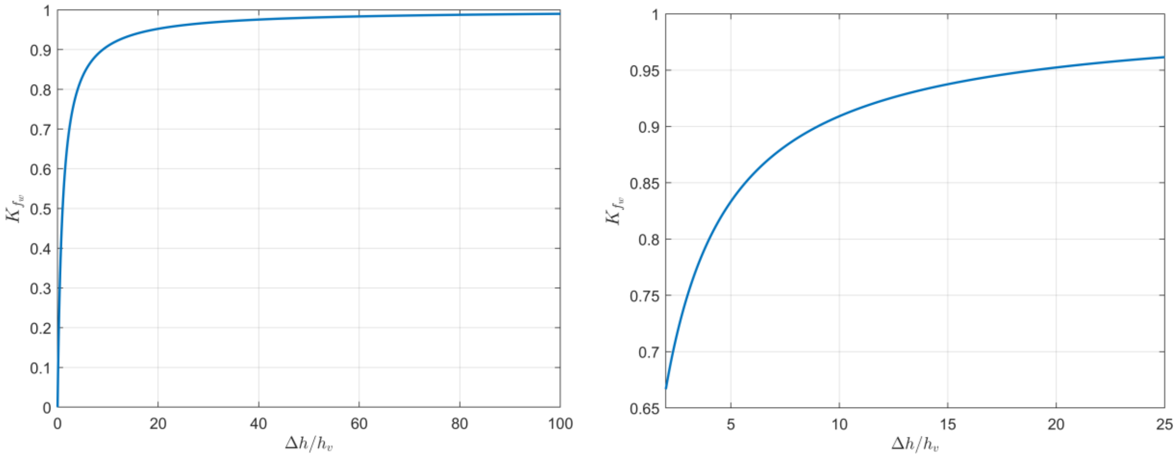

Figure 6.1: Fuel mass fraction at the wall K_{f_w} as a function of the thermochemical parameter $\Delta h/h_v$ for a broad range of values (left) and for typical values in hybrid rockets (right).

Because of the validity of the Reynolds analogy, the blowing parameter B can be evaluated as a function of the thermochemical parameter $\Delta h/h_v$ with equation (2.27). The flame dimensionless velocity cannot be calculated with equation (3.16) derived by Marxman, because, as already mentioned, there is no perfect coherency between B and $\Delta h/h_v$. In fact, it can be easily demonstrated by combining the equations (2.27), (3.16) and (6.2), that for $B \to 0$ it is $K_{f_w} < 0$. Therefore, combining equations (2.27) and (6.2), without any assumption on the flame dimensionless velocity value, yields to an expression for the fuel mass fraction at the surface as a function of the blowing parameter B:

$$K_{f_w} = \frac{B}{B+1} \tag{6.3}$$

which has the same trend as equation (6.2): for $B \to 0$ (i.e. no combustion, thus no mass injection) then it is $K_{f_w} \to 0$, while for $B \to \infty$ then K_{f_w} tends monotonically to unity (Fig.6.2).

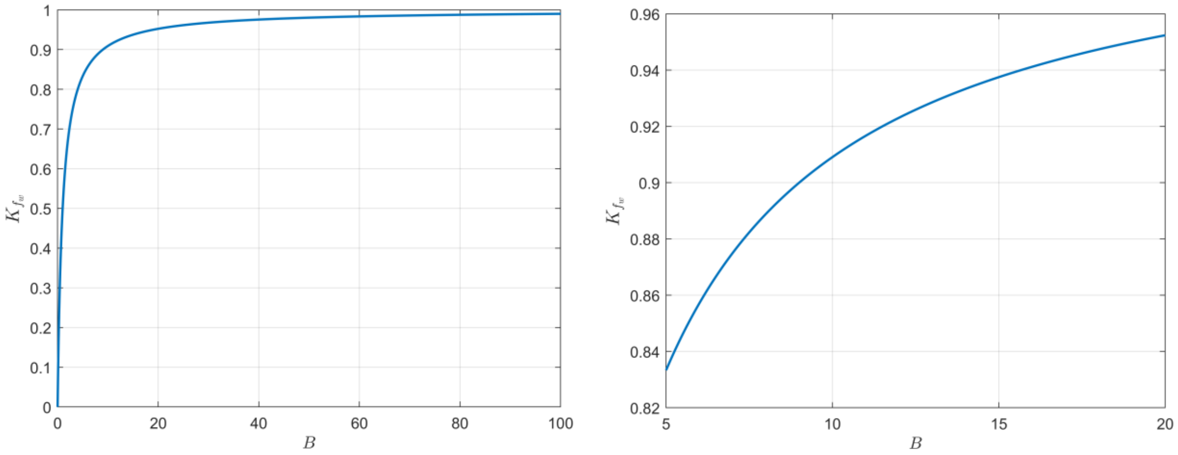

Figure 6.2: Fuel mass fraction at the wall K_{f_w} as a function of the blowing parameter B for a broad range of values (left) and for typical values in hybrid rockets (right).

6.2 Non-reacting Turbulent Boundary Layer

Let's consider a perforated flat plate where two flows are injected, the oxidizer parallel to the plate and the fuel through the holes on the plates. The fuel mass flow rate injected through the plate holes is the same as in the case of hybrid combustion. It is assumed that no combustion process takes place (non-reacting case). A turbulent boundary layer forms above the surface and its dimensionless velocity profile is described by equation (3.9) with $n = 1/7$. Since no combustion takes place, the oxidizer and fuel concentration profiles will extend over the entire boundary layer thickness.

Let's first consider $K_{ox_e} = 1$, i.e. the chemical composition of the oxidizer is pure oxygen. The fuel mass fraction is maximum at the surface, where its value is K_{f_w}, and it is equal to zero at the boundary layer edge. The oxidizer mass fraction is maximum and equal to K_{ox_e} at the boundary layer edge and equal to $1 - K_{f_w}$ at the wall. If the Reynolds analogy is assumed to be valid and $Pr = Le = 1$, then the concentration profiles (Fig.6.3) can be considered linear to the velocity profile. Similarly to what has been done previously, for the oxidizer mass fraction profile the following system of equations must be solved:

$$\begin{cases} K_{ox,nr}(\eta) = a\phi(\eta) + b \\ K_{ox,nr}(\eta = 0) = K_{ox_w} = 1 - K_{f_w} \\ K_{ox,nr}(\eta = 1) = K_{ox_e} = 1 \end{cases} \tag{6.4}$$

where the subscript nr indicates the non-reacting case. Calculations give:

$$K_{ox,nr}(\eta = 0) = a\phi(\eta = 0) + b = 1 - K_{f_w} \rightarrow b = 1 - K_{f_w} \tag{6.5}$$

$$K_{ox,nr}(\eta = 1) = a\phi(\eta = 1) + b = 1 \rightarrow a = K_{f_w} \tag{6.6}$$

Therefore:

$$K_{ox,nr} = 1 + K_{f_w}(\phi - 1) \tag{6.7}$$

The only other component inside the non-reacting boundary layer is the fuel, therefore its mass fraction profile is described by:

$$K_{f,nr} = 1 - K_{ox,nr} = K_{f_w}(1 - \phi) \tag{6.8}$$

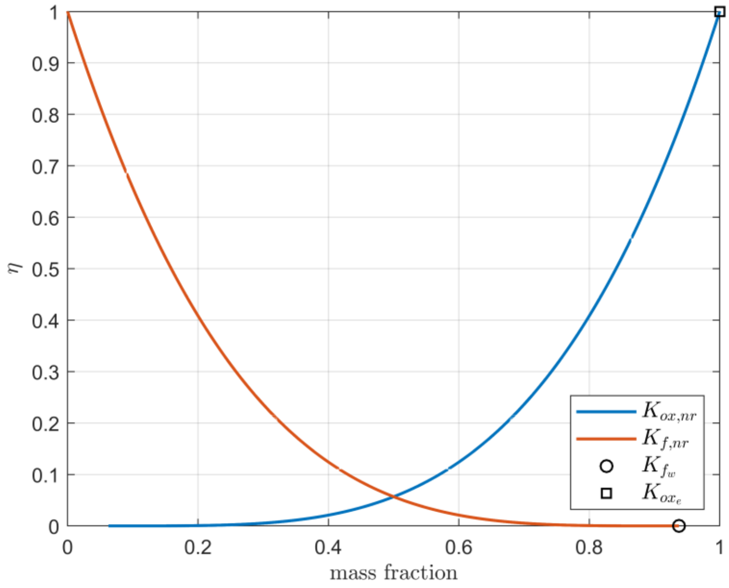

Figure 6.3: Oxidizer and fuel mass fraction profiles in the non-reacting boundary layer as a function of the dimensionless position η for $K_{ox_e} = 1$.

Considering that $K_{f,nr} = 1 - K_{ox,nr}$, the oxidizer/fuel ratio at the coordinate η is:

$$[O/F]_{nr}(\eta) = \frac{K_{ox,nr}}{K_{f,nr}} = \frac{1}{K_{f_w}(1 - \phi)} - 1 \tag{6.9}$$

Solving the previous equation for ϕ, the value of the dimensionless velocity at the point where the concentrations ratio is equal to $[O/F]_{nr}$, namely ϕ_{nr}, is obtained:

$$\phi_{nr} = 1 - \frac{1}{K_{f_w}([O/F]_{nr} + 1)} \tag{6.10}$$

The dimensionless position where the concentrations ratio is equal to $[O/F]_{nr}$, namely η_{nr}, can be evaluated from equation (3.9):

$$\eta_{nr} = \left[\frac{-1+\sqrt{1+2B(1+0.5B)\phi_{nr}}}{B}\right]^{1/n} \tag{6.11}$$

Fig.6.4 and 6.5 show the dimensionless velocity ϕ_{nr} and position η_{nr} respectively as a function of the $[O/F]_{nr}$ ratio for several values of fuel mass fraction at the surface K_{f_w}, i.e. for several values of the blowing parameter B and therefore of mass injected through the holes of the plate. A higher $[O/F]_{nr}$, while K_{f_w} is constant, is obtained at a greater distance from the surface, thus at a higher dimensionless speed. If $[O/F]_{nr}$ is constant, a higher K_{f_w} (i.e. higher mass injected) leads to an increase in the height from the surface where the oxidizer/fuel ratio is verified because of the reduction, at the same location, of the dosage ratio due to the increase of the fuel concentration at the wall. Moreover, it can be observed that for a value of K_{f_w} there is a minimum value of $[O/F]_{nr} = \frac{K_{ox_w}}{K_{fw}} = \frac{1-K_{fw}}{K_{fw}}$ achieved at the wall $(\eta = 0, \phi = 0)$. This is related to the fact that as K_{f_w} decreases, the minimum value of $[O/F]_{nr}$, which occurs at the surface of the plate where the fuel and oxidizer mass fractions are maximum and minimum respectively, increases. Consequently, all $[O/F]_{nr}$ values lower than this minimum value cannot be achieved.

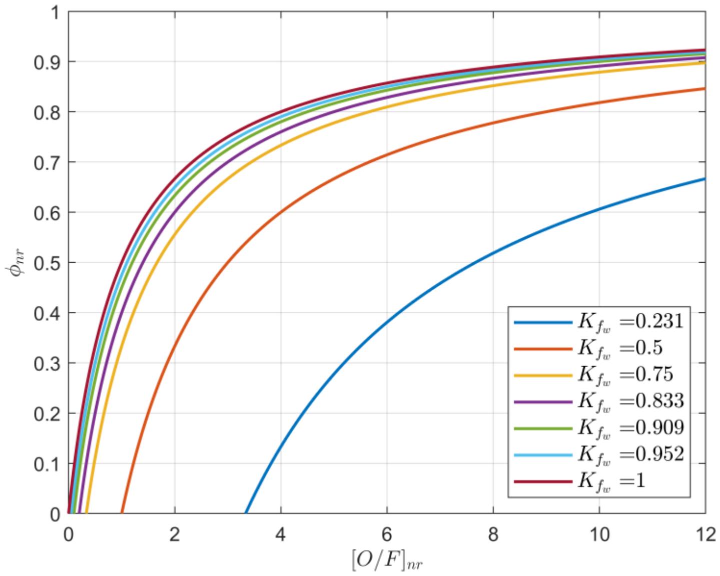

Figure 6.4: Dimensionless velocity ϕ_{nr} as a function of the $[O/F]_{nr}$ ratio $\left(K_{ox_e} = 1\right)$ for several values of fuel mass fraction at the surface K_{f_w}.

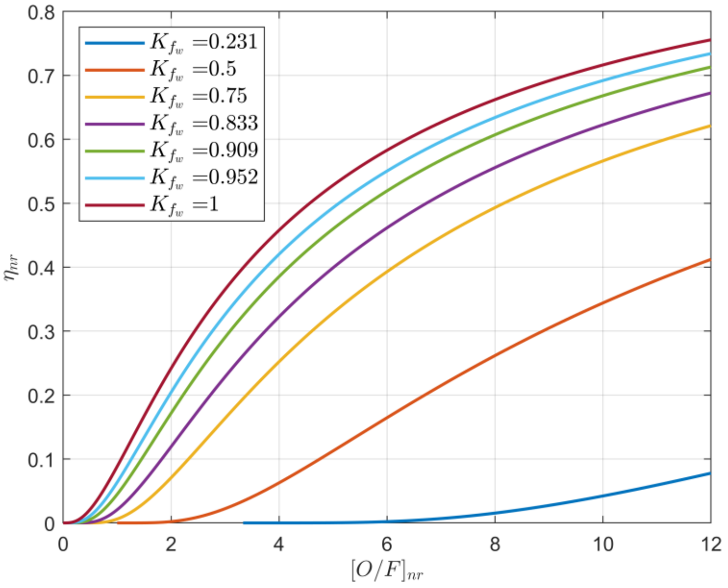

Figure 6.5: Dimensionless position η_{nr} as a function of the $[O/F]_{nr}$ ratio $\left(K_{ox_e} = 1\right)$ for several values of fuel mass fraction at the surface K_{f_w}.

If the oxidizer is diluted, then $K_{ox_e} < 1$. Since there is no combustion, the ratio between the oxygen and the diluent mass fraction is constant over the entire boundary layer thickness, i.e. $\frac{K_{in}}{K_{ox}} = \text{const}$. At any dimensionless position must be $K_{ox} + K_{in} + K_f = 1$. Because K_{f_e} is still equal to zero at the edge of the boundary layer, here it is $K_{ox_e} + K_{in_e} = 1$. At the wall surface, it is $K_{ox_w} + K_{in_w} + K_{f_w} = 1$, thus:

$$\frac{K_{in}}{K_{ox}} = \text{const} = \frac{K_{in_e}}{K_{ox_e}} = \frac{K_{in_w}}{K_{ox_w}} = \frac{\left(K_{in_w} + K_{ox_w}\right) - K_{ox_w}}{K_{ox_w}} = \frac{1 - K_{f_w}}{K_{ox_w}} - 1 \tag{6.12}$$

Solving for K_{ox_w} yields to:

$$K_{ox_w} = K_{ox_e}\left(1 - K_{f_w}\right) \tag{6.13}$$

where the composition $\frac{K_{in_e}}{K_{ox_e}}$ of the external flow is known. Therefore:

$$K_{in_w} = \left(1 - K_{ox_e}\right)\left(1 - K_{f_w}\right) \tag{6.14}$$

For the oxidizer mass fraction profile, the following system of equations must be solved:

$$\begin{cases} K_{ox,nr}(\eta) = a\phi(\eta) + b \\ K_{ox,nr}(\eta = 0) = K_{ox_w} \\ K_{ox,nr}(\eta = 1) = K_{ox_e} \end{cases} \tag{6.15}$$

therefore:

$$K_{ox,nr} = K_{ox_e}\phi + K_{ox_e}\left(1 - K_{f_w}\right)(1 - \phi) \tag{6.16}$$

Similarly, the inert mass fraction profile is:

$$K_{in,nr} = K_{in_e}\phi + \left(1 - K_{ox_e}\right)\left(1 - K_{f_w}\right)(1 - \phi) \tag{6.17}$$

The fuel mass fraction profile is still evaluated with equation (6.8), because its boundary conditions doesn't change between the diluted and pure oxidizer cases.
Fig.6.6 shows an example of mass fraction distribution in the non-reacting boundary layer for a diluted freestream.

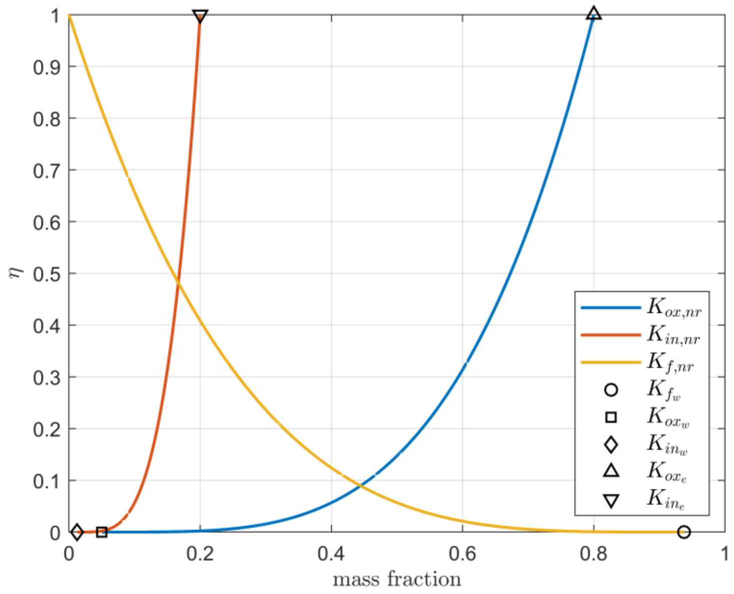

Figure 6.6: Oxidizer and fuel mass fraction profiles in the non-reacting boundary layer as a function of the dimensionless position η for $K_{ox_e} = 0.8$.

In this case, the oxygen to fuel ratio at the coordinate η is:

$$[O/F]_{nr}(\eta) = \frac{K_{ox,nr}}{K_{f,nr}} = \frac{K_{ox_e}\phi + K_{ox_e}\left(1 - K_{f_w}\right)(1 - \phi)}{K_{f_w}(1 - \phi)} \qquad (6.18)$$

Solving the previous equation for ϕ, the value of the dimensionless velocity at the point where the concentrations ratio is equal to $[O/F]_{nr}$, namely ϕ_{nr}, is obtained:

$$\phi_{nr} = 1 - \frac{K_{ox_e}}{K_{f_w}\left([O/F]_{nr} + K_{ox_e}\right)} \qquad (6.19)$$

For $K_{ox_e} = 1$, equation (6.19) is equal to equation (6.10). The dimensionless position where the concentrations ratio is equal to $[O/F]_{nr}$, namely η_{nr}, can still be evaluated with equations (6.11).

Fig.6.7 and Fig.6.8 show the dimensionless velocity ϕ_{nr} and position η_{nr} respectively as a function of the $[O/F]_{nr}$ ratio for several values of fuel mass fraction at the surface K_{f_w}. The trend is similar to the one explained above for $K_{ox_e} = 1$. However, the reduction of K_{ox_e} allow to reduce the minimum value of $[O/F]_{nr}$ ratio at the wall.

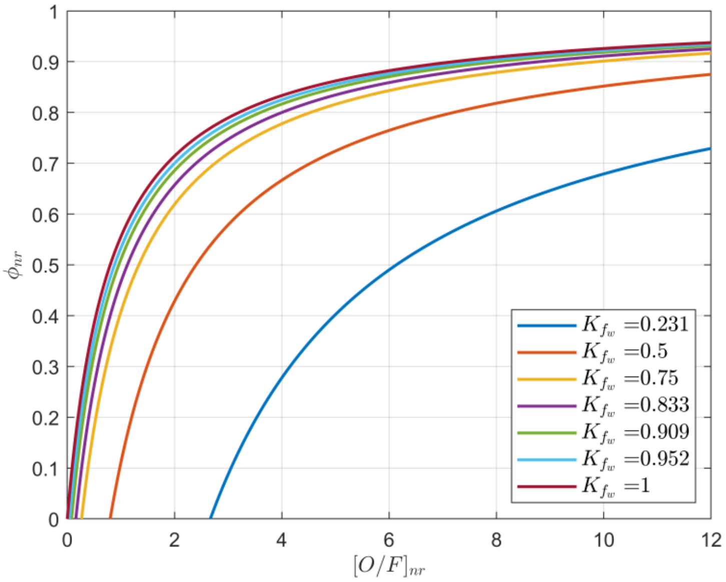

Figure 6.7: Dimensionless velocity ϕ_{nr} as a function of the $[O/F]_{nr}$ ratio $\left(K_{ox_e} = 0.8\right)$ for several values of fuel mass fraction at the surface K_{f_w}.

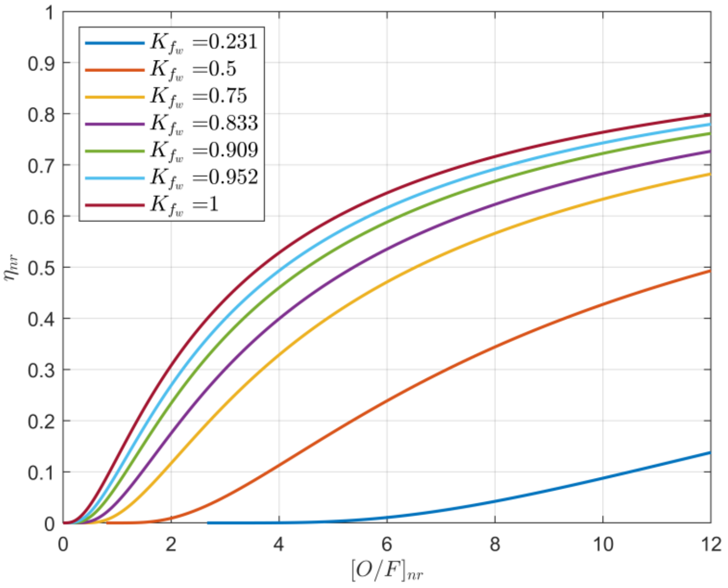

Figure 6.8: Dimensionless position η_{nr} as a function of the $[O/F]_{nr}$ ratio $\left(K_{ox_e} = 0.8\right)$ for several values of fuel mass fraction at the surface K_{f_w}.

In the following paragraphs, extensive use will be made of the analogy between the boundary layer in the non-reactive case and the one in the reactive case, in order to obtain some correction of Marxman's theory which will be used in the numerical modelling of hybrid rocket boundary layer combustion. The validity of this comparison is ensured by the assumption of constant density over the entire boundary layer thickness and that the velocity profile is not altered because of combustion.

6.2.1 Determination of Fuel Mass Fraction at the Surface in the Non-reactive Turbulent Boundary Layer

For the case of turbulent boundary layer with combustion, the fuel mass fraction at the wall K_{f_w} can be expressed, exploiting the Reynolds analogy, with the equation (6.3). In the non-reactive case, however, there is no combustion. Consequently, it is necessary to verify that this expression is still valid in this case. Let's make an analogy between the mass injection from the plate holes (representative of the sublimation phenomenon in hybrid combustion) and the evaporation of a liquid film in flowing air [32][33]. Let's consider an incompressible and stationary oxidizer flow above the grain flat surface. A boundary layer develops. It is assumed that the axial pressure gradients are negligible and that the properties of the fluid $(\rho, \mu, \alpha, \mathcal{D})$ are uniform and constant over the boundary layer thickness. Quantities referred to the solid surface are indicated by subscript s, to the fuel by f, to the oxidizer by ox (here it is assumed $K_{ox_e} = 1$, but the following demonstration is valid also in the case of a diluted oxidant) and to the oxidizer and fuel mixture by g. The subscript w refers to the quantities at the grain wall, while I refers to the quantities at the solid/gas interface. Mass flux conservation through the solid/gas interface can be written as:

$$\rho_{g_w}\left(v_{g_w} - v_I\right) = \rho_{s_w}\left(v_{s_w} - v_I\right) = \dot{m}_f'' \tag{6.20}$$

where v_I is the solid/gas interface velocity and $\dot{m}_f''$ is the fuel mass flux at the wall. Assuming the sublimated fuel vertical flow much greater than the linear regression of the wall, as a first approximation the solid surface can be considered at rest, thus $v_{s_w} = 0$. Therefore,

$$|v_I| = \left|v_I - v_{s_w}\right| = \frac{\rho_{g_w}}{\rho_{s_w}}\left|v_I - v_{g_w}\right| \tag{6.21}$$

In the case of solid/gas interface $\rho_{s_w} \gg \rho_{g_w}$, which gives:

$$\frac{\rho_{s_w}}{\rho_{g_w}} = \frac{\left|v_I - v_{g_w}\right|}{\left|v_I - v_{s_w}\right|} = \frac{\left|v_I - v_{g_w}\right|}{|v_I|} \gg 1 \tag{6.22}$$

Then, $\left|v_{g_w}\right| \gg |v_I|$ and $v_{g_w} - v_I \approx v_{g_w}$. Finally, equation (6.20) can be rewritten as $\dot{m}_f'' = \rho_{g_w} v_{g_w}$. The oxidizer does not dissolve into the solid surface, so that $\rho_{ox_w} v_{ox_w} = 0$ and:

$$\dot{m}_f'' = \rho_{g_w} v_{g_w} = \rho_{f_w} v_{f_w} + \rho_{ox_w} v_{ox_w} = \rho_{f_w} v_{f_w} \tag{6.23}$$

The fuel mass flux can be split into contributions of convective flux and diffusive flux (Fick diffusion law):

$$\rho_{f_w} v_{f_w} = K_{f_w} \rho_{g_w} v_{g_w} - \rho_{g_w} \mathcal{D}_{g_w} \left.\frac{\partial K_f}{\partial y}\right|_w \tag{6.24}$$

Equation (6.23) can therefore be rewritten as:

$$\dot{m}_f'' = \rho_{f_w} v_{f_w} = K_{f_w} \rho_{g_w} v_{g_w} - \rho_{g_w} \mathcal{D}_{g_w} \left.\frac{\partial K_f}{\partial y}\right|_w = K_{f_w} \dot{m}_f'' - \rho_{g_w} \mathcal{D}_{g_w} \left.\frac{\partial K_f}{\partial y}\right|_w \quad (6.25)$$

Assuming that the flow properties are uniform and constant over the boundary layer, then $\rho_{g_w}\mathcal{D}_{g_w} = \rho_g \mathcal{D}_g$. An expression of the specific evaporated flux is derived as a function of the fuel mass fraction and concentration gradient at the wall:

$$\dot{m}_f'' = -\frac{\rho_g \mathcal{D}_g}{1 - K_{f_w}} \left.\frac{\partial K_f}{\partial y}\right|_w \quad (6.26)$$

The previous equation is used to describe mathematically the evaporation phenomenon and shows that a high specific evaporated flux is equivalent to a high value of fuel mass fraction at the surface.

If the Reynolds analogy between the freestream and the wall is assumed to be valid, then:

$$\frac{1}{u_e - u_w} \left.\frac{\partial u}{\partial y}\right|_w = \frac{1}{T_e - T_w} \left.\frac{\partial T}{\partial y}\right|_w = \frac{1}{K_{f_e} - K_{f_w}} \left.\frac{\partial K_f}{\partial y}\right|_w \quad (6.27)$$

Equation (6.26) gives:

$$\left.\frac{\partial K_f}{\partial y}\right|_w = -\frac{\dot{m}_f''}{\rho_g \mathcal{D}_g}\left(1 - K_{f_w}\right) = \frac{\dot{m}_f''}{\rho_g \mathcal{D}_g}\left(K_{f_w} - 1\right) \quad (6.28)$$

therefore, considering $u_w = 0$, the equivalence of the first and third terms of the equation (6.27) yields to:

$$\frac{1}{u_e} \left.\frac{\partial u}{\partial y}\right|_w = \frac{1}{K_{f_e} - K_{f_w}} \left.\frac{\partial K_f}{\partial y}\right|_w = \frac{\dot{m}_f''}{\rho_g \mathcal{D}_g} \frac{K_{f_w} - 1}{K_{f_e} - K_{f_w}} \quad (6.29)$$

Considering the definition of the shear stress at the wall:

$$\tau_w = \mu \left.\frac{\partial u}{\partial y}\right|_w = \frac{1}{2} C_f \rho_e u_e^2 \tag{6.30}$$

yields to:

$$\left.\frac{\partial u}{\partial y}\right|_w = \frac{1}{2} C_f \rho_e u_e^2 \frac{1}{\mu} \tag{6.31}$$

Substituting equation (6.31) into equation (6.29) gives:

$$\underbrace{\frac{\dot{m}_f''}{\frac{1}{2} C_f \rho_e u_e}}_{B} = \frac{K_{f_e} - K_{f_w}}{K_{f_w} - 1} \underbrace{\frac{\rho_g \mathcal{D}_g}{\mu}}_{\frac{1}{Sc}=1} \tag{6.32}$$

$$B = \frac{K_{f_e} - K_{f_w}}{K_{f_w} - 1} \tag{6.33}$$

generally referred to as the Spalding mass transfer number [32][33]. Solving the previous equation for K_{f_w} gives:

$$K_{f_w} = \frac{K_{f_e} + B}{1 + B} \tag{6.34}$$

The fuel mass fraction at the boundary layer edge can be assumed to be zero, thus $K_{f_e} = 0$. Under this condition, the fuel mass fraction at the wall in the case of non-reactive turbulent boundary layer can be still evaluated as a function of the blowing parameter with equation (6.3).

6.2.2 Determination of the Boundary Layer Thickness

In the non-reacting boundary layer, defined the velocity profile and the injected mass flow rate, it is not possible to fix both the fuel mass fraction at the wall K_{f_w} and the boundary layer thickness δ, otherwise mass continuity is not verified. Therefore, only one of those parameters can be fixed, i.e. K_{f_w} calculated with equation (6.3), while the boundary layer thickness becomes a dependent variable.

If $\dot{m}_{f,x} = \int_0^x \rho_f \dot{r}\, dx$ is the cumulative fuel mass flow rate injected through the holes of the plate at the position x, the boundary layer must have a thickness δ that verify that the inflow oxidizer mass flow rate, which is equal to the total mass flow rate inside the boundary layer minus the vaporized fuel mass flow from the surface, is also equal to the oxidizer mass flow rate inside the boundary layer determined by the corresponding mass fraction distribution. Therefore, must be verified the condition:

$$\dot{m}_{ox,bl} = \dot{m}_\delta - \dot{m}_{f,x} = \dot{m}_{\delta,ox,nr} \tag{6.35}$$

where $\dot{m}_\delta = \delta G_{ox} \int_0^1 \phi\, d\eta$, $\dot{m}_{\delta,ox,nr} = \delta G_{ox} \int_0^1 K_{ox,nr}\phi\, d\eta$ and $K_{ox,nr}$ is defined by equation (6.7) (in fact, K_{ox_e} value doesn't matter in a continuity equation). Because of the flow rates definitions, it is also guarantied the equivalence $\dot{m}_{\delta,f,nr} = \delta G_{ox} \int_0^1 K_{f,nr}\phi\, d\eta = \dot{m}_{f,x}$. The oxidizer flow rate within the boundary layer can be written as:

$$\dot{m}_{\delta,ox,nr} = \delta G_{ox} \int_0^1 \phi\, d\eta + \delta G_{ox} K_{f_w} \int_0^1 \phi(\phi - 1)\, d\eta \tag{6.36}$$

Substituting the expression (6.36) into equation (6.35) yields to:

$$\delta G_{ox} \int_0^1 \phi\, d\eta + \delta G_{ox} K_{f_w} \int_0^1 \phi(\phi - 1)\, d\eta = \delta G_{ox} \int_0^1 \phi\, d\eta - \int_0^x \rho_f \dot{r}\, dx \tag{6.37}$$

$$\delta G_{ox} K_{f_w} \int_0^1 \phi(\phi - 1)\, d\eta = -\int_0^x \rho_f \dot{r}\, dx \tag{6.38}$$

Finally, the following expression for the boundary layer thickness that verify mass continuity, given the fuel mass fraction K_{f_w} and the flow rate injected from the plate, is obtained:

$$\delta = \frac{-\int_0^x \rho_f \dot{r}\, dx}{G_{ox} K_{f_w} \int_0^1 \phi(\phi - 1)\, d\eta} \tag{6.39}$$

In the case of a closed duct, G_{ox} must be replaced with the local mass flux at the axis of the duct, i.e. $G_e = \rho_e u_e$.
For example, let's consider the regression rate equation (2.28), which can be rewritten as:

$$\dot{r} = \frac{0.03}{\rho_f}\left(\frac{C_f}{C_{f_0}}\right)\rho_e u_e Re_x^{-0.2} B = \frac{0.03}{\rho_f}\left(\frac{C_f}{C_{f_0}}\right) B G_{ox}^{0.8} \mu^{0.2} x^{-0.2} \tag{6.40}$$

Therefore:

$$\int_0^x \rho_f \dot{r}\, dx = 0.0375\left(\frac{C_f}{C_{f_0}}\right) B G_{ox}^{0.8} \mu^{0.2} x^{0.8} \tag{6.41}$$

Substituting equation (6.41) into equation (6.39) yields to:

$$\delta = \frac{-0.0375\left(\frac{C_f}{C_{f_0}}\right) G_{ox}^{-0.2} \mu^{0.2} B x^{0.8}}{K_{f_w} \int_0^1 \phi(\phi - 1)\, d\eta} \tag{6.42}$$

Fig.6.9 shows the boundary layer thickness calculated with equation (6.42) as a function of the dimensionless position along the grain port for different values of the blowing parameter B. The thickness of the boundary layer obtained according to Marxman's theory (with the same value of B) is also depicted for comparison. In order to verify continuity equation, the boundary layer thickness in the non-reacting case is greater than the value provided by Marxman's theory.

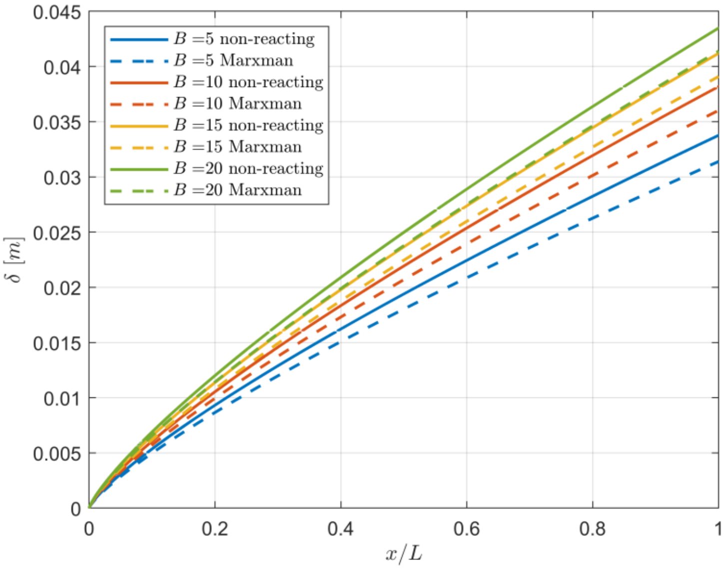

Figure 6.9: Boundary layer thickness δ as a function of the dimensionless position along the grain port for different values of the blowing parameter B. The thickness of the boundary layer obtained according to Marxman's theory (with the same value of B) is also depicted for comparison.

In the non-reactive boundary layer, the pyrolyzed fuel mass flow is represented by the mass injected from the plate holes, therefore the blowing parameter is the same in both cases. The local blowing parameter can be evaluated from its aerodynamical definition (2.26):

$$B(x) = \left[\frac{\rho_f \dot{r}(x)}{\rho_e u_e(x) \dfrac{C_{f_0}(x)}{2}} \right]^{\frac{1}{0.32}} \tag{6.43}$$

where it is assumed C_f/C_{f_0} evaluated with equation (2.31) (for typical blowing parameter values for hybrid rockets) and $\dot{r}$ is the regression rate expressed by Marxman equation (2.28) or by a generic formula (2.35).

6.2.3 Flame Position Estimation

As described in the previous paragraph, the oxidizer and fuel mass fraction distributions in a non-reacting boundary layer extend over the entire boundary layer thickness. According to diffusion flame combustion theory [33], the vaporized fuel diffuses (by convection and molecular diffusion) away from the plate, while the oxidizer diffuses towards it. The flame is defined to exist where the fuel and oxidizer meet in the correct O/F ratio (i.e. the stoichiometric one). Hence, the flame position in the reacting boundary layer can be estimated from the non-reacting case by evaluating the position where it is verified $\frac{K_{ox,nr}}{K_{f,nr}} = [O/F]_{react}$. In fact, the use of the Reynolds analogy $(Le = 1, Pr = 1)$ allows to relate the mass and heat transfers, therefore establishing an equivalence between the velocity, the enthalpy and the Shvab-Zeldovich scalar variable $(z = K_{f,nr} - K_{ox,nr}/[O/F]_{react})$ profiles [61]. The $[O/F]_{react}$ is computed by considering the combustion to be stoichiometric. Therefore, the Reynolds analogy can be written as:

$$\frac{u}{u_e} = \frac{h - h_w}{h_e - h_w} = \frac{z - z_w}{z_e - z_w} \tag{6.44}$$

From the previous equation, it is possible to retrieve the flame distance to the fuel surface by applying $z = 0$, which results in:

$$\frac{u_b}{u_e} = \phi_b = \frac{-z_w}{z_e - z_w} \tag{6.45}$$

K_{ox_e} is chosen to be equal to the unity, because, as already mentioned, if the oxidizer is diluted it is possible to still consider $K_{ox_e} = 1$ if the $[O/F]_{react}$ value is properly chosen. Therefore, substituting $K_{ox_w} = 1 - K_{f_w}$ and $K_{f_e} = 0$ in the expressions of the Shvab-Zeldovich scalar variable it can be easily demonstrated that the value of the dimensionless velocity ϕ_b in the reactive case corresponds to the value obtained with equation (6.10) in the non-reactive case.

In the reactive case, the number of components of the mixture inside the boundary layer increases to three: the oxidizer, the fuel and the combustion products. The oxidizer mass fraction has its maximum value K_{ox_e} at the boundary layer edge and goes to zero at the flame. The fuel concentration goes from K_{f_w} at the wall to zero at the flame. The products mass flow rate is equal to the reactants mass flow rate and diffuses towards both the surface and the boundary layer edge. Combustion products mass fraction is equal to unity at the flame, it is zero at the boundary layer edge and it is equal to $1 - K_{f_w}$ at the grain surface. Note that, although the fuel and oxidizer are consumed at the flame, the equivalence ratio (i.e. the ratio between the O/F ratio of reaction and the stoichiometric one) still has meanings here since the product composition relates to a unique value of equivalence ratio.
Equations (3.31) and (3.34) for the oxidizer and products mass fraction respectively above the flame are still valid. Equations (3.28) and (3.29) for the fuel and products concentrations below the flame must be corrected considering that $K_{f_w} < 1$. For the fuel mass fraction profile, the following system must be solved:

$$\begin{cases} K_f(\eta) = a\phi(\eta) + b \\ K_f(\eta = 0) = K_{f_w} \\ K_f(\eta = \eta_b) = 0 \end{cases} \tag{6.46}$$

Calculations give:

$$K_f(\eta = 0) = a\phi(0) + b = K_{f_w} \rightarrow b = K_{f_w} \tag{6.47}$$

$$K_f(\eta = \eta_b) = a\phi_b + b = 0 \rightarrow a = -\frac{K_{f_w}}{\phi_b} \tag{6.48}$$

Therefore:

$$K_f = K_{f_w}\left(1 - \frac{\phi}{\phi_b}\right) \qquad (0 \leq \eta \leq \eta_b) \tag{6.49}$$

Considering that below the flame must be $K_f + K_{pr} = 1$ yields to the following equation for the combustion products mass fraction profile:

$$K_{pr} = 1 - K_f = 1 - K_{f_w}\left(1 - \frac{\phi}{\phi_b}\right) \qquad (0 \leq \eta \leq \eta_b) \qquad (6.50)$$

Fig.6.10 shows an example of the species concentration profiles for both the non-reactive and reactive case. The flame dimensionless position in the reactive case corresponds to the position in the non-reactive boundary layer where the ratio between the oxidizer and fuel mass fractions is equal to the O/F ratio of reaction.

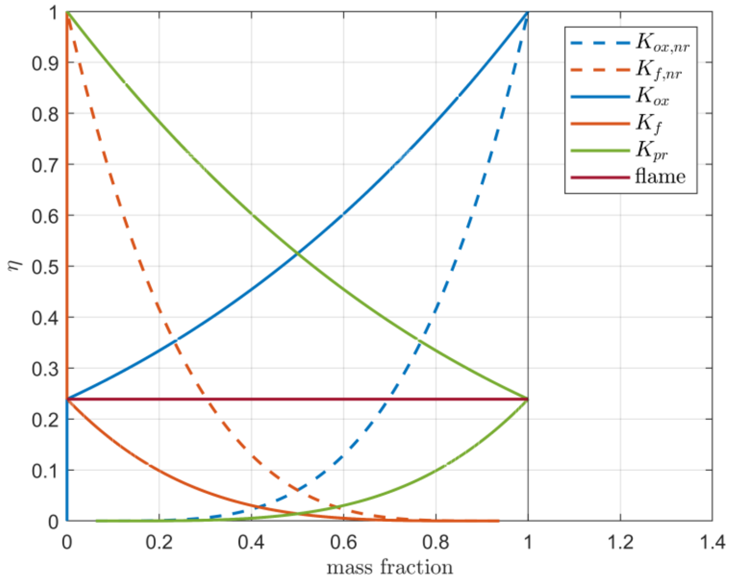

Figure 6.10: Concentration profiles as a function of dimensionless position η in the boundary layer for the non-reacting case (dotted lines) and for the reacting case (continous lines).

The boundary layer model that will be proposed is based on the verification of the flow rates conservation through the boundary layer, towards the flame and on the cross section of the duct. The evaluation of the flame position with the non-reactive case analogy previously described leads to an error if compared to its value obtained from mass conservation. This error is presumably related to the fact that the theory of diffusive flame combustion considers the position of the flame as the position in which the correct O/F ratio occurs starting from the resolution of the concentration profiles alone (i.e. considering only the diffusion), without taking into account the velocity profile of the species.

From simulations of the boundary layer, it can be seen that the error tends to be minimum as long as the boundary layer is developing, while after merging the error becomes important. To be consistent with the rest of the model, therefore it has been decided to use the value of the flame position such that the flame O/F ratio obtained from the mass conservation condition is equal to the stoichiometric one.

6.2.4 Determination of the Freestream Oxidizer Mass Fraction after Boundary Layer Merging

Let's consider the flow in a circular tube (Fig.6.11) where the fluid enters with a uniform velocity. When the fluid makes contact with the duct walls, the effects of viscosity become important, and a boundary layer develops with increasing x. The development of the boundary layer occurs at the expense of a shrinking of the inviscid flow region and concludes with boundary layer merger at the centreline. Beyond this position, the viscosity affects the entire cross section, and the velocity profile remains unchanged with increasing x. The flow is then said to be fully developed, and the distance from the entrance at which this condition is achieved is termed the hydrodynamic entry length, $x_{fd,h}$. In the case of laminar flow, the fully developed velocity profile is parabolic, while in the case of turbulent flow the velocity profile is flattened due to turbulent mixing in the radial direction. Although there is no satisfactory general expression, as a first approximation the hydrodynamic entry length in turbulent flow can be considered $10 \lesssim x_{fd,h} \lesssim 60$ [1][22].

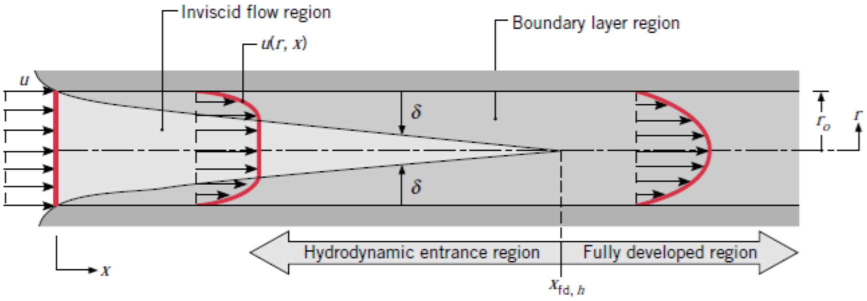

Figure 6.11: Hydrodynamic boundary layer development in a circular tube [1].

The same phenomenon occurs in the hybrid combustion turbulent boundary layer. However, since the mass injection from the grain surface tends to thicken the boundary layer, merging is expected to occur for values of x around the lower limit of $x_{fd,h}$. Moreover, the condition of fully developed flow is never achieved due to the continuous fuel flow injected from the grain wall which tends to accelerate the main flow.

In the boundary layer, the combustion products diffuse towards both the surface and the boundary layer edge. Prior to merging, the presence of oxidant outside the boundary layer ensures that its mass fraction at the boundary layer edge is always constant. After the merging, the combustion products diffuse towards the centre of the duct and the oxidizer diffuses towards the flame, causing the oxidizer mass fraction at the boundary layer edge to decrease. As a result, in order to achieve the correct O/F ratio of reaction, the flame moves towards the duct axis, reaching it when all the oxidizer flow above the flame is consumed. For the remaining part of the grain, the flow will be subject to a dilution because of the fuel pyrolysis due to the heat exchanged with the freestream where there is no combustion.
To evaluate the variation of the oxidizer mass fraction after the boundary layer merging, an analogy can be made once more with the non-reactive case. Because the boundary layer thickness is constant and equal to the radius of the duct (equal to half the height in the case of a rectangular duct), in the non-reactive case the increase of the fuel flow rate leads to a reduction in the oxidizer concentration in order to verify mass continuity. The same reduction happens in the reactive case, where the reduction of the oxidizer flow is due to its diffusion towards the flame where it is consumed. The condition to be verified is:

$$\dot{m}_{\delta,ox,nr} = \dot{m}_{\delta} - \dot{m}_{f,x} \tag{6.51}$$

where $\dot{m}_{\delta} = \delta G_e \int_0^1 \phi \, d\eta$, $\dot{m}_{\delta,ox,nr} = \delta G_e \int_0^1 K_{ox,nr} \phi \, d\eta$ and $\delta = R$ (or $h/2$ for a rectangular cross section duct). Here the oxidizer mass fraction profile has its maximum value $K_{ox_e} \leq 1$ (not because of dilution) at the duct axis and its minimum value $1 - K_{f_w}$ at the grain surface, therefore the following system of equations must be solved:

$$\begin{cases} K_{ox,nr}(\eta) = a\phi(\eta) + b \\ K_{ox,nr}(\eta = 0) = K_{ox_w} = 1 - K_{f_w} \\ K_{ox,nr}(\eta = 1) = K_{ox_e} \end{cases} \tag{6.52}$$

Calculations give:

$$K_{ox,nr}(\eta = 0) = a\phi(\eta = 0) + b = 1 - K_{f_w} \rightarrow b = 1 - K_{f_w} \tag{6.53}$$

$$K_{ox,nr}(\eta = 1) = a\phi(\eta = 1) + b = K_{ox_e} \rightarrow a = K_{ox_e} - \left(1 - K_{f_w}\right) \tag{6.54}$$

Therefore:

$$K_{ox,nr} = \left[K_{ox_e} - \left(1 - K_{f_w}\right)\right]\phi + \left(1 - K_{f_w}\right) \tag{6.55}$$

Because of the flow rates definitions, it is also guarantied the equivalence $\dot{m}_{\delta,f,nr} = \delta G_e \int_0^1 K_{f,nr}\phi \, d\eta = \dot{m}_{f,x}$, where:

$$K_{f,nr} = 1 - K_{ox,nr} = K_{f_w} - \left[K_{ox_e} - \left(1 - K_{f_w}\right)\right]\phi \tag{6.56}$$

The oxidizer flow rate within the boundary layer can be written as:

$$\dot{m}_{\delta,ox,nr} = \delta G_e K_{ox_e} \int_0^1 \phi^2 \, d\eta + \delta G_e\left(1 - K_{f_w}\right) \int_0^1 (1 - \phi)\phi \, d\eta \tag{6.57}$$

Substituting the expression (6.57) into equation (6.51) yields to:

$$\begin{aligned} \delta G_e K_{ox_e} \int_0^1 \phi^2 \, d\eta + \delta G_e\left(1 - K_{f_w}\right) \int_0^1 (1 - \phi)\phi \, d\eta \\ = \delta G_e \int_0^1 \phi \, d\eta - \int_0^x \rho_f \dot{r} \, dx \end{aligned} \tag{6.58}$$

Finally, the following expression for the oxidizer mass fraction at the boundary layer edge is obtained:

$$K_{ox_e} = \frac{\int_0^1 \phi \, d\eta - \frac{1}{\delta G_e}\int_0^x \rho_f \dot{r} \, dx - \left(1 - K_{f_w}\right)\int_0^1 (1 - \phi)\phi \, d\eta}{\int_0^1 \phi^2 \, d\eta} \tag{6.59}$$

The position $x_{m,f}$ where the flame reaches the duct axis is expected to be the one for which the $[O/F]_{react}$ ratio is achieved at the edge of the boundary layer (i.e. $\phi_{nr} = 1$) in the non-reactive case:

$$[O/F]_{react} = \left.\frac{K_{ox,nr}}{K_{f,nr}}\right|_{\phi_{nr}=1} = \left.\frac{\left[K_{ox_e} - \left(1 - K_{f_w}\right)\right]\phi + \left(1 - K_{f_w}\right)}{K_{f_w} - \left[K_{ox_e} - \left(1 - K_{f_w}\right)\right]\phi}\right|_{\phi_{nr}=1} \tag{6.60}$$

which corresponds to a value of oxidizer mass fraction at the duct axis equal to:

$$\left.K_{ox_e}\right|_{\phi_{nr}=1} = \frac{[O/F]_{react}}{[O/F]_{react} + 1} \tag{6.61}$$

For what was said before about the error on the flame position in the analogy between the non-reactive case and the reactive case, the actual value of $\left.K_{ox_e}\right|_{\phi_b=1}$ will be slightly different from the one calculated with equation (6.61).

6.3 Numerical Modelling of Hybrid Combustion Incompressible Boundary Layer

In the following, a numerical model of hybrid combustion boundary layer is presented. Three configurations will be analysed: the flat plate in an open environment, the rectangular duct with two slabs and the cylindrical duct. Several hypotheses are applied to reduce the complexity of the physics of the problem and are meant to be applied to classical combinations of propellants for hybrid rocket engines:

- The injection of oxidizer is considered to be axial, uniform, completely gaseous and generating a turbulent flow regime. The dependent variables are all interpreted as mean values and no turbulent fluctuations are considered.

- Dimensionless numbers Pr and Le are taken equal to unity.

- To describe the combustion process inside the boundary layer an infinitely fast chemistry (equilibrium) assumption is made, therefore the thickness of the reactive zone is assumed to be infinitely thin, and the flame is considered to take place at stoichiometric conditions.

- The combustion phenomenon is assumed to not alter the velocity profile, which can be described with equation (3.9), where $n = 1/7$ for flat grain surface and $n = 1/9$ for a tube. The validity of Reynolds analogy and the assumption that $Pr = Le = 1$, allow to describe the concentration and temperature as linear to the velocity profile.

- The flow is assumed to be incompressible with a density value equal to that of the flow outside the boundary layer.

- Pressure gradient in the axial direction is assumed to be zero.

In the following simulations the classic combinations of $HTPB$ (Hydroxyl-terminated polybutadiene) and GOX (gaseous O_2) is used. The corresponding stoichiometric combustion reaction is:

$$2C_4H_6 + 11O_2 \rightarrow 8CO_2 + 6H_2O \tag{6.62}$$

The molar and mass stoichiometric ratio are $[O/F]_{st,molar} = 5.5$ and $[O/F]_{st,mass} = 3.26$ respectively. The O/F ratio at the flame is evaluated as the ratio between the oxidizer and fuel mass flow that reach the flame and it is assumed to be equal to the stoichiometric one, i.e. $[O/F]_{react} = [O/F]_{st,mass} = 3.26$. The value of the thermochemical parameter $\Delta h/h_v$ for this pair of propellants is 13.96 [10].

6.3.1 Hybrid Boundary Layer over a Flat Plate

A schematic of the flow above a flat plate in an open environment model is depicted in Fig.6.12. Because of the open environment configuration only the developing region exists. The flow is divided into two zones along the y – direction. The first one corresponds to the inviscid core flow region, where the thermodynamic and mechanical variables characterizing the flow (velocity, temperature) are considered to remain constant both in y – direction and axial position. The second zone corresponds to the boundary layer, whose characteristic thickness δ is defined as the distance normal to the wall where the velocity of the flow has reached its streamwise value, u_e. The corresponding control volumes of the two regions for an element of size dx are represented in the figure. The two control volumes are coupled through the boundary conditions at the boundary layer edge.

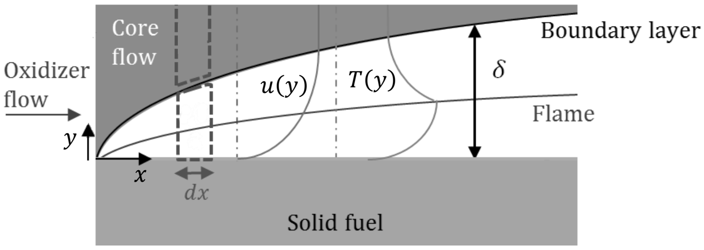

Figure 6.12: Schematic of the flow above a flat plate in an open environment model. Adapted from [61].

The species mass fraction distribution over the boundary layer thickness is evaluated with equations (3.31), (3.34), (6.49) and (6.50). The temperature profile above the flame is calculated with equation (3.41), while that below the flame must be corrected to consider that $K_{f_w} < 1$. The boundary condition for the temperature profile at the wall can be evaluated as the average temperature weighted on the individual chemical species concentrations:

$$T_w(x) = T_b K_{pr_w}(x) + T_b K_{f_w}(x) \tag{6.63}$$

where the local fuel mass fraction at the wall is evaluated with equation (6.3). At the wall, $K_{pr_w}(x) = 1 - K_{f_w}(x)$, therefore:

$$T_w(x) = T_b + K_{f_w}(x)\left(T_f - T_b\right) = T_f + K_{pr}(x)\left(T_b - T_f\right) \tag{6.64}$$

with T_f the fuel temperature at the wall.

The boundary layer thickness is evaluated using the analogy with the non-reactive case with equation (6.39). Since the characteristics of the flow outside the boundary layer do not change, the only degree of freedom of the problem is the position of the flame $y_b(x)$. The condition that must be satisfied is:

$$[O/F]_{flame}(x) = \frac{\dot{m}_{ox,flame}(x)}{\dot{m}_{f,flame}(x)} = \frac{\dot{m}_{\delta}(x) - \dot{m}_{f,x}(x) - \dot{m}_{\delta,ox}(x)}{\dot{m}_{f,x}(x) - \dot{m}_{\delta,f}(x)} = [O/F]_{react} \quad (6.65)$$

therefore:

$$[O/F]_{react} = \frac{\delta(x) G_{ox} \int_0^1 \phi(x,\eta)\, d\eta - \int_0^x \rho_f \dot{r}(x)\, dx - \delta(x) G_{ox} \int_0^1 K_{ox}(x,\eta)\phi(x,\eta)\, d\eta}{\int_0^x \rho_f \dot{r}(x)\, dx - \delta(x) G_{ox} \int_0^1 K_f(x,\eta)\phi(x,\eta)\, d\eta} \quad (6.66)$$

where the regression rate is evaluated with Marxman's equation (2.28) and the blowing parameter is calculated combining equations (2.27) and (3.16). Fig.6.13 to 6.15 show the results of the numerical simulation. As expected, the flame dimensionless position and velocity are in good agreement with what Marxman predicted and with the non-reactive case. The main difference is in the boundary layer thickness, which is slightly larger than that predicted by Marxman.

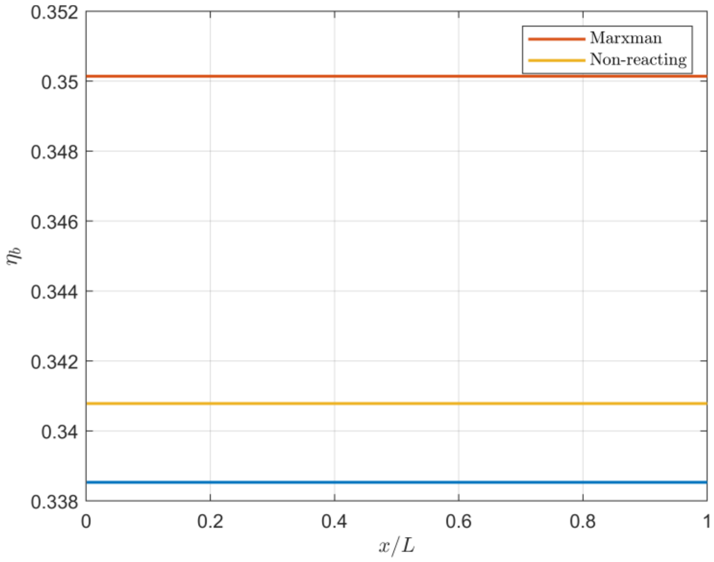

Figure 6.13: Dimensionless flame position η_b as a function of dimensionless position along the grain.

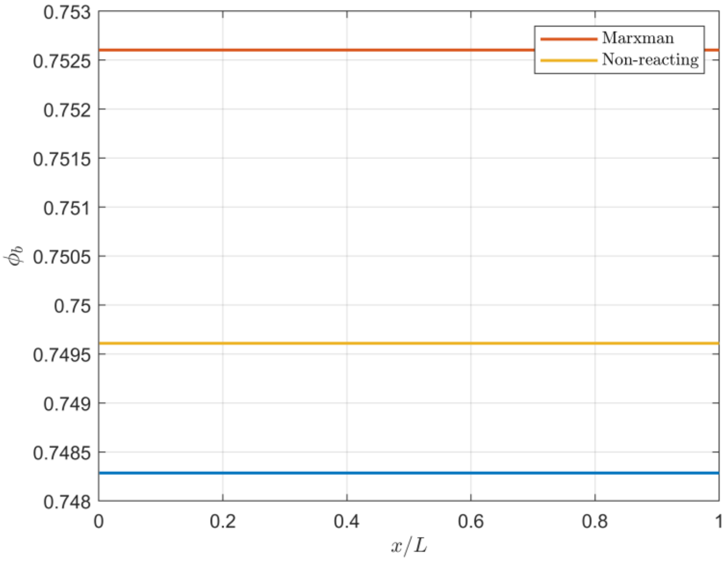

Figure 6.14: Dimensionless flame velocity ϕ_b as a function of dimensionless position along the grain.

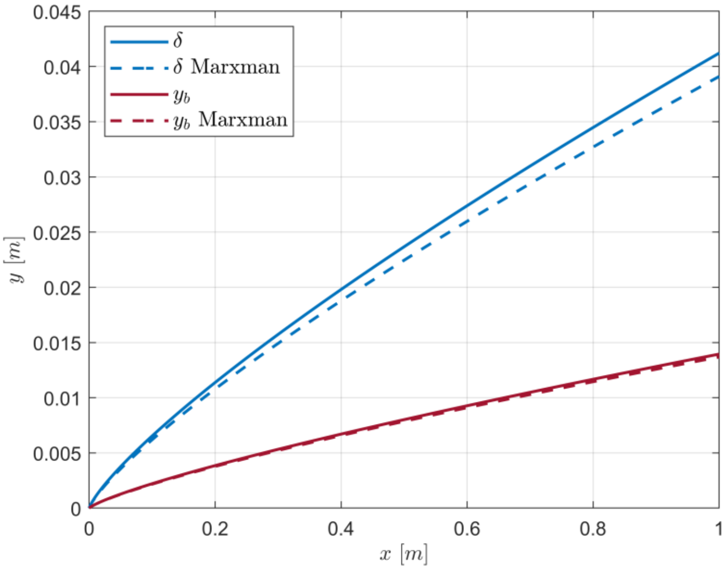

Figure 6.15: Boundary layer thickness δ and flame position y_b as a function of the position x along the grain. The corresponding values derived by Marxman's theory are also depicted for comparison.

6.3.2 Hybrid Boundary Layer in a Rectangular Port Duct

A schematic of the flow in a rectangular port duct model is depicted in Fig.6.16. The channel has a rectangular section $w \times h$, with two active walls (i.e. where there is the propellant grain) facing each other; the other two walls are assumed to be inert and to not disturb the flow in any way (i.e. no viscous effects). The boundary layer can follow two different configurations: a developing flow configuration, where the boundary layer is growing inside the channel, and a fully developed flow one, where it occupies the entire cross section of the channel. In the entrance region, the flow is divided into two zones along the y – direction. The first one corresponds to the inviscid core flow region, while the second one corresponds to the boundary layer, similarly to the previous case. The two control volumes are coupled through the boundary conditions at the boundary layer edge. In the fully developed flow configuration, no core flow is present and only one control volume over the y – direction is defined for an infinitesimal element.

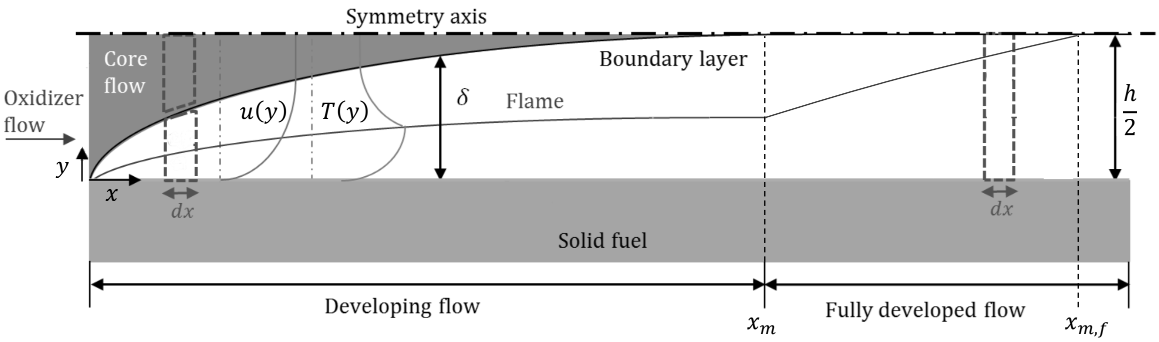

Figure 6.16: Schematic of the flow in a rectangular port duct model. Adapted from [61].

Marxman's equation (2.28) is no longer valid due to the close duct. Therefore, the regression rate is calculated with the generic expression (2.35), where the regression rate coefficients are evaluated from literature [4][29]. Here the blowing parameter must be evaluated from its aerodynamic definition with equation (6.43).

To numerically solve the hybrid boundary layer model, it is useful to distinguish the conditions to verify between before and after the boundary layer merging.

Before the merging, the boundary layer is developing, thus the boundary layer thickness can be evaluated by the non-reactive analogy with equation (6.39), which in this case is written as:

$$\delta(x) = \frac{-\int_0^x \rho_f \dot{r}(x)\, dx}{G_e(x) K_{f_w}(x) \int_0^1 \phi(x,\eta)(\phi(x,\eta) - 1)\, d\eta} \tag{6.67}$$

The mass flux at the axis $G_e(x)$ and the flame position $y_b(x)$ are therefore the two degrees of freedom of the problem, thus two conditions are necessary. The first condition consists in verifying the oxidizer to fuel ratio at the flame, which must be equal to the reaction one (i.e. stoichiometric). Mathematically this condition is written as:

$$[O/F]_{flame}(x) = \frac{\dot{m}_{ox,flame}(x)}{\dot{m}_{f,flame}(x)} = \frac{\dot{m}_\delta(x) - \dot{m}_{f,x}(x) - \dot{m}_{\delta,ox}(x)}{\dot{m}_{f,x}(x) - \dot{m}_{\delta,f}(x)} = [O/F]_{react} \tag{6.68}$$

therefore:

$$[O/F]_{react} = \frac{\delta(x) G_e(x) \int_0^1 \phi(x,\eta)\, d\eta - \int_0^x \rho_f \dot{r}(x)\, dx - \delta(x) G_e(x) \int_0^1 K_{ox}(x,\eta)\phi(x,\eta)\, d\eta}{\int_0^x \rho_f \dot{r}(x)\, dx - \delta(x) G_e(x) \int_0^1 K_f(x,\eta)\phi(x,\eta)\, d\eta} \tag{6.69}$$

The second condition requires the mass continuity to be verified:

$$\begin{aligned} G(x) &= \frac{2\dot{m}_\delta(x) \cdot w + G_e(x) \cdot w\big(h - 2\delta(x)\big)}{h \cdot w} \\ &= \frac{2\delta(x) G_e(x) \int_0^1 \phi(x,\eta)\, d\eta + G_e(x) \cdot \big(h - 2\delta(x)\big)}{h} \end{aligned} \tag{6.70}$$

Iteratively solving the two conditions allows to solve the internal ballistic in the sections preceding the merging one.

When the boundary layer thickness is equal to half the height of the duct, i.e. $\delta(x = x_m) = h/2$, the merging of the boundary layer occurs, and the boundary layer fills the entire cross section. After the merging, the combustion products diffuse towards the centre of the duct and the oxidizer diffuses towards the flame, causing the oxidizer mass fraction at the boundary layer edge to decrease. The variation of K_{ox_e} can be evaluated with equation (6.59), which in this case is written as:

$$K_{ox_e}(x) = \frac{\int_0^1 \phi(x,\eta)\, d\eta - \frac{2}{hG_e(x)} \int_0^x \rho_f \dot{r}(x)\, dx - \left(1 - K_{f_w}(x)\right) \int_0^1 (1-\phi(x,\eta))\phi(x,\eta)\, d\eta}{\int_0^1 \phi(x,\eta)^2\, d\eta} \tag{6.71}$$

The wall temperature can still be calculated with equation (6.64). After the merging the temperature at the duct axis increase due to the diffusion of the combustion products and can be calculated as the average temperature weighted on the individual chemical species concentrations. If K_{ox_e} is the oxidizer mass fraction at the axis, then the products mass fraction here is equal to $1 - K_{ox_e}$. If T_{ox} is the temperature of the oxidizer, the temperature at the duct axis T_e is:

$$T_e(x) = T_b K_{pr_e}(x) + T_{ox} K_{ox_e}(x) \tag{6.72}$$

that can be rewritten as:

$$T_e(x) = T_b + (T_{ox} - T_b) K_{ox_e}(x) = T_{ox} + (T_b - T_{ox}) K_{pr_e}(x) \tag{6.73}$$

The boundary layer thickness is constant and equal to $h/2$, therefore $G_e(x)$ and the flame position $y_b(x)$ are still the two degrees of freedom of the problem. The first condition consists in verifying the oxidizer to fuel ratio at the flame with equation (6.69). The second condition requires the mass continuity to be verified with equation (6.70) that can be rewritten as:

$$G(x) = G_e(x) \int_0^1 \phi(x,\eta)\, d\eta \tag{6.74}$$

Solving equations (6.69) and (6.74) allows to solve the internal ballistic in the sections following the merging section to the position where the flame reaches the duct axis. In this position, as already mentioned, it is expected to have $K_{ox_e}\big|_{\phi_b=1}$ similar to the value that can be estimated with equation (6.61). When the flame reaches the duct axis, all the oxidizer mass flow in consumed in the combustion process. Therefore, from this point onwards, only the continuity condition must be satisfied through equation (6.74).

6.3.2.1 Numerical Results

In the following, the results of a numerical simulation will be reported. The duct has a rectangular section of dimensions $w \times h = 0.1 \times 0.1\ m$ and an oxidizer mass flux $G_{ox} = 100\ kg/(m^2 s)$ is used. Fig.6.17 shows that the mass fluxes steadily increase prior to the merging section due to the thickening of the boundary layer enhanced by the fuel pyrolysis. At the merging section (i.e. $x = x_m$) the total oxidizer mass flow that enters in the boundary layer by diffusion from the freestream is equal to the oxidizer mass flow injected in the duct (i.e. $\dot{m}_{ox,bl} = \dot{m}_{ox}/2w$). For $x > x_m$ the fuel mass flow rate in the boundary layer $\dot{m}_{\delta,f}$ increases more than for $x < x_m$ mainly due to the rise of the flame from the surface, while the oxidizer mass flow progressively reaches the flame and thus reducing with x. For $x = x_{m,f}$ the flame reaches the centre of the channel, the oxidizer flow rate inside the boundary layer is completely burned and the further vaporized fuel accumulates in the main stream without producing any combustion process.

Fig.6.18 show the dimensionless position and velocity of the flame as a function of the dimensionless position x/h. The corresponding quantities according to Marxman's theory and to the non-reactive case are also represented for comparison. As expected, the merging of the boundary layer takes place for values of $x_m/h \sim 10$. The flame position before merging has almost the same value as that expected by Marxman's theory or by the analogy with the non-reactive case, while for $x > x_m$ the difference becomes significant. After merging, the flame will tend to rise to verify the correct O/F ratio at the reaction zone. As mentioned above, the use of the analogy with the non-reactive case for the estimation of the flame position leads to an error that results in failing to verify the correct O/F ratio at the flame (Fig.6.19).

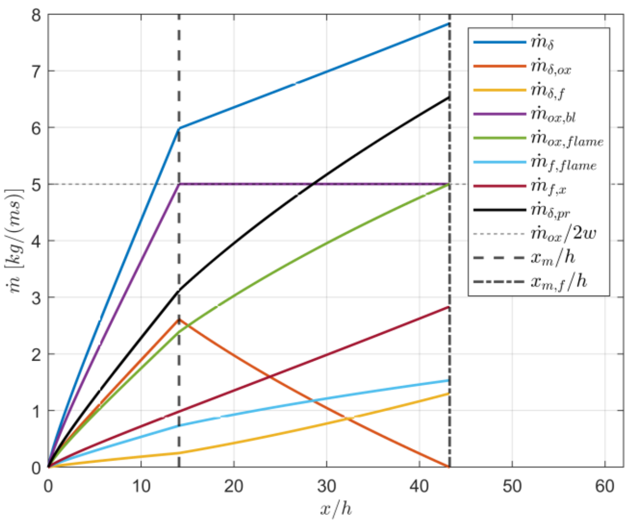

Figure 6.17: Mass flow rates as a function of the dimensionless position x/h.

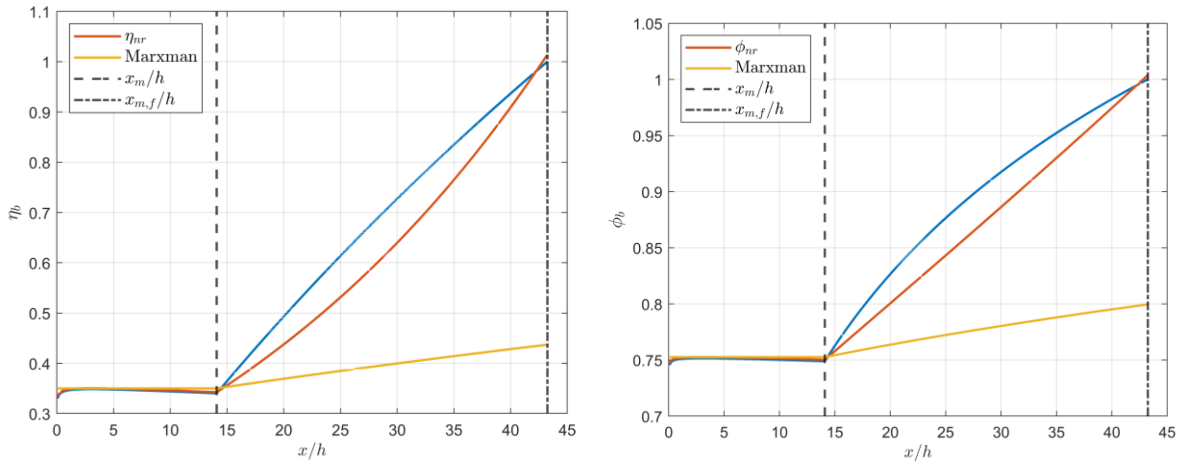

Figure 6.18: Dimensionless flame position η_b and velocity ϕ_b as a function of the dimensionless position x/h.

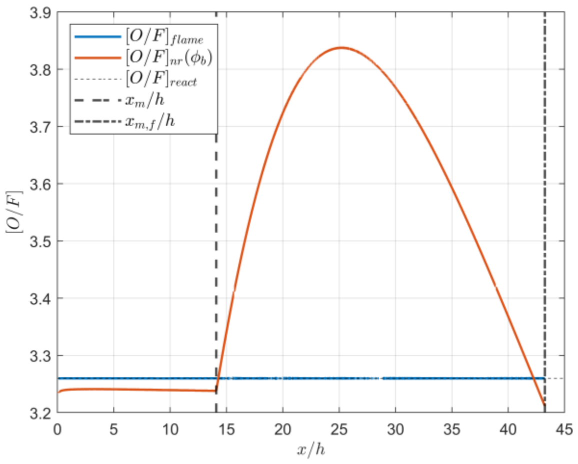

Figure 6.19: Comparison between $[O/F]_{flame}$ and its corresponding value calculated with the non-reactive case analogy for the same flame velocity as a function of the dimensionless position x/h.

As expected, the regression rate shows the typical trend for hybrid combustion in a closed duct (Fig.6.20). Initially, it decreases due to the thickening of the boundary layer. This reduction is countered by the progressive accumulation of flow that enhanced the heat exchange by convection. Once a minimum condition is reached, the regression rate tends to increase as the flux effect prevails. Fig.6.21 shows the blowing parameter B evaluated with its aerodynamic definition (6.43). B is a non-linear function of the regression rate, the skin-friction coefficient C_{f_0} and the specific flow at the duct axis (Fig.6.22); therefore, the blowing parameter will not be constant, but its value does not differ much from what Marxman's theory predicts. The reduction of B according to Marxman's theory is due to the flame approaching the duct axis because of the reduction of $K_{ox_e}(x)$.

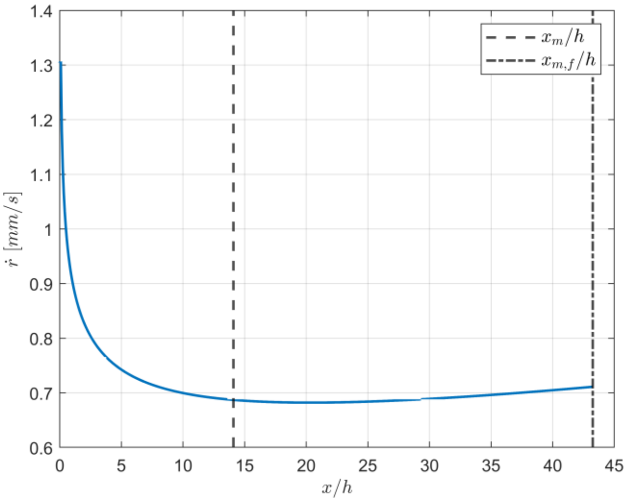

Figure 6.20: Regression rate $\dot{r}$ as a function of the dimensionless position x/h.

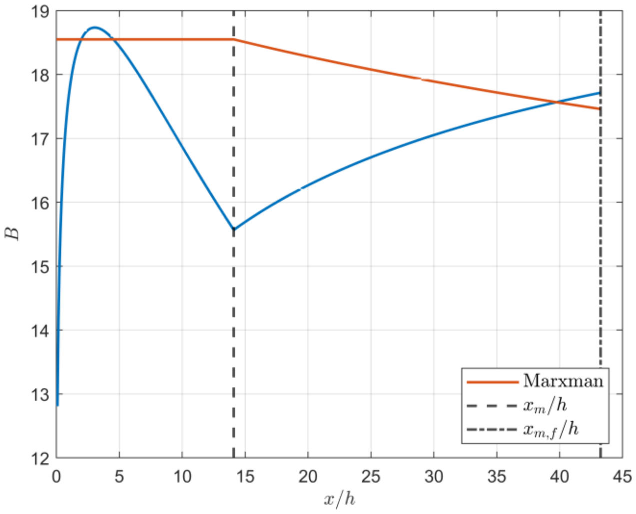

Figure 6.21: Blowing parameter B as a function of the dimensionless position x/h. The value of B according to Marxman’s theory is also depicted for comparison.

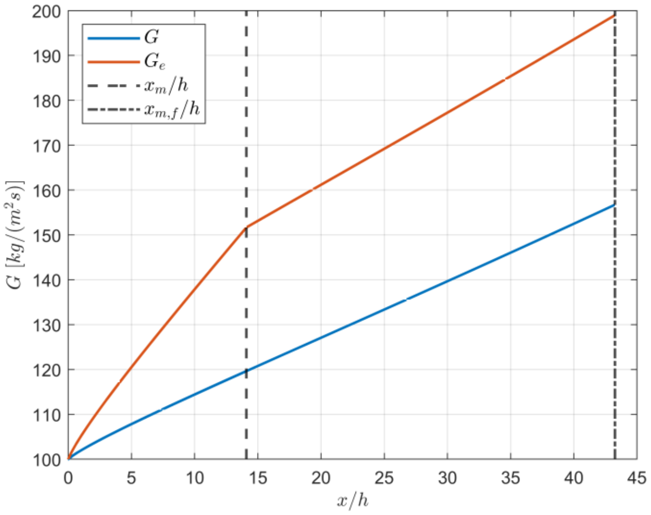

Figure 6.22: Average mass flux, G, and mass flux at the duct axis, G_e, as a function of the dimensionless position x/h.

Fig.6.23 shows the comparison between the presented model and Marxman's theory for the boundary layer thickness, δ, and flame position, y_b, as a function of the dimensionless position x/h. Because of the flat wall of the duct, a slight deviation from the values predicted by Marxman's theory due to the acceleration of the main flow is expected and confirmed.

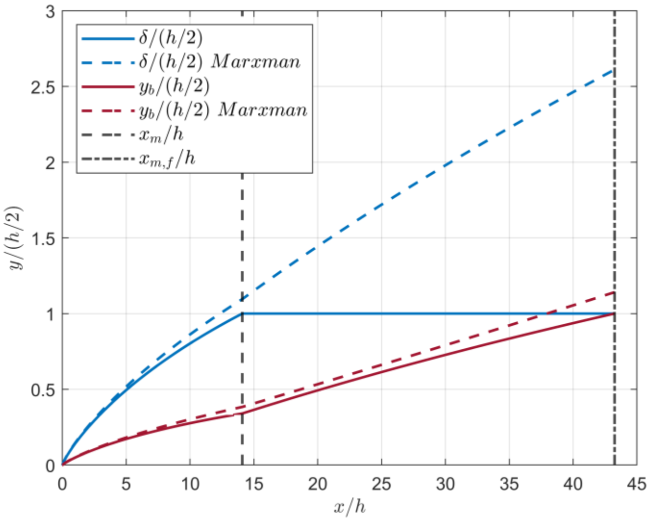

Figure 6.23: Dimensionless boundary layer thickness, δ, and flame position, y_b, as a function of the dimensionless position x/h. The corresponding values according to Marxman's theory are also depicted for comparison.

Fig.6.24 shows distribution of the fuel mass fraction at the grain surface, K_{f_w}, and the oxidizer mass fraction at the duct axis, K_{ox_e}. The value for K_{f_w} is determined with equation (6.3), therefore has the same trend of the blowing parameter. The value of K_{ox_e} remains constant before merging and then tends to decrease. It is interesting to observe that the value of K_{ox_e} when the flame reaches the middle of the duct is slightly different from what is predicted by the analogy with the non-reactive case, as previously mentioned.

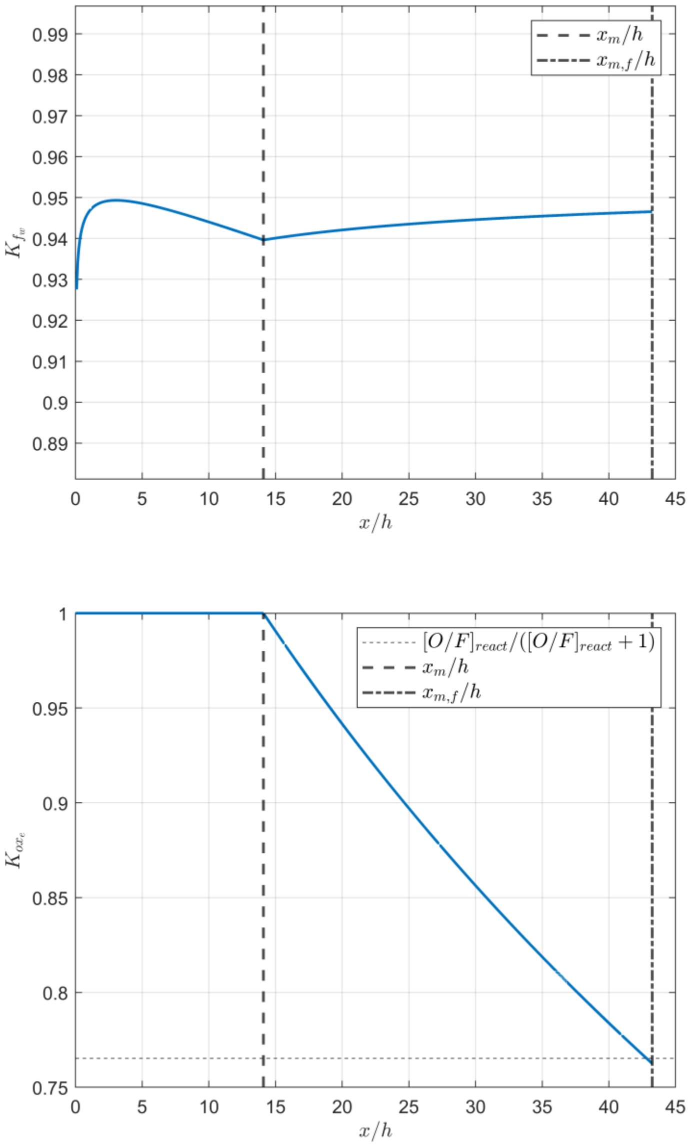

Figure 6.24: Fuel mass fraction at the grain surface, K_{f_w} (top), and the oxidizer mass fraction at the duct axis, K_{ox_e} (bottom) as a function of the dimensionless position x/h.

Fig.6.25 shows the distribution of the O/F ratio at the position x, $[O/F]_x = \dot{m}_{ox}/\dot{m}_f(x)$, and the $[O/F]_{bl}$ (3.98), confirming the typical characteristic of hybrid engines. As the total fuel mass flow rate increases along the grain port, the global O/F ratio decreases reaching and keeping a value equal to $[O/F]_{bl}$ at the boundary layer merging and beyond, because of the equivalence of $\dot{m}_{ox}$ and $\dot{m}_{ox,bl}$. The boundary layer merging condition occurs for a value of $[O/F]_x$ greater than the reaction one, while the condition of the flame at the centre of the duct corresponds to a value of $[O/F]_x$ lower than the reaction one. Typically, the $[O/F]_x$ value used in the grain design (i.e. $[O/F]_{glob}$) is close to the stoichiometric one in order to maximize c^*. Therefore, the amount of fuel required to consume all the injected oxidizer is greater than the quantity that is strictly necessary to obtain $[O/F]_{glob}$. As a result, the flow will be strongly stratified, with a fraction of unburned oxidizer in the centre of the duct.

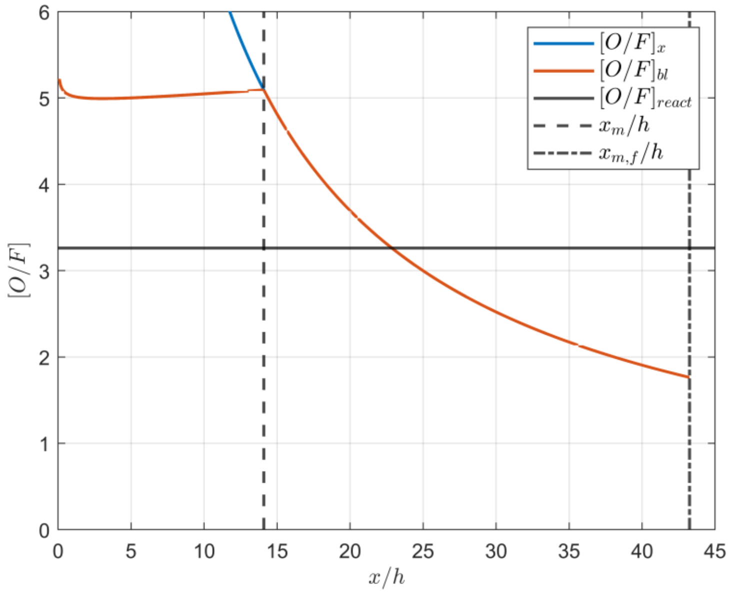

Figure 6.25: $[O/F]_x$ and the $[O/F]_{bl}$ as a function of the dimensionless position x/h.

The above considerations translate into different values of propellant combustion efficiencies at different positions. Fig.6.26 shows the trend of fuel combustion efficiency (3.99) and of oxidizer combustion efficiency, the latter defined both as a function of the oxidizer flow rate entering the boundary layer (3.100) and as a function of the flow rate injected at the head of the grain (namely, $\eta_{comb,ox,tot}$). The relationship described above between $[O/F]_x$ and $[O/F]_{react}$ depending on the position x explains why the condition of $\eta_{comb,ox,tot}$ equal to 1 (i.e. when the flame reaches the axis of the duct and all oxidizer is consumed) can only be obtained at the expense of a reduction of $\eta_{comb,f}$, i.e. by using a greater amount of fuel than the quantity that is strictly necessary to obtain $[O/F]_{react}$.

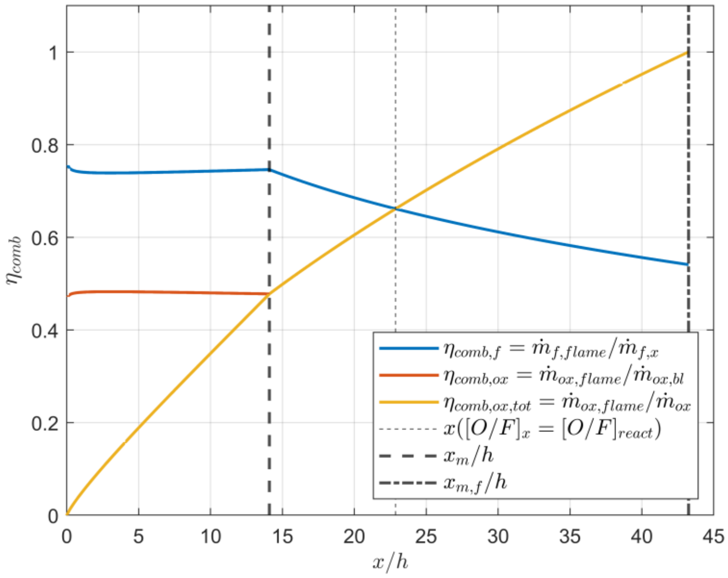

Figure 6.26: Fuel and oxidizer combustion efficiencies as a function of the dimensionless position x/h.

The parametric study of the hybrid boundary layer will be treated in the case of cylindrical channel, which is the common grain configuration used in hybrid propulsion. In any case, similar considerations can also be made for the presented model of rectangular duct with two grain slabs.

6.3.3 Hybrid Boundary Layer in a Circular Port Duct

A schematic of the flow in a circular port duct model is depicted in Fig.6.27. Once more, the boundary layer can follow two different configurations: a developing flow configuration, where the boundary layer is growing inside the channel, and a fully developed flow one, where it occupies the entire cross section of the channel. In the entrance region, the flow is divided into two zones along the radial direction. The first one corresponds to the inviscid core flow region, while the second one corresponds to the boundary layer. The two control volumes are coupled through the boundary conditions at the boundary layer edge. In the fully developed flow configuration, no core flow is present and only one control volume over the radial direction is defined for an infinitesimal element dx.

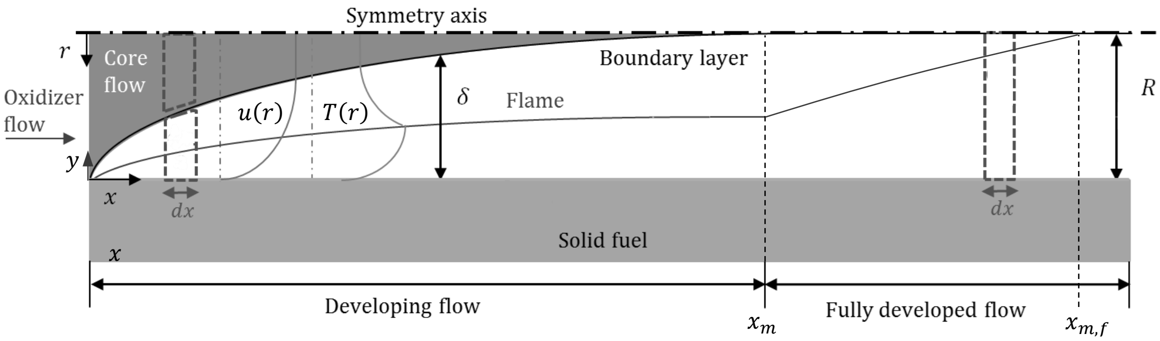

Figure 6.27: Schematic of the flow in a circular port duct model. Adapted from [61].

6.3.3.1 Velocity and Mass Fraction Profiles

The axisymmetric geometry of the cylindrical configuration allows the definition of velocity and concentration profiles as a function of radial r and axial x coordinates only, regardless of azimuth coordinate θ. The dimensionless velocity profile is still defined by the expression (3.9) as a function of the dimensionless coordinate $\eta = \frac{y}{\delta} \in [0,1]$ evaluated from the grain surface. For a tube it is $n = 1/9$ [10], therefore the velocity profile in a tube is "fatter" than that for a flat plate with $n = 1/7$ (Fig.6.28).

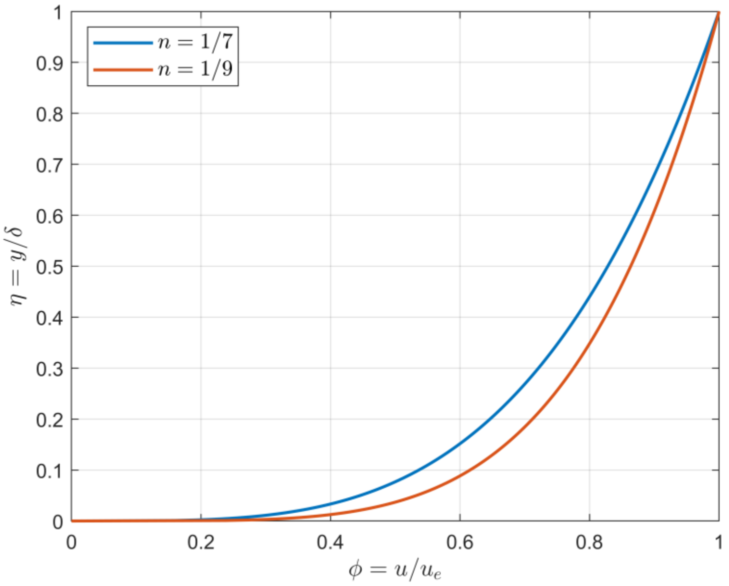

Figure 6.28: Comparison of the dimensionless velocity profiles for a tube ($n = 1/9$) and for a flat plate ($n = 1/7$) for the same value of the blowing parameter B.

To write the dimensionless velocity profile as a function of r, the following change of variable can be assumed between the cartesian coordinate y and the radial coordinate r: $r = R - y$, thus $y = R - r$. Therefore, the radial coordinate of the boundary layer edge is $r_\delta = R - \delta$, while that of the flame is $r_b = R - y_b$. The dimensionless velocity profile in radial coordinates is:

$$\phi(r) = \frac{\left(\frac{R-r}{\delta}\right)^n \left[1 + 0.5B\left(\frac{R-r}{\delta}\right)^n\right]}{1 + 0.5B} \qquad (r_\delta \le r \le R) \tag{6.75}$$

Therefore, $\phi(r_\delta) = 1, \phi(r_b) = \phi_b$ and $\phi(R) = 0$.

The concentration profiles in the reactive case can be described as linear function of the velocity profile with the same expressions obtained for the flat plate case, here as a function of the radial coordinate:

$$K_{ox}(r) = \begin{cases} 1 & (0 \le r \le r_\delta) \\ K_{ox_e} \dfrac{\phi(r) - \phi_b}{1 - \phi_b} & (r_\delta \le r \le r_b) \\ 0 & (r_b \le r \le R) \end{cases} \tag{6.76}$$

$$K_f(r) = \begin{cases} 0 & (0 \leq r \leq r_\delta) \\ 0 & (r_\delta \leq r \leq r_b) \\ K_{f_w}\left(1 - \dfrac{\phi(r)}{\phi_b}\right) & (r_b \leq r \leq R) \end{cases} \tag{6.77}$$

$$K_{pr}(r) = \begin{cases} 0 & (0 \leq r \leq r_\delta) \\ 1 - K_{ox}(r) & (r_\delta \leq r \leq r_b) \\ 1 - K_f(r) & (r_b \leq r \leq R) \end{cases} \tag{6.78}$$

In the analogy between the reactive and non-reactive cases, the velocity profile is assumed to be unchanged. The concentration profiles are the same as those of the rectangular duct, but defined as a function of the radial coordinate r:

$$K_{ox,nr}(r) = \begin{cases} 1 & (0 \leq r \leq r_\delta) \\ \left[K_{ox_e} - \left(1 - K_{f_w}\right)\right]\phi(r) + \left(1 - K_{f_w}\right) & (r_\delta \leq r \leq R) \end{cases} \tag{6.79}$$

$$K_{f,nr}(r) = 1 - K_{ox,nr}(r) = \begin{cases} 1 & (0 \leq r \leq r_\delta) \\ K_{f_w} - \left[K_{ox_e} - \left(1 - K_{f_w}\right)\right]\phi(r) & (r_\delta \leq r \leq R) \end{cases} \tag{6.80}$$

6.3.3.2 Determination of the Mass Flow Rates

In a circular port duct, mass flow rates are expressed as the integral of the mass flux (ρu) over the cross section. In the hypothesis that the density is constant and equal to ρ_e, each of the mass flow rates in the boundary layer is evaluated as:

$$\dot{m}_i = \rho_e \int K_i(r) u(r)\, dA = \rho_e \int K_i(r) u(r)\, 2\pi r\, dr \tag{6.81}$$

Therefore:

$$\dot{m}_\delta = 2\pi G_e \int_{r_\delta = R-\delta}^{R} \phi(r) r\, dr \tag{6.82}$$

$$\dot{m}_{\delta,ox} = 2\pi G_e \int_{r_\delta=R-\delta}^{r_b=R-y_b} K_{ox}(r)\phi(r)r\, dr \tag{6.83}$$

$$\dot{m}_{\delta,f} = 2\pi G_e \int_{r_b=R-y_b}^{R} K_f(r)\phi(r)r\, dr \tag{6.84}$$

$$\dot{m}_{\delta,pr} = 2\pi G_e \int_{r_{\delta=R-\delta}}^{R} K_{pr}(r)\phi(r)r\, dr \tag{6.85}$$

The total fuel mass flow rate pyrolyzed from the grain and the inflow oxidizer mass flow rate from the freestream outside the boundary layer are respectively:

$$\dot{m}_f = 2\pi R \cdot \dot{m}_{f,x} = 2\pi R \int_0^x \rho_f \dot{r}\, dx \tag{6.86}$$

$$\dot{m}_{ox,bl} = \dot{m}_\delta - \dot{m}_f \tag{6.87}$$

Applying mass conservation equations allows to evaluate the fuel and oxidizer mass flow rates that reach the flame and thus to determine the O/F ratio at the flame.

6.3.3.3 Numerical Resolution

Marxman's equation (2.28) is no longer valid due to the close duct. Therefore, the regression rate is calculated with the generic expression (2.35), where the regression rate coefficients are evaluated from literature [4][29]. Here the blowing parameter must be evaluated from its aerodynamic definition with equation (6.43). The skin friction coefficient C_{f_0} can be evaluated for a cylindrical duct from literature [34][35]. To numerically solve the hybrid boundary layer model, it is useful to distinguish the conditions to verify between before and after the boundary layer merging. Those conditions are the same as in the case of a rectangular duct.

Before the merging, the boundary layer is developing, thus the boundary layer thickness can be evaluated by the non-reactive analogy imposing the condition (6.35), that for the cylindrical channel is written as:

$$\dot{m}_{\delta,ox,nr}(x) = \dot{m}_{\delta}(x) - \dot{m}_f(x) \tag{6.88}$$

Therefore, the equation that must be numerically solved to evaluate the boundary layer thickness $\delta(x)$ is:

$$\begin{aligned} &\int_{r_\delta(x)=R-\delta(x)}^{R} K_{ox,nr}(x,r)\phi(x,r) r\, dr \\ &\qquad = \int_{r_\delta(x)=R-\delta(x)}^{R} \phi(x,r) r\, dr - \frac{R}{G_e(x)} \int_0^x \rho_f \dot{r}(x)\, dx \end{aligned} \tag{6.89}$$

The mass flux at the duct axis $G_e(x)$ and the flame position $r_b(x)$ are still the two degrees of freedom of the problem, therefore two conditions must be verified. The first condition consists in verifying the oxidizer to fuel ratio at the flame with equation:

$$[O/F]_{flame}(x) = \frac{\dot{m}_{ox,flame}(x)}{\dot{m}_{f,flame}(x)} = \frac{\dot{m}_{\delta}(x) - \dot{m}_f(x) - \dot{m}_{\delta,ox}(x)}{\dot{m}_f(x) - \dot{m}_{\delta,f}(x)} = [O/F]_{react} \tag{6.90}$$

therefore:

$$\begin{aligned} &[O/F]_{react} = \\ &\frac{\int_{r_\delta(x)=R-\delta(x)}^{R} \phi(x,r) r\, dr - \frac{R}{G_e(x)} \int_0^x \rho_f \dot{r}(x)\, dx - \int_{r_\delta(x)=R-\delta(x)}^{r_b(x)=R-y_b(x)} K_{ox}(x,r)\phi(x,r) r\, dr}{\frac{R}{G_e(x)} \int_0^x \rho_f \dot{r}(x)\, dx - \int_{r_b(x)=R-y_b(x)}^{R} K_f(x,r)\phi(x,r) r\, dr} \end{aligned} \tag{6.91}$$

The second condition requires the mass continuity to be verified with equation:

$$\begin{aligned} G(x) &= \frac{\dot{m}_\delta(x) + G_e(x)\pi\big(R - \delta(x)\big)^2}{\pi R^2} \\ &= G_e(x)\frac{2\int_{r_\delta(x)=R-\delta(x)}^{R} \phi(x,r) r\, dr + \big(R - \delta(x)\big)^2}{R^2} \end{aligned} \tag{6.92}$$

Iteratively solving the two conditions allows to solve the internal ballistic in the sections preceding the merging one.

When the boundary layer thickness is equal to the channel radius, i.e. $\delta(x = x_m) = R$, the merging of the boundary layer occurs, and the boundary layer fills the entire cross section. The variation of K_{ox_e} due to the diffusion of products toward the centreline and of oxidizer towards the flame can be evaluated imposing the condition (6.51) that for the cylindrical channel is written as equation (6.88). Therefore, the equation that must be numerically solved to evaluate the oxidizer mass fraction at the duct axis $K_{ox_e}(x)$ is:

$$K_{ox_e}(x) = \frac{\int_0^R \phi(x,r) r\, dr - \frac{R}{G_e(x)}\int_0^x \rho_f \dot{r}(x)\, dx - \Big(1 - K_{f_w}(x)\Big)\int_0^R \big(1 - \phi(x,r)\big)\phi(x,r) r\, dr}{\int_0^R \phi(x,r)^2 r\, dr} \tag{6.93}$$

The first condition to verify is the correct O/F ratio at the flame, thus equation (6.91) with $r_\delta(x) = 0$. The second condition requires the mass continuity to be verified with equation (6.92), which is simplified after the boundary layer merging as:

$$G(x) = G_e(x)\frac{2\int_0^R \phi(x,r) r\, dr}{R^2} \tag{6.94}$$

Solving equations (6.91) and (6.94) allows to solve the internal ballistic in the sections following the merging section to the position where the flame reaches the duct axis. In this position, as already mentioned, it is expected to have $K_{ox_e}\big|_{\phi_b=1}$ similar to the value that can be estimated with equation (6.61).

6.3.3.4 Numerical Results

In the following, the results of a numerical simulation will be reported. It is considered a cylindrical channel with diameter $D = 0.1\ m$ and an oxidizer mass flux $G_{ox} = 100\ kg/(m^2 s)$ is used. The distribution of the quantities inside the cylindrical duct is qualitatively similar to that observed in the rectangular duct, except for some peculiarities due to the axisymmetric geometry of the channel. Fig.6.29 shows the mass flow rates as a function of the position along the grain port. The first increasing and then decreasing trend of the oxidizer mass flow rate within the boundary layer is due to the superimposition of a positive effect due to the extension of the boundary layer towards the duct axis and the simultaneous lowering of the flame dimensionless position, and a negative effect due to the fact that the flow rate is calculated on a section closer to the origin of the cylindrical reference system.

Once more, because the mass flow rates integrals are calculated with respect to a radial coordinate reference system, a lower dimensionless position of the flame, compared to that which occurs in the rectangular duct, is expected and verified (Fig.6.30). Moreover, the greater surface subject to pyrolysis area with the (almost) same port area with respect to the rectangular cross-section duct case, leads to an increase in the evaporated fuel flow rate. As a result, the boundary layer in the cylindrical duct reaches the merging condition much sooner than in case of the rectangular duct with two slabs.

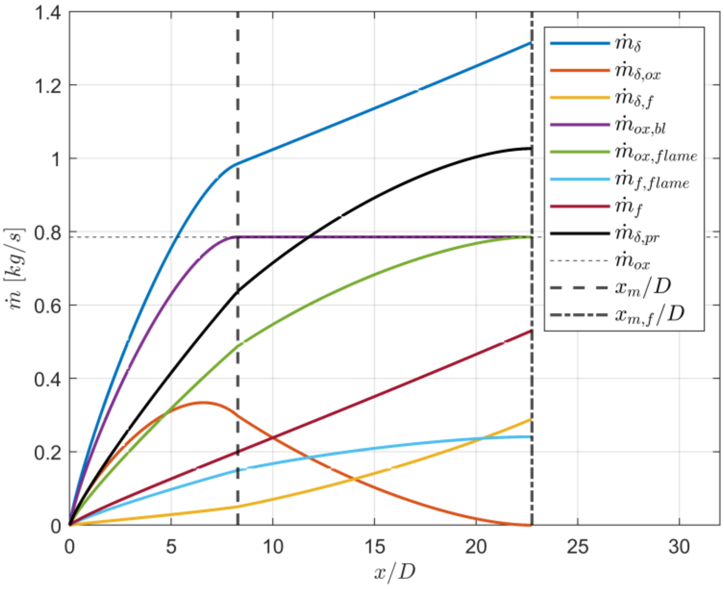

Figure 6.29: Mass flow rates as a function of the dimensionless position x/D.

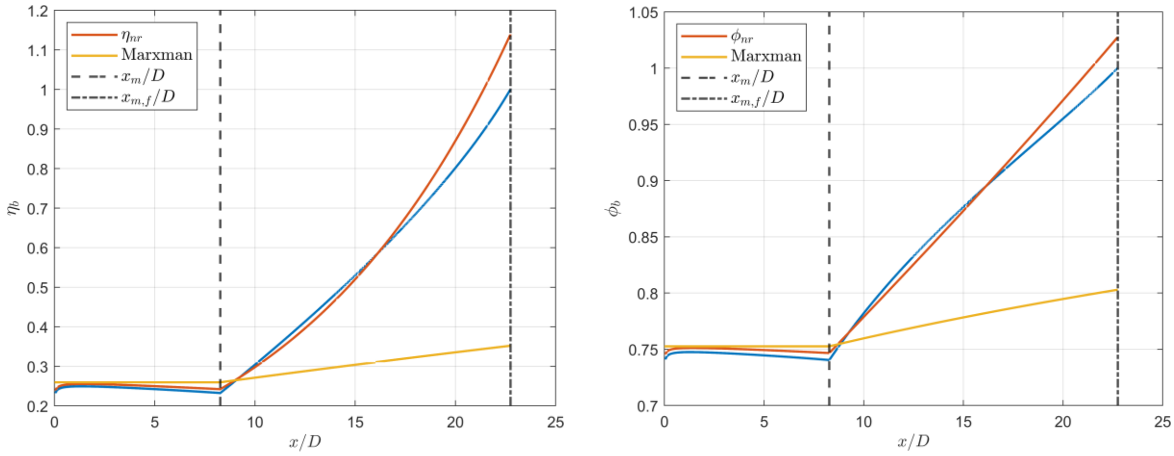

Figure 6.30: Dimensionless flame position η_b and velocity ϕ_b as a function of the dimensionless position x/D.

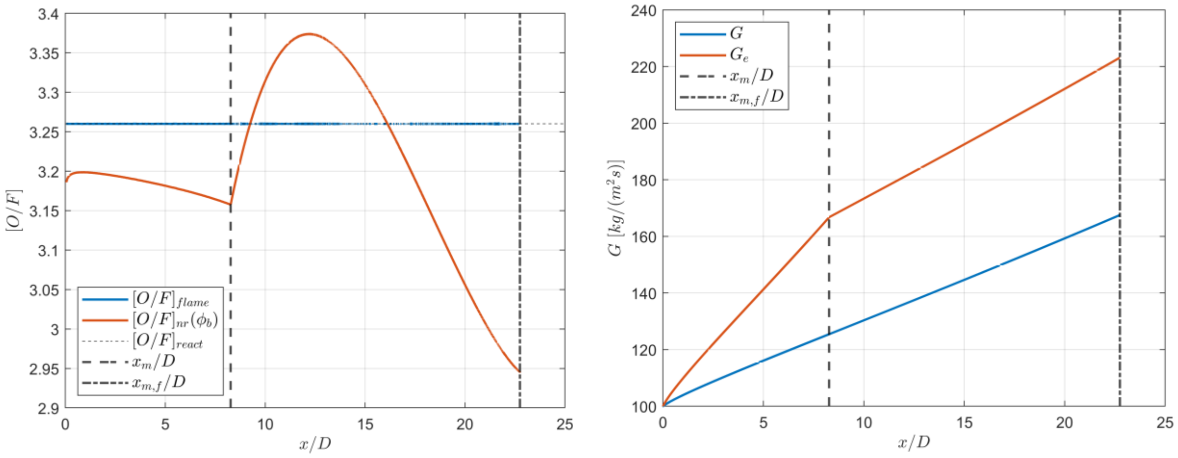

Figure 6.31: Comparison between the O/F ratio at the flame, $[O/F]_{flame}$, and the one calculated with the non-reactive case analogy for the same flame velocity (left). Average mass flux, G, and mass flux at the duct axis, G_e, as a function of the dimensionless position x/D (right).

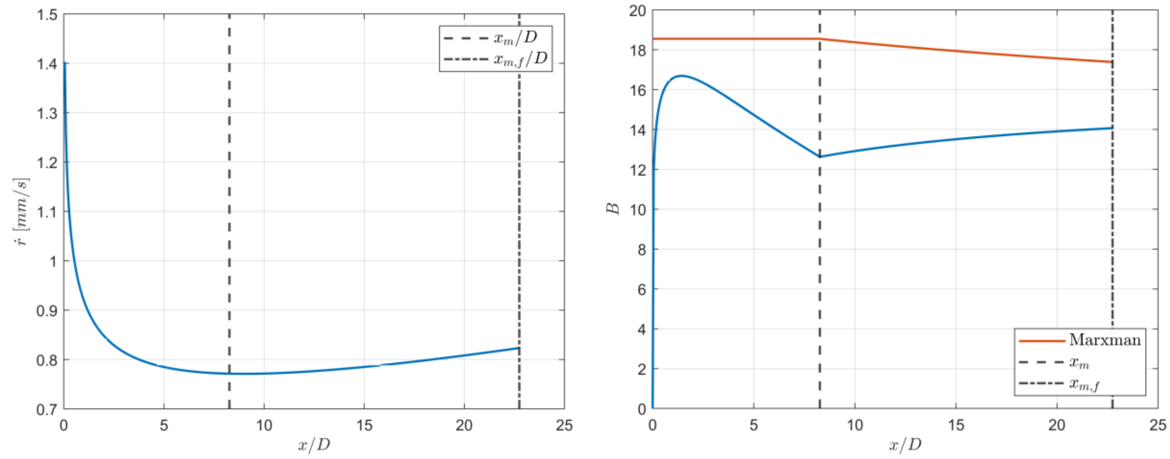

Figure 6.32: Regression rate $\dot{r}$ (left) and blowing parameter B (right) as a function of the dimensionless position x/D.

In the case of cylindrical channel configuration, the difference in the values of the boundary layer thickness and of the flame position (the latter especially after merging) compared to what is predicted by Marxman's theory is much greater than in the case of a rectangular port duct (Fig.6.33). In addition, similarly to the rectangular section duct case, the value of K_{ox_e} that corresponds to the flame reaching the centre of the channel is slightly different from that predicted by the analogy with the non-reactive case (Fig.6.34).

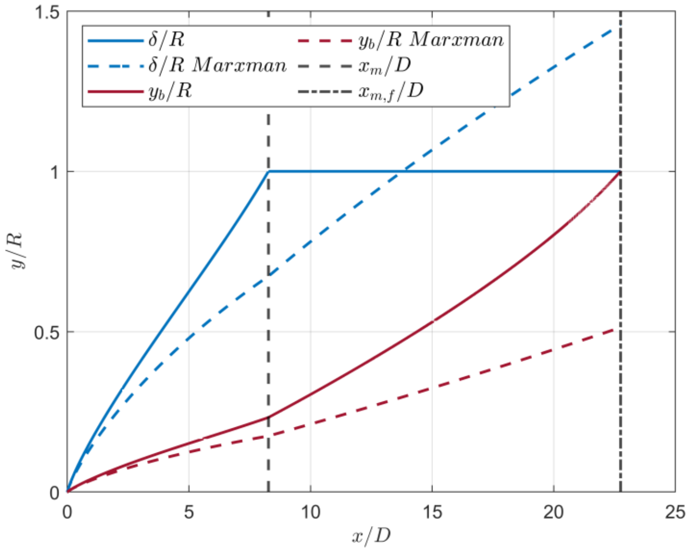

Figure 6.33: Dimensionless boundary layer thickness, δ, and flame position, y_b, as a function of the dimensionless position x/D. The corresponding values according to Marxman's theory are also depicted for comparison.

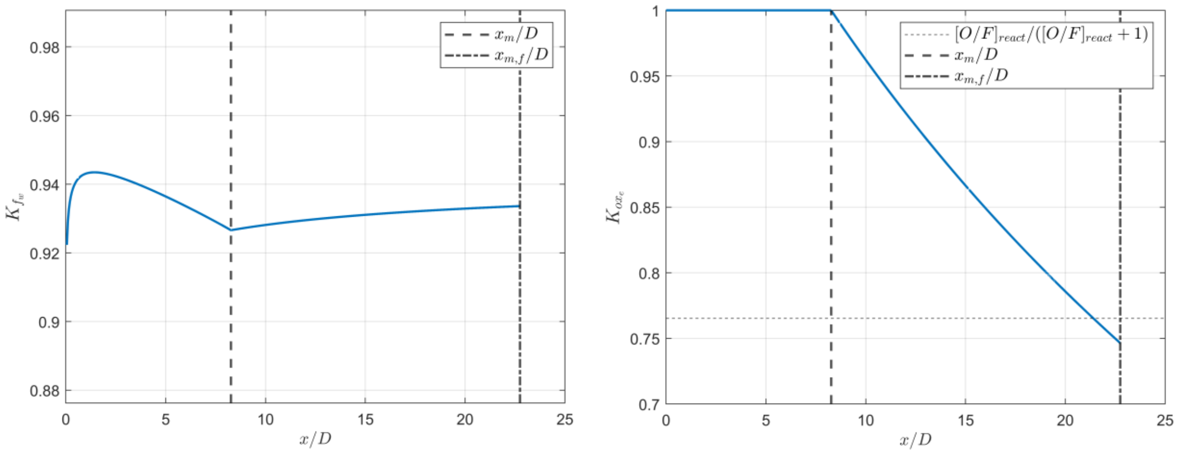

Figure 6.34: Fuel mass fraction at the grain surface K_{f_w} (left) and oxidizer mass fraction at the duct axis K_{ox_e} (right) as a function of the dimensionless position x/D.

Similarly to the rectangular section duct case, it can be observed the peculiar characteristics of hybrid systems for which the value of $[O/F]_{react}$ (generally not too different from the $[O/F]_{glob}$ value of the grain design) is obtained in an intermediate section between the merging section and the one for which the flame reaches the duct axis (Fig.6.35). With the cylindrical configuration, however, a closer proximity of this position to the merging position is observed, which allows to obtain a higher fuel combustion efficiency if the grain is designed to end at this point (Fig.6.36).

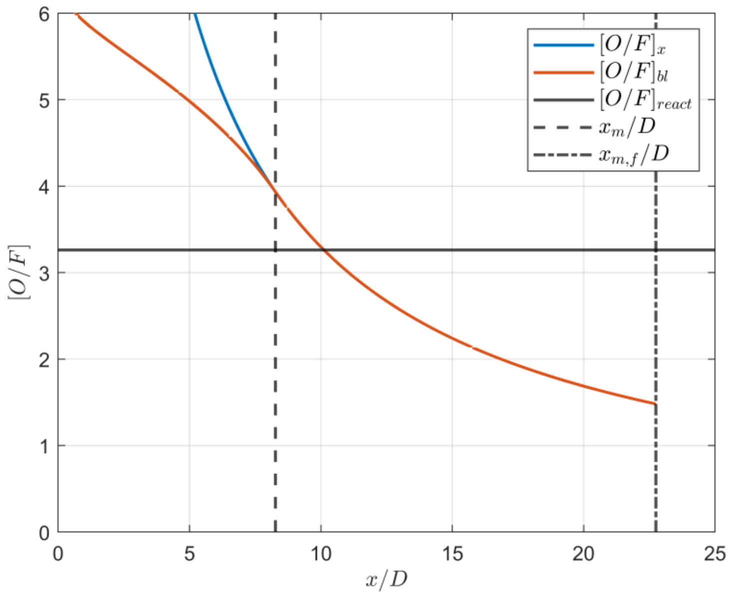

Figure 6.35: $[O/F]_x$ and the $[O/F]_{bl}$ as a function of the dimensionless position x/D.

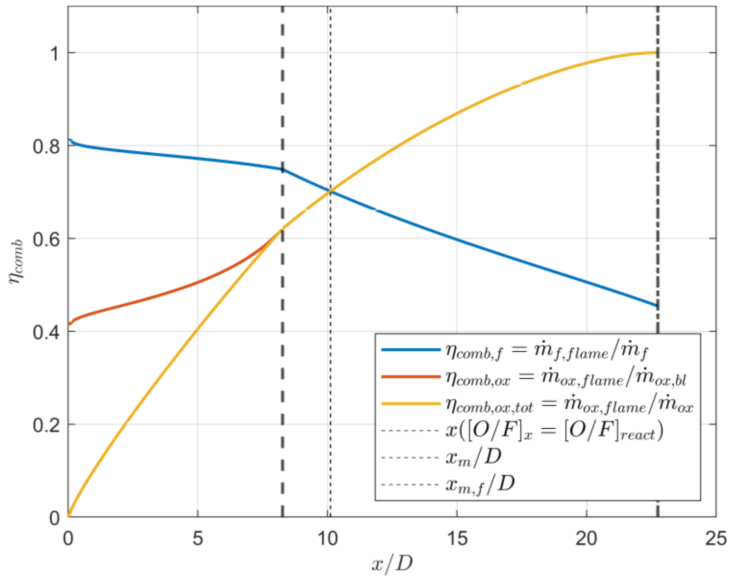

Figure 6.36: Fuel and combustion efficiencies as a function of the dimensionless position x/D.

6.3.3.5 Parametric Study of the Hybrid Boundary Layer in a Circular Port Duct

In this paragraph, a parametric study of the hybrid boundary layer in a cylindrical channel is performed in order to evaluate the consequences of the design choices. The influence of the port diameter, the oxidizer mass flux and the dilution of the oxidizer will be studied. Each parameter will be analysed individually, keeping the other parameters unchanged.

Influence of the port diameter. Increasing the port diameter leads to an increase of the merging dimensionless position x_m/D (Fig.6.37). This happens because of the scale-up effect, i.e. the reduction of the mass flux due to a greater port area that leads to a reduction of the regression rate. Therefore, also the fuel mass flow injected decrease, leading to a lower extension of the boundary layer required to verify mass continuity. The same effect is responsible for increasing the dimensionless distances $x_{m,f}/D$ and $x([O/F]_x = [O/F]_{react})$ (Fig.6.38). It can also be observed that the variation of the ratio between x_m and $x_{m,f}$ is negligible, as well as that of $x([O/F]_x = [O/F]_{react})$ and x_m or $x_{m,f}$, involving a sort of "proportionality" of positions as the port area changes (Fig.6.39).

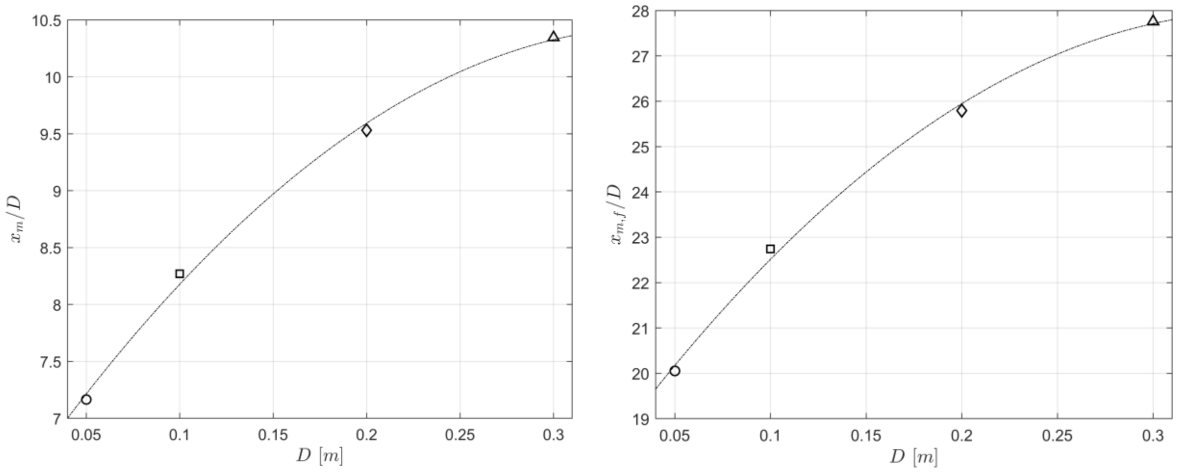

Figure 6.37: Dimensionless positions x_m/D (left) and $x_{m,f}/D$ (right) as a function of the port diameter D.

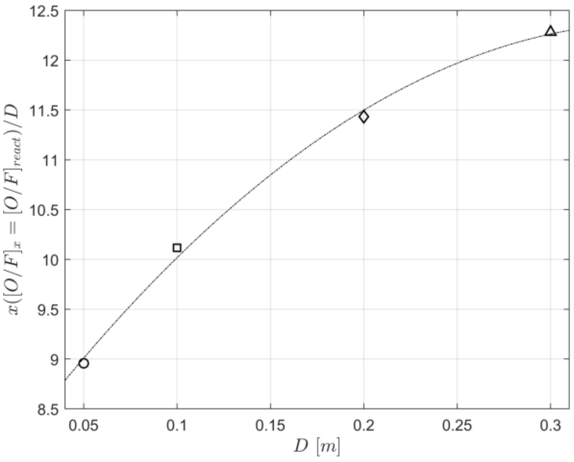

Figure 6.38: Dimensionless positions $x([O/F]_{ox} = [O/F]_{react})/D$ as a function of the port diameter D.

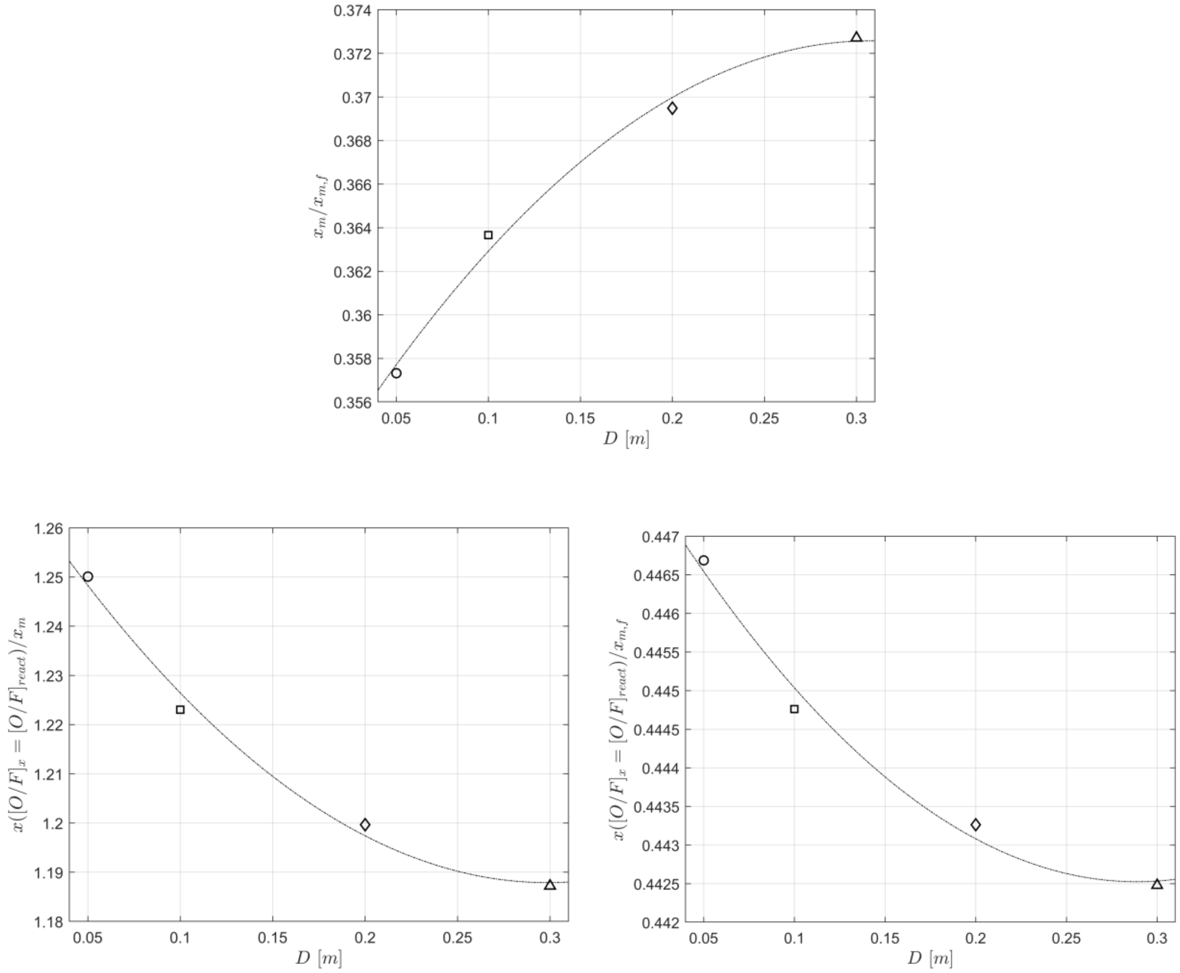

Figure 6.39: Ratios between $x_m, x_{m,f}$ and $x([O/F]_x = [O/F]_{react})$ as a function of the port diameter D.

Fig.6.40 shows the effects of port diameter on the propellant combustion efficiency at $x_m, x_{m,f}$ and $x([O/F]_x = [O/F]_{react})$. As the port diameter increase, the fuel combustion efficiency tends to decrease for all those three positions, especially at the merging section of the boundary layer, because of the more downstream position of x_m with the port diameter. The oxidizer combustion efficiency at $x\left([O/F]_{global} = [O/F]_{react}\right)$ (which is equal to $\eta_{comb,f}$ at this position) decrease with the port diameter, while that at the merging section tends to increase.

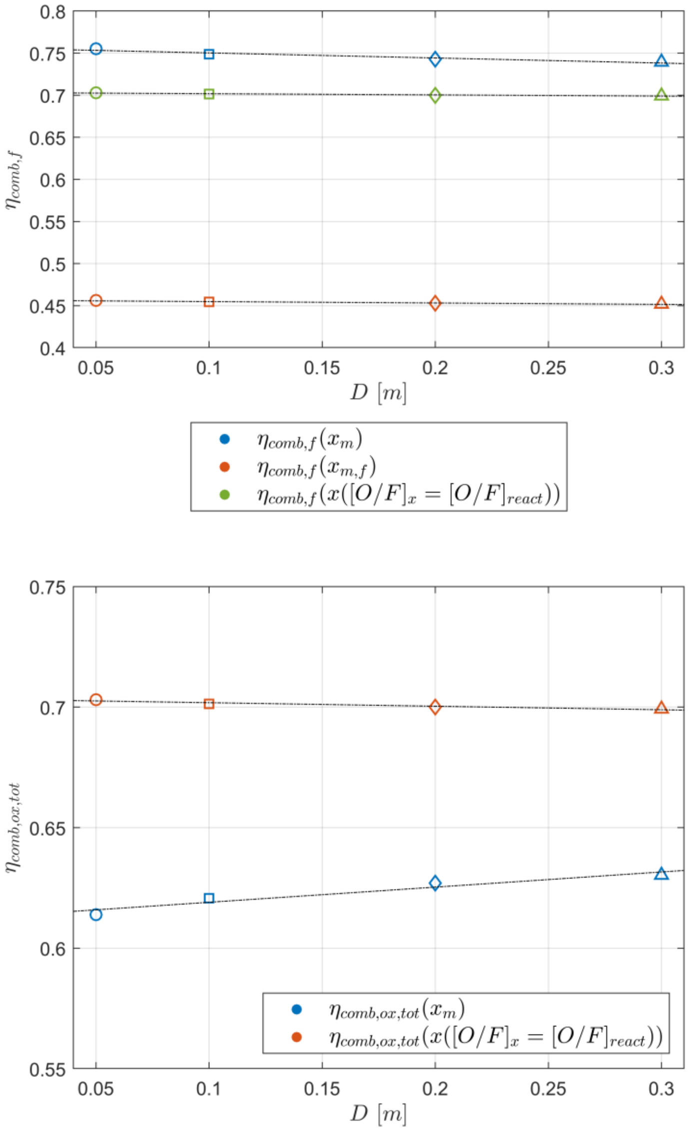

Figure 6.40: Fuel combustion efficiency $\eta_{comb,f}$ (top) and oxidizer combustion efficiency $\eta_{comb,ox,tot}$ (bottom) at $x_m, x_{m,f}$ and $x([O/F]_x = [O/F]_{react})$ as a function of the port diameter D.

Influence of oxidizer mass flux. The increase of the oxidizer flux G_{ox} leads to an increase in the fuel flow rate injected from the grain surface. Its contribution to the increase of the boundary layer thickness is overcome by the reduction of its extension due to the greater external flow. As a result, the dimensionless position of the boundary layer merging increase (Fig.6.41). A greater G_{ox} also leads to an increase in the dimensionless positions for which the flame reaches the channel axis and for which the condition $[O/F]_x = [O/F]_{react}$ is achieved, although, as for the influence of the port diameter, the ratios between those positions is almost constant (Fig.6.42).

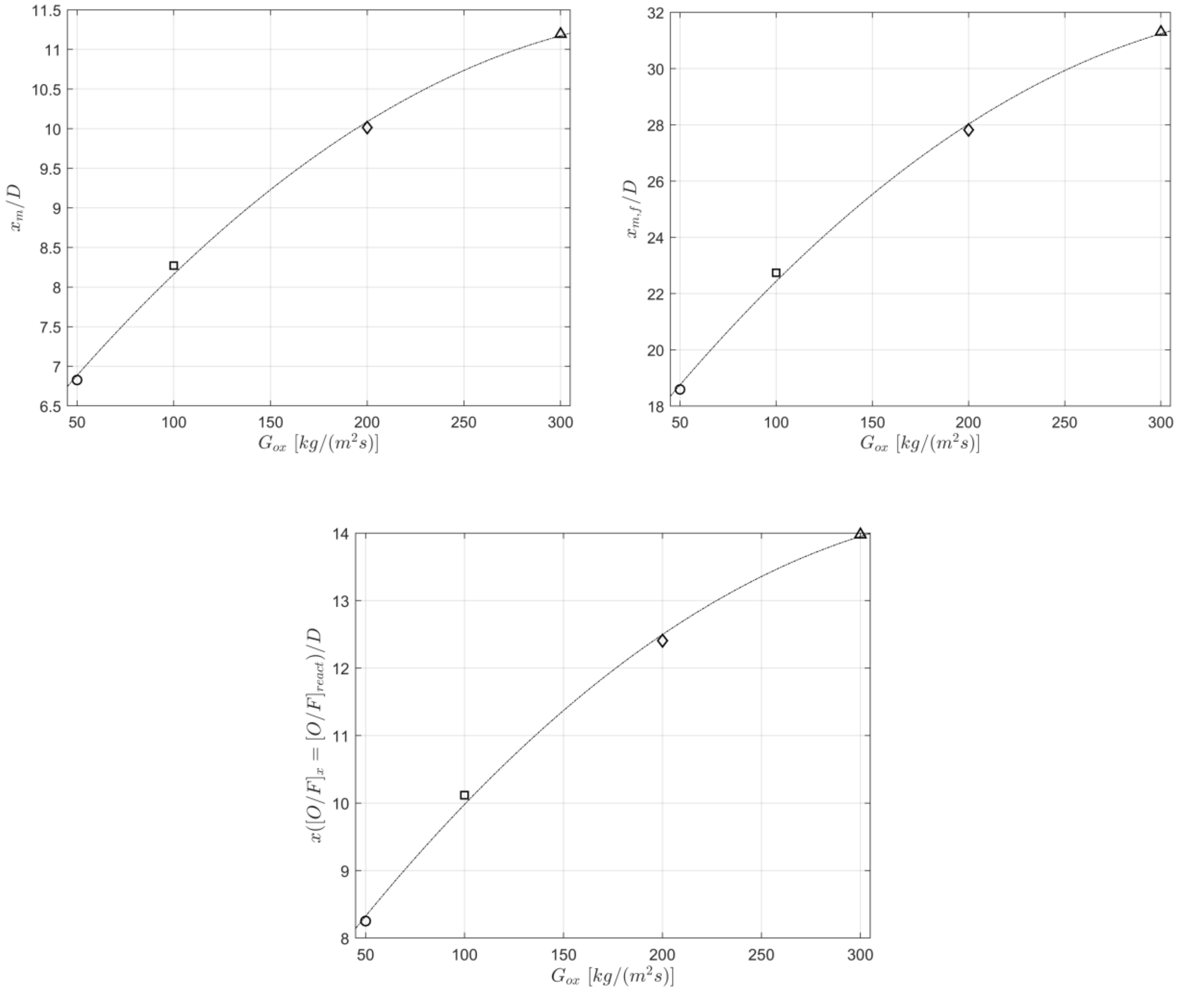

Figure 6.41: Dimensionless positions x_m/D (top left), $x_{m,f}/D$ (top right) and $x([O/F]_x = [O/F]_{react})/D$ (bottom) as a function of the oxidizer mass flux G_{ox}.

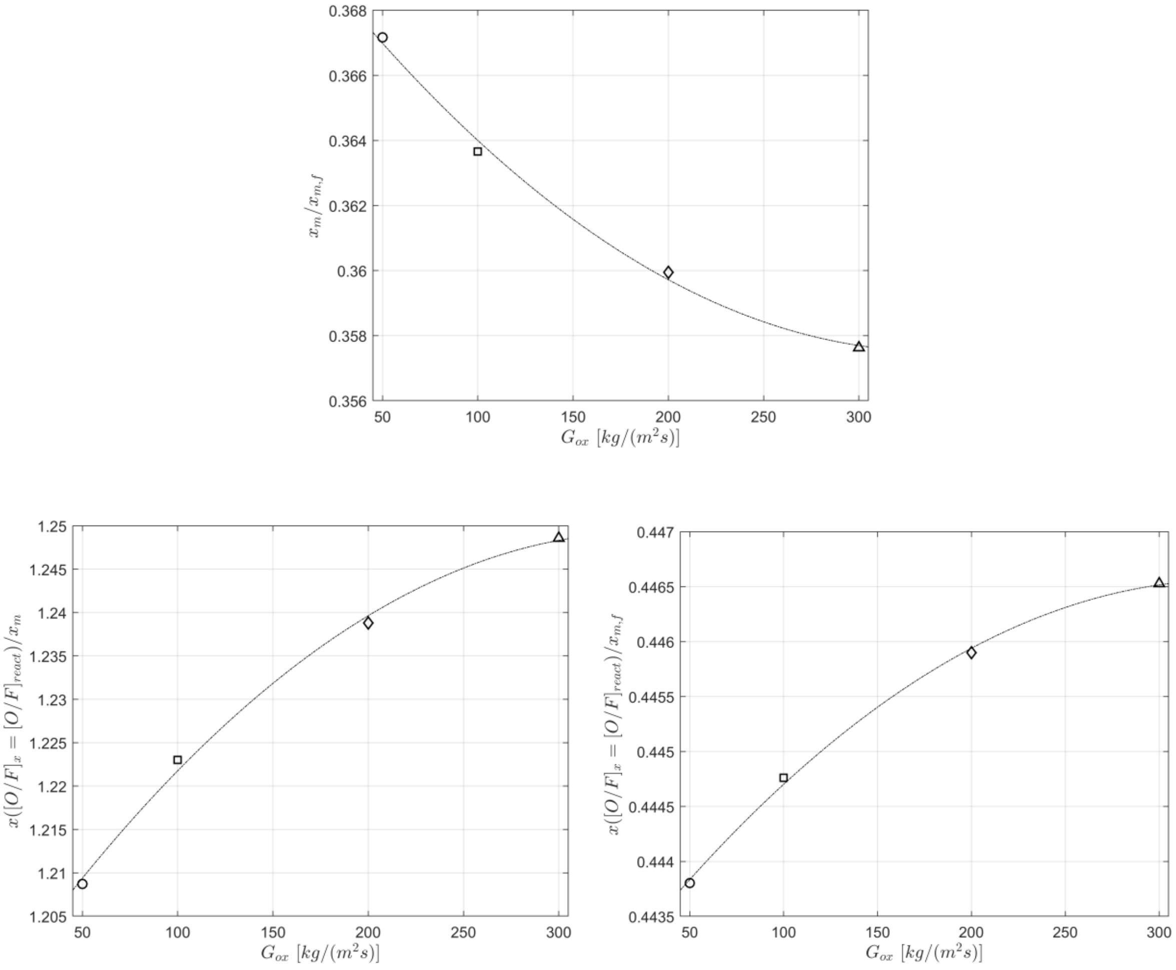

Figure 6.42: Ratios between $x_m, x_{m,f}$ and $x([O/F]_x = [O/F]_{react})$ as a function of the oxidizer mass flux G_{ox}.

The greater oxidizer flux leads to a small increase of the fuel combustion efficiency $\eta_{comb,f}$ in all three positions and reduces the oxidizer combustion efficiency $\eta_{comb,ox,tot}$ at the merging section (Fig.6.43).

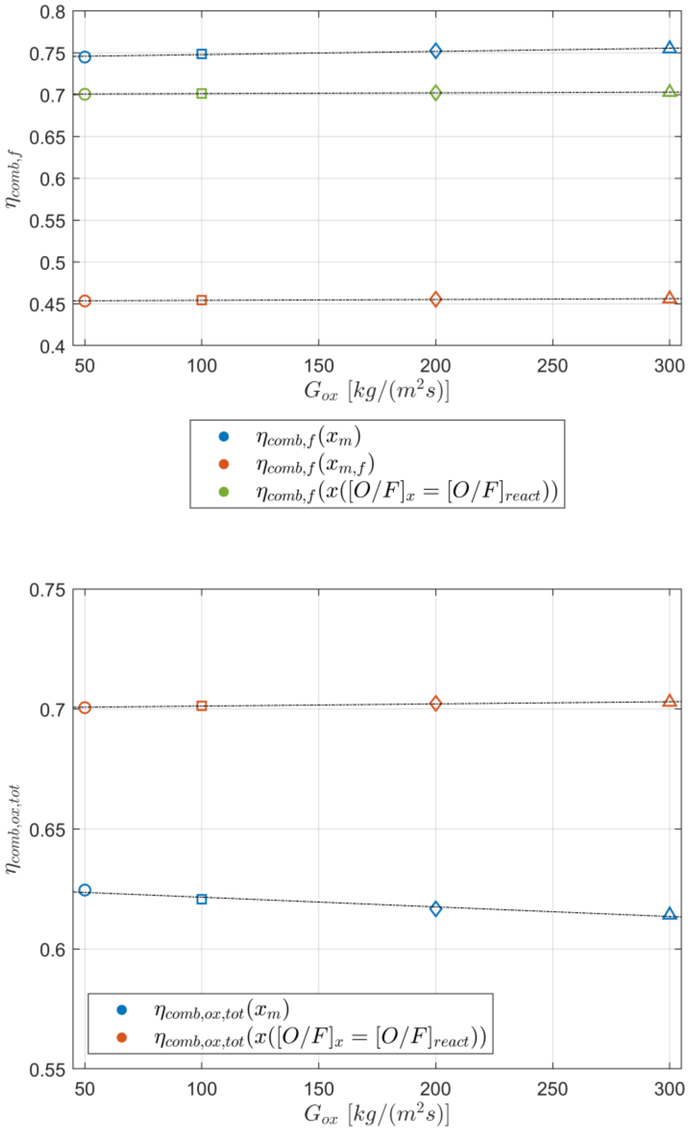

Figure 6.43: Fuel combustion efficiency $\eta_{comb,f}$ (top) and oxidizer combustion efficiency $\eta_{comb,ox,tot}$ (bottom) at $x_m, x_{m,f}$ and $x([O/F]_x = [O/F]_{react})$ as a function of the oxidizer mass flux G_{ox}.

Influence of dilution of the oxidizer. The evaluation of the influence of dilution of the oxidizer is made with the comparison between pure oxygen (GOX), hydrogen peroxide (H_2O_2) (100%) and nitrous oxide (N_2O) as oxidizer. As described in Chapter 3, it is equivalent to consider K_{ox_e} equal to the percentage of oxygen ξ_{ox} and $[O/F]_{st\,(O_2)}$ or assume that all the oxidizer is oxygen (i.e. $K_{ox_e} = 1$) and use the stoichiometric O/F ratio with the diluted oxidant. Therefore, in the simulations is assumed $K_{ox_e} = 1$ and $[O/F]_{react}$ equal to the stoichiometric value for the reaction of $HTPB$ with the diluted oxidant.
In the case of $HTPB - GOX$, the mass stoichiometric ratio is $[O/F]_{st\,(O_2),mass} = 3.26$.
In the case of $HTPB - H_2O_2(100\%)$, the stoichiometric reaction is:

$$C_4H_6 + 11H_2O_2 \rightarrow 4CO_2 + 14H_2O \tag{6.93}$$

therefore, the molar and mass stoichiometric ratio are $[O/F]_{st\,(H_2O_2),molar} = 11$ and $[O/F]_{st\,(H_2O_2),mass} = 6.93$ respectively.
In the case of $HTPB - N_2O$, the stoichiometric reaction is:

$$C_4H_6 + 11N_2O \rightarrow 4CO_2 + 3H_2O + 11N_2 \tag{6.94}$$

therefore, the molar and mass stoichiometric ratio are $[O/F]_{st\,(N_2O),molar} = 11$ and $[O/F]_{st\,(N_2O),mass} = 8.96$ respectively.

The position of the merging section does not change due to the independence of the boundary layer thickness on the flame O/F ratio (Fig.6.44). After merging, the analogy with the non-reactive case allows to state that the value of K_{ox_e} for which the flame reaches the duct axis is influenced by the flame O/F ratio and tends to increase with it (Fig.6.45). In fact, if the O/F ratio of reaction increase then the flame take place at further dimensionless distance from the wall, therefore causing the flame to reach the channel axis in less space. In addition, the position for which the condition $[O/F]_x = [O/F]_{react}$ occurs tends to move towards the head of the grain as the value of $[O/F]_{react}$ increases due to the reduction of the evaporated fuel flow to reach that O/F ratio (Fig.6.46). For the case in which H_2O_2 or N_2O are used as oxidizer, the condition $[O/F]_x = [O/F]_{react}$ occurs before the boundary layer merging (Fig.6.47). The variability of $x_m/x_{m,f}$, unlike the previous cases, leads to a variation of the ratios between the particular positions.

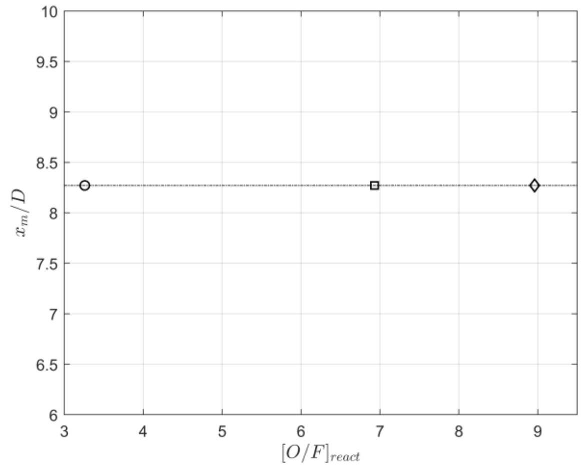

Figure 6.44: Dimensionless positions x_m/D as a function of the oxidizer.

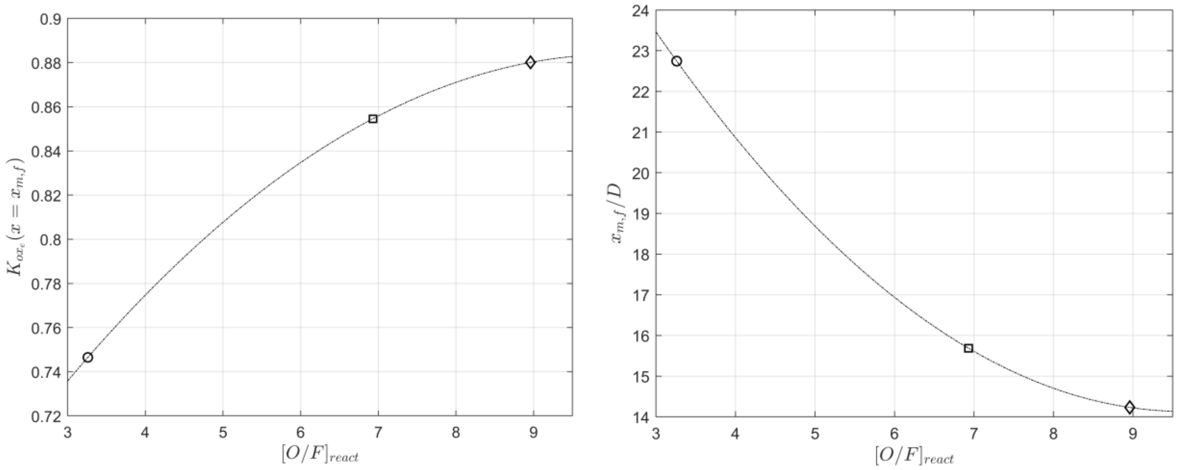

Figure 6.45: Oxidizer mass fraction at $x_{m,f}$ (left) and dimensionless position $x_{m,f}/D$ (right) as a function of the oxidizer.

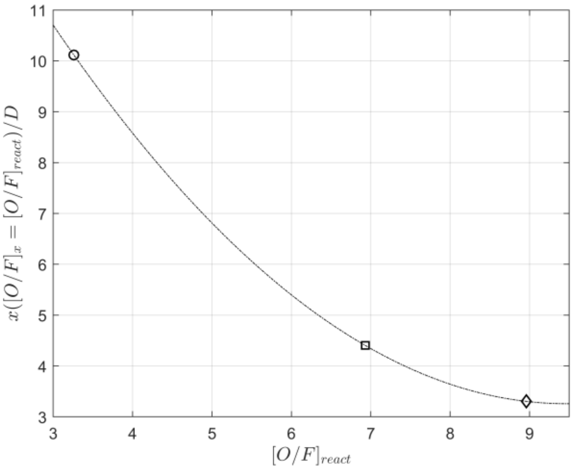

Figure 6.46: Dimensionless positions $x([O/F]_x = [O/F]_{react})/D$ as a function of the oxidizer.

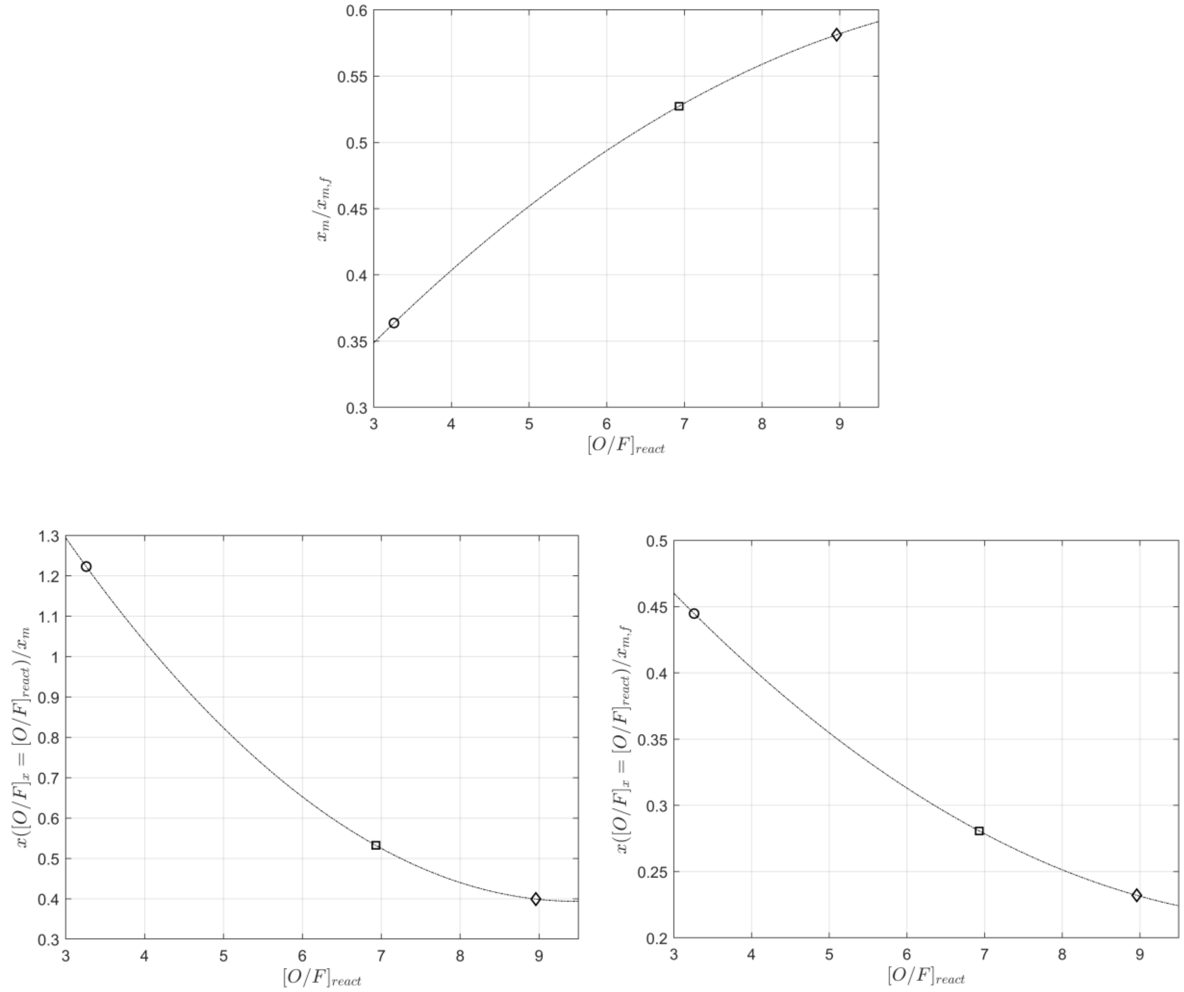

Figure 6.47: Ratios between $x_m, x_{m,f}$ and $x([O/F]_x = [O/F]_{react})$ as a function of the oxidizer.

The type of oxidizer and therefore of the $[O/F]_{react}$ ratio has an important influence on the propellant combustion efficiency. For a given combination of propellants, the relationship of combustion efficiencies at various locations is influenced by the magnitude of $x([O/F]_x = [O/F]_{react})$ with respect to x_m (Fig.6.48). For the case of $HTPB + GOX$, since $x([O/F]_x = [O/F]_{react}) > x_m$ and the fuel combustion efficiency is always decreasing, then $\eta_{comb,f}(x_m) > \eta_{comb,f}\left(x([O/F]_x = [O/F]_{react})\right)$. On the contrary, for the cases of $HTPB + H_2O_2$ and $HTPB + N_2O$, since the condition $[O/F]_x = [O/F]_{react}$ occurs before the merging of the boundary layer, then $\eta_{comb,f}(x_m) < \eta_{comb,f}\left(x([O/F]_x = [O/F]_{react})\right)$. In any case, the value of the fuel combustion efficiency at the section where the flame reaches the centreline is always the minimum one (Fig.6.49). The same considerations can also be made for the oxidizer combustion efficiency that, unlike the fuel one, has an increasing trend with the position along the grain port (Fig.6.50).

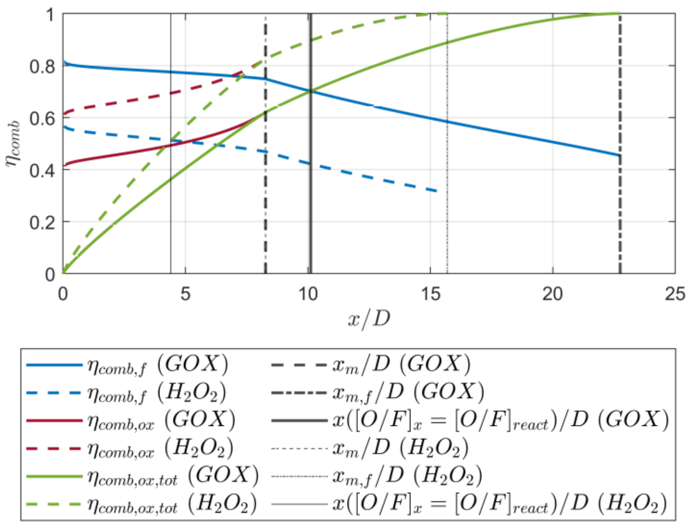

Figure 6.48: Comparison between $HTPB + GOX$ and $HTPB + H_2O_2$ of the propellant combustion efficiencies values as a function of the dimensionless position x/D.

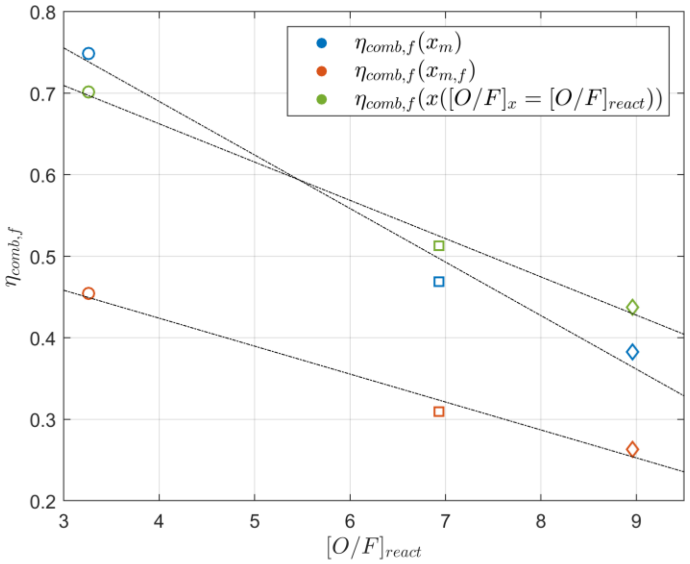

Figure 6.49: Fuel combustion efficiency $\eta_{comb,f}$ at $x_m, x_{m,f}$ and $x([O/F]_x = [O/F]_{react})$ as a function of the oxidizer.

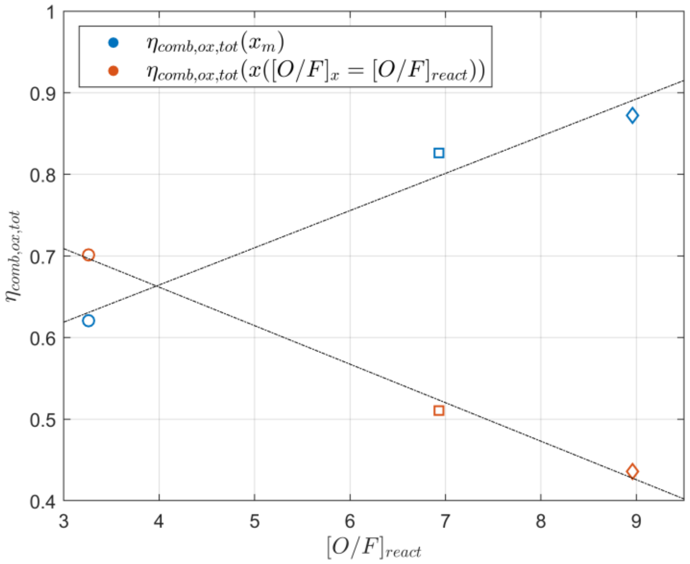

Figure 6.50: Oxidizer combustion efficiency $\eta_{comb,ox,tot}$ at x_m and $x([O/F]_x = [O/F]_{react})$ as a function of the oxidizer.

Chapter 7

1D with Boundary Layer Combustion Chamber Model

In this chapter a 1D with boundary layer model for the cylindrical combustion chamber of a hybrid rocket is developed with the purpose of its integration in a system design tool used for engine predesign phases. Therefore, a good compromise of simplicity and accuracy is required. To reduce the computational time without sacrificing the solution accuracy, the model here presented consists of an approximation of the internal ballistic of the flow through the coupling of the 1D model described in Chapter 5 and the hybrid combustion boundary layer model proposed in Chapter 6. The 1D with boundary layer model takes into consideration the information in the boundary layer to obtain a better evaluation of the reactant mass flow rates and thus of the heat flux released to the flow by the combustion. The resolution of the equations in the axial direction provides the information about the propulsive performance of the motor, while the resolution of the boundary layer delivers an approximation of the fluid dynamics of the boundary layer, providing useful information such as the combustion efficiency.

7.1 Mathematical Model

The model for the combustion chamber of a hybrid rocket engine consists of an approximation of the internal ballistic of the flow through the coupling of the 1D model and the hybrid combustion boundary layer model. The hypothesis applied are therefore the same of the two already described models, for which reference is made to Chapters 5 and 6. The main difference is in the coupling of the two models. The 1D model needs the information about the amount of reactant in the combustion at the flame, while the boundary layer model requires the knowledge of the external (to the boundary layer) density. Moreover, at any timestep the regression rate is assumed to be constant around the circumference of the fuel port at any given axial position and equal to the average value (2.60) of the real distribution. Therefore, also the port diameter is assumed to be constant. This assumption is a fairly good approximation for circular ports and allows to describe the fluid dynamics of the boundary layer in a much simpler way (i.e. over a surface with the same radial coordinate at any given axial position).

In this work, the following algorithm is used. The numerical domain is subjected to a discretization in the time (dt) and in the space (dx) domains. In each control volume of size dx, 1 and 2 refers to the terms at the entrance and at the exit cross sections respectively. For each time step, the global continuity equation can be solved for any control volume at the beginning of the calculation, because of its dependency only on the average specific flux G and on the regression rate which are coupled through equation (2.35). Then, the coupling between the 1D and the boundary layer model is considered. For each time step, the pressure at the head of the grain is assumed. For each control volume, the velocity u_2 at the exit of the control volume is estimate, leading to the calculation of the average density $\rho_2 = G_2/u_2$. With this information, the boundary layer is solved at the cross section 2, providing the knowledge of the oxidizer and fuel mass flow rate that participate in the combustion process. The momentum (5.9), energy (5.10) and ideal gas law (5.13) are then solved, leading to a new value for u_2 which is compared to the estimated one, therefore iteratively preceding until convergence on the u_2 value is achieved. The above algorithm is repeated for each control volume. Once that the pressure distribution in the combustion chamber is known, the pressure at the end of the propellant grain is compared to the one obtained from the expression of the chocked mass flow through the nozzle (5.21). The value of the pressure at the head of the grain is then corrected and the algorithm is iterated until convergence is achieved, thus moving to the next timestep.

By coupling the 1D model to the boundary layer model, the resolution of the 1D with boundary layer model makes it possible to evaluate, in addition to the internal ballistics of the engine, also the chemical composition of the gases leaving the combustion chamber and therefore the real characteristic velocity c^*_{real}:

$$c^*_{real} = \frac{1}{\sqrt{k}}\left(\frac{k+1}{2}\right)^{\frac{k+1}{2(k-1)}} \sqrt{\frac{\mathcal{R}T_0}{M_m}} \tag{7.1}$$

with k, T_0, M_m calculated at the end of the propellant grain (i.e. at the nozzle entrance). Therefore, it is possible to have an estimation of the use of propellant and combustion efficiencies, respectively calculated as:

$$\eta_{comb,f} = \frac{\dot{m}_{f,flame}}{\dot{m}_f} \tag{7.2}$$

$$\eta_{comb,ox,tot} = \frac{\dot{m}_{ox,flame}}{\dot{m}_{ox}} \tag{7.3}$$

$$\eta_{c^*} = \frac{c^*_{real}}{c^*_{th}} \tag{7.4}$$

where $\dot{m}_{\delta,f} = \dot{m}_{\delta,f}(x = L), \dot{m}_f = \dot{m}_f(x = L)$ and c^*_{th} is the theoretical characteristic velocity evaluated with a thermochemical code.

7.2 Numerical Results

In the following, the results of a numerical simulation with the proposed model are reported. Here the hybrid engine is designed to provide a constant thrust of $1000\ N$ for $t_b = 5\ s$ which corresponds to a lab-scale engine. The propellant is $HTPB + GOX$ and the average

O/F ratio required is assumed to be $[O/F]_{glob} = 3$. The trend of the internal ballistics proprieties is similar to what has been already seen in Chapter 5, where the change in slope of pressure and Mach number (Fig.7.1) distributions is due to the lower acceleration of the flow at the duct axis after the boundary layer merging (Fig.7.2) and to the reduction of heat released by the combustion.

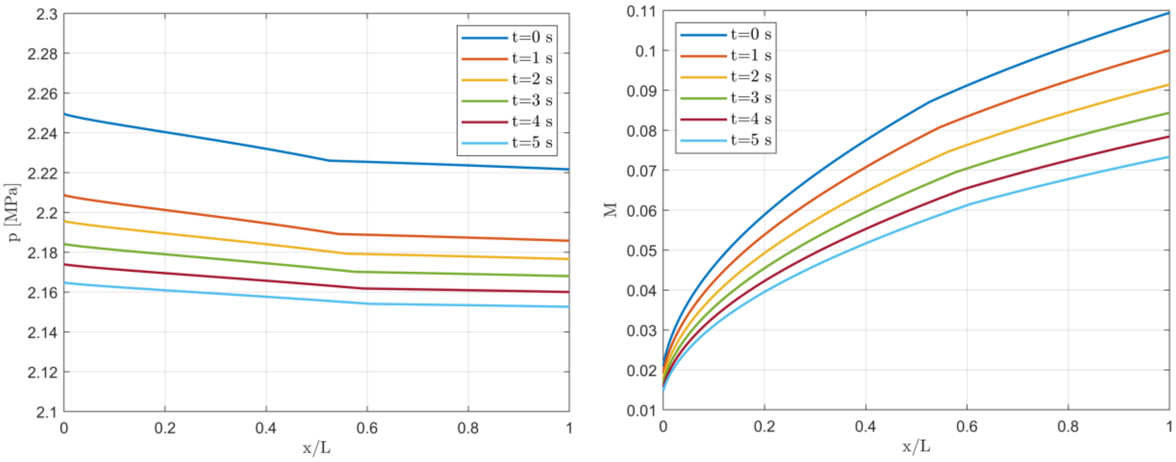

Figure 7.1: Pressure (left) and Mach number (right) distributions as a function of the dimensionless position x/L and time.

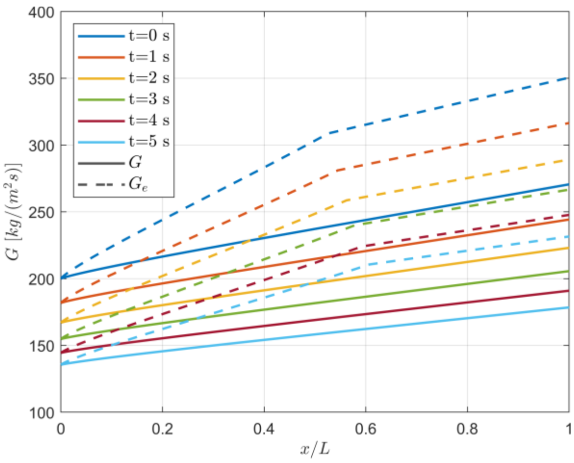

Figure 7.2: Average mass flux G and mass flux at the duct axis G_e distributions as a function of the dimensionless position x/L and time.

The change in slope of the temperature distribution (Fig.7.3) is caused by the progressively higher flame position from the grain surface, which in turns reduces the quantity of reactants and therefore the heat released during combustion. Fig.7.4 shows the real regression rate distribution and the average port diameter. The motor O/F ratio as a function of time and the local O/F ratio are depicted in Fig.7.5, while Fig.7.6 shows the thrust time history.

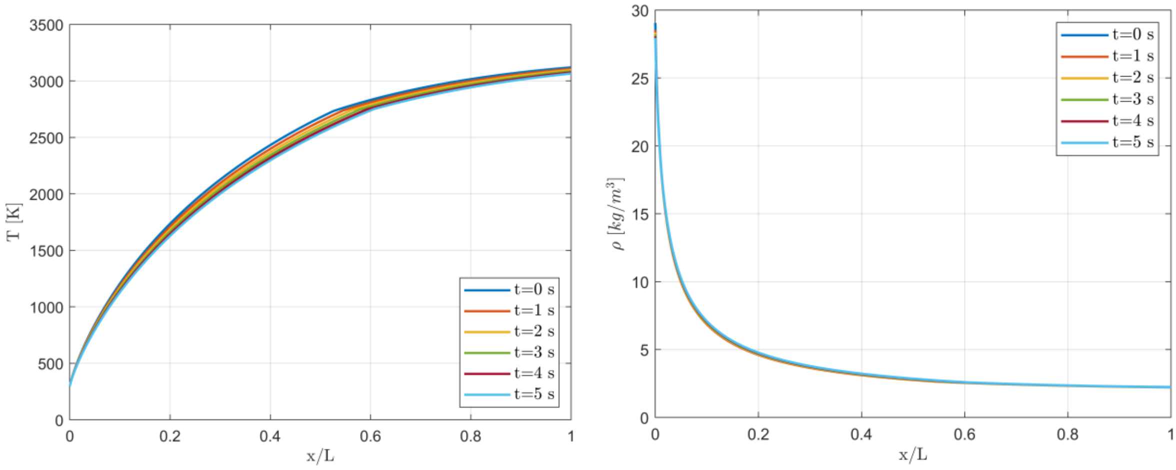

Figure 7.3: Temperature (left) and density (right) distributions as a function of the dimensionless position x/L and time.

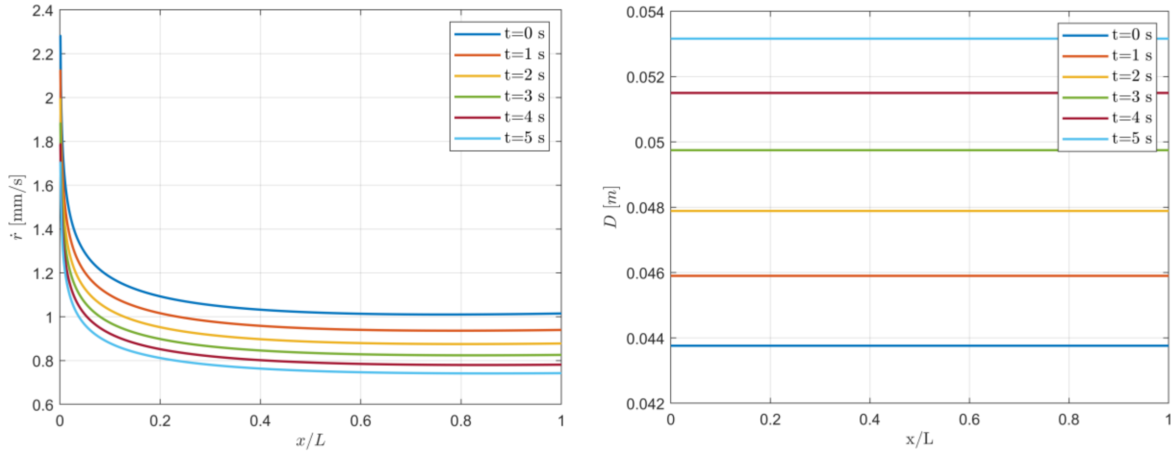

Figure 7.4: Regression rate (left) and port diameter (right) distributions as a function of the dimensionless position x/L and time.

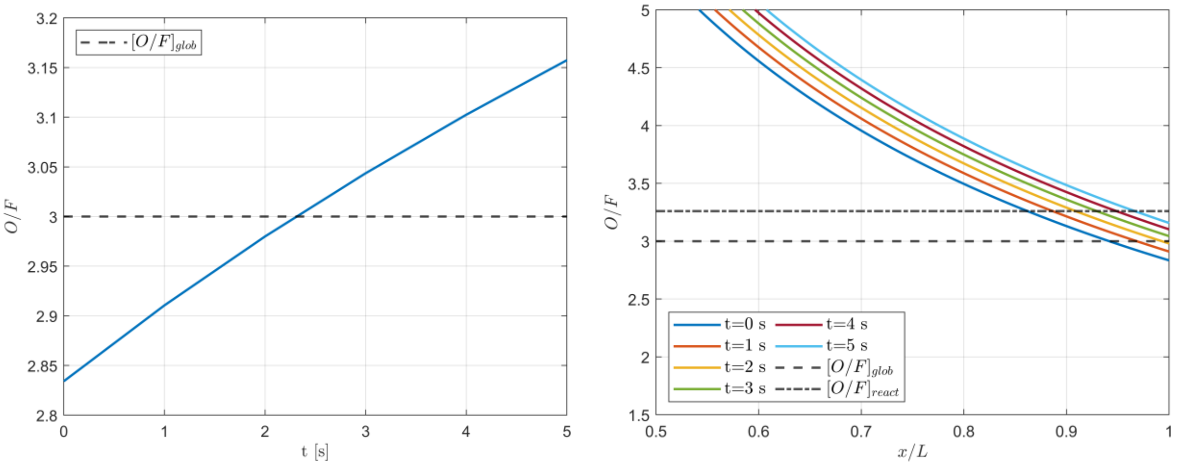

Figure 7.5: Motor O/F ratio as a function of time (left) and local O/F ratio as a function of the dimensionless position x/L and time (right).

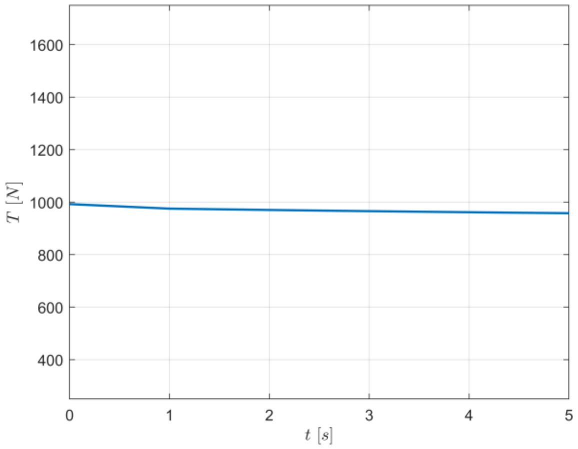

Figure 7.6: Motor thrust as a function of time.

The resolution of the boundary layer sub-model allows to evaluate the characteristic of the boundary layer (Fig.7.7 to 7.10).

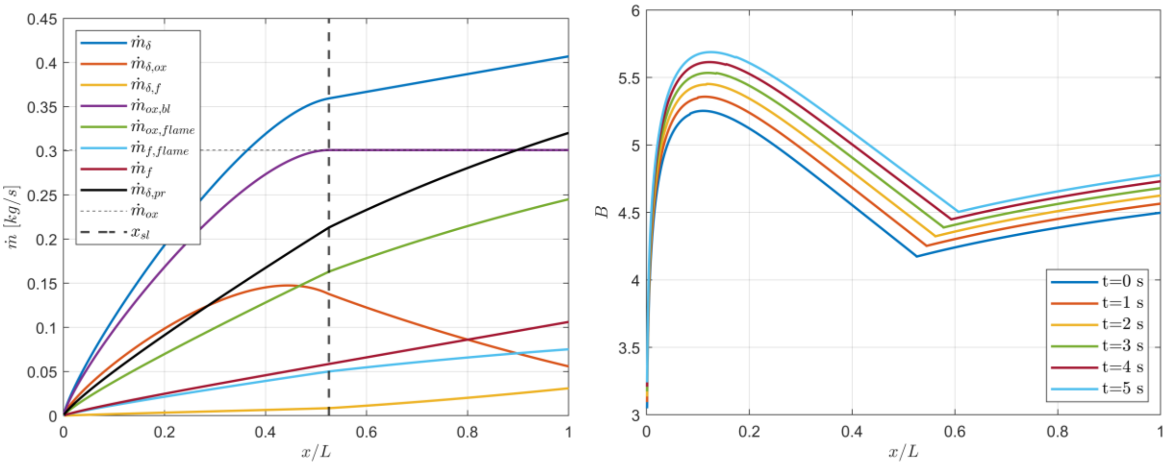

Figure 7.7: Mass flow rates at $t = 0$ (left) and blowing parameter B (right) as a function of the dimensionless position x/L and time.

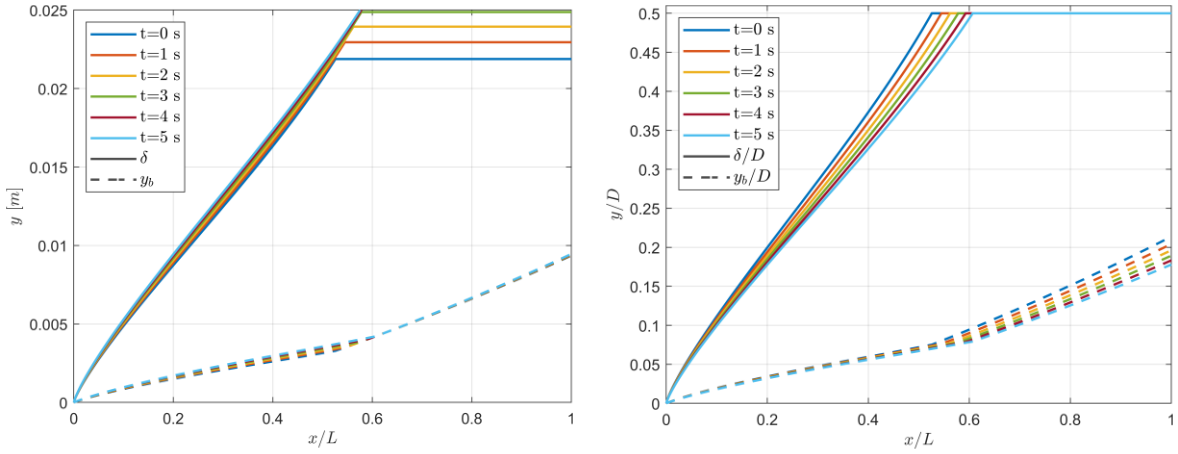

Figure 7.8: Absolute boundary layer thickness δ and flame position y_b (left) and dimensionless boundary layer thickness δ/D and flame position y_b/D (right) as a function of the dimensionless position x/L and time (right).

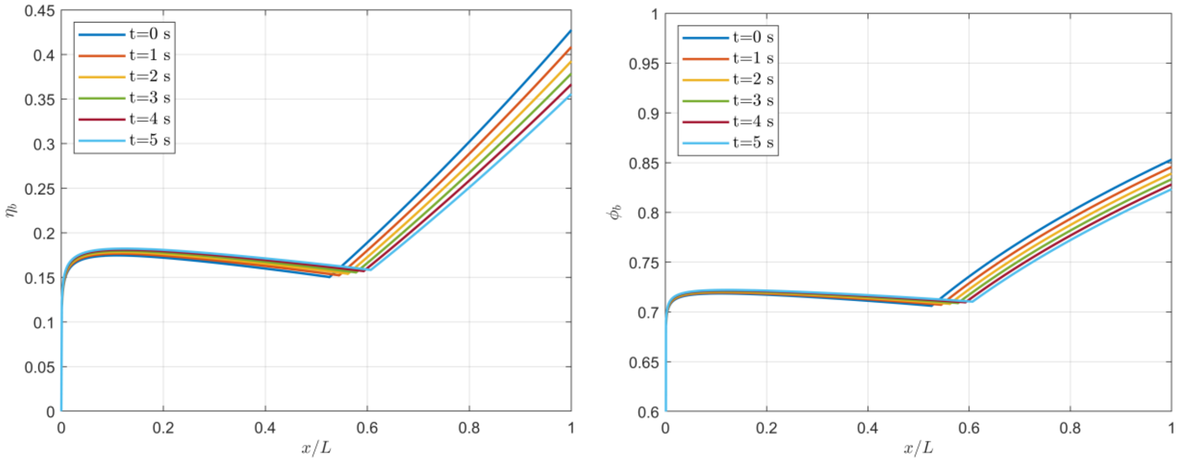

Figure 7.9: Dimensionless flame position η_b (left) and velocity ϕ_b (right) as a function of the dimensionless position x/L and time.

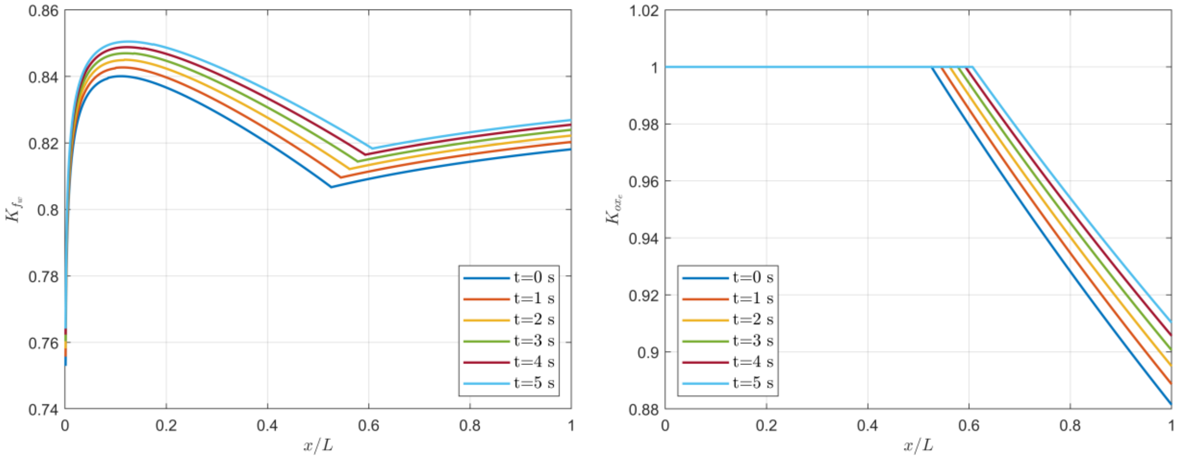

Figure 7.10: Fuel mass fraction at the wall K_{f_w} (left) and oxidizer mass fraction at the duct axis K_{ox_e} (right) as a function of the dimensionless position x/L.

Finally, the 1D with boundary layer model provide the propellant combustion efficiency (Fig.7.11) and the combustion efficiency (Fig.7.12). Therefore, all the parameter needed to evaluate the result of the preliminary design are obtained.

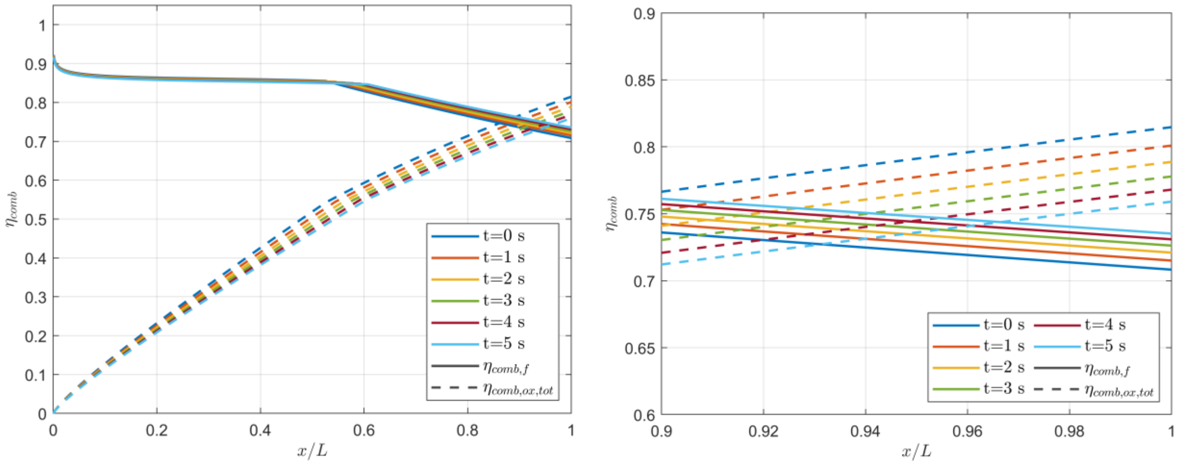

Figure 7.11: Propellant combustion efficiencies as a function of the dimensionless position x/L and time.

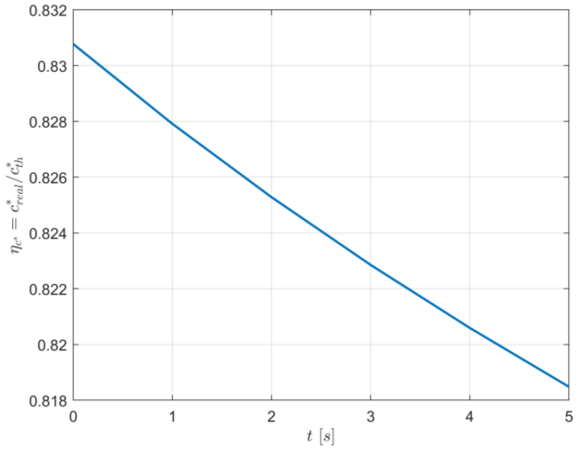

Figure 7.12: Combustion efficiency η_{c^*} as a function of time.

7.3 Comparison of the Numerical Results with Experimental Data

Unfortunately, most of the experimental and numerical simulations data are more focused on the evaluation of the regression rate rather than the internal ballistics and the combustion efficiency. Acknowledging the low combustion efficiency typical of a hybrid engine (of the order of 70-90%), most real engine and thus experimental configuration incorporates mixing devices (e.g. diaphragms within the fuel port or mixing devices in the post chamber), which are not considered in this work. Under this consideration, the validation of the present model is not so simple and requires an extensive numerical analysis through numerical fluid dynamics simulations in which the variation of several parameters (e.g. engine size, oxidizer mass flow, type of oxidizer) has to be evaluated.

A preliminary validation of the presented 1D with boundary layer model it is done through the comparison between the numerical results and the experimental data collected about the scaling effects in hybrid rocket motors [18]. In this test program $PMMA$ (Plexiglas) was used as the fuel grain and gaseous oxygen (GOX) was used as oxidizer. The stoichiometric reaction for oxygen $PMMA$ system is:

$$C_5O_2H_8 + 6O_2 \rightarrow 5CO_2 + 4H_2O \tag{7.5}$$

Therefore, the stoichiometric O/F ratios are $[O/F]_{st\,(O_2),molar} = 6$ and $[O/F]_{st\,(O_2),mass} = 1.92$.

The tested motors had initial port diameters of $7.5, 10, 15, 23, 34$ and $40\ mm$ and initial geometric proportions, length-to-port diameter ratio, $L/D = 10$. The chamber pressure was always higher than 25 bar in all of the tests, therefore also in the simulations the throat area is sized to verify this condition. Fig.7.13 shows the test setup. At the head end of the grain an aft mixing chamber is placed, followed by a converging nozzle. The motor test duration was scaled linearly with motor initial port diameter, i.e. $t_b \propto D$, up to a maximum value of $16\ s$ for motors of initial port diameter equal to or higher than $34\ mm$. Two test series were carried out, series I at approximately constant value of $\dot{m}_{ox}/D = 15\ g/(s \cdot cm)$ $\left(G_{ox}D = 19\ g/(s \cdot cm)\right)$ and series II at approximately constant value of $\dot{m}_{ox}/D = 8\ g/(s \cdot cm)$ $\left(G_{ox}D = 10\ g/(s \cdot cm)\right)$.

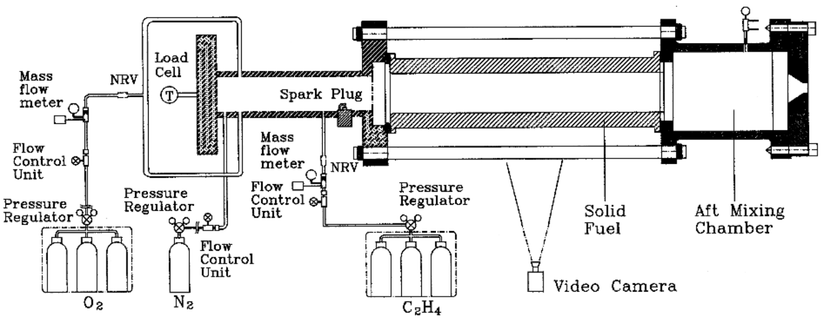

Figure 7.13: Hybrid rocket test setup [18].

Fig.14 (left) shows the test results on the combustion efficiency (defined as the ratio between the experimental and theoretical characteristic velocity c^*), which has a pretty constant value of the order of $0.8 - 0.9$ for the entire range in both series.

The combustion efficiency values calculated with the 1D with boundary layer model for the same test series are expected to be similar but in the lower range of the experimental one, because of the absence of the aft mixing chamber. Fig.14 (right) summarizes the numerical result using the same motor characteristics (initial port diameter and grain length, burn time, initial oxidizer mass flux). The numerical results are in good agreement with the experimental data. The deviation from the experimental results is presumably due to the differences with the real experimental apparatus. The higher values of combustion efficiency in the experimental data are certainly due to the presence of the mixing chamber, while the deviation from the lower efficiencies is attributable to the lack of heat exchange with the external environment that is instead present in the experimental test [18]. In addition, the uncertainty about the actual value of the regression rate coefficients a, n, m contributes to the deviation from the experimental results.

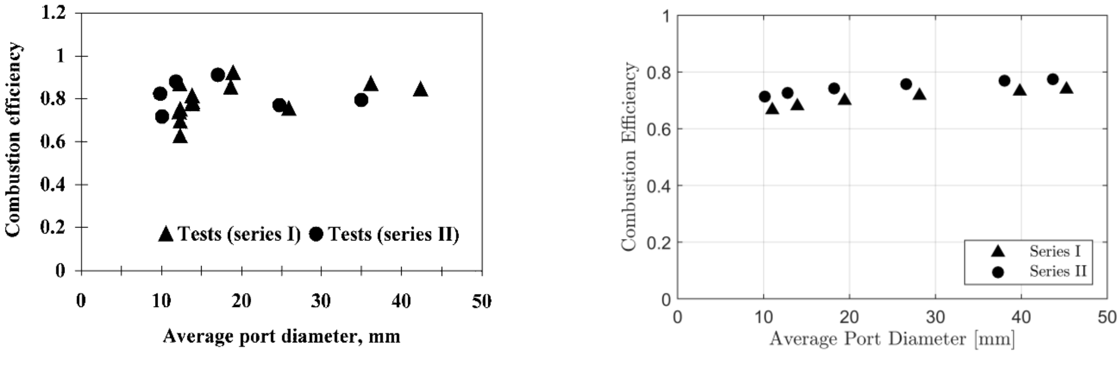

Figure 7.14: Variation of combustion efficiency with combustor average port diameter from experimental tests [18] (left) and obtained with the proposed 1D with boundary layer model (right).

Fig.15 shows the comparison between the thrust values for the two test series obtained experimentally [18] and the corresponding values obtained in the numerical simulation. Although there are some differences probably due to the error in the regression rate coefficient values, the trend and the values of the engine thrust obtained numerically is in good agreement with the experimental data.

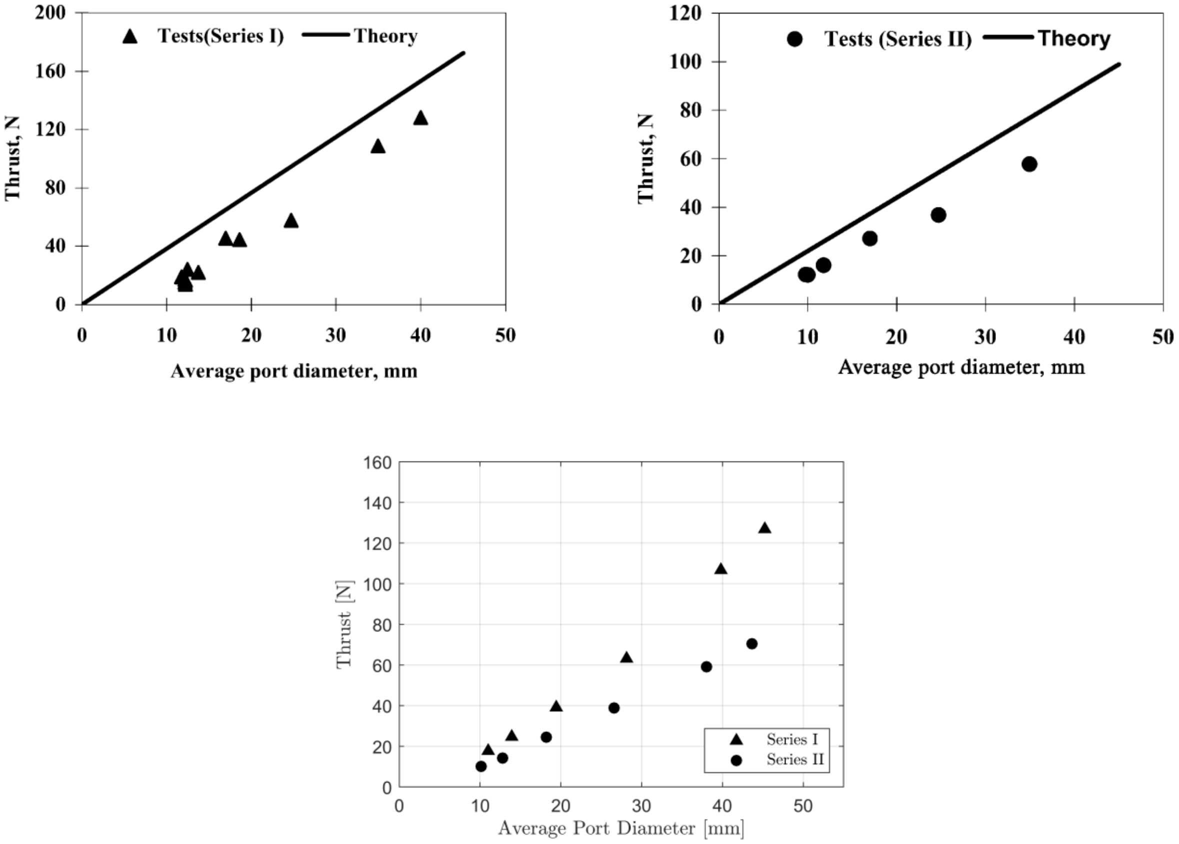

Figure 7.15: Motor thrust variation with port diameter for Series I (top left) and Series II (top right) measured experimentally [18] and numerically simulated (bottom).

Chapter 8

Summary and Conclusions

In this work, several models have been proposed that can be integrated into a system design tool for the preliminary sizing of a hybrid engine using classic propellants. The use of those models, which can be easily implemented in a MATLAB code, allows to obtain a good compromise between simplicity (and therefore the computational cost) and accuracy of the results.

The accurate description of Marxman's theory made it possible to evaluate which are the key parameters that influences the combustion in a hybrid engine. Despite the many simplifications made in this theory, it still represents an excellent starting point for more complex and exhaustive studies. Starting from the hybrid combustion theory, one of the possible algorithms for the preliminary sizing of a hybrid engine has been proposed, and the effects of the design choices analysed. A 0D model was then provided, with which it is possible to verify the actual achievement of the mission requirements by the designed engine. The accurate description of the engine's performance must necessarily pass through the study of internal ballistics. In Chapter 5 a simple quasi-stationary 1D model based on the equations of continuity, momentum, energy and the equation of state of ideal gases has been proposed. The model allows to describe the internal ballistics of a hybrid engine and to appreciate the effect of changing the design parameters.

The limit of the proposed 1D model is related to the lack of knowledge of the reactants mass flow participating to the combustion. For this reason, a model of the boundary layer inside the combustion chamber was developed, with the aim of providing, albeit in an approximate way, a description of the fluid dynamics inside the grain port. In the proposed model, some corrections have been made to Marxman's theory to make it more valid in the case of a closed duct. The key element of this model is the analogy between the reactive (i.e. with combustion) and the non-reactive boundary layers. This analogy allows to solve the main problems of Marxman's theory. In fact, with this theory, when applied in closed duct configurations, the mass continuity does not verify either the flame position where the O/F ratio is equal to the stoichiometric one or the boundary layer thickness. First, the actual fuel mass fraction (lower than unity) was evaluated from the general theory of evaporation of a liquid film in a fluid stream. In the analogy with the non-reactive case, it was therefore assumed that the thickness of the boundary layer must be the one that guarantees the respect of mass conservation if no combustion process takes place. The validity of this analogy is guaranteed by the hypothesis of constant and uniform density, and that the combustion does not alter the velocity profile within the boundary layer.

Using the diffusive flame combustion theory, the position of the flame was also estimated. However, numerical simulations have pointed out that this position does not actually guarantee the correct oxidizer to fuel ratio at the flame. Therefore, for consistency in the entire model, it has been chosen to not use this analogy to identify the flame position but rather use the mass conservation condition.

Another problem that arises when considering a closed duct is to understand what happens after the merging of the boundary layer. In this condition, the diffusion of combustion products towards the centre of the duct and of the oxidant towards the flame tend to reduce the oxidizer mass fraction at the duct axis, once more described with the non-reactive case analogy. To verify the correct dosage ratio at the reaction zone, the flame must necessarily move towards the duct centre. When the flame reaches the axis, all the oxidizer injected into the combustion chamber has been burn. From this point on, the sublimation of the grain produces a dilution of the main flow.

After describing the bases of the proposed model, three configurations have been presented: flat plate in an open environment, rectangular port duct with two active walls and circular port duct. While in the case of flat plate the differences with Marxman's theory are minimal, already in the case of rectangular duct some differences can be identified and in the case of circular port duct the typical characteristics of a hybrid engine can be appreciated. In the cases of closed ducts, the calculation domain has been divided into two control volumes, inside the boundary layer and the core flow, coupled by the boundary conditions at the boundary layer edge. The division of the channel into developing flow and fully developed flow regions made it possible to distinguish the degrees of freedom of the problem. In both zones, the conditions to be verified are based on continuity: the verification of the oxidizer to fuel ratio at the flame (imposed to be equal to the stoichiometric one) and of the mass continuity on the cross-section of the duct. The missing information, i.e. the boundary layer thickness before merging and the oxidizer mass fraction at the duct axis after, were obtained from the analogy with the non-reactive case. The parametric study of the boundary layer with hybrid combustion inside a circular port grain made it possible to highlight some peculiarities of this type of system. It has been observed that the boundary layer reaches the merging condition around $10\ D$, a value that is mainly dependent on the port size and on the oxidizer mass flux injected into the combustion chamber. The position in which the flame reaches the duct axis, on the other hand, is greatly influenced by the type of oxidizer used, in particular whether it is diluted or not. In the case where the oxidizer is pure oxygen, the flame reaches the duct axis of the around $25 - 30\ D$, while in the case where the oxidizer is diluted, this position is around $15\ D$. In addition, the dilution of the oxidizer plays a fundamental role on the position in which the local O/F ratio is equal to the stoichiometric one, which in turns is generally close to that required globally by the engine to optimize performances. If the oxidizer is sufficiently diluted, this condition occurs before the merging of the boundary layer, resulting in a much shorter engine. On the other hand, if the oxidizer is not diluted, this condition is reached in an intermediate position between that of boundary layer merging and the one in which the flame reaches the axis of the duct. In particular, it has been confirmed that for a hybrid engine it is not possible to obtain a high efficiency in the use of propellant and therefore a high combustion efficiency for fuel and oxidizer at the same time. In fact, the complete consumption of one of the two reactants requires the use of a large amount of the other, which ultimately remains in the main stream.

In chapter 7 the 1D with boundary layer model has been proposed. This model couples the 1D model for the study of internal ballistics with the boundary layer model to evaluate the actual amount of reactants participating in the combustion process. The main goal of this model, apart from the characterization of the internal ballistics, is to provide an estimate of the combustion efficiency when the engine configuration does not involve the use of mixing enhancing devices (e.g. diaphragms, mixing chambers). This model can then be integrated into a system design tool for the preliminary design of a hybrid engine using classic propellants. The preliminary validation of the model was carried out by comparing the results of the numerical simulations with those obtained experimentally [18]. Except for small differences, the obtained results are in good agreement with what has been experimentally evaluated.

The further validation of the proposed model requires future work based on computational fluid dynamics numerical simulations and experimental tests, with the aim of better characterizing the behaviour of the boundary layer (especially in the modelling of its variable-density characteristic), the effect of the design parameters and to evaluate the possibility to extend the model (with appropriate corrections) also to liquefying propellants.

Bibliography

[1] Incropera, Frank P. *Fundamentals of Heat and Mass Transfer*. 6. ed, J. Wiley, 2007.

[2] Anderson, John David. *Modern Compressible Flow: With Historical Perspective*. 2. ed, McGraw-Hill, 1990.

[3] Sutton, George P. *Rocket Propulsion Elements*. 9. ed., Wiley, 2017.

[4] Humble, Ronald W., et al. *Space Propulsion Analysis and Design*. Revised ed, The McGraw-Hill companies, 1995.

[5] Kuo, Kenneth K., and Martin J. Chiaverini, eds. *Fundamentals of hybrid rocket combustion and propulsion*. American Institute of Aeronautics and Astronautics, 2007.

[6] Karabeyoglu, M. Arif, Brian J. Cantwell, and Greg Zilliac. "*Development of scalable space-time averaged regression rate expressions for hybrid rockets*." 41st AIAA/ASME/ASEE Joint Propulsion Conference, Tucson AZ, July 2005.

[7] Marquardt, Timohty, and Joseph Majdalani. "*A Primer on Classical Regression Rate Modeling in Hybrid Rockets*." AIAA Propulsion and Energy 2020 Forum. 2020.

[8] Marxman, Gerald A. "*Combustion in the turbulent boundary layer on a vaporizing surface*." Symposium (International) on Combustion. Vol. 10. No. 1. Elsevier, 1965.

[9] Marxman, G. A., C. E. Wooldridge, and R. J. Muzzy. "*Fundamentals of hybrid boundary-layer combustion*." Progress in Astronautics and Rocketry. Vol. 15. Elsevier, 1964. 485-522.

[10] Zilliac, Gregory, and M. Karabeyoglu. "*Hybrid rocket fuel regression rate data and modeling*." 42nd AIAA/ASME/SAE/ASEE Joint Propulsion Conference & Exhibit. 2006.

[11] Marxman, G., and M. Gilbert. "*Turbulent boundary layer combustion in the hybrid rocket*." Symposium (International) on Combustion. Vol. 9. No. 1. Elsevier, 1963.

[12] Cpropep (thermochemical code).

[13] Barato, Francesco, Enrico Paccagnella, and Daniele Pavarin. "*Explicit analytical equations for single port hybrid rocket combustion chamber sizing*." Journal of Propulsion and Power 36.6 (2020): 869-886.

[14] Faenza, M., Barato, F., Lazzarin, M., & Pavarin, D. (2015). *Hybrid Rocket Motor Regression Rate Prediction trough CFD Simulations*. In 6th European Conference for Aeronautics and Space Sciences (EUCASS) 2015.

[15] Rampazzo, Alessandro, and Francesco Barato. "*Modeling and CFD simulation of regression rate in hybrid rocket motors*." Fire 6.3 (2023): 100.

[16] F. Barato. "*Numerical and Experimental Investigation of Hybrid Rocket Motors Transient Behavior*". PhD thesis. Università degli Studi di Padova, 2013.

[17] Bellomo, N., Lazzarin, M., Barato, F., & Grosse, M. (2010, July). *Numerical Investigation of the Effect of a Diaphragm on the Performance of a Hybrid Rocket Motor*. In 46th AIAA/ASME/SAE/ASEE Joint Propulsion Conference & Exhibit (p. 7033).

[18] Swami, R. D., & Gany, A. (2003). *Analysis and testing of similarity and scale effects in hybrid rocket motors*. Acta Astronautica, 52(8), 619-628.

[19] Bonacina, Cesare, et al. *Trasmissione del calore*. 3. ed. rist. riv, CLEUP, 1987.

[20] Schlichting, Hermann, and Klaus Gersten. *Boundary-layer theory*. springer, 2016.

[21] Kundu, Pijush K., Ira M. Cohen, and David R. Dowling. *Fluid mechanics*. Academic press, 2015.

[22] Gerhart, Philip M., Andrew L. Gerhart, and John I. Hochstein. Munson, Young and Okiishi's. *Fundamentals of fluid mechanics*. John Wiley & Sons, 2016.

[23] Cavallini, Alberto, e Lino Mattarolo. *Termodinamica applicata*. 2. rist. riveduta e Corretta, Cleup, 1992.

[24] Anderson, John, *Fundamentals of Aerodynamics*. McGraw-Hill, 2017.

[25] Alessandro Rampazzo, Francesco Barato, Daniele Pavarin. "*Investigation of the influence of gas phase molecular mass variations on hybrid rocket regression rate*". 74th International Astronautical Congress (IAC). IAC-23-C4.4.5.

[26] Maurice J. Zucrow, Joe D. Hoffman. *Gas Dynamics*, Volume I. New York: J. Wiley, 1976.

[27] Shapiro, A.H., *The Dynamics and Thermodynamics of Compressible Fluid Flow*, 2 vols., Ronald, New York, 1953

[28] Carmicino, C. "*Alcuni aspetti della balistica interna di un endoreattore a propellenti ibridi e del comportamento di ugelli a spina troncata*". PhD thesis. Università degli studi di Napoli Federico II, 2002.

[29] Karp, Ashley Chandler, and Elizabeth Therese Jens. *Hybrid Rocket Propulsion Design Handbook*. Academic Press, 2023.

[30] Netzer, David W. *Hybrid Rocket Internal Ballistics*. Laurel, MD: Chemical Propulsion Information Agency, 1972.

[31] Karabeyoglu, Arif, Brian Cantwell, and Jose Stevens. "*Evaluation of the homologous series of normal alkanes as hybrid rocket fuels*." 41st AIAA/ASME/SAE/ASEE Joint Propulsion Conference & Exhibit. 2005.

[32] Pierre, T., and V. Philippe. "*Heat and mass transfer analogies for evaporation models at high evaporation rate*." 6th AIAA Atmospheric and Space Environments Conference, American Institute of Aeronautics and Astronautics. 2014.

[33] Turns, Stephen R. *An Introduction to Combustion : Concepts and Applications*. 2. ed, McGraw-Hill, 2000.

[34] MIZUSHINA, TOKURO, et al. "*Flow in the entrance region of a circular tube*." *JOURNAL OF CHEMICAL ENGINEERING OF JAPAN* 3.1 (1970): 34-38.

[35] Na, Tsung-Yen, and Y. P. Lu. "*Turbulent flow development characteristics in channel inlets*." Applied Scientific Research 27 (1973): 425-439.

[36] Prandtl, Ludwig. "*Report on investigation of developed turbulence*." *Zeitschrift fuer Angewandte Matematik und Mechanik* 5.NACA-TM-1231 (1949).

[37] Nikuradse, Johann. "*Laws of flow in rough pipes*." (1950).

[38] Barato, Francesco, Elena Toson, and Daniele Pavarin. "*Variations and control of thrust and mixture ratio in hybrid rocket motors*." Advances in Astronautics Science and Technology 4 (2021): 55-76.

[39] Jens, Elizabeth T., Victor A. Miller, and Brian J. Cantwell. "*Schlieren and OH* chemiluminescence imaging of combustion in a turbulent boundary layer over a solid fuel*." Experiments in Fluids 57.3 (2016): 39.

[40] Gariani, Gabriela, Filippo Maggi, and Luciano Galfetti. "*Numerical simulation of HTPB combustion in a 2D hybrid slab combustor*." Acta Astronautica 69.5-6 (2011): 289-296.

[41] Merotto, Laura, and Alessandro Mazzetti. "*Numerical simulations of combustion processes in hybrid rocket engines using OpenFoam and COOLFluiD codes*." Proc., 5th European Conf. for Aeronautics and Space Sciences, EUCASS Association, Munich, Germany. 2013.

[42] Rouvreau, S., Joulain, P., Wang, H. Y., Cordeiro, P., & Torero, J. L. (2002). *Numerical evaluation of boundary-layer assumptions used for the prediction of the standoff distance of a laminar diffusion flame*. Proceedings of the Combustion Institute, 29(2), 2527-2534.

[43] Funami, Yuki, and Toru Shimada. "*Hybrid Rocket Performance Prediction with Coupling Method of CFD and Thermal Conduction Calculation*." Transactions of the Japan

Society for Aeronautical and Space Sciences, Aerospace Technology Japan 10.ists28 (2012): Pa_71-Pa_76.

[44] Funami, Yuki, and Toru Shimada. "*Numerical evaluation of hybrid rocket internal ballistics with thermal radiation effect*." Transactions of the Japan Society for Aeronautical and Space Sciences, Aerospace Technology Japan 12.ists29 (2014): Pa_21-Pa_30.

[45] Ueda, T., Ooshima, A., Saito, N., & Mizomoto, M. (1991). *Aerodynamic structure of a laminar boundary layer diffusion flame over a horizontal flat plate: experimental analysis*. JSME international journal. Ser. 2, Fluids engineering, heat transfer, power, combustion, thermophysical properties, 34(4), 527-532.

[46] Paul, P. J., H. S. Mukunda, and V. K. Jain. "*Regression rates in boundary layer combustion*." Symposium (International) on Combustion. Vol. 19. No. 1. Elsevier, 1982.

[47] SENDA, Mamoru, Kenjiro SUZUKI, and Takashi SATO. "*Study on turbulent boundary layer with injection and combustion*." Memoirs of the Faculty of Engineering, Kyoto University 38.1 (1976): 21-36.

[48] Boyarshinov, B.F., Volchkov, É.P. & Terekhov, V.I. *Structure of a boundary layer with injection and combustion of ethanol*. Combust Explos Shock Waves 28, 235–242 (1992).

[49] Jens, Elizabeth T. *Hybrid rocket combustion and applications to space exploration missions*. Stanford University, 2015.

[50] Ananth, R., Tatem, P.A., and Ndubizu, C.C., "*A numerical Model for the Development of a Boundary Layer Diffusion Flame Over a Porous Flat Plate*", NRL Memorandum Report NRL/MR/6183-01-8547, Naval Research Laboratory, Washington, DC, 2001.

[51] Zilliac, G., Story, G. T., Karp, A. C., Jens, E. T., & Whittinghill, G. (2020). *Combustion efficiency in single port hybrid rocket engines*. In AIAA Propulsion and Energy 2020 Forum (p. 3746).

[52] Volchkov, E. P., Viktor Ivanovich Terekhov, and Vladimir Victorovich Terekhov. "*Flow structure and heat and mass transfer in boundary layers with injection of chemically reacting substances (Review)*." Combustion, Explosion and Shock Waves 40 (2004): 1-16.

[53] Lukashov, Vladimir Vladimirovich, Vladimir Victorovich Terekhov, and Viktor Ivanovich Terekhov. "*Near-wall flows of chemical reactants: A review of the current status of the problem*." Combustion, Explosion, and Shock Waves 51 (2015): 160-172.

[54] Durand, J. É., Raynaud, F., Lestrade, J. Y., & Anthoine, J. (2019). *Turbulence modeling effects on fuel regression rate in hybrid rocket numerical simulations*. Journal of Propulsion and Power, 35(6), 1127-1142.

[55] Volchkov, E. P., Vladimir Victorovich Terekhov, and Viktor Ivanovich Terekhov. "*Effect of flow history on combustion in a laminar boundary layer*." Combustion, Explosion, and Shock Waves 46 (2010): 615-622.

[56] Conte, A., Contadin, S., Karp, A. C., Jens, E. T., Vaughan, D., & Pastrone, D. G. (2017). *CFD Simulation of Hybrid Rocket Motors for Interplanetary CubeSats*. *7th*, 3-6.

[57] Coronetti, Andrea, and William A. Sirignano. "*Numerical analysis of hybrid rocket combustion*." Journal of Propulsion and Power 29.2 (2013): 371-384.

[58] Quero Granado, E., Hijlkema, J., Lestrade, J. Y., & Anthoine, J. (2021). *Development and Validation of a 1.5-D Combustion Chamber Model for a Hybrid Rocket Engine Applied to a Cylindrical HDPE Chamber*. In AIAA Propulsion and Energy 2021 Forum (p. 3495).

[59] Granado, E. Q., Hijlkema, J., Lestrade, J. Y., & Anthoine, J. (2022, June). *Parametric study of a 1.5-D combustion chamber model on the hybrid rocket engine performances.* In 9TH EUROPEAN CONFERENCE FOR AERONAUTICS AND SPACE SCIENCES EUCASS-3AF 2022.

[60] Granado, E. Q., Pelenghi, G., Hijlkema, J., Anthoine, J., & Lestrade, J. Y. (2022, September). *A new system design tool for a hybrid rocket engine application*. In 73rd International Astronautical Congress (IAC 2022).

[61] Quero Granado, E., Hijlkema, J., Lestrade, J. Y., & Anthoine, J. (2022). *Pseudo-Two-Dimensional Modeling and Validation of a Hybrid Rocket Combustion Chamber*. Journal of Propulsion and Power, 38(6), 957-972.

[62] Karabeyoglu, M. A., Altman, D., & Cantwell, B. J. (2002). *Combustion of liquefying hybrid propellants: Part 1, general theory*. Journal of propulsion and power, 18(3), 610-620.

[63] Karabeyoglu, M. A., & Cantwell, B. J. (2002). *Combustion of liquefying hybrid propellants: Part 2, stability of liquid films*. Journal of Propulsion and Power, 18(3), 621-630.

[64] Theba, R., Veale, K. L., & Bemont, C. P. (2017). *Development of a combustion visualisation hybrid rocket motor*. *R&D Journal*, *33*, 97-104.

[65] Chandler, A. A., Jens, E. T., Cantwell, B. J., & Hubbard, G. S. (2012, October). *Visualization of the liquid layer combustion of paraffin fuel at elevated pressures*. In 63rd International Astronautical Congress. Paris, France: International Astronautical Federation (IAF).

[66] Carmicino, C., & Sorge, A. R. (2006). *Influence of a conical axial injector on hybrid rocket performance*. Journal of Propulsion and Power, 22(5), 984-995.

[67] Carmicino, C., & Sorge, A. R. (2005). *Role of injection in hybrid rockets regression rate behaviour*. Journal of propulsion and power, 21(4), 606-612.

[68] Karabeyoglu, M. A., De Zilwa, S., Cantwell, B., & Zilliac, G. (2005). *Modeling of hybrid rocket low frequency instabilities.* Journal of propulsion and power, 21(6), 1107-1116.

[69] Paccagnella, E., Barato, F., Pavarin, D., & Karabeyoğlu, A. (2017). *Scaling parameters of swirling oxidizer injection in hybrid rocket motors*. Journal of Propulsion and Power, 33(6), 1378-1394.

[70] Glassman, Irvin, et al. *Combustion*. 5. ed., Academic press, 2015.